271724

MASSACHUSETTS INSTITUTE OF TECHNOLOGY
LINCOLN LABORATORY

PHASED ARRAY RADAR STUDIES

1 JULY 1960 to 1 JULY 1961

J. L. ALLEN   A. J. FALLO   J. R. SKLAR

L. CARTLEDGE   W. J. INCE   S. SPOERRI

W. P. DELANEY   K. SIEGEL   J. H. TEELE

J. DiBARTOLO   D. H. TEMME

Group 41

E. A. DAVIDSON

Group 71

TECHNICAL REPORT NO. 236

13 NOVEMBER 1961

TISIA   A

Best Available Copy
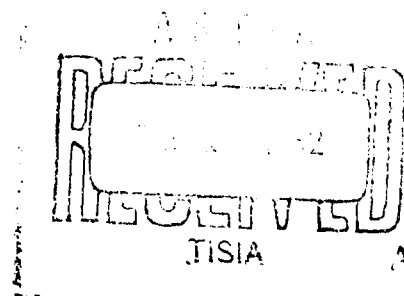
ABSTRACT

This is the second in a series of reports describing the work of the
Lincoln Laboratory phased array project. This report covers the
period from 1 July 1960 to 1 July 1961; the effort prior to this time
is covered in Lincoln Laboratory Technical Report No. 228.

The project effort is mainly directed toward investigation of com-
ponents, techniques and the fundamental theoretical limitations of
arrays for long-range radar applications.

Research on components for arrays continues to cover a broad spec-
trum of effort, including such diverse topics as low-noise RF ampli-
fiers, high-power modular transmitters, high-speed building blocks
for data-processing systems, high-speed microwave switches and
several types of phase-shifting devices. The techniques work has
seen increased emphasis on low-loss simultaneous beam-forming
techniques for array receivers, with decreased interest in configu-
rations requiring a complete receiver behind each antenna. Studies
of various radar problems of interest to this group have indicated
that the most technically feasible approach to the transmitter prob-
lem remains that of a separate transmitter behind each element.
Several innovations on this technique point toward realizing relatively
inexpensive transmitter modules. The techniques of controlling and
monitoring arrays making use of the transmitting and receiving ap-
proaches outlined above are also under investigation.

The linear test array continues to be operated as both a usable test
radar and a useful test bed for already developed components. The
results obtained to date on life tests of some of the earlier compo-
nents are reported, and modifications suggested by the experience
with these components are outlined.

Studies of the fundamentals of arrays have been largely confined to
efforts toward better understanding of the phenomena of mutual cou-
pling in antenna arrays and the effects of "errors," both unintentional
and intentional, on the properties of array patterns. The question of
the bandwidth of "phased" arrays has also received some considera-
tion as reported herein.

All these activities are guided and directed by continuing studies of
systems applications of long-range arrays. Since these studies are
classified, they are not reported in this document.

TABLE OF CONTENTS

ACKNOWLEDGMENT

PART 1

INTRODUCTORY MATERIAL

CHAPTER I
PROJECT AND REPORT ORGANIZATION
J.L. Allen

A. INTRODUCTION

This report describes the activity for the period 1 July 1960 to 1 July 1961 of the phased array radar program carried out by members of the Special Radars Group of Lincoln Laboratory. This is the second report of this project, the first being Lincoln Laboratory Technical Report No. 228.[*]

This report, like the earlier one, is in the nature of a progress report and reports all work carried out during the stated period, plus work still in progress. The work is reported in considerable detail, each section being written by the engineer directly responsible for the investigation. The report is largely intended for other workers in the field, and is so written.

B. PROJECT PHILOSOPHY

The past few years have seen a marked increase in interest in array radars as a solution to long-range radar problems. This increased interest has further served to point out the need for the development of improved techniques and components for array radars. This project was conceived to help fulfill this need by concentrating efforts on the conception, design, construction and continued improvement in techniques and components for such arrays.

Whereas a separate project concerned only with the development of components and techniques might sometimes have been of questionable value in the conventional radar environment, it is clear that such work assumes a new important stature in the array radar environment. The justification for this statement lies in the fact that array radars are composed of very large numbers of duplicate parts, with only a few distinct types being used. This situation is directly analogous to that commonly encountered in digital computers. That is, just as manufacturers of "building blocks" for digital computers have made possible the economic and speedy construction of such computers, the development of such components for arrays can make possible the reasonably economical and rapid construction of array radars. Indeed, with the present interest on "one-of-a-kind" arrays on the part of the various using agencies, an effort toward standardizing components for arrays may represent the only method for realizing the mass production economics commonly associated with array construction. For example, our studies and conversations with tube manufacturers have indicated that the ultimate low cost in transmitting tube development is not realized until a manufacturer reaches the level of a sustained production of hundreds or thousands of tubes per month. Thus, it is clear that one large array, even if any associated development costs are discounted, cannot realize true production economy on a one-of-a-kind basis.

Thus, guided by systems studies of potential long-range radar uses (such as satellite surveillance and tracking, and missile detection and discrimination), the members of this project are attempting to help fulfill the need for "building blocks" for long-range array use. Toward this

---

[*] J.L. Allen, et al., "Phased Array Radar Studies, 1 July 1959 to 1 July 1960," Technical Report No. 228 [U], Lincoln Laboratory, M.I.T. (12 August 1960), ASTIA 249470, H-335.

y d. in addition to the direct wor'c in component gn and development, special test facilities have been constructed for thoroughly testing such ts in appropriate environments over long periods of time. These test facilities are modif' from time to time as required to keep track of changing parameters in component development.

In order to guide the technique and compone 1 velopment, in addition to the systems studies previously mentioned, a continuing program of ies of the fundamental limitations of arrays is carried out.

To be of maximum benefit to the over-all fort, a project such as this must maintain a high degree of information interchange with ot workers in array technology. Members of this project have continued their attempt to main i close contact with similar work by other organizations and have encouraged others to become familiar with this effort. Publication of reports such that reports only part of the effort in this direction. We attempt to maintain personal contact with other government-supported array work in the country and have in the past encouraged workers in both government and industry visit with us here at the Laboratory. Despite the burden that such visits impose upon the available time of personnel, it is felt that the results have been well worth while, and it is intended to continue this policy in the future. In order to maximize the utility of future meetings, however, it is hoped that those contemplating discussion with us will first avail themselves of the background information contained in this report and in TR-228 on subjects of interest.

C. REPORT CONTENTS AND ORGANIZATION

As stated in the Introduction, this report is in the nature of a progress report, describing the work both completed and in progress during the reporting period covered. We have attempted to report all the significant work in detail, including projects that were unsuccessful, where the lack of success would be meaningful to others in the field.

Since the responsibility for various facets of the projects has been undertaken by individual engineers, the report has been written by the people directly concerned, with a minimum of alteration on the part of the editors. In order to promote further interchange on the topics discussed, the authors of the individual sections have been cited with the appropriate sections. Where no author's name appears on the section, the author is the same as the name given on the next highest division of the report.

Since the individual sections of the report are written by people quite close to the material on which they are writing, the report runs the usual danger in that authors may be guilty of presuming considerable prior knowledge of the subject on the part of the reader. The editors have attempted, within the bounds of reasonable limits, to encourage the authors to give sufficient background information or references to enable the interested person to profit from the material contained herein. Also, each chapter of the report has been preceded by a brief summary of the material contained therein. These summaries, along with the Table of Contents, should enable the casually interested reader to easily grasp the over-all content of the report and hopefully direct the interested reader to material of primary interest to him.

The report is divided into three parts. The first contains the introductory material, a summary of the test facilities of the project, and the information that has been gleaned from the past year's operation of various components in the test facility. The second part deals with the component and technique development of the project and is subdivided into one chapter for each major area of component and technique development. Part 3 deals with the supporting studies of the array fundamentals.

2

CHAPTER II

TEST FACILITY

Edited by S. Spoerri

A. INTRODUCTION AND SUMMARY

This chapter provides a brief description of the current Group 44 facilities for the testing of array components and techniques. The over-all performance of the linear array radar facility with its present components is also discussed.

The test facility described in TR-228 has been expanded and improved since the writing of that report. The original equipment complex is referred to here as the linear array radar facility to differentiate it from the high-power testing facility and the transmitter test facility which have now been added.

The linear array radar facility occupies one large room of the Building C penthouse in addition to the 55-foot rigid radome (Fig. 1-1). The transmitter test facility is housed in a new penthouse which was erected to the right of the main penthouse. The high-power testing facility occupies a room adjoining the linear array facility in the main Building C penthouse. It is centrally located between the various RF power sources whose outputs are brought into the room through high-power transmission lines.

A more detailed description of the various test facilities is given in the following sections by the persons primarily responsible.

B. LINEAR ARRAY RADAR FACILITY   S. Spoerri

1. Descriptive Summary

The linear array radar facility is an outgrowth of the test facility described in TR-228. This section provides a brief description of the components that make up the linear array radar facility. More detailed descriptions of some of the parts are provided in other sections of this chapter, in Part 2 of this report and, in some cases, in TR-228.

Receiving Antenna and Feed System:— The receiving antenna for the linear array radar facility is a solid-surfaced, offset-fed, parabolic cylinder. The reflector, shown in Figs. 1-2 and 1-3, has a vertical aperture of 15 feet, a horizontal width of 22 feet and a focal length of 5 feet. The reflector is provided with mounting arms capable of supporting a 10-foot linear array and the associated electronic equipment mounted in a box suspended below the antenna array bridge.

The present feed consists of (nominally)* vertically polarized, log-periodic elements spaced 0.58 λ. The 16 log-periodic elements will be replaced by dipoles in the near future.

The entire structure is mounted in a 55-foot rigid radome on the roof of one of the Lincoln Laboratory buildings.

Radar Transmitter and Transmitting Antenna:— Figure 1-3 shows the transmitter antenna mounted on the back of the receiving antenna reflector. It is used with the radar transmitter to illuminate a 90° azimuth sector (with a 5° elevation beamwidth) so that the linear array receiver and data-processing equipment can be tested in a radar environment.

The transmitter antenna, constructed by D. S. Kennedy & Company, consists of a waveguide-fed array of vertically polarized dipoles.

---

* See Part 2, Ch. II.

3
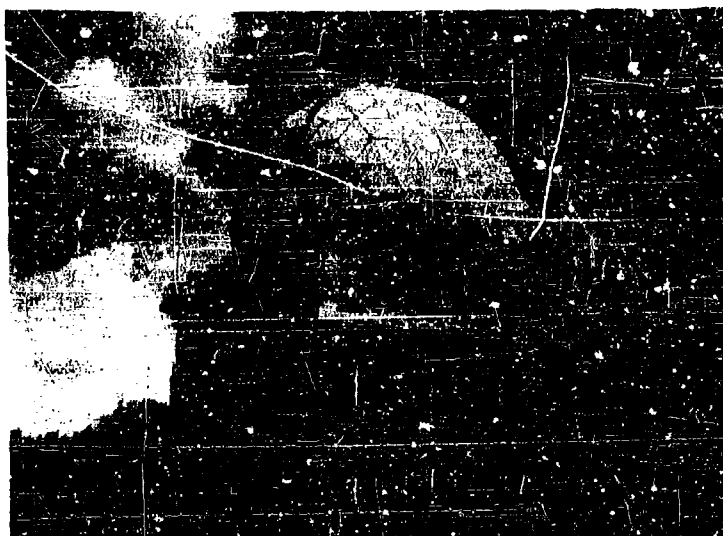
Fig. 1-1. Penthouse and radome.

Fig. 1-2. Photograph of test facility reflector and array mount (through wide-angle lens).
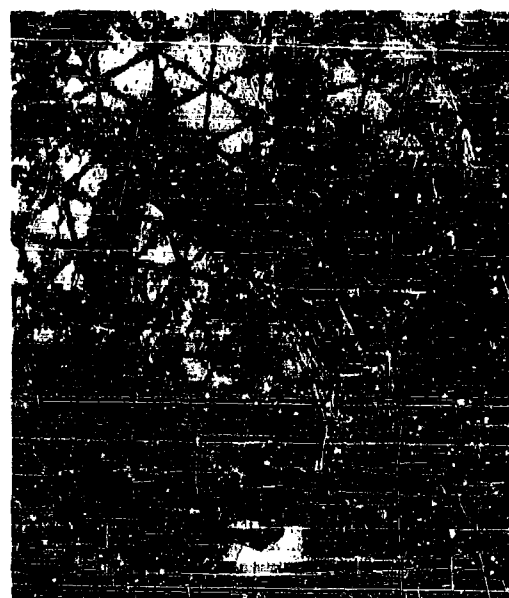
Fig. 1-3. Transmitting antenna mounted on present receiving reflector.

The radar transmitter produces up to 20 kw of peak power and 200 watts of average power at a pulsewidth of 10 μsec. The operating frequency is 900 Mcps.

This transmitting arrangement will be replaced by an electronically scanned, 16-element transmitting array (see Par. 2, Ch. V, Sec. C).

Receivers:— The receiving array equipment box contains 16 receiver strips which have final outputs at 2 Mcps (Fig. 1-4). These outputs are combined in a resistive adder to provide the receiver beam output for the display and data-processing equipment.

Digital Diode Phase Shifters:— The receiver beam is electronically steered by means of controlled phase fronts introduced in the 28-Mcps local oscillator voltages supplied to the receiver strips. The steering phase shifts are generated by the digital diode phase shifters located on a platform behind the receiving antenna reflector (Fig. 1-5).

Beam-Steering Computer and Display:— The phase shifters are controlled by the beam-steering computer located in the receiver equipment room of the main Building C penthouse (Fig. 1-6). This computer also provides transmitter trigger pulses and a receiver gate signal (for the receiver shunt-diode protective switches).

The display equipment provides a choice of a PPI radar presentation or an array antenna pattern display. Switches are provided which allow any of the receiver channel outputs to be disconnected from the beam-forming summing network so that the effect on the array antenna pattern can be observed.

Test Equipment:— The local oscillator signals for the receiving array can be obtained from independent crystal oscillator/multiplier chains located in a box back of the antenna reflector (Fig. 1-7). Alternatively, a coherent set of local oscillator and test signals can be supplied by the coherent frequency synthesizer (Fig. 1-8) in the receiver room.

Other test equipment includes automatic phase and amplitude monitoring equipment (Fig. 1-9), an antenna pattern recorder, and a remote control test transmitter (Fig. 1-10) located 1700 feet away at Katahdin Hill. The last two items are used for antenna pattern measurements. Another antenna test facility is located in Bedford, Massachusetts.*

2. Receiver and Test Equipment Details

The equipment box of the 16-element test receiving array has been modified (since TR-228) to facilitate installation of a second generation of receiver strips. All power supplies were removed from the box because they proved to be difficult to maintain in their former location. A new power supply harness was fabricated which connects to each receiver strip through a single power connector instead of the cumbersome barrier strip which was used previously.

The receiver strips are now divided into two distinct sections. The RF amplifier and crystal mixer comprise the first section (Fig. 1-11), and the IF amplifier, second mixer, and phase shifter make up the second section (Fig. 1-12). These changes have greatly reduced the time required to replace a defective receiver strip, since it is now necessary to replace only the section of the receiver strip which is defective. In addition, the changeover from the 7077 RF amplifier/single-ended mixer combination to the Adler electron-beam parametric amplifier/balanced mixer, which is due to take place soon, will be facilitated.

---

*A. Cohen and A.W. Maltese, "The Lincoln Laboratory Antenna Test Range," Microwave J. _4_, 57 (April 1961).

Fig. 1-4. Receiving array equipment box.
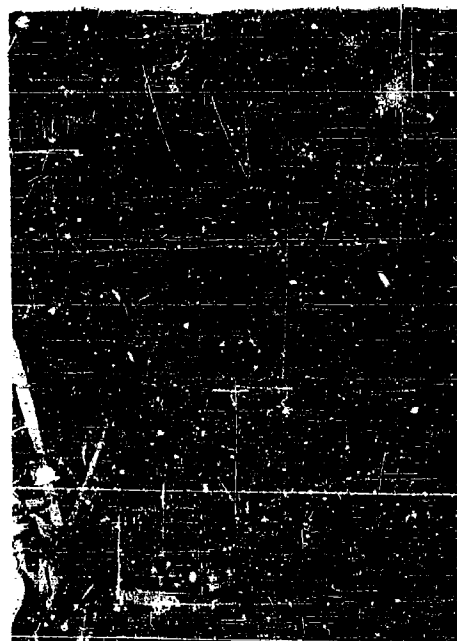
Fig. 1-5. Digital diode phase shifters.

7
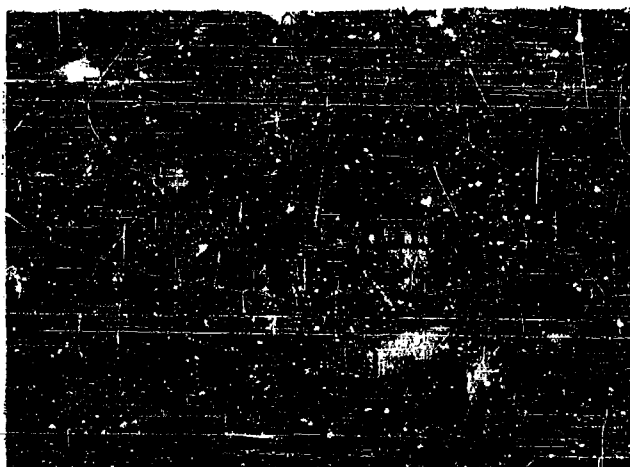
Fig. 1-6. Beam-steering computer and display equipment.

Fig. 1-7. Local oscillator cabinet and power supplies.
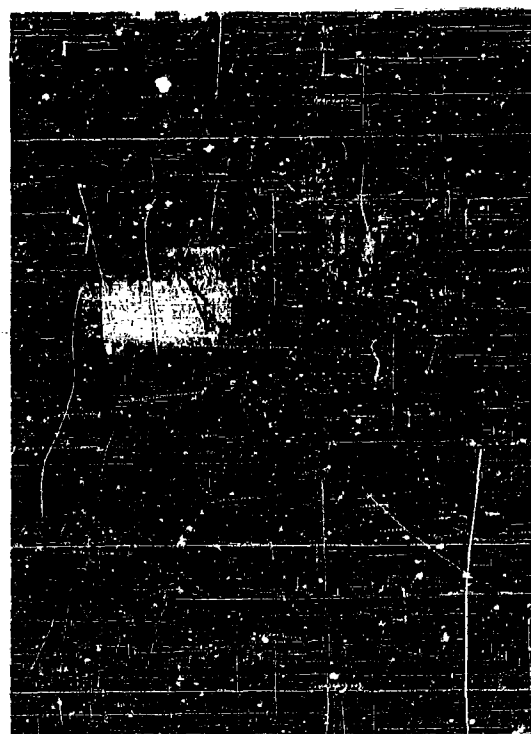
Fig. 1-8. Coherent frequency synthesizer.

Fig. 1-9. Phase and amplitude monitoring equipment (test system).
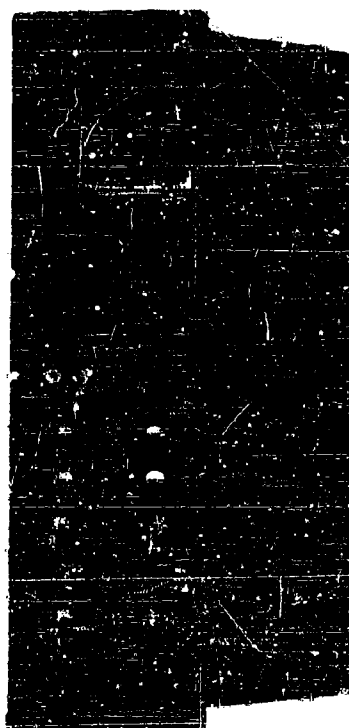
(a) Front view.

(b) Rear view.

Fig. 1-10. Remote test transmitter.

(a) 7077 RF amplifier.
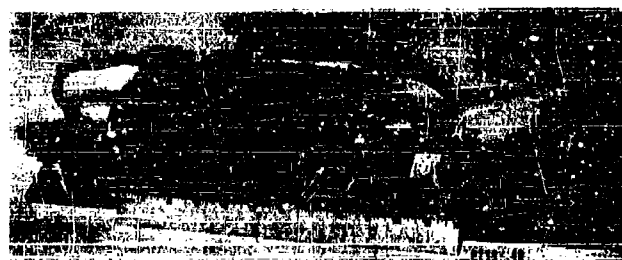
(b) Electron-beam parametric amplifier.

Fig. 1-11. RF section of receiver strips.
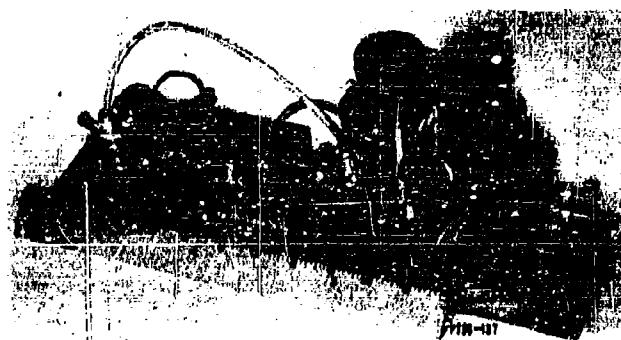
Fig. 1-12. IF section of receiver strips.
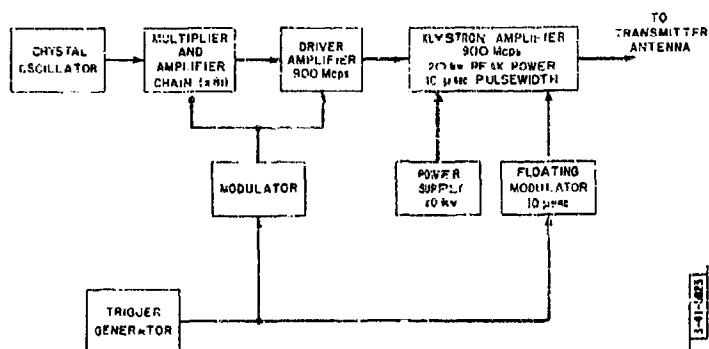
Fig. 1-13. Block diagram of radar transmitter.

Fig. 1-14. Radar transmitter.

12

The new version of the IF amplifiers is described in Part 2 of this report. The special-purpose test equipment which was developed for testing and monitoring phased array receivers and components is also covered in Part 2 of this report.

3. Radar Transmitter Details   M. Siegel

The transmitter for the linear array radar was implemented for the purpose of investigating the behavior and properties of the phased array receiver and data-processing equipment in a radar environment prior to the construction of a phased transmitting array.

A fan beam is produced by feeding the transmitter antenna from the output of a crystal-controlled klystron power amplifier. The beam can be moved by mechanical rotation of the antenna. The final amplifier is an L-band (modified to operate at 900 Mcps), electrostatically focused, 3-cavity, 30-db gain klystron (modified Sperry Gyroscope SAL-89). It produces up to 20 kw of peak power and 200 watts of average power at a pulsewidth of 10 μsec. Provisions have been made in this system to parallel two of these tubes if this is desired at a later date. A block diagram of the radar transmitter is shown in Fig. 1-13. Figure 1-14 is a photograph of the completed transmitter. The crystal-controlled exciter and driver rack is at the left, the high-voltage supply and control and monitoring panel is at the right, and the klystron amplifier, together with its modulator and ground deck amplifier, is in the center.

4. Discussion of Reliability of Test Array Components   A. J. Fallo

Introduction:— This section is devoted to general observations of over 2000 hours of test array operation and the results of specific controlled tests. Component failures in general, and also for each type of unit, are discussed and summarized. Information regarding data gained by removing the amplifier strips from the array for electrical and mechanical inspection is summarized. There is also a discussion of a number of specific controlled tests designed to ascertain variations in the phase and amplitude of each amplifier strip, and the net effect of these changes on the array sidelobe levels.

Component Failures:— The log-periodic antenna elements, the directional couplers and the 900-Mcps hybrid corporate feed have been intact since their original installation. The 870-Mcps local oscillator corporate feed has had two defective hybrids. Loose type N connector contacts seem to have caused the difficulty. One of these defective 870-Mcps hybrids caused the last eight channels of the array to shift in phase by more than 20° with respect to the first eight channels without affecting the first mixer crystal currents or the amplitude of the channel outputs.

The vacuum tube RF amplifiers have been practically trouble free. All but three of these units are still operating with the originally installed G. E. 7077 tubes. In the first detector crystal mixers, which follow the RF amplifiers, two diodes have been changed for better stability.

The IF amplifiers have had no transistors or components changed. The 2-Mcps phase shifters have experienced two breakdowns: one was the result of a bad transistor; another was caused by a broken connection in the unit itself.

13

Electrical and Mechanical Inspection of Receiver Strips:— After the system had clocked 2700 operational hours, the receiver strips were removed from the array two at a time. The RF amplifier tubes and socket connections were inspected and cleaned, and each unit was re-aligned for a gain of 13.5 to 15 db. Each RF amplifier, with its associated crystal mixer, was then fed into a test IF strip — a spare of the type used in the system. Each combination had a gain of 68.5 to 69.5 db.

Simultaneously, at another test bench, the IF strips were tested and aligned. The gain of these units ranged from a low of 70 db to a high of 75.5 db at maximum gain. The completed strips were then adjusted for a gain of 70 db by means of the gain control located in each IF amplifier.

About 250 operational hours later, the 28-Mcps local oscillator inputs to the receiver strips were individually padded to make the strips limit more uniformly.

Specific Controlled Tests:— The realigned receiver strips were in service for over 1000 hours when controlled reliability tests were conducted to determine how much the amplitude and phase of each receiver strip would change and how the sidelobes of the antenna pattern display would be affected under various test conditions.

For the first test, the array was operated on a 24-hour schedule. Phase and amplitude levels were recorded three to six times each day. The antenna pattern sidelobe level was also recorded. The first eight channels of the array utilized the new wideband IF strips (see Part 2, Ch. V) in the IF section of the receiver strips. Channels 9 through 16 operated with the old IF amplifiers (described in TR-228). The results of this 120-hour test for amplitude, phase and sidelobe changes are listed in Tables 1-I and 1-II, respectively. The differential amplitude errors were of the order of 1 db with phase errors of about 8°. The sidelobes were better than −22 db except for one reading of −21 db.

The next test was to ascertain the effects of cycling the system on and off. The system was operated during the working day and turned off for the night. When the system was turned on the following morning, some channels differed considerably from the previous day's phase and amplitude readings. For example, channel 2 changed 30°, channel 3 changed 19° and channel 6 changed 23°, whereas channel 15 changed only 4°. Therefore, the changes in phase ranged from a low of 4° to a high of 30°. The amplitude changes were not so radical. Differences in amplitude from the previous day ranged from 1 to 2 db. The system required about 3 hours of warm-up time to return to phase and amplitude readings comparable to those of the previous day.

In order to ascertain the reason for this long warm-up time, all the power supplies were left on except for the RF amplifier supply which was turned off. The following morning, phase and amplitude were again radically changed. Indications were that the RF amplifier required a long warm-up time. In order to verify this, all power supplies were turned off the following night. Only the RF amplifier power was left on. The following morning, when all other power supplies were turned on, the phase and amplitude readings were comparable to those recorded during the 24-hour scheduled testing period. The cycling test described above was repeated. The conclusion was that the RF amplifiers require 2 to 3 hours of warm-up time. The G.E. 7077 ceramic triode used in the RF amplifier was run near maximum dissipation for optimum noise figure, and the heat from the tube was probably affecting the physical dimensions of the output cavity (Q ≈ 300), thus altering the tuning. A second continuous operating test was conducted for another period of 120 hours. The results were approximately the same as in the first continuous operating test.

TABLE 1-1
NORMALIZED AMPLITUDE READINGS FOR 120-HOUR TEST*

Channel	1000 hrs. 6/26/61	1100 hrs. 6/26/61	1500 hrs. 6/26/61	0900 hrs. 6/27/61	1100 hrs. 6/27/61	1330 hrs. 6/27/61	1530 hrs. 6/27/61	0900 hrs. 6/28/61	1000 hrs. 6/28/61	1630 hrs. 6/28/61	0830 hrs. 6/29/61	1030 hrs. 6/29/61	1430 hrs. 6/29/61	1630 hrs. 6/29/51	0830 hrs. 6/30/61	1030 hrs. 6/30/61	1400 hrs. 6/30/61	1600 hrs. 6/30/61
1	—	—	—	.98	—	—	—	.98	.98	.98	.95	.95	.98	.95	—	—	—	.98
2	—	—	—	—	—	—	—	—	—	.92	.98	.93	.95	.90	.95	.95	—	—
3	.95	.95	.98	—	—	—	.98	—	—	.92	.97	.93	.95	.90	.98	.98	.98	—
4	.98	.98	—	.98	.92	—	1.02	.90	1.02	—	—	1.05	1.15	1.1	.98	.98	—	.98
5	—	—	—	—	—	—	—	.98	.97	.90	.98	.93	.90	.90	—	.98	—	—
6	—	.98	—	—	—	—	1.05	—	.97	.95	—	.95	.95	.93	—	—	—	—
7	—	—	1.05	.95	—	1.05	—	—	1.02	—	—	.98	.98	.98	—	—	1.05	.95
8	—	—	—	—	—	—	—	—	.98	.90	—	.95	.92	.93	—	—	—	—
9	—	—	—	.95	—	—	—	—	—	—	.98	—	1.05	1.03	—	—	—	—
10	—	—	—	.92	.98	.98	—	.90	.97	.98	.95	.90	.97	.95	—	—	—	.95
11	—	—	1.05	.95	—	1.02	1.02	1.05	1.05	1.05	—	.98	—	—	—	—	—	.92
12	1.02	1.02	1.1	.85	.92	1.02	1.05	1.02	1.02	1.07	.90	—	1.05	1.07	1.02	1.02	1.1	.95
13	—	—	1.02	.85	.92	.95	—	.90	.95	.98	.88	.95	—	—	—	—	1.1	.85
14	.98	.98	—	.88	.98	—	—	.90	.97	.98	.90	.97	1.02	1.05	.98	.98	1.02	.85
15	—	—	1.05	.88	.98	.98	—	.90	.95	.95	.90	.93	—	—	—	—	1.05	.88
16	—	—	1.05	.85	.95	.98	—	.90	.97	—	.88	.93	1.07	1.07	—	—	1.05	.85

*Time is real time, not elapsed time.

15

TABLE 1-11
RELATIVE PHASE READINGS FOR 120-HOUR TEST*

Reference Channel

Channel	6/26/61 1000 hrs.	6/26/61 1100 hrs.	6/26/61 1300 hrs.	6/27/61 0900 hrs.	6/27/61 1100 hrs.	6/27/61 1330 hrs.	6/27/61 1530 hrs.	6/28/61 0900 hrs.	6/28/61 1000 hrs.	6/28/61 1630 hrs.	6/29/61 0530 hrs.	6/29/61 1030 hrs.	6/29/61 1430 hrs.	6/29/61 1630 hrs.	6/30/61 0830 hrs.	6/30/61 1030 hrs.	6/30/61 1400 hrs.	6/30/61 1600 hrs.
1	+1	+1	+2	-8	-2	+2	-5	-2	-14	+3	-2	+4	+6	+4	+2	+4	+6	+7
2	0	-4	0	-6	-1	+5	+8	0	+8	+12	+2	+6	+4	+8	+3	+8	+9	+10
3	+1	-1.5	-1	-10	-17	-1.5	-1	-12	-2	-.5	-3	+3	+4	+4	+4	+4	+4	+6
4	+1	+3	+4	0	+4	+6	+8	-1	+3	+4	+2	+6	+9	+8	+1	+6	+8	+8
5	+.5	0	+2	-6	0	+5	+8	+2	+8	+8	-1	+6.5	+10	+10	+2	+7	+10	+10
6	+.5	+2	+3	-3	.5	+4	+6	0	+5	+6	+2	+4	+5	+4	+3	+5	+4	+7
7	+.5	+2	+2	-1.5	+4	+3	+4	-1	+4	-2	+1.5	+4	+5	+4	+2.5	+4	+5	+7
8	0	-1.5	-4	-7	-1.5	-2	-3	-3	-2	+8	+8	+6	+5	+4	+4	+5	+4	+7
9	0	-1.5	-4	-5	-4	-1	-2	-1.5	0	-7	0	-1	-4	-5	-1	-1	+3	-2
10	+1	0	-3	-7	-2	0	+1	-2	+2	-1	0	+2	+1	-2	0	+2	+3	+5
11	+1	-2	-1	-7	+.5	0	0	0	+2	-3	+1	+2	-1	-7	0	+1	.5	+3
12	-1	+1	-6	-6	-8	+1	-4	+1	+1	-4	0	-4	-8	-3	-2	-4	-1	-3
13	+.5	-.5	-4	-10	+2	-6	0	-7	-7	-2	-5	-3	+4	+6	-9	-5	0	+6
14	+.5	-.5	-4	+1	-1	+2	0	+5	+5	-4	+5	+3	-4	-6	+2	+2	-2	+2
15	+1	-1.5		-4		-.5	-1	+3	+4	-4	+5	+4	+2	+3	+2	+3	+8	+10
16																		
Sidelobes in dB	25	24	23	25	25	24	23	25	23	23	24	24	2?	22	23	23	22	22

*Time is real time, not elapsed time.

General Remarks on Array Maintainability:— The problems involved in maintaining a 16-channel phased array are many and varied. However, it is felt that one or two personnel of the technician level who possess a knowledge of radar componentry and an ability for trouble shooting can readily handle the problems that arise on an array of this modest size. For a much larger array (in terms of numbers of elements), it is obvious that maintenance duties would increase, that more problems would arise, and that more personnel would be required. With this point in mind, it seems appropriate that, as the array becomes more complex, special thought should be given to how to simplify the maintenance, testing, trouble shooting, recording and interpreting of data, and modification procedures associated with an experimental array.

In order to alleviate the maintenance problem, the semiautomatic equipment already in use could be expanded. Trouble shooting probably could be simplified if, wherever feasible, test points or jacks were installed on each unit. Schematic diagrams with DC voltages, waveform shapes and levels also would be helpful. In addition, it would be advisable for maintenance personnel to keep systematic records of changes and failures as a guide to component improvement.

5. **Performance of Group 41 Linear Test Array**   J. H. Teele
   as a Radar System

The Group 41 linear array has been "on the air" as an active radar system for approximately six months. During that time, the radar system has been operated in the PPI or surveillance mode.

Insertion of the system parameters into the tracking-radar range equation gives a range of approximately 10 n.mi for an 80 per cent probability of detection and 10^{-3} false alarms per second.* Because of the high data rate employed (55 msec) and the integrating, raster-type display, considerably higher false-alarm rates are tolerable.

Many aircraft targets have been observed out to ranges of approximately 25 n.mi. The false-alarm rate during most observation times was estimated at about 10 per second. The low transmitted power (10-μsec pulse, 20-kw peak power) and high system noise temperature (about 3000°K) greatly limit system performance.

The performance of the radar system has severely limited the possible operational studies that could be carried out on the linear array. System changes in two areas will improve performance to the point where several interesting experiments are possible.

(a) The present floodlighting scheme, whereby the klystron transmitter
illuminates an entire 90° sector (in azimuth), will be discarded in
favor of a steerable transmitting array of sixteen 5-kw peak, 50-watt
average, transmitting elements. Hence, we will obtain a fourfold in-
crease in effective radiated power due to increased transmitter power,
as well as a sixteenfold increase in ERP due to increased transmitter
antenna gain. The corresponding increase in range performance is a
factor of about 2.8.

(b) The present 7077 vacuum tube RF amplifiers in the radar receiving
system are deficient in several respects. These RF amplifiers have
only 13-db gain and a high noise figure of about 7 db. On or about
1 September 1961, the first of sixteen Zenith-Adler fast-wave para-
metric amplifiers will be installed in the test array. These ampli-
fiers have a double channel noise figure in the neighborhood of 1 db.
The range of the linear array radar system will be approximately
doubled by this change alone.

* 1 kcps prf.

47

The single-hit range of the radar system, with all these improvements, will be increased to about 60 n.mi on the same 1-m^2 target. This increased performance will allow several operational studies to be implemented.

Certain experiments in waveform design, with application to the problem of target detection and parameter estimation, will also be possible.

A monopulse angle-interpolation system is currently in the hardware development stage, with a completion date to match the schedule of array improvements.

C. HIGH-POWER TESTING FACILITY   L. Cartledge

A facility for testing RF components at moderately high power levels has been added to the other test facilities. High-power RF sources include a 1215- to 1350-Mcps tunable magnetron transmitter capable of about 400 kw peak at a 0.0012 duty cycle, and a 600- to 985-Mcps tunable CW source capable of some 1500 watts. The 20-kw peak, 200-watt average power radar transmitter for the linear array (Sec. B) may also be used for component testing. Each of the sources is provided with an isolator so that reflected power from the component under test can be tolerated. Directional couplers and instrumentation are provided so that direct and reflected power to and from the component under test can be measured.

D. TRANSMITTER TEST FACILITY   M. Siegel

A penthouse 27 × 18 × 10 feet (high) was constructed for performance testing and life testing transmitter modules and tubes suitable for array use. Provisions have been made to life test and performance monitor sixteen phased array transmitter modules simultaneously. The following facilities are available within this penthouse:

(1) 70 kw of 3-phase primary power,

(2) A 5000-volt supply capable of providing up to 20 kw of DC power for the first transmitting array (which uses tetrodes) to be supplemented later by higher-voltage, high-power DC supplies for other transmitting arrays,

(3) Modulator driver racks to drive all sixteen of the modulators included within the transmitter modules,

(4) A water purifier and cooler capable of providing ion-free cooling water for the sixteen transmitter modules,

(5) An RF screen room 10 × 7 × 8 feet to contain the transmitter modules undergoing life test.

It is expected that this facility will be used to construct, debug and life test all future transmitter modules prior to their installation in the main linear array facility.

PART 2

TECHNIQUES AND COMPONENTS

Edited by J. Coffey

Introduction and Abstract

This section, as its title implies, deals with the hardware develop-
ments in the phased array project. It is divided into nine chapters, each
of which describes one part of a phased array radar. Each chapter is
preceded by a brief summary. It is hoped that these summaries, along
with the Table of Contents, will guide the reader to material of interest
to him.

CHAPTER I

RF BEAM FORMING AND ANTENNAS

SUMMARY

W. P. Delaney

The major portion of this chapter is devoted to a theoretical and experimental study of an
RF beam-forming technique. This technique uses a matrix of microwave devices to simultane-
ously form n overlapping beams in space from an n-element linear array. The theoretical per-
formance of the RF matrix is discussed in Sec. B-1. A general far-field relationship is derived
and then used to study several characteristics of the matrix beams. The technique of beam com-
bining to form nonuniform aperture illuminations is discussed in Sec. B-2. Sections B-3 and B-4
present experimental measurements and antenna patterns on a 16-element beam-forming matrix.
Patterns for all uniform-illumination beams and several tapered-illumination beams are pre-
sented. The experimental results agree very well with theoretical predictions. Some problems
related to the realization and the operation of RF matrices are discussed in Sec. B-5.

Some brief work on antenna elements for phased array application is reported in Sec. C of
this chapter. A scimitar antenna is shown to have certain characteristics which make it undesir-
able for array application.

A. INTRODUCTION

The technique of multiple beam forming[*] directly at the carrier frequency is being investi-
gated as part of the phased array program. In the past year, work in this area has concentrated
on theoretical and experimental studies of the beam-forming matrix described by Butler and
Lowe,[†] and by Shelton and Kelleher.[‡] The information presented here will be a summary of deri-
vations and extensive experimental results contained in another report.[§]

---

[*] J.L. Allen, et al., "Phased Array Radar Studies, 1 July 1959 to 1 July 1960," Technical Report No. 228 [U],
Lincoln Laboratory, M.I.T. (12 August 1960), pp. 217-230, ASTIA 249470, H-335.

[†] J. Butler and R. Lowe, "Beam Forming Matrix Simplifies Design of Electronically Scanned Antennas," Electronic
Design 9, 170 (12 April 1961).

[‡] J.P. Shelton and K.S. Kelleher, "Multiple Beams from Linear Arrays," Trans. IRE, PGAP AP-9, 154 (1961).

[§] W.P. Delaney, "An RF Multiple Beam Forming Technique," 41G-0012 [U], Lincoln Laboratory, M.I.T.
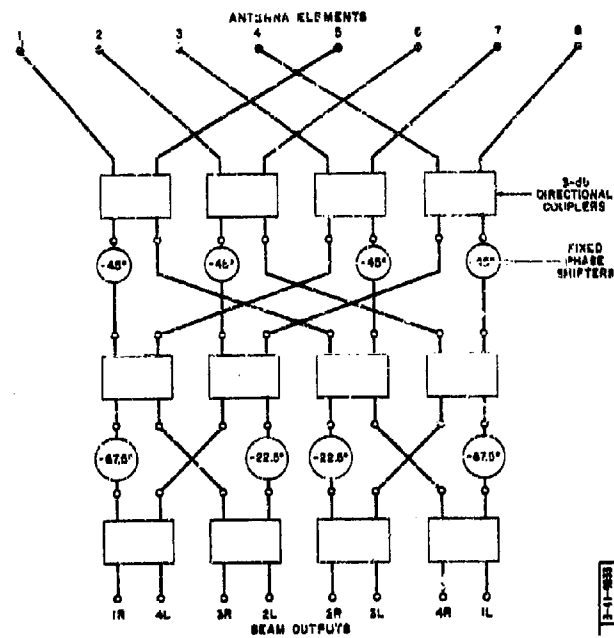(9 August 1961), ASTIA 262017, H-334.

Fig. 2-1. 8-element beam-forming matrix.

The RF beam-forming technique discussed here possesses several advantages. It forms simultaneous multiple beams, each of which has the full gain of the array aperture. The technique is passive and should be very reliable. Since the beam forming is done at the RF carrier frequency, numerous phase- and gain-stable receivers will not be required in many applications. The beam-forming matrix is theoretically lossless and, in practice, can be built with low insertion loss. In essence, this beam-forming technique eliminates the phase shifting required to scan a receiver beam and substitutes instead the problem of beam selection. The continuing advances in low-level microwave switching (see Ch. II, Sec. D) make RF beam selection appear attractive.

This RF beam-forming technique has certain disadvantages. It is a complex interconnection of microwave devices; thus, fabrication and packaging of large matrices is a problem. Since the matrix forms fixed beams in space, complete flexibility in beam positioning is not possible. The matrix is power limited, but the limit is not yet well defined. These problem areas are presently under investigation.

B. RF BEAM FORMING   W. P. Delaney

The basic components of the beam-forming matrix are 3-db directional couplers (or hybrid rings) and fixed phase shifters. Figure 2-1 shows the schematic[*] of an 8-element matrix which can be used for reference in the following discussions. This matrix forms eight overlapping beams in space from an 8-element linear array. Some basic characteristics of this type of beam-forming matrix are outlined below.

Number of Beams:— The number of beams formed is equal to the number of antenna elements used. The number of antenna elements in the array must be equal to a power of 2, namely, 2, 4, 8, 16, 32 etc.

Number of Directional Couplers:— The number of directional couplers used is $(N/2) \log_2 N$, where N is the number of elements in the array.

Number of Fixed Phase Shifters:— The number of phase shifters required is $(N/2) [(\log_2 N) - 1]$.

Operating Frequency:— The operating frequency is limited only by the practicality of building and interconnecting fixed phase shifters and directional couplers or hybrid rings. At very low frequencies, hybrid transformers can be used instead of microwave hybrids.

Bandwidth:— The components of the matrix (couplers and phase shifters) can be built with bandwidths greater than 30 per cent; however, certain problems are involved in operating phased arrays over bandwidths of this size.

Insertion Loss:— The beam-forming technique is theoretically lossless. The insertion loss of the matrix will be determined by the RF losses in the matrix components. For example, a 16-element matrix at 900 Mcps which uses strip transmission line has an insertion loss of 0.7 db. (In this case, no attempt was made to achieve a particularly low-loss matrix.)

Antenna Taper:— The matrix provides a uniform illumination of the array elements. However, simple beam-combining techniques can yield $(\cosine)^n$ illuminations.

---

[*] The 8-element schematic shown on p.219 of TR-. is in error.

1. Theoretical Performance in an Antenna System

This section discusses the far-field performance of a linear array antenna fed by a beam-forming matrix. A relationship for the far-field response is found, and this relationship is then used to study positions of beam peaks, positions of beam nulls, sector coverage, beam cross-over positions and levels, and beam movement with changes in frequency.

The discussion is limited to matrices using directional couplers. Similar results can be obtained for matrices using hybrid rings.

The normalized magnitude of the field intensity in the far-field of a linear array of n isotropic sources is given[*] by

$$|E| = \frac{1}{n} \frac{\sin(n\psi/2)}{\sin(\psi/2)} \quad , \tag{1}$$

where

$$\psi = 2\pi d/\lambda \sin\alpha - \delta \quad , \tag{2}$$

d = element spacing,
λ = wavelength,
α = angle from array normal,
δ = element-to-element phase shift,
n = number of antenna elements.

The element-to-element phase shift, δ, can be found by referring to the schematic diagram of the particular matrix under consideration. Taking an 8-element array as an example, and therefore referring to the matrix schematic of Fig. 2-1, it is seen that the directional coupler which connects to antenna element 1 also connects to antenna element 5. Similarly, elements 2 and 6 are fed by a common directional coupler. The first beam from broadside is formed when an incident wavefront excites currents in elements 1 and 5 (and thus elements 2 and 6, 3 and 7, etc.) with a phase difference of 90°. Similarly, the second beam from broadside is formed when the phase difference is 270° and, in general, the Kth[†] beam is formed when the phase difference between elements 1 and 5 is $(2K - 1)(\pi/2)$ radians. Therefore, for an 8-element array, the element-to-element phase shift, δ, for the Kth beam is $(2K - 1)(\pi/8)$ radians.

Generalizing this result to an n-element array,

$$\delta_K = \frac{(2K - 1)\pi}{n} \quad , \tag{3}$$

Combining this result with Eqs. (1) and (2), the normalized far-field amplitude of the Kth beam from broadside is

$$|E_K| = \frac{1}{n} \frac{\sin n[\frac{\pi d}{\lambda} \sin\alpha - (\frac{2K-1}{n})\frac{\pi}{2}]}{\sin[\frac{\pi d}{\lambda} \sin\alpha - (\frac{2K-1}{n})\frac{\pi}{2}]} \quad , \tag{4}$$

[*] J. D. Kraus, Antennas (McGraw-Hill, New York, 1950), p.78.

[†] K is defined as the beam number. Values of K are limited to positive nonzero integers. When these values of K are used, the equations that follow apply only to beams to the right of the array normal. However, since the matrix forms beams located symmetrically about the array normal, this restriction does not hinder the usefulness of the results. The mathematical simplicity more than compensates for the slight loss in generality.

where

$|E_K|$ = normalized (peak = 1) magnitude of far-field voltage,

K = beam number (K = 1 for the first beam to the right or left
of broadside, etc.).

Equation (4) is a general relation which can be used to study several characteristics of this beam-forming technique.

Positions of Beam Peaks:— The peaks of various beams occur at values of the angle α which make the numerator and denominator of (4) equal to zero. Designating these angles as α_p,

$$\sin \alpha_p = \frac{\lambda}{2d}\left(2q + K - \frac{1}{2}\right) \quad , \tag{5}$$

where q is any integer. A value of q = 0 yields the position of the main beam. Nonzero values of q give the positions of grating lobes.

Positions of Beam Nulls:— Pattern nulls occur at those zeros of the numerator of (4) which are not accompanied by zeros in the denominator. Designating the angles of nulls by α_o,

$$\sin \alpha_o = \frac{\lambda}{nd}\left(m + K - \frac{1}{2}\right) \quad , \tag{6}$$

where m = 1, 2, 3, etc., but $m \neq qn$ where q = any integer.

Relative Positions of Peaks and Nulls:— Equations (5) and (6) point out two interesting characteristics of this beam-forming technique:

(a) All the nulls of all the beams occur at certain common angles.

(b) The peak of any beam occurs at one of these same common angles.

These characteristics are summarized in Fig. 2-2, which shows three typical matrix beams.

Sector Coverage:— The angular sector $\ominus$, covered by the multiple beams from the matrix, can be found from (5). $\ominus$ is the angle between the peaks of the extreme right and extreme left beams.

$$\ominus = 2 \sin^{-1}\left[\frac{\lambda}{2d}\left(1 - \frac{1}{n}\right)\right] \quad . \tag{7}$$

For a large number of elements in the array (n >> 1),

$$\ominus \approx 2 \sin^{-1}\left(\frac{\lambda}{2d}\right) \quad . \tag{8}$$

Thus, in a large array the sector coverage is determined only by the element spacing and the wavelength.

Positions and Levels of Beam Crossovers:— The angular position at which two adjacent beams cross over can be found from (4) by equating the amplitudes of the Kth beam and the adjacent $(K + 1)^{th}$ beam. Defining α_c as the angular position of this crossover,

$$\alpha_c = \sin^{-1}\left(\frac{K\lambda}{nd}\right)^* \quad , \tag{9}$$

---

*Due to the restriction on the values of K discussed earlier, this formula cannot be used to calculate the crossover position of beams 1 right and 1 left. The crossover of these beams occurs at $\alpha = 0^\circ$.
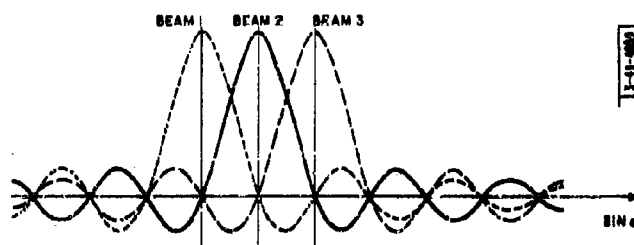
Fig. 2-2. Typical matrix beams.

where

K = beam number of beam nearest broadside,

λ = wavelength,

d = element spacing,

n = number of elements in array.

Substituting (9) into (4) will yield the beam crossover level,

$$|E_K|_c = \frac{4}{n} \frac{1}{\sin\left(\frac{\pi}{2n}\right)}$$ (10)

For values of n > 10,

$$|E_K|_c \approx \frac{2}{\pi}$$ (11)

It should be noted that the beam crossover level is independent of beam number, element spacing and wavelength. For arrays of more than ten elements, the crossover level effectively becomes constant at $2/\pi$. Since the peak of any beam has an amplitude of 1.0 due to the normalization of (4), the crossover level is approximately −4 db (−3.92 db).

Beam Movement with Changes in Frequency:-- As mentioned earlier, the matrix components can be built with relatively large bandwidths. However, (5) shows that the position of the peak of any matrix beam varies with frequency. The amount of beam position variation is also a function of beam position as evidenced by the beam number K in (5). This fact will complicate any compensation scheme designed to allow operation over wide instantaneous bandwidths. The change in beam position with frequency is given by

$$d\alpha_p = \tan\alpha_p\left(\frac{d\lambda}{\lambda}\right)$$ (12)

where

α_p = angular position of beam peak,

λ = wavelength.

For beams near broadside, Eq. (12) is approximated by

$$\frac{d\alpha_p}{\alpha_p} = \frac{d\lambda}{\lambda}$$ (13)

and for beams near endfire, where α_p approaches 90°, Eq. (12) can be solved to give

$$\frac{\Delta\alpha_p}{\alpha_p} = \frac{2\sqrt{2}}{\pi}\sqrt{\frac{\Delta\lambda}{\lambda}}$$ (14)

2. Beam Combining

The beam-forming matrix provides a uniform illumination of the antenna array. While this illumination provides the narrowest beamwidth and the greatest directivity, it has a relatively high first sidelobe level (−13 db). Lower sidelobes can be achieved at the expense of beamwidth by combining the output beams of the matrix. Simple combination of n + 1 matrix beams will yield

25

(cosine)^n amplitude tapers. Allen[*] has shown that it is possible to achieve arbitrary aperture illuminations by using weighted addition of selected beams.

A signal arriving on the peak of a particular beam experiences a certain net phase shift as it proceeds through the matrix to the particular beam terminal. The amount of net phase shift is different for various beams. Hence, if several beams are to be added to form an amplitude taper, corrective phase shifts must be introduced in some of the beams to guarantee a true addition process. The amount of corrective phase shift necessary can be found by tracing[†] through the matrix for the beams of interest.

Cosine Illumination Beams:- The addition (after phase correction) of two adjacent beams will result in a cosine illumination of the aperture. This fact is readily demonstrated by adding the illuminations[‡] of the Kth and the $(K + 1)^{th}$ beams.

$$I_K = e^{j(2K-1)\beta} \quad ,$$

$$I_{K+1} = e^{j(2K+1)\beta} \quad ,$$

where

I_K = illumination of Kth beam,

$\beta = \dfrac{\pi}{2}\dfrac{x}{l}$.

l = array length,

x = length variable along array.

$$I_K + I_{K+1} = e^{j(2K-1)\beta} + e^{j(2K+1)\beta} \quad ,$$

$$= e^{j2K\beta}[e^{-j\beta} + e^{+j\beta}] \quad ,$$

$$= (2\cos\beta)\,e^{j2K\beta} \quad . \tag{15}$$

Thus, the amplitude of the new illumination is a cosine function, and the phase distribution of the new illumination points a beam halfway between the K and the $K + 1$ component beams.

The general far-field relations for a cosine beam can be found by simply adding the far-field responses of the two component beams. Once the component beams have been phase corrected, the addition of their magnitudes [Eq. (4)] will yield the magnitude of the cosine-beam response. For example, the far-field response of the cosine beam formed by adding the Kth and the $(K + 1)^{th}$ beams is

$$|E_K|' = \frac{1}{\sqrt{2}}\,\frac{1}{n}\left[\frac{\sin n\,[\frac{\pi d}{\lambda}\sin\alpha - (\frac{2K-1}{n})\frac{\pi}{2}]}{\sin[\frac{\pi d}{\lambda}\sin\alpha - (\frac{2K-1}{n})\frac{\pi}{2}]} + \frac{\sin n\,[\frac{\pi d}{\lambda}\sin\alpha - (\frac{2K+1}{n})\frac{\pi}{2}]}{\sin[\frac{\pi d}{\lambda}\sin\alpha - (\frac{2K+1}{n})\frac{\pi}{2}]}\right] \quad . \tag{16}$$

The $1/\sqrt{2}$ factor is introduced to keep the total power in the two beams the same as in a single beam so that the performance of uniform- and cosine-illumination beams can be compared.

---

[*] J. L. Allen, et al., op. cit., pp. 221-223.

[†] For an example of a phase correction calculation, see Sec. 4.1 of W. P. Delaney, op. cit.

[‡] In the interest of mathematical simplicity, the array illumination is replaced by a line source.

The relative gain and the beam crossover level can be found by using (16); however, it is easier to find these values by using a graphical approach. Reference to Fig. 2-3 shows the addition (on a power basis) of adjacent uniform-illumination beams to form cosine-illumination beams. The peak of the cosine beam falls at the point where the two component beams cross over. Referring[*] to (9) and defining the angle of the cosine beam peak as α'_p.

$$\alpha'_p = \sin^{-1}(\frac{K\lambda}{nd}) \quad .$$

(17)

Figure 2-3 shows that the peak value of the cosine beam is $2\sqrt{2}/\pi = 0.9$. (Note that the peak value of the component beams is normalized to 1.0.) Thus, the peak gain of the cosine beams is 0.92 db less than that of the uniform-illumination beams. The crossover level between the adjacent cosine beams is $1/\sqrt{2}$. Thus, the crossover point is 2.1 db down from the peaks of the cosine beams. It can also be noted from Fig. 2-3 that the null-to-null beamwidth of the cosine beam is one and one-half times wider than the uniform-taper beam.

There are some limitations on forming adjacent tapered-illumination beams as shown in Fig. 2-3. Allen has shown[†] that the beam shape and the beam spacing obtainable from a <u>lossless</u> beam-forming matrix are not completely arbitrary. The results of his analysis indicate that if the beam-forming matrix is to be lossless, the crossover level of adjacent tapered-illumination beams cannot be higher than the crossover level of the uniform-illumination beams. Thus, the adjacent cosine beams of Fig. 2-3 cannot be realized in a lossless manner. This fact is easily recognized if one tries to build a beam combiner to simultaneously form the beams of Fig. 2-3. One typical scheme is shown in Fig. 2-4. The power in each beam is split in the power divider, and adjacent beams are then added in a hybrid ring. When a received signal arrives on the peak of the 1R + 2R cosine beam, part of the received energy is coupled to the 2R + 3R hybrid adder and part is coupled to the 1R + 1L adder because of the power divider action. This energy is lost to the 1R + 2R beam, and thus this beam-combining technique is lossy.

This beam-combining problem can be restated as follows: if the beam-combining technique is to form simultaneous tapered-illumination beams in a lossless manner, no uniform-illumination beam can be used in more than one beam addition[‡] process. Thus, for the example of Fig. 2-3, a cosine beam of 1R + 2R can be formed, but the 2R + 3R cosine beam cannot be formed simultaneously if the process is to be lossless.

The characteristics of cosine beams which are formed in a <u>lossless</u> manner can be found from the previous comments and the general far-field relations. The position of the peak of a particular cosine beam formed by the Kth and the $(K + 1)^{th}$ beam is given by (17). The gain and null-to-null beamwidth are the same as already found from Fig. 2-3. Since one cosine beam is the sum of the Kth and the $(K + 1)^{th}$ beams and the other cosine beam is the sum of the $(K + 2)^{th}$ and $(K + 3)^{th}$ beams, Eq. (4) can be used to calculate the angular position and the level of the crossover between these cosine beams. The results are

$$\sin \alpha'_c = \frac{\lambda}{d} (\frac{K + 1}{n}) \quad ,$$

(18)

---

[*] The restriction on (9) applies here also.

[†] J.L. Allen, "A Theoretical Limitation on the Formation of Lossless Multiple Beams in Linear Arrays," Trans. IRE, PGAP AP-9, 350 (1961).

[‡] A particular beam may be used in an addition and a subtraction process such as taking the sum and difference of two beams in a hybrid ring.
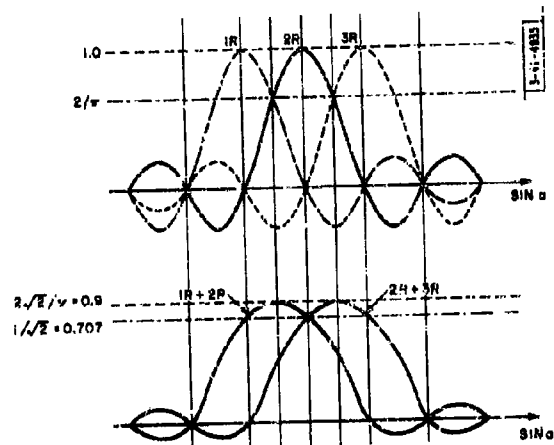
Fig. 2-3. Formation of cosine-illumination beams.
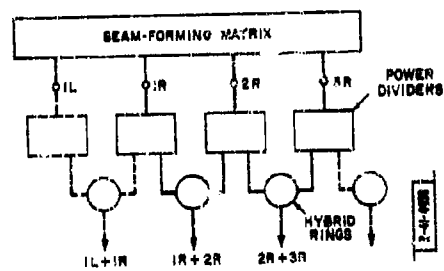
Fig. 2-4. Lossy beam-combining network.

where α'_c is the angular position of the crossover. and

$$|E_K|_c = \frac{1}{\sqrt{2}n} \left[\frac{1}{\sin\frac{\pi}{2n}} - \frac{1}{\sin\frac{3\pi}{2n}} \right] \qquad . \tag{19}$$

where $|E_K|_c$ is the crossover level. For large arrays where n > 30, Eq. (19) is accurately approximated by

$$|E_K|_c \approx \frac{1}{\sqrt{2}n} \left[\frac{2n}{\pi} - \frac{2n}{3\pi} \right] = \frac{2\sqrt{2}}{3\pi} = 0.30 \qquad . \tag{20}$$

Recalling that the peak of the cosine beam has a value of 0.9 (due to the normalization of the uniform-illumination beam and the $1/\sqrt{2}$ factor in the beam addition), the crossover level is 9.5 db down from the peak of the beam.

When two beams are combined in a hybrid ring, the output from the sum port of the hybrid ring is a cosine-illumination beam, and the output from the difference port of the hybrid is a difference beam (sine illumination) with a sharp null at the same angle as the peak of the sum beam. This difference beam may be useful for increased angular-resolution via beam-interpolation techniques.

    Cosine-Squared Illuminations:— Three uniform-illumination beams can be combined to form a cosine-squared illumination. By a judicious choice of how these beams are combined, it is possible to achieve cosine-squared-on-a-pedestal illuminations. Using an approach similar to that used for the cosine beams, the illuminations of the Kth, $(K + 1)^{th}$ and $(K + 2)^{th}$ beams are

$$I_K = Ae^{j(2K-1)\beta} \qquad ,$$

$$I_{K+1} = 1e^{j(2K+1)\beta} \qquad ,$$

$$I_{K+2} = Ae^{j(2K+3)\beta} \qquad .$$

Considering the matrix from a transmitting standpoint, the Kth and the $(K + 2)^{th}$ beams are not driven at the same voltage level as the $(K + 1)^{th}$ beam, as evidenced by the factor A in the illuminations. Now, adding the illuminations,

$$I_K + I_{K+1} + I_{K+2} = 1e^{j(2K+1)\beta} + A \left[e^{j(2K-1)\beta} + e^{j(2K+3)\beta} \right]$$

$$= e^{j(2K+1)\beta} \left[1 + A(e^{-j2\beta} + e^{+j2\beta}) \right] \qquad . \tag{21}$$

Now, if A = 1/2, Eq. (21) becomes

$$I_K + I_{K+1} + I_{K+2} = [1 + \cos 2\beta] e^{j(2K+1)\beta}$$

$$= [2 \cos^2 \beta] e^{j(2K+1)\beta} \tag{22}$$

Thus, the amplitude of the illumination is a $(\cos)^2$ function, and the phase of the illumination points the beam in the same direction as the $(K + 1)^{th}$ beam (the middle beam of the three beams used).

    To obtain a cosine-squared-on-a-pedestal illumination, A is allowed to equal some value less than 1/2. Equation (21) can be written as

Fig. 2-5. Cosine-squared-on-a-pedestal illumination.

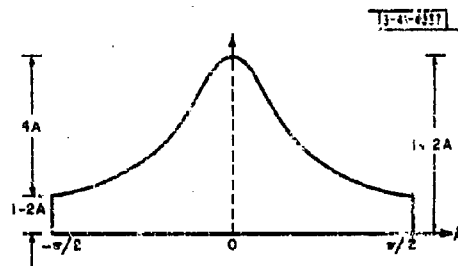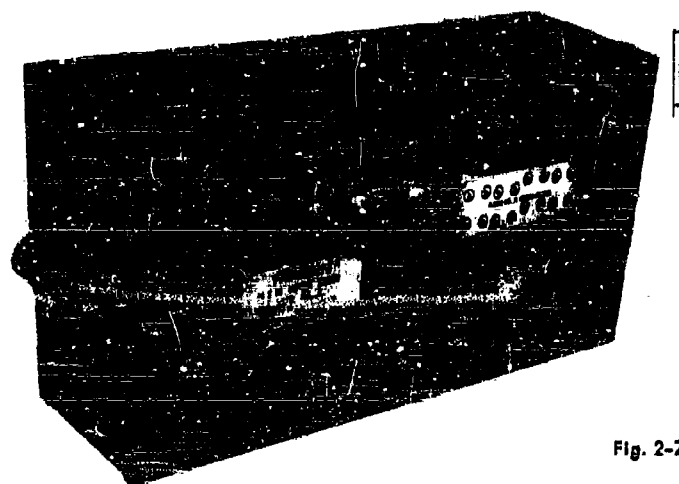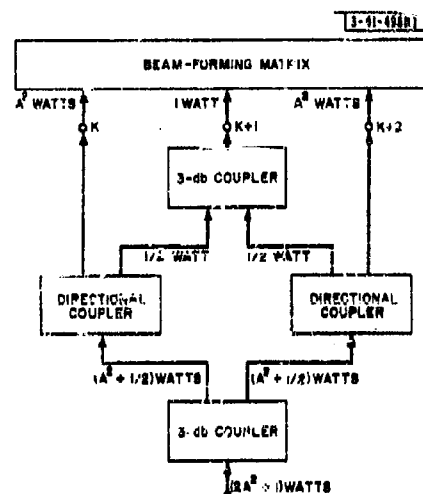Fig. 2-6. Beam-combining network for cosine-squared-on-a-pedestal illuminations.

Fig. 2-7. 16-element matrix.

30

$$I_K + I_{K+1} + I_{K+2} = e^{j(2K+1)\beta} [1 - 2A + 2A + A(e^{-j2\beta} + e^{j2\beta})]$$

$$= e^{j(2K+1)\beta} \left[(1 - 2A) + 2A \left(1 + \frac{e^{-j2\beta} + e^{j2\beta}}{2} \right) \right]$$

$$= e^{j(2K+1)\beta} [(1 - 2A) + 4A \cos^2 \beta] \qquad (23)$$

A sketch of the magnitude of Eq. (23) is shown in Fig. 2-5. The pedestal height is $1 - 2A$. The ratio of pedestal to peak of the illumination is

$$\text{pedestal ratio} = \frac{1 - 2A}{1 + 2A} \qquad (24)$$

Thus, the amount of pedestal in the cosine-squared illumination can be controlled by the value of A.

Figure 2-6 shows a generalized beam-combining network which will yield (in a lossless[*] manner) a cosine-squared-on-a-pedestal illumination. The beam combiner is considered from a transmitting standpoint, and the power levels at various points in the network are indicated. It should be noted that this network provides A volts, 1 volt and A volts drive to three adjacent beams (K, K + 1 and K + 2), and thus the general illumination of Fig. 2-5 can be achieved.

As pointed out earlier, the peak of a $(\cos)^2$ beam occurs at the peak of the center component beam. It can be readily shown that the gain of the $(\cos)^2$ beam (no pedestal) is 1.76 db below the gain of the flat-illumination beam. Also, by using the graphical approach of Fig. 2-3, the null-to-null beamwidth of the $(\cos)^2$ beam is found to be twice that of the flat-illumination beam.

3. Description and RF Performance of a 16-Element Beam-Forming Matrix

A 16-element beam-forming matrix has been tested extensively in the laboratory and in a linear array antenna system. The matrix was designed and built for Lincoln Laboratory by Sanders Associates. The measurements reported in this section were made at Lincoln Laboratory at 900 Mcps and at Sanders Associates at 890, 1025 and 1160 Mcps. The results of the antenna testing of the matrix appear in Sec. 4.

Description of 16-Element Matrix:- Figure 2-7 shows the 16-element matrix, and Fig. 2-8 shows a schematic diagram of this matrix. No attempt was made to achieve an especially compact package. The use of strip transmission line techniques permitted several directional couplers and phase shifters to be fabricated on the same board. The boards were then interconnected by using coaxial fittings. The directional couplers used in the matrix are the coupled strip type[†] which have good directivity and coupling properties over a bandwidth of 30 per cent. The fixed phase shifters are also a coupled strip type[‡] with bandwidths greater than 30 per cent. These wideband components were used to more fully explore the possibilities of this beam-forming technique. For narrow-bandwidth operation, branch-line directional couplers or

---

[*] If this beam-combining scheme is considered from a receiving standpoint, some power will be dissipated in the terminations on the fourth port of the directional couplers. However, the combining network is considered lossless because this loss accounts for the reduced aperture efficiency of the tapered illumination. On transmit, no power is lost in the combining network.

[†] J.K. Shimizu, "Strip Line 3 db Directional Couplers," 1957 IRE WESCON Convention Record, Part 1, pp. 4-15.

[‡] B.M. Schiffman, "A New Class of Broadband Microwave 90 Degree Phase Shifters," Trans. IRE, PGMTT MTT-6, 732 (1958).

Fig. 2-8. Schematic of 16-element matrix.

32

hybrid rings could be used as the combining elements, and differential transmission-line lengths could be used as phase shifters.

Results of RF Measurements

(1) Input and Output VSWR: The beam-forming matrix is a matched device at all input and output terminals. Input and output VSWR's averaged about 1.2 with a highest value of 1.48 at 1160 Mcps. The highest VSWR at 900 Mcps was 1.27.

(2) Isolation Between Terminals: Any beam terminal of the matrix is isolated from any other beam terminal due to the inherent isolation of the directional couplers. At 900 Mcps, the average isolation is about 28 db, with a lowest value of 15 db. The isolation stays in this range for the other three frequencies.

The antenna terminals are isolated from each other in the same manner. The average isolation was about 30 db at 900 Mcps, with a worst case of 20 db. Antenna terminal isolations were not measured at the other frequencies.

(3) Amplitude of Illumination and Insertion Loss: If one beam terminal of the matrix is driven at a certain power level, this power should be split sixteen equal ways as it travels to the antenna terminals. However, the insertion loss of the matrix and slight variations in the coupling ratios of the directional couplers will cause deviations from this ideal situation. The insertion loss will reduce the gain of an antenna system and increase the system noise temperature. The variations in coupling ratios cause errors in the aperture illumination which lead to reduced gain and higher sidelobes.

Table 2-I shows the coupling from any beam terminal to all antenna terminals at a frequency of 900 Mcps. In an ideal 16-element matrix, these coupling values would all be 12 db (16-way power split). The average of all coupling values is -12.74 db, indicating an insertion loss of 0.74 db. Most of this insertion loss is due to the strip transmission line which has a loss of about 0.18 db per foot at 900 Mcps. [A new strip line material, Teflon 3A, has a much lower loss (see Ch. II, Sec. B).] A small portion (about 3 per cent) of the measured insertion loss is due to the nonperfect isolation between beam terminals. It should be possible to reduce the insertion loss of the matrix by a factor of three or four by using the new material and new construction techniques.

(4) Phase of the Illumination: Table 2-II shows the differential phase shift between antenna elements for all beams. The ideal element-to-element phase shift is given by Eq. (3). For a 16-element matrix, Eq. (3) becomes:

TABLE 2-1
COUPLING TO EACH ANTENNA TERMINAL (in db) FROM EACH BEAM
(Frequency: 900 Mcps)

Beam Number	Antenna Terminal Number																Average
	A_0	B_0	C_0	D_0	E_0	F_0	G_0	H_0	I_0	J_0	K_0	L_0	M_0	N_0	O_0	P_0	
1R	13.5	12.8	12.9	13.0	13.0	12.5	12.7	12.1	13.2	13.0	12.9	12.4	13.0	12.4	12.6	12.0	12.76
2R	13.3	12.5	13.0	12.0	13.0	12.5	12.7	12.3	13.2	13.0	13.3	12.4	13.1	12.4	12.6	12.3	12.73
3R	12.9	12.8	12.7	12.1	13.0	13.1	13.0	12.3	12.6	12.3	12.6	12.5	13.0	13.0	13.9	12.6	12.72
4R	12.7	13.0	12.9	13.3	13.2	13.1	13.2	12.8	13.1	13.1	12.9	13.1	13.2	13.0	13.2	12.8	13.04
5R	13.0	13.1	13.1	13.2	12.7	12.3	13.0	12.6	13.0	12.6	13.2	12.9	12.7	12.9	12.9	12.6	12.94
6R	12.8	12.4	13.4	12.4	12.7	12.3	12.6	12.4	12.4	12.3	13.3	12.7	12.8	12.5	12.0	12.4	12.68
7R	12.6	12.6	12.8	12.6	12.8	12.8	12.8	13.2	12.4	12.6	12.9	12.8	12.7	12.4	12.8	13.0	12.74
8R	12.6	12.4	13.0	12.8	12.8	12.1	13.4	13.0	12.7	12.0	13.2	12.8	12.9	12.6	13.5	13.1	12.81
1L	12.0	12.7	12.7	13.0	12.4	12.8	12.8	12.5	12.2	12.4	12.6	13.1	12.8	12.9	12.7	13.7	12.71
2L	12.5	12.8	12.5	13.1	12.5	13.0	12.7	13.2	12.4	12.5	12.4	12.8	12.1	12.8	12.6	13.3	12.70
3L	12.6	13.5	13.0	13.2	12.3	12.7	12.4	12.8	12.5	12.9	13.0	13.2	12.1	12.8	12.4	13.0	12.73
4L	12.6	13.1	12.8	13.2	12.6	12.9	12.7	13.0	12.7	13.0	12.8	13.3	12.8	12.8	12.9	12.8	12.88
5L	12.6	13.0	12.6	12.0	13.1	12.4	12.8	13.2	12.6	12.2	12.4	12.2	12.3	12.5	12.9	12.7	12.56
6L	12.5	12.9	12.4	12.7	12.8	12.4	12.4	12.9	12.4	12.6	12.4	12.5	12.4	12.3	12.6	12.6	12.55
7L	13.0	13.0	12.5	12.8	12.5	12.9	12.3	12.7	12.9	13.0	12.6	12.8	12.4	13.0	12.2	12.6	12.70
8L	13.0	13.5	12.4	13.0	12.9	13.0	12.4	12.6	13.0	13.2	12.5	12.5	13.1	12.8	12.2	12.3	12.79
																Average	12.74

34

TABLE 2-11

DIFFERENTIAL PHASE SHIFT (in degrees) BETWEEN ANTENNA TERMINALS FOR EACH BEAM
(Frequency: 900 Mcps)

Antenna Terminals	Beam Numbers								Beam Numbers							
	1R	2R	3R	4R	5R	6R	7R	8R	1L	2L	3L	4L	5L	6L	7L	8L
A_0-B_0	10°	33°	53°	81°	99°	123°	133°	169°	11°	45°	56°	77°	99°	126°	146°	177°
B_0-C_0	12	29	56	71	107	119	158	154	17	23	59	82	107	125	151	169
C_0-D_0	9	36	54	84	100	126	134	171	7	45	55	79	102	126	143	169
D_0-E_0	17	35	61	77	106	124	159	170	11	20	54	76	97	127	145	165
E_0-F_0	6	29	54	77	96	109	138	165	14	48	62	77	105	129	152	172
F_0-G_0	12	34	58	72	105	135	153	166	14	25	57	77	105	121	146	168
G_0-H_0	9	34	56	90	103	122	138	169	11	45	56	78	107	124	148	175
H_0-I_0	12	41	58	87	99	132	157	176	5	22	51	83	87	123	135	169
I_0-J_0	9	33	53	82	101	122	135	169	9	45	56	77	101	126	150	170
J_0-K_0	14	30	57	69	103	120	156	152	18	24	61	79	109	122	168	168
K_0-L_0	7	33	54	82	97	128	133	173	8	60	55	79	99	127	148	171
L_0-M_0	17	36	52	78	105	124	162	158	12	20	54	75	99	119	143	164
M_0-N_0	5	29	47	79	97	118	132	66	14	45	60	82	106	127	148	174
N_0-O_0	15	32	61	74	107	124	158	167	14	24	56	77	103	124	149	164
O_0-P_0	12	35	58	80	99	122	137	169	12	46	58	75	100	120	147	171
Average	11.0	33.2	55.4	78.2	101.2	123.2	145.5	168.2	11.8	35.8	56.6	78.4	101.7	124.4	143.0	169.3

$$\delta_K = (2K - 1)\ 11.25° \quad ,$$

where K = the beam number. Thus, the ideal differential phase shifts for beams 1, 2, 3 and 4 are: 11.25°, 33.75°, 56.25° and 78.75°, respectively. While the individual phase shifts shown in Table 2-II deviate considerably from these values, the average phase-shift value of each beam is close to the ideal value.

Rms Amplitude and Phase Errors:— The rms amplitude and phase errors have been calculated from the previous data. The results are shown in Table 2-III. Relatively large phase errors occur in beams 2L and 7R. Reference to the matrix schematic of Fig. 2-8 shows that these beams share a common directional coupler (coupler 29) and phase shifter. The differential phase shifts (Table 2-II) for these two beams alternate about the design value in a very regular manner, indicating that the most likely source of the large phase error is the phase shifter connected to directional coupler 29. This phase error demonstrates the danger of getting systematic errors in the aperture illumination when this beam-forming technique is used. As a further example, consider what happens when a large coupling error exists in a directional coupler at the bottom of the matrix. Injecting a signal into this coupler and observing the amplitude of the illumination shows a systematic "ripple" in the illumination. This ripple tends to support endfire beams (for element spacings close to one-half wavelength), and thus the sidelobe levels will be increased in the area 90° removed from broadside.

TABLE 2-III		
RMS AMPLITUDE AND PHASE ERRORS FOR EACH BEAM		
Beam Number	Rms Amplitude Error (db)	Rms Phase Error (degrees)
1R	0.38	3.5
2R	0.41	3.1
3R	0.30	5.5
4R	0.17	4.7
5R	0.26	3.1
6R	0.33	5.6
7R	0.20	11.5
8R	0.40	3.4
1L	0.38	3.4
2L	0.32	12.9
3L	0.31	2.8
4L	0.21	2.2
5L	0.35	4.7
6L	0.19	2.8
7L	0.26	6.5
8L	0.35	3.2
Average	0.30	4.8

Systematic errors become more undesirable when one considers large antenna arrays because the effect[*] of a certain sized systematic error does not decrease as the number of elements is increased, whereas the effect of a certain sized random error does decrease with increasing array size.

In general, the rms errors of Table 2-III should not produce significant increases in the near-in sidelobe levels of uniform-illumination beams. In a particular system, the errors in other parts of the RF portion of the receiver (antennas, interconnecting cables, etc.) can be significant compared with the matrix errors. The performance of the 16-element matrix in an actual antenna system is discussed in Sec. 4.

4. Antenna Performance of 16-Element Matrix

The proof of the effectiveness of any beam-forming scheme lies in its performance in an antenna system. This section presents the antenna patterns[†] which have been taken by using the 16-element beam-forming matrix at a frequency of 900 Mcps. The Lincoln Laboratory Antenna Test Range[‡] was used for all antenna measurements. A Scientific-Atlanta model APR-120 recorder was used to take the patterns.

Figure 2-9 shows the 16-element array used in the antenna testing. Crossed dipoles spaced 0.58λ apart and 0.25λ above the ground plane were used. All patterns shown were taken using the vertical dipoles, hence the array is a parallel array of dipoles (as opposed to collinear array). The horizontal dipole member is well isolated from the vertical member (~25 db). All dipoles had VSWR's less than 1.3 as measured in the array. The dipoles were connected to the matrix by 12-foot lengths of RG-9B/U cable which were cut to an accuracy of ±1 mm (±1.1° at 900 Mcps). Figure 2-10 shows the average antenna pattern of the sixteen dipoles of the array.

In an attempt to analyze the gain variations among the dipoles, the pattern of Fig. 2-11 was constructed from all the individual dipole patterns. The patterns of all dipoles except the two end elements are contained within the shaded area. The end-element patterns are shown where they exceed the shaded area. (This pattern "squint" is common in end elements of an array.) The gain variations are quite large at angles greater than 72° from broadside. The large amplitude errors in these regions primarily affect the far-out sidelobe levels of the matrix beams.

Uniform-Illumination Antenna Patterns:— Figure 2-12 shows the main lobes of the sixteen matrix beams. The peak gains of these beams follow the average element pattern of Fig. 2-10 quite closely (as would be expected from the principle of pattern multiplication). The angular section covered by all beams is 107°, which agrees closely with the value of 108° predicted by Eq. (7) for an element spacing of 0.58λ.

Figures 2-13 through 2-28 show individual patterns for the sixteen matrix beams. The element spacing of 0.58λ allows grating lobes to form for beams farther than 45° off broadside. The start of a grating lobe structure is evident in beams 6 right, 6 left, 7 right and 7 left, with a well-defined beam emerging in 8 right and 8 left.

---

[*] J. Ruze, "Physical Limitations on Antennas," Technical Report No. 248 [U], Research Laboratory of Electronics, M.I.T. (30 October 1952).

[†] All patterns were taken on Scientific-Atlanta No. 121 paper which has a 40-db scale. The horizontal scale used was 360° per cycle.

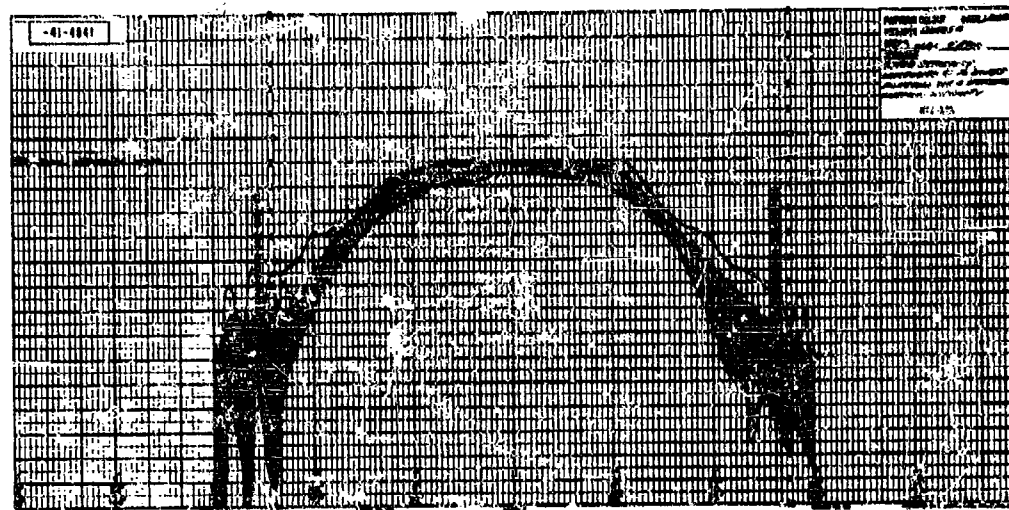[‡] A. Cohen and A.W. Maltese, "The Lincoln Laboratory Antenna Test Range," Microwave J. 4, 57 (April 1961).

Fig. 2-9.   16-element linear array.

Fig. 2-10.   Average antenna pattern of the 16 dipoles.

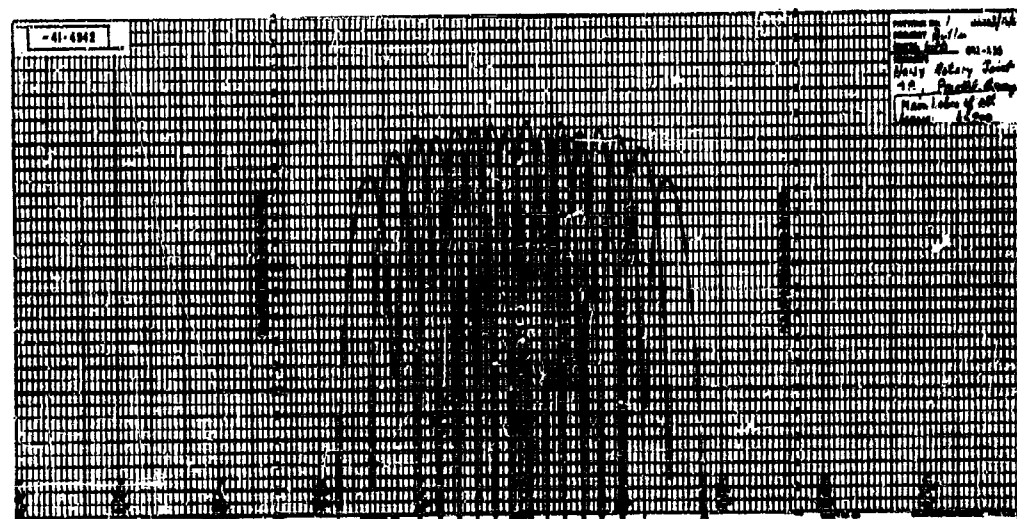Fig. 2-11. Dipole gain variation pattern.

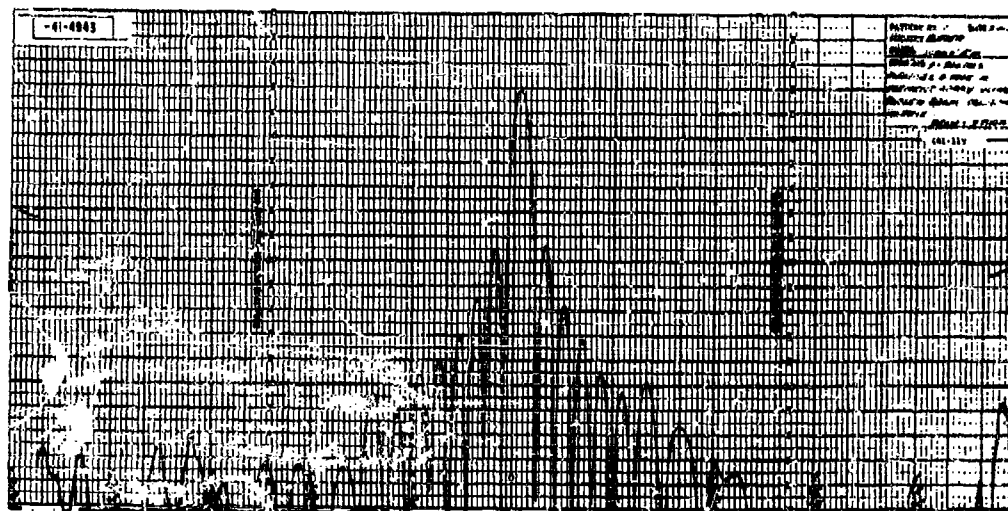Fig. 2-12. Main lobes of the 16 matrix beams.

39

Fig. 2-13.   Beam 1 right (horizontal scale = 360°; vertical scale = 40 db).
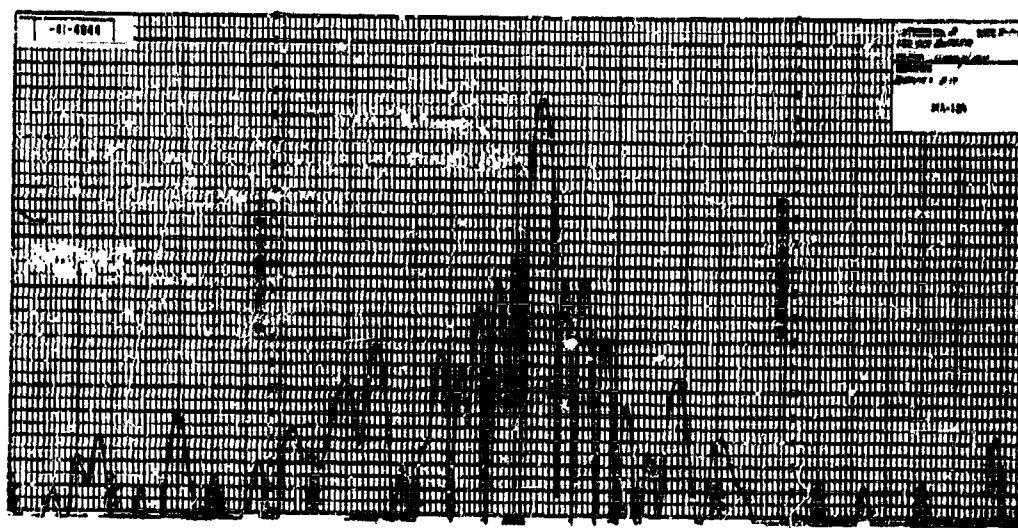

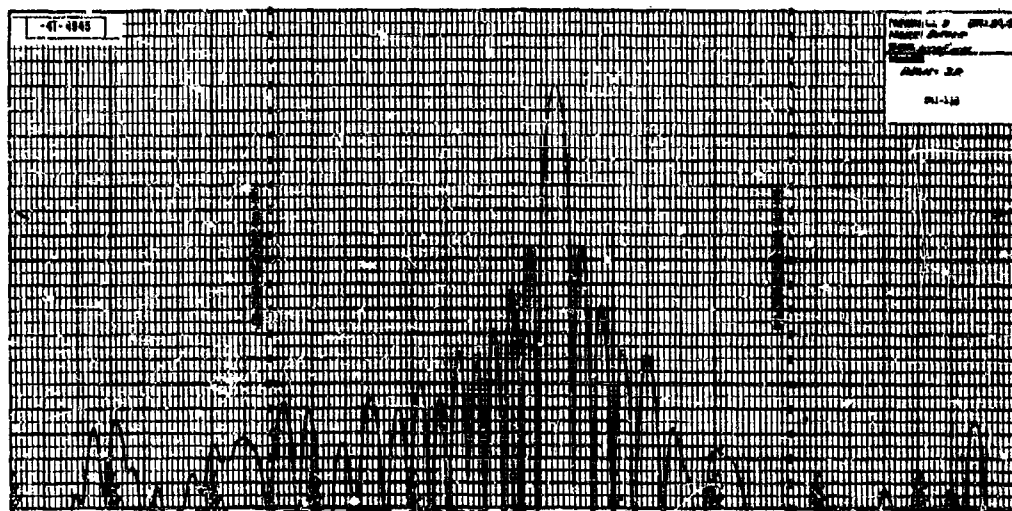Fig. 2-14.   Beam 2 right.

Fig. 2-15. Beam 3 right.

Fig. 2-16. Beam 4 right.

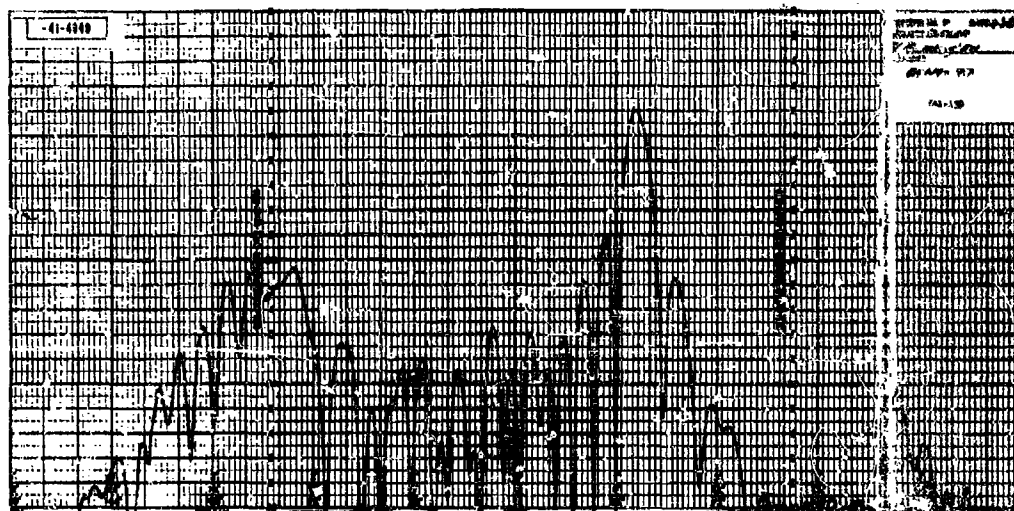Fig. 2-17. Beam 5 right.

Fig. 2-18. Beam 6 right.

Fig. 2-19. Beam 7 right.

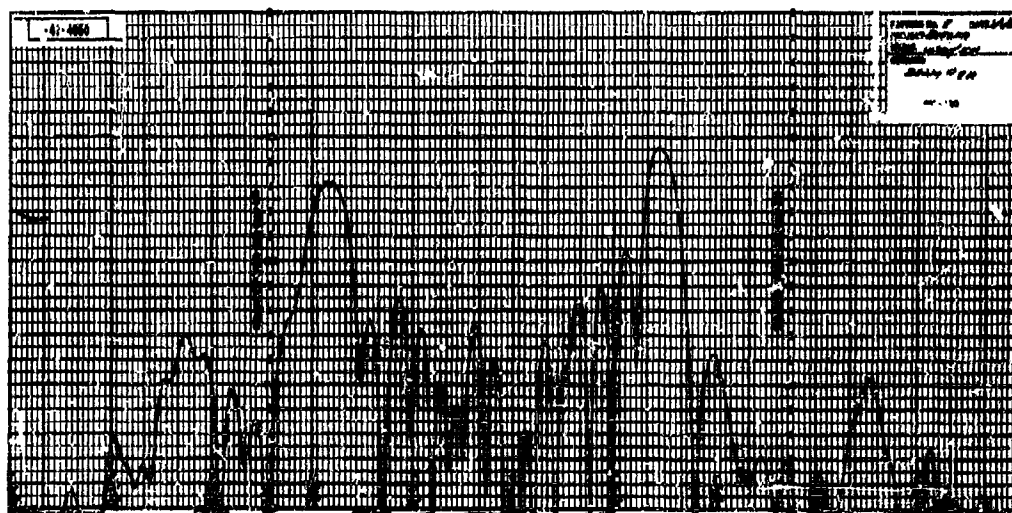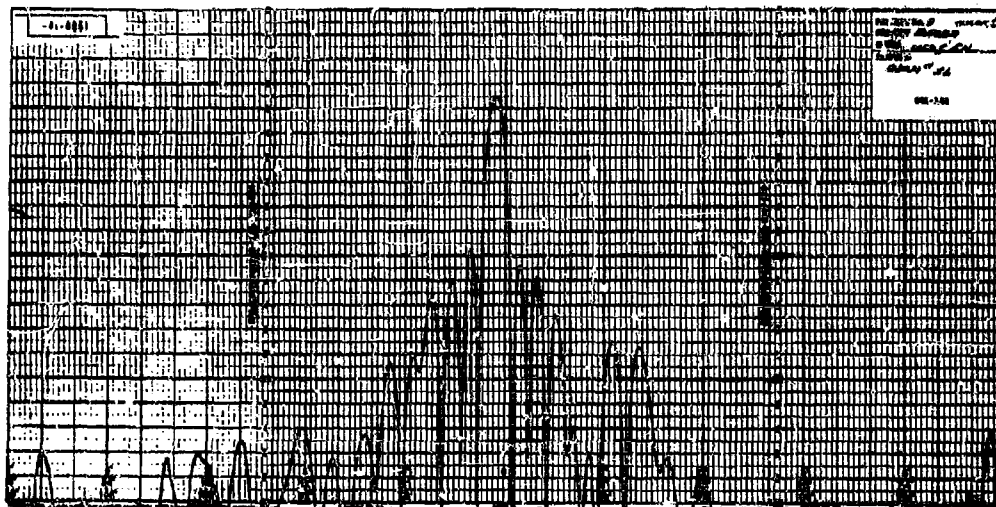
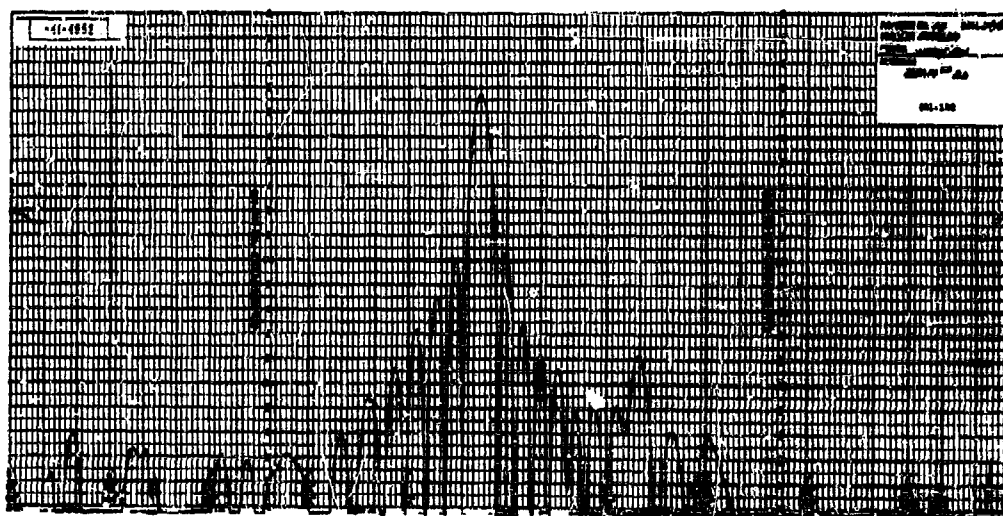Fig. 2-20. Beam 8 right.

Fig. 2-21. Beam 1 left.

Fig. 2-22. Beam 2 left.

44

Fig. 2-23. Beam 3 left.

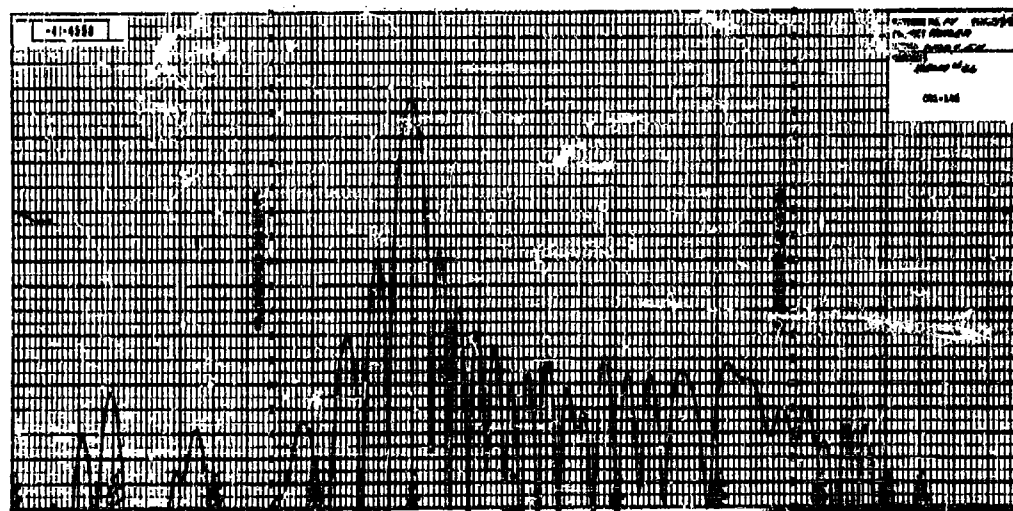Fig. 2-24. Beam 4 left.

45

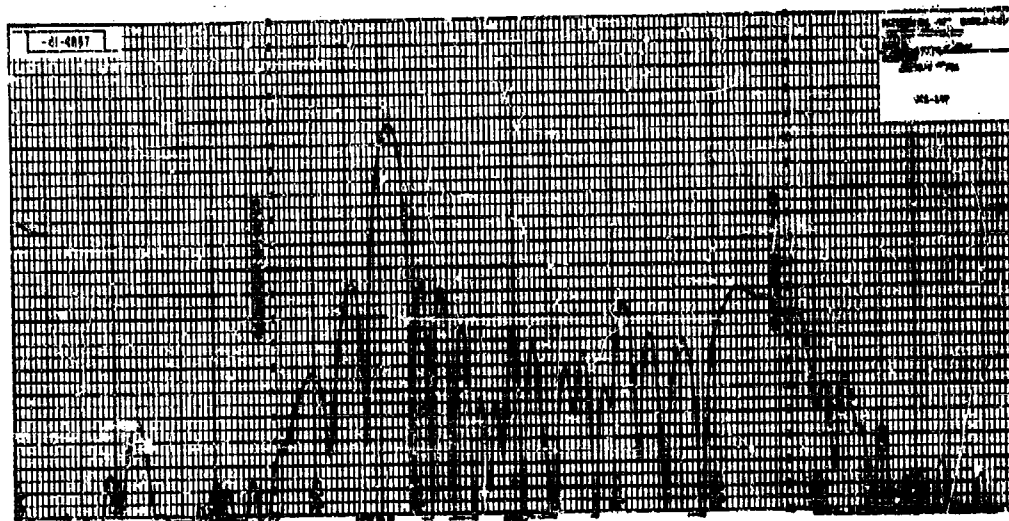Fig. 2-25. Beam 5 left.

Fig. 2-26. Beam 6 left.
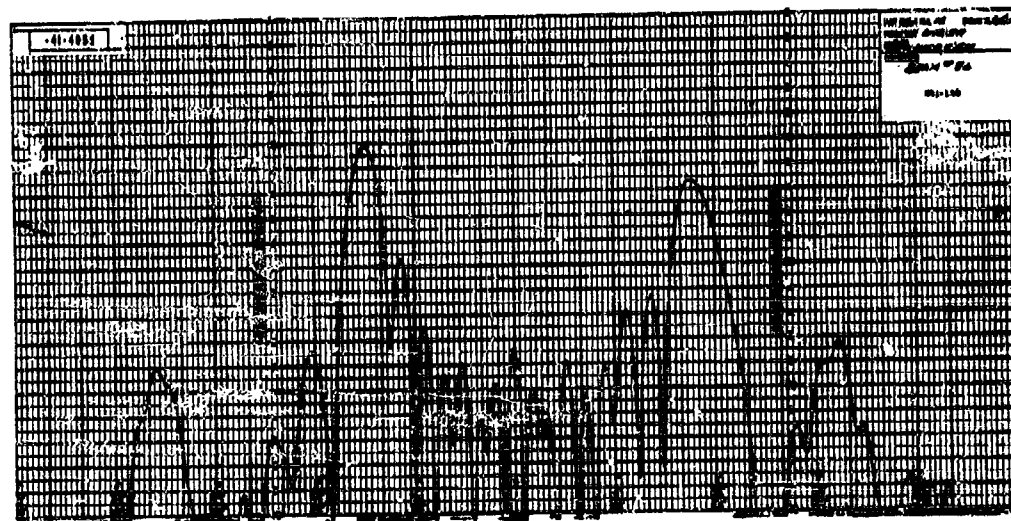
Fig. 2-27.   Beam 7 left.

Fig. 2-28.   Beam 8 left.

The beam peaks are very close to the theoretical positions given by Eq. (5). The worst case is beam 8R which peaks at 52° instead of the theoretical value of 54°.

The sidelobe performance of all the beams is quite good (theoretical first sidelobe level = -13.2 db). Beams 1R through 4R and 1L through 7L, have first sidelobes below 12 db. The worst first sidelobe (-8.5 db) occurs in beam 8R. The average antenna element pattern (Fig. 2-10) tends to suppress sidelobes on one side of the main beam and emphasize them on the other side (good examples: beams 3R and 4L).

Cosine and Cosine-Squared Illumination Beams:- It was shown earlier that a cosine illumination of the aperture could be achieved by adding two adjacent beams. Antenna patterns have been taken for all adjacent beam combinations, using a hybrid ring as an adder. The appropriate phase correction was obtained by the use of coaxial line stretchers. The hybrid ring also provides the difference of the two adjacent beams (corresponding to a sine illumination). This difference pattern has a sharp null at the same position as the peak of the sum beam. Figures 2-29 through 2-31 show some typical sum and difference patterns obtained by adding adjacent matrix beams. Figure 2-29 was the best cosine-illumination pattern obtained. All sidelobes of the sum beam are below -24 db (theoretical first sidelobe of a cosine taper in a 16-element array is -24.3 db).

The difference pattern has a 32-db null at the theoretically correct position. Figure 30 shows the sum and difference of the 1 right and 1 left beams. The highest sidelobe in this case is -20 db. The difference-pattern null, which is correctly located at 0°, is 23 db deep. Figure 2-31 shows cosine-illumination patterns formed by adjacent far-out beams. The high sidelobe located at 90° to the right of broadside is due to addition of the grating lobes of the two component beams.

A few cosine-squared illuminations were tested experimentally. Unfortunately, a beam combiner such as the one shown in Fig. 2-6 was not available at the time, and a "lash-up" of a power divider, line stretchers and attenuators was used to form a lossy beam combiner. Figure 2-32 shows a cosine-squared-illumination antenna pattern formed by combining beams 1L, 2L and 3L. The first sidelobes are down 27 db and 32 db (theoretical = 32 db). Figure 2-33 shows the pattern of a cosine-squared-on-a-pedestal illumination. The pedestal height was about 24 per cent (theoretical highest sidelobe = -27 db. The measured first sidelobes are both -27 db. In both patterns, the far-out sidelobes are higher than expected because of phase and amplitude errors in the antenna system and the beam combiner. As expected, the pedestal illumination produces a narrower beam than the pure cosine-squared illumination. Both beams have peaks at the peak of the middle component beam (2L) as expected.

5. Other Investigations in RF Beam Forming

Several problem areas presently under study are related to RF beam forming. Since some of these investigations are just beginning and the others are planned for the near future, not much is available in the way of concrete results.

Beam-Forming Matrix Layout and Fabrication:- A major drawback of the RF beam-forming technique is the complexity of the matrix arrangement. For example, a 64-element linear array requires a matrix containing 192 directional couplers and 160 fixed phase shifters. The interconnection of these components leads to numerous transmission line crossovers. If the matrix is not packaged in a compact form, the insertion loss due to line loss may become intolerable.

48
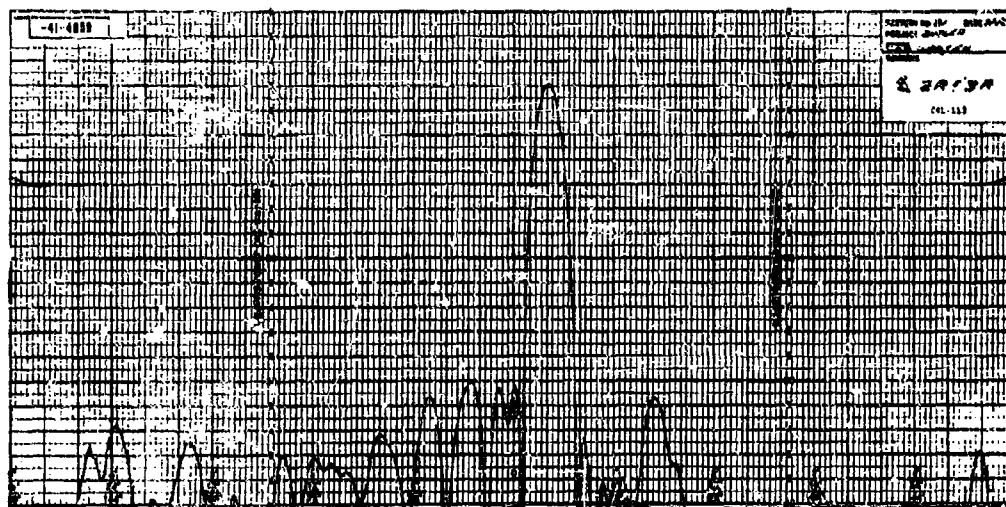
(a)
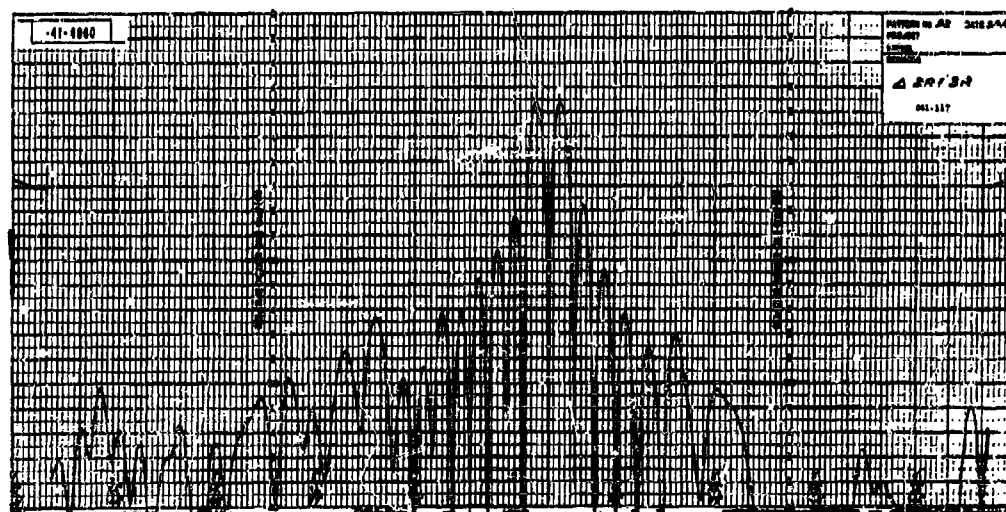
(b)

Fig. 2-29. Cosine-illumination patterns using beams 2 right and 3 right: (a) sum beam; (b) difference beam.

(a)

(b)

Fig. 2-30. Cosine-illumination patterns using beams 1 left and 1 right: (a) sum beam; (b) difference beam.

(a)

(b)

Fig. 2-31. Cosine-illumination patterns using beams 6 left and 7 left: (a) sum beam; (b) difference beam.

Fig. 2-32. Cosine-squared illumination beam.

Fig. 2-33. Cosine-squared-on-a-pedestal illumination beam.

52

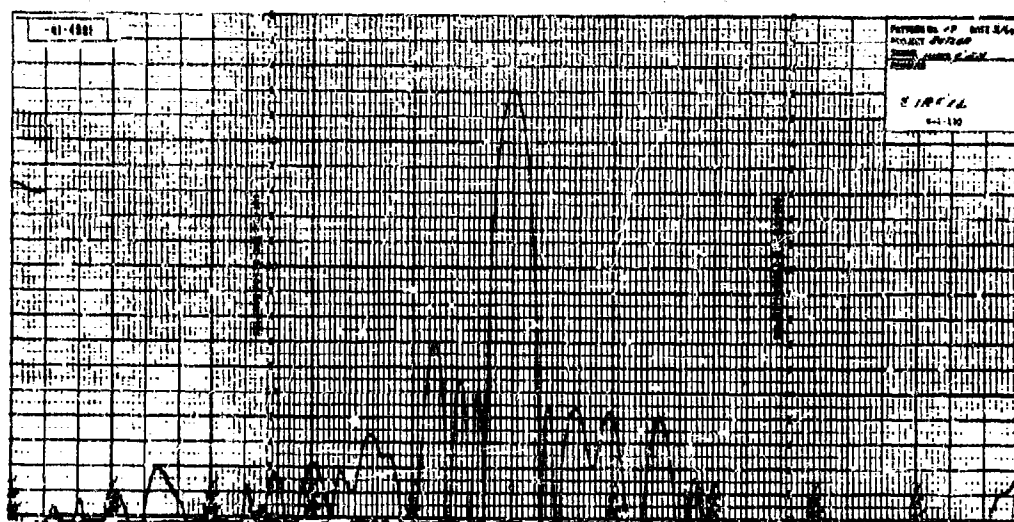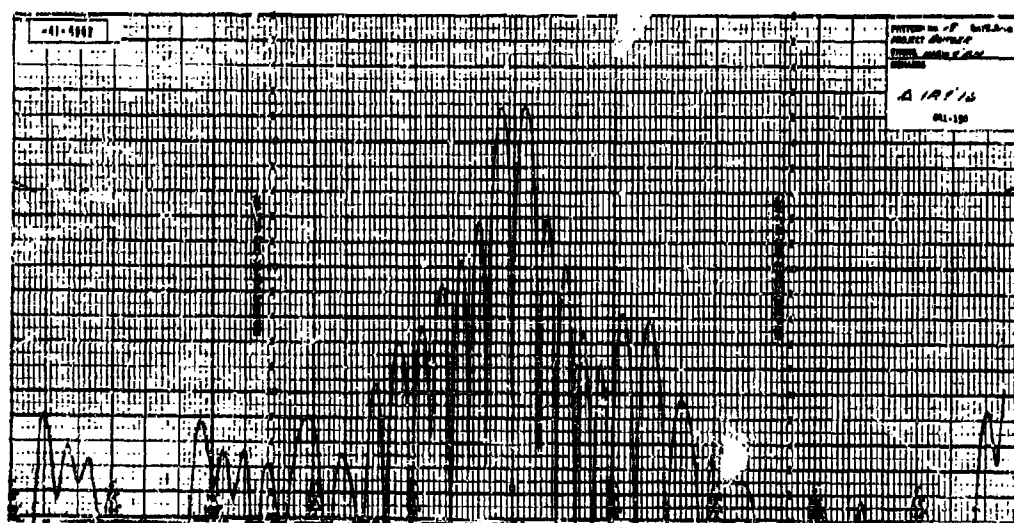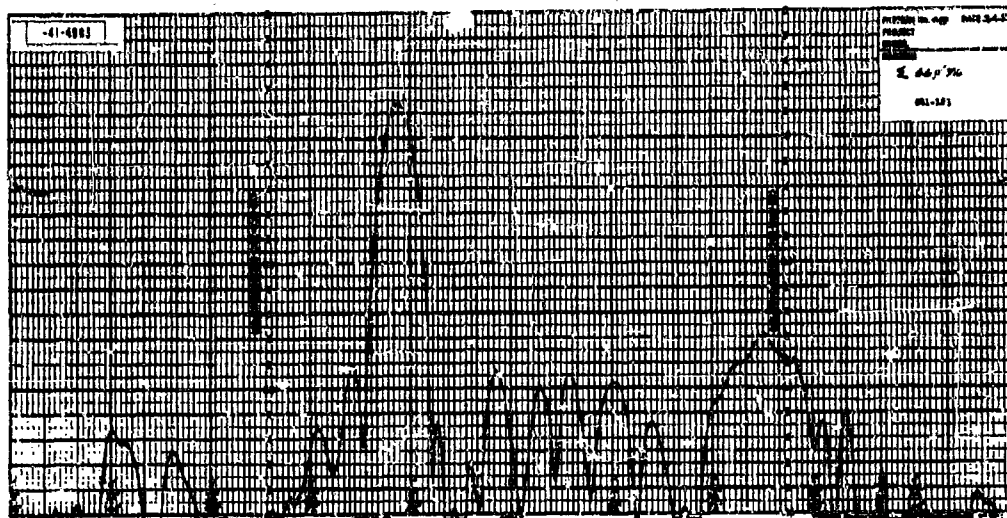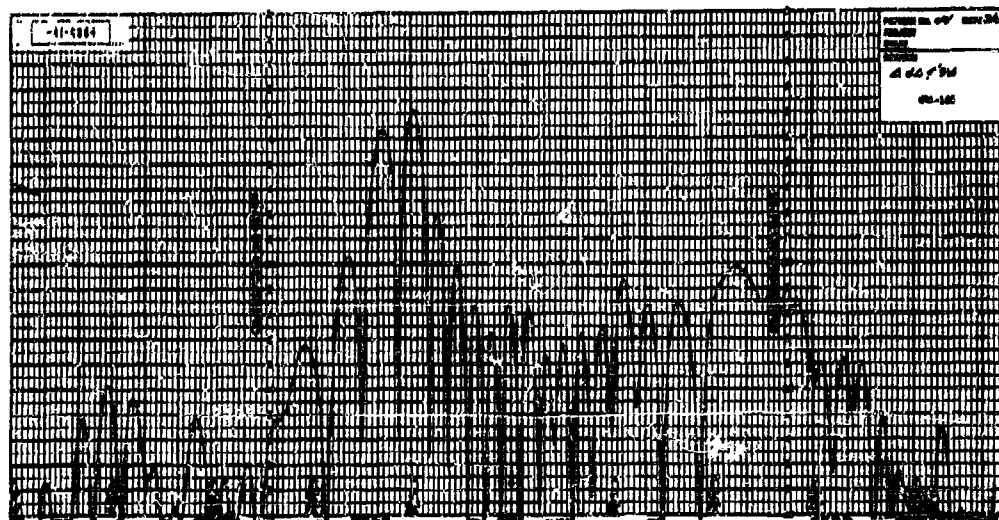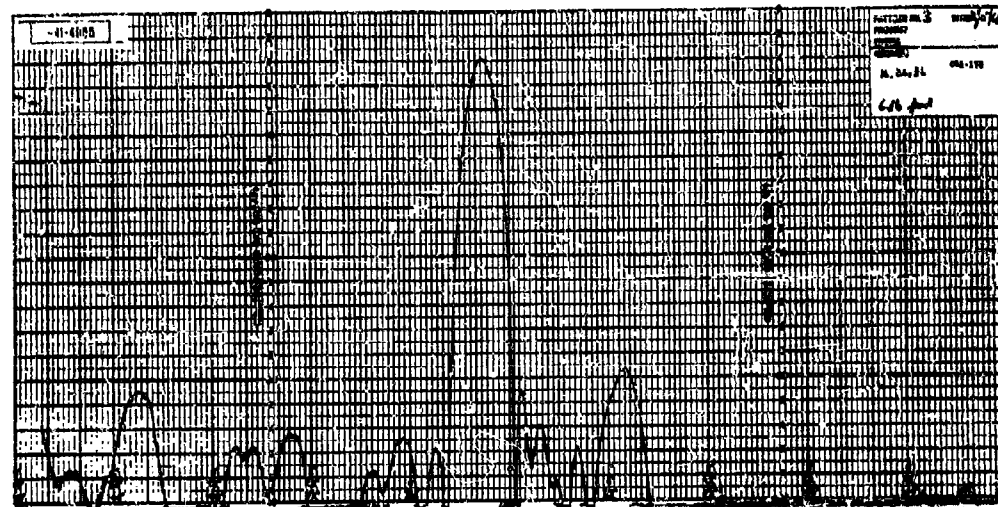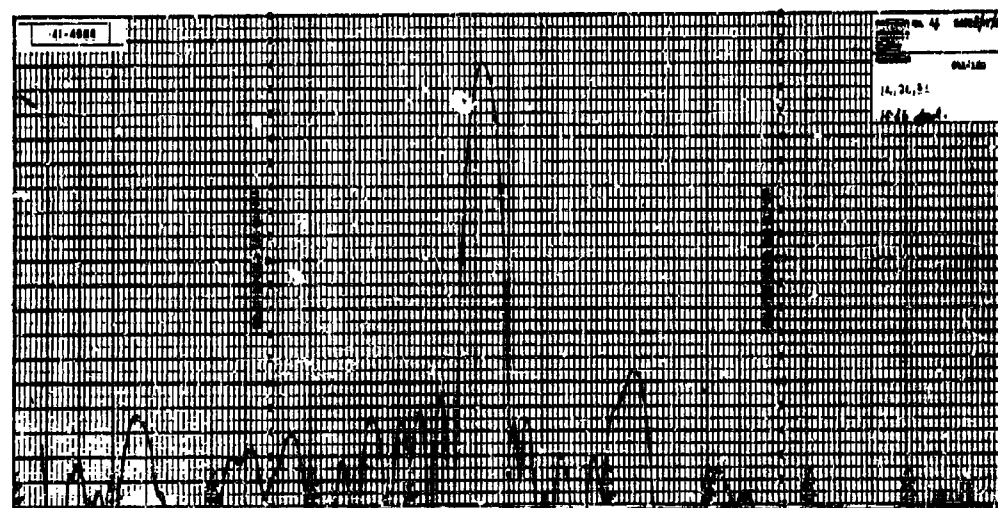Strip transmission line interconnection and crossover techniques are being investigated. It is also planned to use a new strip transmission line material* to reduce the insertion loss.

Beam Selection and Combination Techniques:– The beam-forming matrix provides n beams from an n-element array. In many applications, it is not necessary to observe the output of all beams simultaneously; thus, a receiver could be time-shared among several matrix beams. A beam-selection network using solid state microwave switches[†] will be built in the near future. This network will select any beam of the 16-element matrix and will also provide the sum and difference (cosine and sine aperture illuminations) of any two adjacent beams. This beam-forming and beam-selection combination will then be installed in the 16-element test array to study control and display problems in a realistic environment.

Possibilities of High-Power Operation: The beam-forming matrix is limited in power-handling capability (from a transmitting standpoint) by the high-power characteristics of the transmission line used. The complexity of large matrices discourages the use of coaxial line or waveguide, and thus the power limit is set by the strip transmission line. Also, since the matrix behaves like a corporate feed or power divider, the bottom directional couplers and phase shifters will have to handle much higher powers than the upper ones.

Equipment to test the peak and average power capability of strip transmission line has just recently been assembled, and some early results[‡] are available. While it is somewhat unlikely that a strip-line matrix could be used in the high-power sections of the phased array transmitters being proposed these days, the matrix might be useful in the medium- and low-power sections.

Beam Interpolation:– A possible drawback of this beam-forming technique is that the simultaneous beams are fixed in space. Continuous null tracking of a target using monopulse angular resolution techniques must be replaced by a beam interpolation technique. This problem will be studied in the near future.

C. ANTENNA ELEMENTS   W. P. Delaney and J. Sklar

1. 16-Element Test Array[§]

The log-periodic antenna elements[§] used in the 16-element test array will be replaced by dipoles. The dipoles will allow operation at peak powers of 10 kilowatts for phased array transmitter testing. Also, the dipoles should have more predictable antenna patterns and better polarization properties than the log periodics.

2. Scimitar Antenna

The scimitar antenna (Fig. 2-34) appeared to be an attractive antenna element for phased array applications. It is easily fabricated and can be fed directly from an unbalanced transmission line. The scimitar's traveling-wave operation suggests low mutual impedance, and its flat

---

* The characteristics of this material are discussed by D. H. Temme In Ch. II, Sec. A.

† Those solid state switches are discussed by D. H. Temme In Ch. II, Sec. D.

‡ See Ch. II, Sec. B.

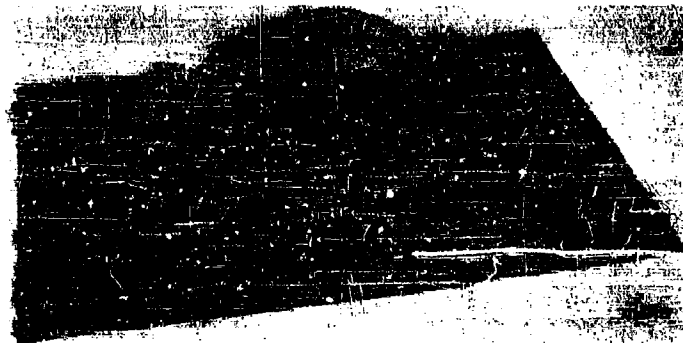§ J. L. Allen, et al., op. cit., pp. 5-13 and 19-24.

Fig. 2-34. Scimitar antenna.

shape indicates linear polarization in at least one plane. Also, it seems reasonable that two scimitars could be crossed to provide two orthogonal polarizations.

In order to test these hypotheses and to become familiar with the properties of scimitar antennas, three models were built. All were tested for impedance characteristics, and the best of these was chosen for pattern measurements.

The patterns resulting from these tests were not very satisfactory. The E-plane pattern was badly squinted off-boresight with a deep valley near the boresight direction. The H-plane pattern had low gain and was not smooth in its angular variation. Figures 2-35 and 2-36 show the E- and H-plane patterns of the scimitar. The patterns of a half-wavelength dipole located a quarter-wavelength above the ground plane are included for comparison. Both the scimitar and dipole patterns were measured with the same receiver gain. The low gain of the scimitar can be partially attributed to its polarization characteristics. Very undesirable polarization properties were found for the scimitar. Extensive measurements indicated that the angle of the polarization ellipse changed radically as the scimitar antenna was rotated in the azimuth plane. Hence, when the scimitar blade was vertical and facing the transmitter (azimuth angle = 0°), the element was vertically polarized. At other azimuth angles, the polarization became elliptical and the major axis of the polarization ellipse was no longer vertical. For an azimuth angle of 60°, the element was almost horizontally polarized. In Fig. 2-37, the angle of the major axis of the polarization ellipse is plotted against azimuth angle. For comparison, the same measurements for a dipole and a printed circuit logarithmic periodic element[*] are shown.

Since all the aforementioned measurements were made on a single sample, and since the tested model was mounted on only a small ground plane, unqualified conclusions cannot be made. However, the polarization properties of the scimitar antenna are bad enough to make one very suspicious of its value as an array element.

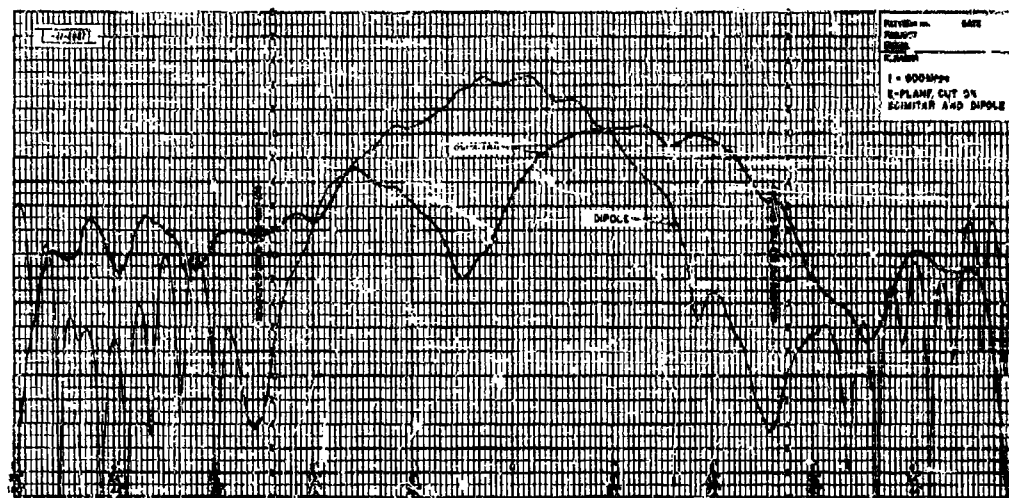[*] J. L. Allen, et al., op. cit., p. 19.

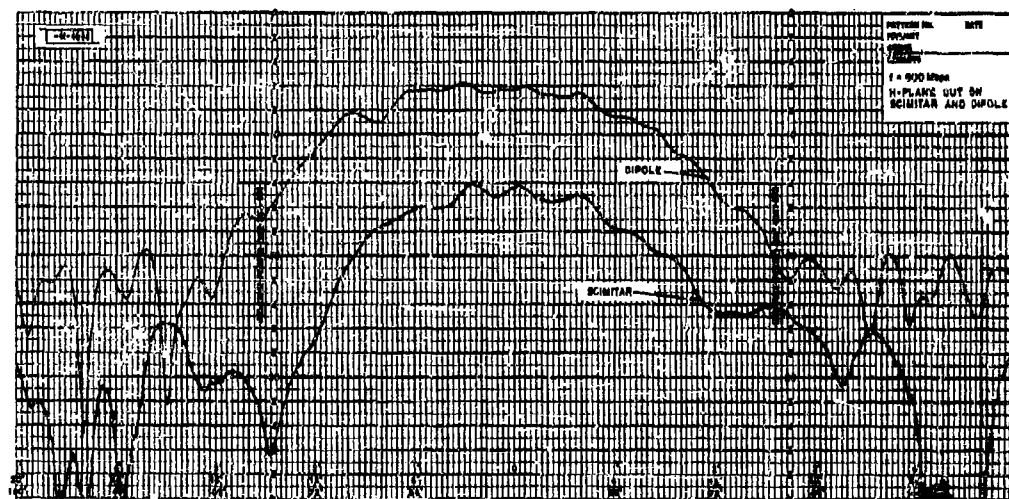Fig. 2-35. E-plane pattern of scimitar and dipole.

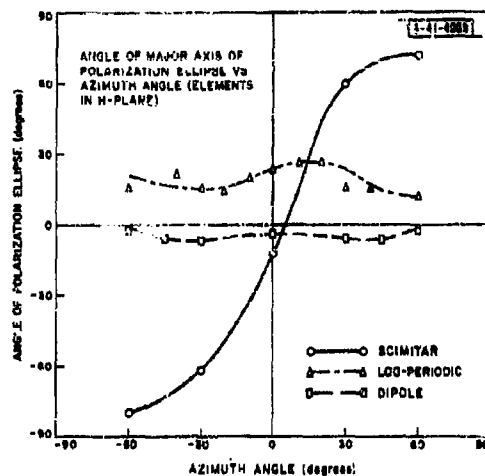Fig. 2-36. H-plane pattern of scimitar and dipole.

Fig. 2-37. Polarization properties of scimitar antenna (log-periodic and dipole antennas included for comparison).

CHAPTER II
STRIP TRANSMISSION LINE COMPONENTS: PHASE SHIFTERS AND SWITCHES

SUMMARY   D. H. Temme

This chapter is concerned with the development of phase shifters and microwave switches
for array applications, and with correlary areas of interest such as strip transmission line tech-
niques for such components.

Section B reports the results of some measurements on new low-loss copper-clad material
for strip transmission line and its fabrication properties. Next, some preliminary experimental
and theoretical results on the power-handling capability of such lines are presented. The con-
cluding section on strip transmission line outlines some techniques for fabrication of such lines
which yield an ease of breadboarding comparable to that usually associated with lumped circuitry.

Section D reports the developments since TR-228 in the area of low-loss RF diode switches
for the control of microwave signals. Finally, Section E reports the developments in the appli-
cation of these and other switches to the problems of development and fabrication of digital phase
shifters and time delays.

A. INTRODUCTION

Two crucial components of most array systems are microwave switches and variable phase
shifters, their relative importance being dependent upon the exact array configuration chosen.
The necessity of fast-acting (microsecond time) switches capable of handling microwave signals
in a low-loss manner is apparent in systems making use of such techniques as the simultaneous
beam-forming techniques described in the previous chapter. In such applications, the switches
find use for signal routing from the simultaneous beam-forming matrix to receivers. Further,
as outlined in TR-228, the development of quality microwave switches makes possible the cor-
relary development of discrete phase shifters and time delays using these switches. This chap-
ter reports the developments in these areas since TR-228.

Further, since the compactness and ease of reproducibility of strip transmission line appear
to make this a highly desirable technique for array component fabrication, a great deal of work
during the past year has gone into the development of improved strip transmission line compo-
nents in support of the main area of interest. This work is also reported in this chapter.

B. MEASUREMENTS ON STRIP TRANSMISSION LINE MATERIALS

This section reports the results of measurements on a new material for microwave strip
transmission lines, Teflon 3A, manufactured by Tell Manufacturing, Orange, New Jersey.
Some of the manufacturer's specifications are:

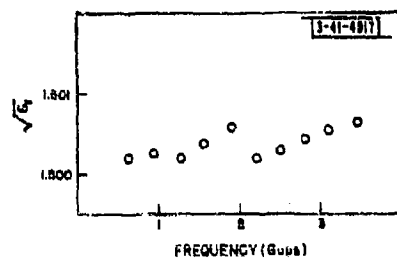|	
Dielectric constant	2.31 at 1 Mcps
	2.25 from 1 to 7 Gcps
Dissipation factor	<0.0002 from 1 to 7 Gcps
Dielectric strength	466 volts/mil
Operating Temperature	
Continuous	100°C
Intermittent	260°C
Peel strength	5 lb/in min
Solder-dip resistance	10 sec at 450°F min

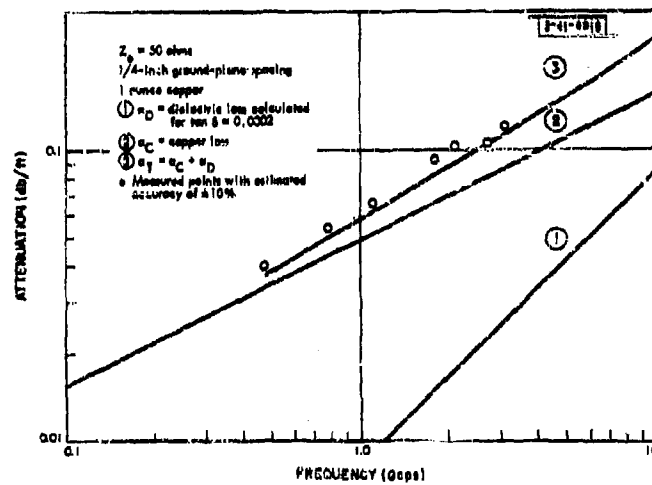Fig. 2-38. Measured Teflon 3A dielectric constant vs frequency.

Fig. 2-39. Teflon 3A attenuation vs frequency.

The experiments that have been conducted to verify the manufacturer's data and to obtain data for component design are described below.

1. Dielectric Constant

The dielectric in Teflon 3A is a modified polyolefin. Schlabach and Colardeau[*] give a good comparison of the dielectric properties of this material with other strip transmission line materials.

A check on the manufacturer's quoted value of the dielectric constant was made between 600 Mcps and 4 Gcps by measuring the wavelength in a Teflon 3A transmission line. A probe consisting of a 1.5-mil copper wire was placed on the center conductor of a 50-ohm line. The wire probe was brought out perpendicularly from the center conductor. A tapered line transformer was used to match the wire probe line to a 50-ohm detector. Nulls at the probe position were detected as the frequency of the signal generator feeding the line was varied. The distance from the probe to the shorted end of the line could easily be measured with an accuracy of 0.2 per cent. Frequency was measured to 0.1 per cent. Any discontinuities introduced by the probe should be negligible according to Altschuler and Oliner.[†] Thus, the value of dielectric constant obtained, 2.25, should have a maximum error of 1 per cent. These values are plotted in Fig. 2-38.

2. Attenuation

Using Cohn's formula,[‡] the calculated attenuation α vs frequency for 50-ohm line is plotted in Fig. 2-39. The attenuation of an isolated section of transmission line is related to the quality factor Q by[§]

$$Q = \frac{\pi}{\lambda \alpha}$$

Using the same type of probe as that used to measure the dielectric constant, the Q of a line can be determined from the measured 3-db bandwidth of an observed null. This Q is actually the loaded Q. However, if near a null frequency the input impedance of the probe and the impedance of the generator seen from the probe position are very large compared with the input impedance of the shorted line at the probe position, the computed loaded Q is practically the Q of the line. The values obtained for the attenuation are shown in Fig. 2-39. One can see from this figure that the attenuation of Teflon 3A is predominantly a copper loss at VHF and lower UHF frequencies.

It is further interesting to note that strip transmission line attenuation compares favorably with coax. line which uses similar materials and outer conductor dimensions. Gannett, et al.,[¶] have derived a simple general equation for the attenuation for transmission line. For TEM lines, this equation becomes

[*] T.D. Schlabach and R.D. Colardeau, "Low Loss Materials for Printed Microwave Applications," to be presented at AIEE Winter General Meeting, 28 January – 2 February 1962.

[†] H.M. Altschuler and A.A. Oliner, "Discontinuities in the Center Conductor of Symmetric Strip Transmission Line," Trans. IRE, PGMTT MTT-8, 328 (1960).

[‡] S.B. Cohn, "Problems in Strip Transmission Lines," Trans. IRE, PGMTT MTT-3, 120 (1955).

[§] J.F. Reintjes and G.T. Coate, Principles of Radar (McGraw-Hill, New York, 1952), p. 624.

[¶] D.K. Gannett, et al., "A Simple General Equation for Attenuation," Proc. IRE 48, 1161 (1960).

$$\alpha = \frac{MA\sqrt{f}}{a} + D \quad ,$$

where

D = constant depending only on the intrinsic properties of the dielectric,

M = constant depending only on the intrinsic properties of the dielectric and of the conducting material,

A = constant depending on the configuration (but not the scale) of the cross section,

a = selected linear dimension of the cross section specifying its size or scale, all other dimensions having fixed ratios to a,

f = transmitted frequency.

Thus, expressions for A for coaxial line and strip transmission line give the desired comparison. For coaxial line,[*]

$$A = \frac{1 + a/b}{\ln a/b}$$

$$= 3.6$$

for 50-ohm copper line with Teflon dielectric. The A for strip transmission line, extracted from Cohn's attenuation equation,[†] is

$$A = \frac{4\sqrt{\epsilon_r} Z_0}{377} \left\{ \frac{1}{1 - t/b} + \frac{2w/b}{(1 - t/b)^2} + \frac{1}{\pi} \frac{1 + t/b}{(1 - t/b)^2} \ln\left[\frac{\frac{1}{1 - t/b} + 1}{\frac{1}{1 - t/b} - 1}\right] \right\} \quad ,$$

where

ϵ_r = relative dielectric constant,

Z_0 = characteristic impedance,

t = thickness of center conductor,

b = ground-plane spacing,

w = width of center conductor.

For a 50-ohm Teflon 3A line with b = 0.25 inch and 2-ounce copper, A is 3.5.

C. STRIP TRANSMISSION LINE POWER-HANDLING CAPABILITY

The use of strip transmission line in transmitter components may be limited by its power-handling capability. Some initial studies and tests to determine the power-handling capability of strip transmission line are reported in this section.

1. Peak Power

Since dielectric breakdown strengths are generally large, one should be able to transmit large peak powers through dielectric strip transmission line if all air voids can be eliminated. On tests to date, breakdown has occurred with 50-ohm Teflon 3A with $\frac{1}{4}$-inch ground-plane spacing between 150 and 200 kw peak power with a duty cycle of 0.0012. The resulting corona pattern has indicated that all air voids had not been eliminated even though the center conductor was

---

*D.K. Gonnett, loc. cit.

†S.B. Cohn, loc. cit.

coated with Dow Corning DC-4 silicon grease before the line was assembled. Gremar 5586 HN connectors were used. Work is continuing in an effort to find techniques to eliminate air voids.

2. Average Power

The average power-handling capability of strip transmission line is determined by the ability of the line to dissipate the heat due to signal attenuation. An expression for the average power-handling capability of transmission line with negligible dielectric loss is readily attained by analogy between its electric field ($E = \nabla V$) and its temperature gradient field (∇T). This is a consequence of analogous Laplacian equations.

$$\nabla^2 V = 0 \quad,$$

$$\nabla^2 T = 0 \quad.$$

For the parallel-plate electric capacitor and the parallel-plate "heat capacitor," analogous results are shown in Fig. 2-40. Similarly, for strip transmission line with negligible dielectric losses, the map for the electric field and temperature gradient field is similar as a consequence of the Laplacian expression. A plot of the strip transmission line capacitance as given by Cohn[*] is shown in Fig. 2-41. Thus, by analogy for strip transmission line, if one assumes that the dielectric losses are negligible and the heat generated by the RF copper losses of the center conductor all flows perpendicularly from the center conductor through the dielectric (the worst and general case, since very little heat flows along the center conductor),

$$\frac{\Delta H}{\Delta T} = \frac{4\,kw}{b}\,\frac{C}{C_{pp}}\cdot \text{per unit length,}$$

where

      w = center conductor width,

      b = ground-plane spacing,

      C = strip transmission line capacitance per unit length,

      C_{pp} = nonfringing plate-to-plate capacitance per unit length.

The rate of heat flow is determined by the RF attenuation of the center conductor α_{cc}. Extracting from Cohn's formula[*] and including a correction for the change of resistivity with temperature,

$$\alpha_{cc} = \frac{2.02(10^{-6})\,\epsilon_r Z_o \sqrt{f(G_c)}\,[1 + \beta(T - 25)]}{b(1 - t/b)}\left[1 + \frac{w/b}{1 - t/b}\right.$$

$$\left. + \frac{1}{\pi(1 - t/b)}\ln\left(\frac{2b}{t} - 1\right)\right] \text{db per unit length} \quad,$$

where

      β = temperature resistance coefficient (0.0044/°C for electrolytic copper),

      T = temperature of center conductor in degrees centigrade.

Then

$$P_{DCC} = 2\alpha_{cc}(\text{neper/length})\,P$$

$$= 0.231\alpha_{cc}(\text{db/length})\,P \quad,$$

---

[*] S.B. Cohn, loc. cit.
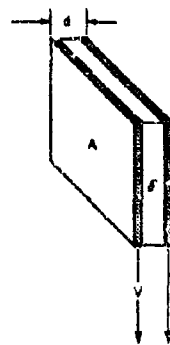
$$C_E = \frac{\Delta Q}{\Delta V} = \frac{\mathcal{E} A}{d}$$

C_E Electrical capacitance
Q Charge
V Voltage
$\mathcal{E}$ Dielectric constant
A Cross-sectional area
d Slab thickness
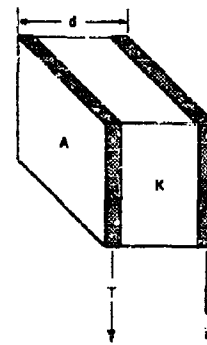
$$C_H = \frac{\Delta H}{\Delta T} = \frac{K A}{d}$$

C_H "Heat capacitance"
H Rate of heat flow (calories/sec)
T Temperature
K Coefficient of thermal conductivity
A Cross-sectional thickness
d Slab thickness

Fig. 2-40. Capacitor analogs.
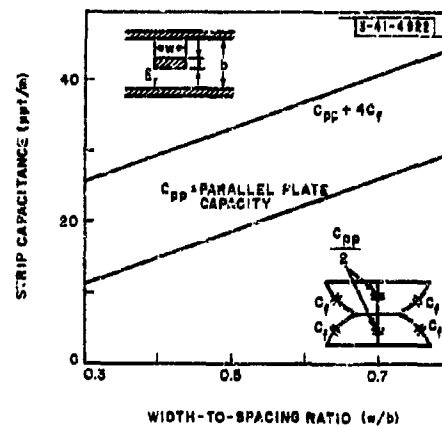
Fig. 2-41. Capacitance data for strip transmission line.

62

where

$$P_{DCC} = \Delta H = \text{power dissipated in center conductor in watts per unit length,}$$

$$\alpha_{cc} = \text{center conductor attenuation in db per unit length,}$$

$$P = \text{power in watts transmitted in the line.}$$

However, the dielectric loss in Teflon 3A 50-ohm line with $\frac{1}{4}$-inch ground-plane spacing at 1 Gcps is about 15 per cent of the center conductor loss. An approximate formula which includes the dielectric loss is readily attained.

The steady-state heat differential equation is*

$$\nabla^2 T = - \frac{g(x, y, z)}{K} \quad ,$$

where

$$g = \text{dielectric heat generated per unit volume,}$$

$$T = \text{temperature,}$$

$$K = \text{thermal conductivity.}$$

The one-dimensional case of the above equation is, in general, readily solvable. A strip transmission line with nonfringing electrical and heat capacitance is a one-dimensional case. The width of a strip D with an associated uniform field but with the same capacitance as the actual strip of width w is

$$D = w \frac{C}{C_{pp}} \quad .$$

Then, the heat equation takes the form

$$\frac{d^2 T}{dx^2} = - \frac{g}{K} \quad ,$$

where

$$g = 2\alpha_D P/Db,$$

$$\alpha_D = \text{dielectric attenuation in nepers per unit length,}$$

$$P = \text{power flowing in the line.}$$

Integrating,

$$\frac{dT}{dx} = - \frac{2\alpha_D Px}{KDb} + C_1 \quad .$$

Since one-half of the heat due to center conductor and dielectric attenuation flows out of the ground plane at $x = 0$ (see Fig. 2-42), and this heat flow is $-KD \left.\frac{dT}{dx}\right|_{x=0}$,

$$C_1 = \frac{(\alpha_{cc} + \alpha_D) P}{KD} \quad ,$$

where α_{cc} is the attenuation of the center conductor in nepers per unit length.

---

*H. S. Carslaw and J. C. Jaeger, Conduction of Heat in Solids (Oxford University Press, 1959), p. 10.

Fig. 2-42. Assumed heat flow configuration when
dielectric loss is included.

Fig. 2-43. Attenuation of Teflon 3A with
Permacel ST6347 center conductor.

In[?]grating again and applying boundary conditions,

$$\frac{dT}{dx} = -\frac{2\alpha_D P x}{kDb} + \frac{(\alpha_{cc} + \alpha_D) P}{KD} ,$$

$$T = -\frac{\alpha_D P x^2}{KDb} + \frac{(\alpha_{cc} + \alpha_D)}{KD} Px + C_2 ,$$

$$T = T_1 \text{ at } x = 0, C_2 = T_1 ,$$

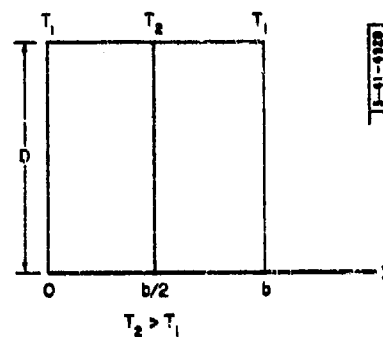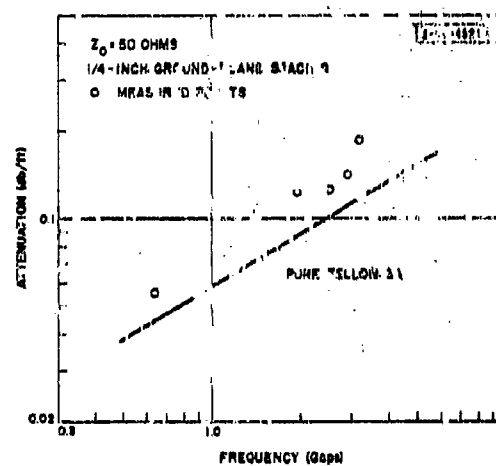$$T = T_2 \text{ at } x = b/2 ,$$

$$\Delta T = T_2 - T_1 = \frac{Pb}{4KD} (2\alpha_{cc} + \alpha_D)$$

For the α's in db per unit length, this expression is

$$\Delta T = \frac{0.02\ Pb}{KD} (2\alpha_{cc} + \alpha_D)$$

A fairly good estimate of the accuracy of this formula can be made. This will be done for a 50-ohm Tellon line with $\frac{1}{4}$-inch ground-plane spacing at 1 Gcps. The contribution of α_{cc} to ΔT is correct and is about 85 per cent of the total. The α_D part for C_{pp} is correct, and this is about 40 per cent of the 15 per cent for α_D. Thus, the accuracy of the formula is well within 6 per cent and the probability within a few per cent.

Experimental verification of the above results is under way.

D. STRIP TRANSMISSION LINE TECHNIQUES   W. J. Ince and D. H. Temme

1.   Breadboards

The ease of reproducibility of strip transmission line microwave components has been one of the main attractive features of strip transmission line described by Barrett.[*] However, an equally important microwave design objective is the ability to fabricate a "microwave bread-board" as easily as a "lumped-circuit breadboard." Over the years, many strip transmission line techniques useful in breadboard fabrication have evolved. This section contains a brief description of the "microwave breadboarding" currently employed by Group 41.

Barrett cut center conductor configurations out of thin metal foil for his breadboards. Accurately cutting the foil is easier if the foil is bonded (chemically or by an adhesive) to the dielectric. Stripping off the undesired copper on many materials is difficult because of the copper bond strength. The use of an adhesive-coated copper foil such as Permacel ST6347 for center conductor material works well for breadboarding. The additional microwave signal attenuation over and above Tellon 3.4 is shown in Fig. 2-43 and usually is inconsequential when breadboarding. The composite dielectric constant is about 2.30; thus, the wavelength is about 1 per cent longer in a breadboard than in pure Tellon.

A height gauge fitted with a knife edge can be used for cutting the foil[†] (Fig. 2-44[‡]). It is possible to obtain accuracies of a few mils with this technique (this is particularly important for precise spacings between laterally coupled lines, i.e., in the directional coupler depicted in

---

[*] R. M. Barrett, "Etched Sheets Serve as Microwave Components," Electronics 25, 114 (June 1952).

[†] This was brought to our attention by Robert Jordan of Sylvania Defense Products.

[‡] These photographs were taken before Permacel ST6347 was available; the adhesive on the foil used was very lossy. The Permacel ST6347 surface is smoother.

Fig. 2-44. Use of height gauge for strip transmission line breadboarding.

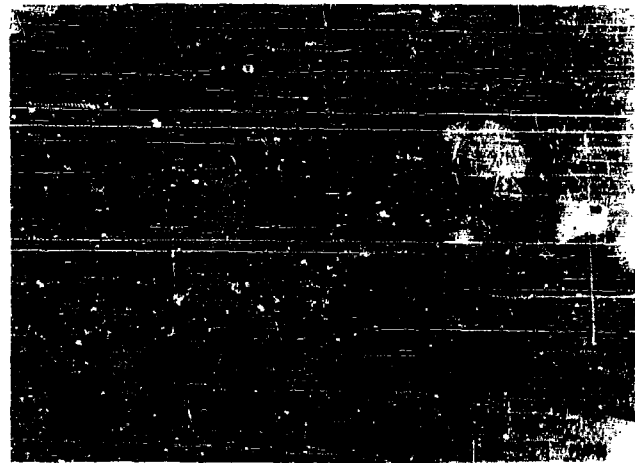Fig. 2-45. Use of some K&E tools for strip transmission line breadboarding.

Fig. 2-46. Use of bellows spring for strip transmission line breadboarding.

Fig. 2-44). In less critical applications, it is more expedient to use a modified Keuffel & Esser circuit path cutting tool (KE3340) in the KE3322 cut "N" strip cutting tools kit shown on the right of Fig. 2-45. The bevel of the cutting edge of the blade has been increased to eliminate drag, and some spacers have been ground to obtain desired spacings between the two cutting edges.

Two methods, both using the Gremar 5804 connector, have been used for electrical connection to the breadboard. In the first method, the head of the brass 2-56 screw used to fasten the center pins is filed until it protrudes $\frac{1}{16}$ inch above the base material surface (Fig. 2-44). This protrusion imbeds into the center conductor when the connector half-sandwich is assembled with the center conductor half-sandwich. In the second method, contact between the center pin of the Gremar connector and the center conductor of the strip transmission line is made with a gold-plated nickel bellows spring manufactured by Servometer Corporation* (Fig. 2-46). These bellows are very versatile and have also been used for making electrical contact to diodes and for sliding short circuits.

The techniques described above have proved to be particularly useful in quickly providing microwave components (i.e., couplers, hybrids, filters) needed in test setups.

2. Teflon 3A Fabrication Properties

Teflon 3A is easy to punch and rivet. However, solder must be applied with care in order to avoid heating the Teflon above its deforming temperature. The technique employed was devised by Ralph Thompson of Group 73. He has prepared a special flux with the following ingredients:

Per Cent by Weight	Ingredient
28	N_2H_5 Br
56	Polyethylene glycol with a molecular weight of 200
16	Water

The solder used with this flux is 40% lead/60% tin eutectic solder. Solder flow occurs readily at about 350°F with this flux as contrasted to about 450°F with conventional low-temperature solders. Care must be taken to remove excess flux after soldering because the flux is slightly corrosive. This is easily accomplished with water since the flux is water soluble.

Teflon warps to some degree when etched. A slight reverse warp can be introduced with a three-roller sheet-metal roller. This eliminates appreciable air voids around the center conductor region when the two half-sandwiches are assembled. The use of a rigid ground plane is also being investigated.

E. RF DIODE SWITCHES

Fast low-loss RF switches have applications of "line stretching" and signal routing in electronic scanning radars. This section reports work on such switches since TR-228, emphasizing the potential microwave switching characteristics of PIN junctions, and the results obtained with some experimental switches.

---

* This was brought to our attention by Roger Colardeau of Bell Telephone Laboratories.

1. Microwave Switching Characteristics of Diode Junctions

An equivalent circuit for a p-n junction was reviewed in TR-228. Some measured values of R_s and C were given for some computer and varactor diodes. These data suggested that for microwave switches the varactor diode is preferable to the computer diode, as would be expected on basis of impurity concentration. However, a diode with a lower operating RC product and higher voltage breakdown is needed in many RF switching applications.

The PIN structure appears capable of meeting these needs, and the use of the PIN diode[*] as an RF switch has been discussed by Uhlir.[†] However, with the exception of a PIN diode developed by Bell Telephone Laboratories[‡] as a protective limiter, extensive application has not been made of this structure at UHF frequencies. An investigation of the effectiveness of the PIN diode as an RF switch is under way. A higher breakdown voltage is readily achieved, and a lower operating RC product is expected. The recovery time of the PIN diode when switched from forward to reversed bias will be larger than for a varactor diode, but it is expected to be about 1 µsec when an adequate reverse bias is applied.

2. Experimental Diode Switches

Diode switches have been reported in numerous places. Probably the most recent and complete article on TEM transmission line diode switches is by Garver.[§] The salient features of diode switches will be briefly enumerated below, and the performance of some experimental strip transmission line switches developed by the writer will be given.

The series resistance R_s of a diode sets the upper limit of the isolation loss (maximum attenuation) of a shunt diode switch and the lower limit of the insertion loss (minimum attenuation) of a series diode switch for a given characteristic impedance line. Similarly, R_s and the operating reverse bias junction capacitance C determine the maximum antiresonant impedance attainable with a diode. This impedance sets the lower limit of the insertion loss for the shunt diode switch and the upper limit of the isolation loss of a series diode switch for a given characteristic impedance line. The series and shunt switches are dual in nature. In fact, the dual of an ideal diode is an ideal diode with reverse polarity.

The realization of the performance limits set forth above is determined by the coupling of the semiconductor wafer to the transmission line. The lead contacts to the semiconductor wafer have a significant inductance, and the diode case has a non-negligible capacitance. Other effects of the diode mount may be equally significant. For example, a typical value of 11 db for isolation at 900 Mcps is obtained when shunting one side of a 50-ohm strip transmission line having $\frac{1}{4}$-inch ground-plane spacing with a Microwave Associates MA-4257 diode. A typical R_s value for this diode is slightly less than 1 ohm and a C of 1.5 pf. Shunting the other side of the strip transmission line with a second diode improves the isolation to at least 25 db. The analysis of these results is not sufficiently complete to report at this time.

[*] R.H. Hall, "Power Rectifiers and Transistors," Proc. IRE 40, 1512 (1952).
  M.B. Prince, "Diffused PIN Junction Silicon Rectifiers," Bell System Tech. J. 35, 661 (1956).
[†] A. Uhlir, "The Potential of Semiconductor Diodes in High-Frequency Communications," Proc. IRE 46, 1099 (1958).
[‡] N.G. Cranna, "Diffused PIN Diodes as Protective Limiters in Microwave Circuits," Tenth Interim Report on Improved Crystal Rectifiers, Signal Corps Contract DA36-039-sc-73224, Bell Telephone Laboratories, Whippany, New Jersey (January 1958) and subsequent reports.
[§] R.V. Garver, "Theory of TEM Diode Switching," Trans. IRE, PGMTT MTT-9, 224 (1961).

A diode stub arrangement was used to fabricate some low-power protective diode switches for the receivers in the test array. The switch consisted of one diode shunting a nearly half-wavelength stub (Fig. 2-47). This arrangement permitted transforming out reactive effects, thus realizing R_s across the strip transmission line junction when the diode was forward biased. Since this required very accurate positioning of the diode, a sliding diode mount over the stub line was used. When the diode is forward biased to provide isolation, it can be subjected to larger amounts of power than when reversed biased. The allowable power for a forward biased diode is the power-dissipation capability of the diode. One-half of the reverse voltage break-down of the diode sets the peak RF voltage; thus, the allowable power for a reversed biased diode.

The stub was extended beyond the diode to tune the junction capacitance to obtain maximum stub impedance at the strip transmission line junction when the diode was reversed biased (a tuning screw was used to vary the effective electrical length of the stub to accommodate the variation of junction capacitance of various diodes). The expected attenuation α resulting from shunting a diode impedance Z across a transmission line having a matched generator and load Z_o is

$$\alpha = \left(1 + \frac{Z_o}{2Z}\right)^2 \quad .$$

For a forward biased MA-4257, $Z = R_s = 1$ ohm, and $Z_o = 50$ ohms, the isolation is 28 db. When the diode is reversed biased, the antiresonant impedance L/CR_s at 900 Mcps is 13K. This causes a negligible insertion loss. The frequency at which the magnitude of the stub impedance becomes $1.4 R_s$ determines the bandwidth where the isolation decreases 3 db from its maximum value. Assuming a half-wavelength stub at 900 Mcps terminated with a 1-ohm resistance, the bandwidth is 12 Mcps or 1.3 per cent. The insertion bandwidth is tens of per cents.

Seventeen units were fabricated for the test array. Performance figures were as follows:

Item	
Isolation	25 to 33 db, 28 db average
Bias for isolation	3 ma
Insertion loss	Less than 0.2 db
Bias for insertion	-4.0 volts
VSWR	Less than 1.1

The peak power-handling capability required was less than $\frac{1}{4}$ watt, a level below its CW capability. No tests have been made to determine the actual power-handling capability. The isolation bandwidth checked as predicted. Insertion about doubled at 50 Mcps from 900 Mcps, the center frequency.

The biasing of the diode was accomplished by providing DC isolation between the ground plane and the diode with an RF ceramic capacitor. The ceramic is 4 mils thick, has a dielectric constant of 2200 and is manufactured by Mullenbach of Los Angeles.

3. Receiver Selector Switch

If an RF multibeam-forming matrix is used for the phasing function in a phased array receiver, a limited number of the total number of output beams will generally be processed at one time. An electronic selector switch could reduce the number of receiver strips required. A

69

(a)

INPUT

OUTPUT
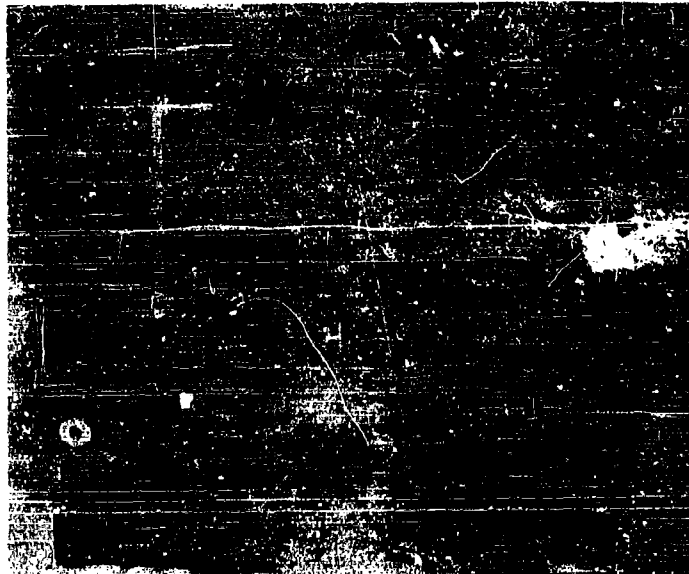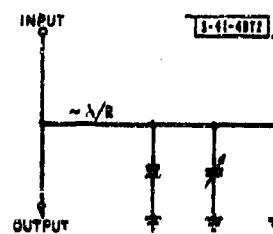
(b)

Fig. 2-47. Low-power protective diode switch: (a) photograph; (b) equivalent circuit.

70

4-position RF diode switch was fabricated to assess its performance. The selector switch was assembled from switches described in the previous section. The printed-circuit configuration is shown in Fig. 2-48. The insertion loss of the transmission path was less than 0.7 db, and an isolation of greater than 25 db existed to the other ports. The teflon glass strip transmission line accounted for about 0.2 db of the insertion loss in the transmission path.

F. MICROWAVE PHASE SHIFTERS AND TIME DELAYS

1. General Considerations

The use of "electronically switched stretchers" for phase shifting was discussed in TR-228. This section extends the TR-228 discussion.

If one attempts to electronically control one or more of the transmission line parameters to change the phase constant (β) of a section of line to effect a change in electrical line length [Fig. 2-49(a)], the characteristic impedance (Z_o) is also generally changed. This creates an undesired mismatch. However, if sections of such line are appropriately used [Fig. 2-49(b)] as arms on a balanced structure as a hybrid, a net change in electrical line length results without input and output mismatches.

The design problem now becomes that of designing low-loss electronically variable β sections of transmission line. There are probably many types and variants. Some nonlinear material properties may not readily be configured to provide 360° of phase shift or time delay desired in one β control section. Thus, cascading hybrids rather than control sections in one arm may be desirable. The choice of discrete phase step (digital) or continuous phase (analog) shifters or time delays will depend upon system application and requirements as well as materials and technique in β control section fabrication.

Table 2-IV is a chart indicating some possible devices and physical phenomena that can be employed for β control sections.

TABLE 2-IV β CONTROL TECHNIQUES				
Controlled by	Circuit Parameter Being Controlled			
	R	G	L	C
E	Diode*	Diode* Gas tube* Cryogenic semiconductor ionization*		Variable capacitor diode Ferroelectric
H	Magnetoresistance* Cryotron*		Ferrite	
F	Mechanical short			

*Discrete phase shift steps.
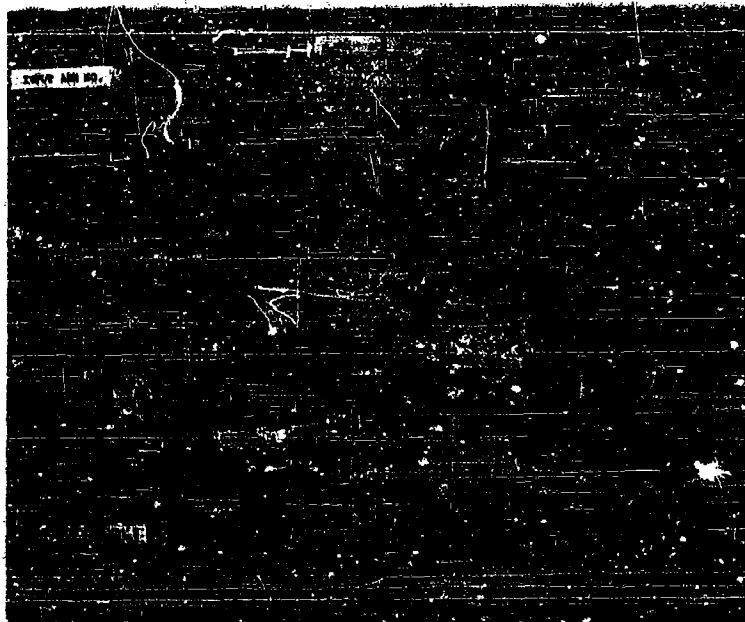
Fig. 2-48. Printed-circuit configuration for a receiver selector switch.

$Z_0 = f(R, C, L, G)$
$= F(\sigma, \mu, \epsilon)$

$\beta = g(R, G, L, G)$
$= G(\sigma, \mu, \epsilon)$
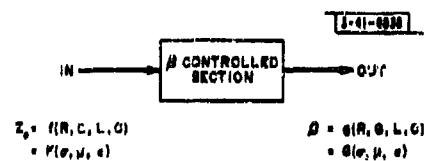
Fig. 2-49. Electronic line stretching:
(a) straight-through structure; (b) bal-
anced structure.
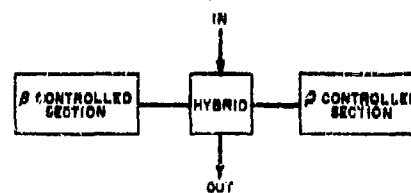
Conductive Class:— With low loss as an objective, only the two extreme values of zero and infinite conductivity are of interest. The diode phase shifter configurations outlined in TR-228 are of this type.

Ferrimagnetic Class:— The use of a ferrite transmission line section like that reported by Stern[*] for a switch appears attractive. The ability to place a control winding and water cooling in contact with the ferrite and the effects of impedance mismatch suggest increased power capability and reduced temperature sensitivity as contrasted to many existing configurations.

Ferroelectric Class:— The loss and temperature sensitivity of ferroelectrics at microwave frequencies have recently been receiving more careful attention.[†] They may be competitive or better than ferrites at L-band and lower frequencies. Provision of control power may be simpler.

2. Current Investigations

Very little work has been done during the past year on phase shifters for receiver applications, since the parallel-fed multibeam-forming matrix discussed in TR-228 promises to be a better solution for the receiver phasing function because of reliability and insertion loss. However, high-power phase shifters appear to be a better solution for the transmitter for reasons discussed below.

Two transmitter approaches are shown in Fig. 2-50. The phasing function in both the multibeam-forming approach and the corporate-feed approach is accomplished by separable phase shifting. Obviously, in both approaches, it is desirable to keep the number of N^2 system elements to the minimum and the element itself as simple and reliable as possible. Consider, for example, the consequences of a simple single-stage terminal amplifier. This means that the input amplifier power should be high. In fact, the row amplifier (N in number) should be at least as large as the terminal amplifier. The consequence of these arguments leads one to search for methods of high-power phasing (other arguments lead to the same conclusion, but none are known which support the opposite conclusion).

Further examination of Fig. 2-50 shows that the high-power phasing function requirement is more severe in the multibeam-forming approach than in the corporate-feed approach. The multibeam-forming approach requires a routing switch and a multibeam-forming matrix which has a power-handling capability P. The corporate-feed approach requires a phase shifter with power-handling capability of only P/N. Thus, the corporate-feed approach is considered the desirable one. Additional considerations in favor of the corporate-feed approach are:

(a) It is easier to build a corporate feed to handle power than a multibeam-forming matrix.

(b) As N is increased and one wishes to maintain a constant P/N power, the routing-switch power-handling capability and amplifier output must increase. The alternative is placing booster amplifiers at appropriate levels [Fig. 2-51(b)] in the multibeam-forming matrix. A similar type of argument applies to the corporate-feed approach [Fig. 2-51(a)], but the number of booster amplifiers required is less than in the multibeam-forming approach.

---

[*] E. Stern, "Fast One-Kilomegacycle Ferrite Switch," International Solid-State Circuits Conference Proceedings, Philadelphia, Pennsylvania (1961).

[†] "Investigation of Microwave Properties of Ferroelectric Materials," Report 2732-4-F, University of Michigan (March 1959).
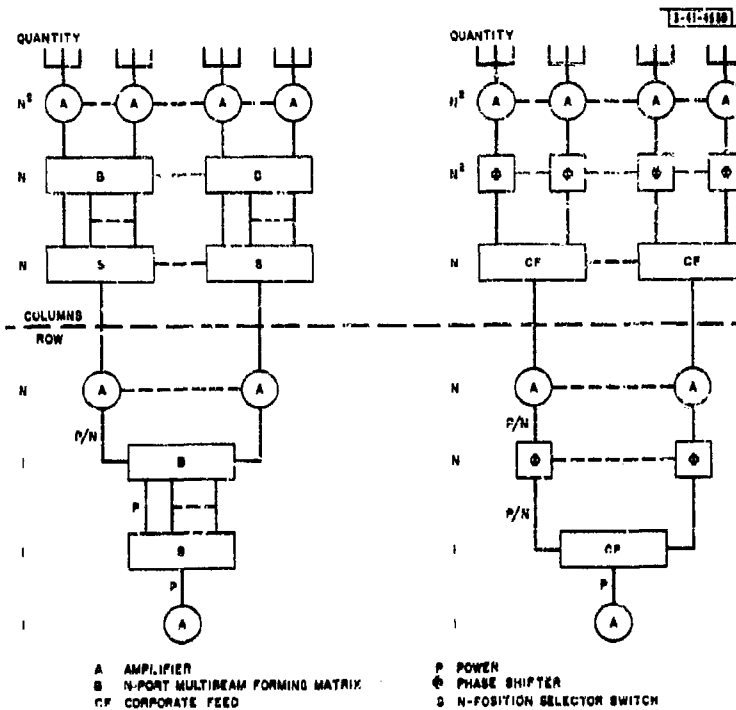
Fig. 2-50. Two transmitter approaches: (a) multibeam-forming; (b) corporate feed.
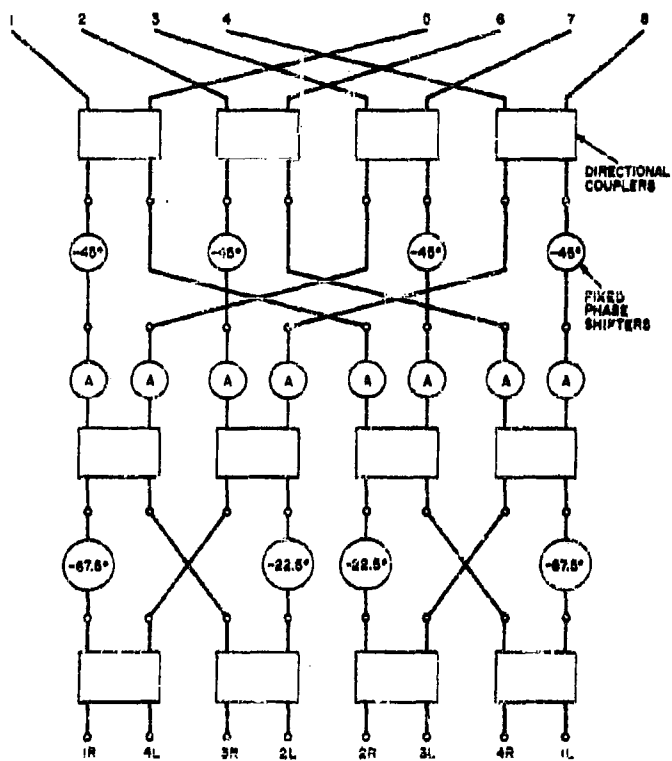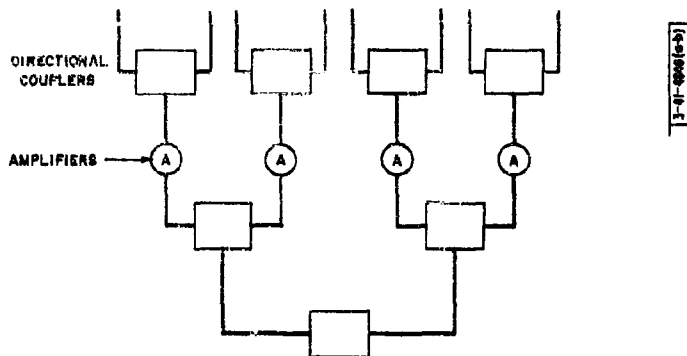
Fig. 2-51. Placement of booster amplifier: (a) corporate feed; (b) multibeam-forming matrix.

In view of the above, a development program on high-power phase shifters is under way. Design objectives are as follows:

Frequency	L-band
Peak power	20 kw
Average power	200 watts
Phase steps*	$\leq$6 bits (λ/64)
Total phase tolerance	$\pm$3°
Insertion loss	Less than 1.5 db
Bandwidth	1 to 10 per cent
Reset time	Less than 10 μsec
Control power	Less than 20 watts average/bit
Mass production price	Less than $100/bit

The use of diodes and ferrites in the β control sections of these phase shifters is the current subject of parallel investigations.

3. An Experimental RF Phase-Shifting Test

One binary section of a cascaded hybrid-ring phase shifter (see TR-228 for a functional explanation) was fabricated with teflon glass strip transmission line and Microwave Associates pill varactor diodes (MA-4257). The measured performance was as follows:

Frequency	900 Mcps
Insertion loss	Less than 0.5 db
Noise figure	Less than 0.5 db
Forward bias	2 ma
Reverse bias	−4 volts

The performance agrees reasonably well with calculated results (for method, see TR-228, p. 106). A closer agreement could be obtained by taking into account the strip transmission line losses.

A traveling-wave strip transmission line coupler instead of a hybrid ring should increase the operating frequency band, permit a more compact package and reduce the strip transmission line losses; future phase shifters will use this configuration.

---

* Since the initiation of this program, Testa has determined that 6 bits are not necessary for the design approach under investigation by Group 41 (see Part 2, Ch. VII).

CHAPTER III
RECEIVER TECHNIQUES

SUMMARY   S. Spoerri

Several topics in phased array receiver techniques are discussed, beginning with a short section on present receiver packaging. The need for including uniform limiting characteristics in the receiver design specifications is emphasized in another section. Additional subjects covered are noise figure and coherent local oscillator noise, and an array application for the idler frequency generated by electron-beam parametric amplifiers.

A. INTRODUCTION

This chapter presents some remarks about the general topic of receivers. The observations are based on experience obtained with the 16-element test array.

A phased array receiver may consist of a large number of identical receiver channels or strips (if complete beam forming is not done immediately at RF). The individual channel design must take account of physical and electrical requirements peculiar to the particular phased array application. The physical design is important because of the quantity of equipment involved. Section B discusses the receiver packaging philosophy which evolved from test array experience.

A characteristic group of electrical design problems associated with phased array receivers is based on stability requirements. A premium is placed on phase and amplitude stability, since phase and amplitude errors degrade array performance. Assuming that stability with time has been achieved, Sec. C makes a case for requiring uniformity of large signal or limiting performance as well.

The last two sections are based on the use of auxiliary phase shifters to achieve special results. Section D presents a way of reducing the effects of coherent local oscillator noise without affecting the signal performance of an array, and Sec. E discusses a possible array application for the idler frequency generated by most parametric amplifiers.

B. PACKAGING

The complexity of a phased array receiver demands that special consideration be given to ease of maintenance and component replacement. Component and system flexibility is also important, especially in a test facility, since system requirements are often quite variable in nature. A rigid system must be used as intended, or discarded, whereas a flexible system may be adapted to new uses with a minimum of rebuilding and new construction.

The current receiver strips for the test array are divided into two separate functional sections. The RF amplifier and first mixer make up the first section (Fig. 1-11 of Part 1), and the IF amplifier, second mixer, and phase shifter form the second section (Fig. 1-12 of Part 1). The individual units that comprise each section have 50-ohm input and output impedances to facilitate testing. Power is supplied to each section through a standard connector which then distributes the required voltages to the individual units. The units are mounted in a manner that permits rapid, one-side removal and replacement.

The IF amplifier units provide about 30 db of gain, which is enough to set the receiver noise figure without limiting the dynamic range. The 50-ohm input/output impedance permits cascading of units for more gain. Interunit filters or attenuators may also be included if desired.

The receiver first IF outputs may be used directly or they may be frequency translated to a second, lower intermediate frequency by using the second mixer or converter units.

C. LIMITING AND DYNAMIC RANGE

Phase and amplitude combining errors play a fundamental role in the determination of phased array performance. The errors can be significant, especially in a system that includes active components between the antennas and the combining or beam-forming matrix. As a result, attention has been focused on the design of phase- and amplitude-stable array components.

Implicit in the usual discussion of array performance is the assumption of linear operation. A few authors have also discussed the deliberate nonlinear operation of a receiving array.[*] In this case, ideal nonlinear operation (mathematical or infinite clipping without zero-crossing shift) is usually assumed.

In both the ideal linear and the ideal single-signal nonlinear cases, the array antenna pattern is independent of signal level if any amplitude tapering is done after limiting. The gain of the array on the beam center is primarily a function of the array aperture (if the combining errors are not inordinately large), and the sidelobe structure is a function of the taper and the combining (phase and amplitude) errors.

The performance of a receiving array, with amplification before the beam-forming combiner, is difficult to determine for a multitarget or cluttered environment. The antenna pattern can no longer be considered independently of signal amplitude, since the receiver channel amplifiers may not limit in a uniform fashion for large signals. As a result, phase and amplitude errors, which are a function of the signal level, modulate the sidelobe structure of the basic array antenna pattern.

The net effect of strong-signal modulation of the sidelobe level is to reduce the discrimination between targets in the main beam and those outside the main beam. A clutter (or jammer) signal which would normally be rejected by 40 db relative to a signal in the main beam might be suppressed only 20 db if it were strong enough to cause severe nonuniform limiting. Amplitude tapering to reduce sidelobes has no effect on the strong-signal modulation effect *per se* if nonuniform limiting occurs in front of the tapering network.

The gain (relative to isotropic) of a single antenna element imbedded in a planar array is roughly 6 db[†] (for 0.5-wavelength element spacing). A typical channel amplifier (e.g., electron-beam parametric amplifier being fed by the antenna element) might have 70 db of dynamic range and an input saturation level of −40 dbm.

A 1-kw jammer with a 10-db gain antenna would just saturate the receiving array amplifiers at a range of about 10 miles. This result is independent of the angular position of the jammer, provided that it is within the beamwidth of the individual antenna element pattern in the receiving array configuration.

The example given above shows that the problem is not too serious if amplifiers with input saturation levels above −40 dbm are used. It would seem prudent, however, to adhere to the following design guide rules.

    (1) Use the minimum individual channel gain (before beam forming) which will satisfy other design requirements.

---

[*] For example, see F.C. Ogg, Jr., "Steerable Array Radars," Trans. IRE, PGMIL. MIL-5, 80 (1961).
[†] See Part 3, Ch. I.

(2) Use amplifiers with a large dynamic range and high saturation level if possible.

(3) Design the array for linear operation under normal signal conditions but require that the limiting characteristics be uniform (in addition to the usual requirements for phase and amplitude stability).

If beam forming is done at a low frequency, or if the receiver channels are specifically designed to limit at low signal levels, it is probable that the receiver channel gain will be quite high. In consequence, the input saturation level is likely to be quite low (-70 to -100 dbm), and uniform limiting becomes very important if strong-signal modulation of the antenna sidelobe levels is to be avoided.

The design of receiver strips which track in phase and amplitude over a wide range of overdrive (or limiting) is no easy task. For this reason, IF beam forming and channel limiting before beam forming appear to be inappropriate techniques for applications involving receiving arrays in hostile or cluttered environments.

B. NOISE FIGURE AND COMMON LOCAL OSCILLATOR NOISE

Preliminary to a discussion of noise figure for a multiport device such as a receiving array, it is well to review the properties of a hybrid ring when used as a power combiner. Such an application is shown in Fig. 2-52.

The sum output of the hybrid is regarded as the useful combined output. G_1 and G_2 are generators with available power outputs of P_1 and P_2, respectively. The generator internal impedances are equal to the impedance level of the hybrid so that all the generators' available power is delivered to the hybrid ring. The available power output of each generator is considered to consist of two components: a coherent component S which is produced by all the waveform components common to G_1 and G_2, and a random component N_1 (N_2) which is independent of N_2 (N_1) and S. The combined (sum) output is $2S + (N_1 + N_2)/2$ or, in other words, random input power averages at the output. This result can be generalized for an n-input hybrid combiner (corporate feed) with the same result (Fig. 2-53). In this figure, any surplus of input power over output power is dissipated in the hybrid difference port terminations.

Thus, a hybrid combiner is seen to be lossless (ideally) only with respect to coherent (identical-waveform, narrowband) input signals. The restriction to narrowband input signals is required because of the bandwidth limitations of the hybrid rings (over which sufficiently accurate summing and differencing occurs).

1. Noise Figure in the Absence of Coherent Local Oscillator Noise

If the properties of a hybrid combiner (discussed in the preceding paragraphs) are kept in mind, it is a simple matter to obtain the effective noise figure of a phased array receiver which consists of antenna elements followed by RF amplifiers and a hybrid combiner. It is assumed that perfect matches obtain everywhere and that all noise sources are independent. Figure 2-54 is a block diagram of the receiver. In this figure, N_t is the available noise power from an input termination at 290°K, N_a is the available noise contribution of an amplifier referred to its input, G_k is the amplifier power gain (which includes any tapering), and F_k is the channel noise figure measured with any tapering pad in place (if the taper is other than flat). Since all noise sources are assumed independent, the hybrid combiner presents the average of all the input noise power to the output.

79

$P_1 = S + N_1$
$P_2 = S + N_2$
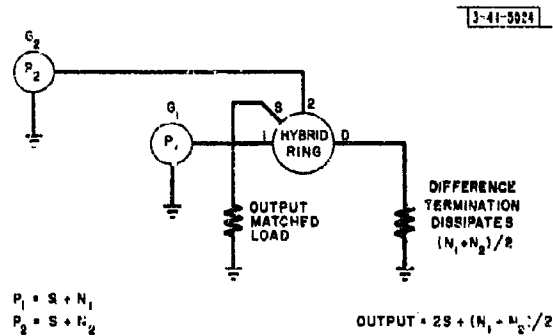
OUTPUT $= 2S + (N_1 + N_2)/2$
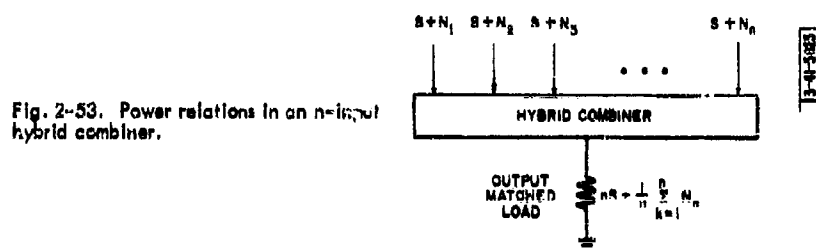
Fig. 2-52. Hybrid ring power combiner.

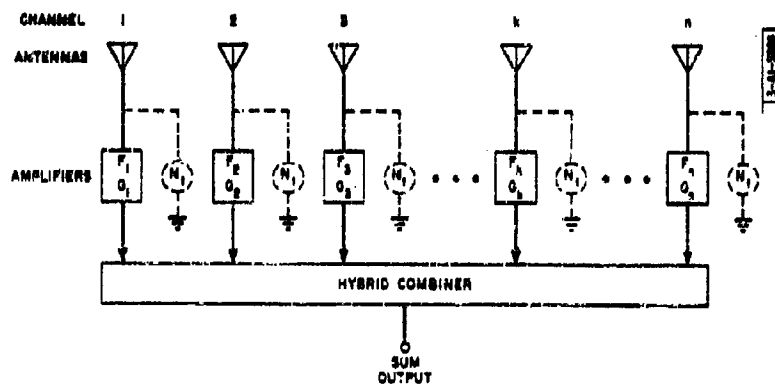Fig. 2-53. Power relations in an n-input hybrid combiner.

Fig. 2-54. Block diagram of phased array receiver.

The noise power out of any channel amplifier is given by $F_k G_k N_t$. Of this, $G_k N_t$ is the amplified noise from the input termination at 290°K, and $(F_k - 1) G_k N_t$ is the noise contribution of the amplifier.

The hybrid combiner averages the noise power supplied to its inputs (since all noise sources are assumed to be independent). The sum output is thus given by

$$\frac{N_t}{n} \sum_{k=1}^{n} G_k + \frac{N_t}{n} \sum_{k=1}^{n} G_k (F_k - 1) \quad ,$$

where the first term represents the noise power output due to the input terminations at 290°K, and the second term is the noise power contributed by the amplifiers.

The effective noise figure of the receiving array is then given by

$$F_{eff} = \frac{\dfrac{N_t}{n} \sum_{k=1}^{n} G_k + \dfrac{N_t}{n} \sum_{k=1}^{n} G_k (F_k - 1)}{\dfrac{N_t}{n} \sum_{k=1}^{n} G_k} \quad ,$$

or

$$F_{eff} = \frac{\dfrac{1}{n} \sum_{k=1}^{n} G_k F_k}{\dfrac{1}{n} \sum_{k=1}^{n} G_k} = \frac{1}{n} \sum_{k=1}^{n} \left(\frac{G_k}{\dfrac{1}{n} \sum_{k=1}^{n}} \right) F_k \quad .$$

The effective noise figure is seen to be equal to the weighted average of the individual channel noise figures, where the weighting factor is the ratio of the channel gain to the average channel gain

$$\frac{G_k}{\dfrac{1}{n} \sum_{k=1}^{n} G_k} \quad .$$

If the channel gains are all equal (identical amplifiers and flat amplitude taper), then the noise figure is given by the simple average of the individual channel noise figures.

For the case of identical channel noise figures, the effective array noise figure is seen to be independent of the antenna amplitude taper.

2. Coherent Local Oscillator Noise in a Phased Array Receiver

The local oscillator (LO) signals required by the mixers in a phased array receiver are usually derived from a single LO source and distributed to the mixers through a corporate feed. This arrangement opens the possibility for noise components that are within the IF signal bandwidth of receiver strips to be introduced via the LO ports of the mixers in a coherent manner. Thus, the discussion of the preceding section, where it was assumed that all noise sources were independent random noise generators, does not apply.

Figure 2-55 shows a phased array receiver that has a mixer in every channel, followed by two separate phase shifters (for convenience in the analysis) and a summation network (combiner) that forms a receiving beam. All phase shifts are shown relative to the corresponding point in a reference channel, channel 0, which is not part of the array. In Fig. 2-55, σ is the (adjacent
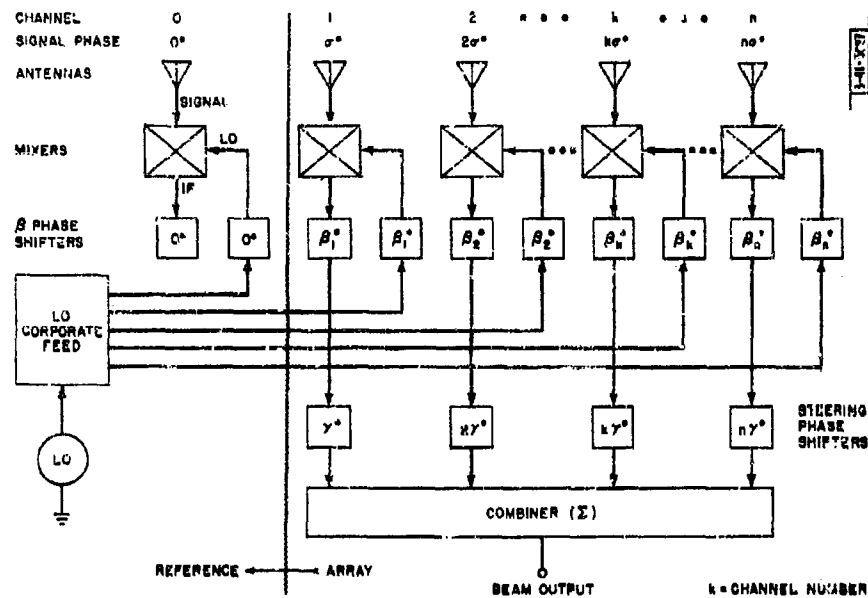
Fig. 2-55. Block diagram of phased array receiver with phase shifters included in each mixer local oscillator and IF output line.
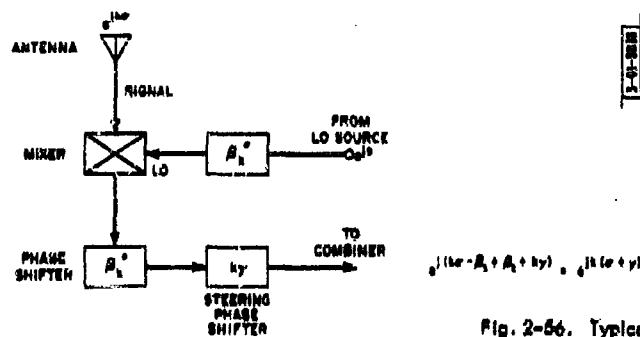

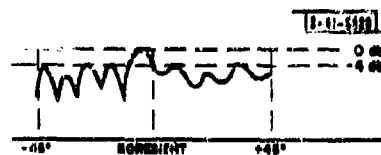Fig. 2-56. Typical channel phase relationships.

Fig. 2-57. Beam output vs scan angle with signal introduced at local oscillator source (for 16-element test array).

channel) phase increment due to signal energy arriving from a general angle φ measured from boresight, γ is the phase increment introduced to steer the beam to a desired position, and β_k is an arbitrary (for the present) phase shift introduced in the kth mixer's local oscillator port as well as its IF output port. A typical receiver channel (the kth) is displayed in Fig. 2-56, which shows the phase vectors in exponential form, where the phase at corresponding points in the reference or 0 channel are taken as the respective references. Since the LO frequency is lower than the signal frequency, the phase of the IF output of the mixer is given by IF phase = signal phase -- LO phase. In the case of the mixers shown, the phase of the IF output due to a signal introduced at the signal port is independent of the phase shift β_k, which is introduced at both the LO and IF ports. However, a signal introduced from the LO source (or LO noise in the signal frequency band which can beat with the LO to produce frequency components within the IF bandpass) arrives at the mixer with a phase shift β_k, hence it looks like a signal introduced at the signal port with relative phase β_k. The IF input to the combiner will thus be $e^{j\beta_k} e^{jk\gamma}$.

Introduction of the β phase shifters is seen to be a means of modifying the phase of the IF output due to signals (or noise) introduced through the LO source while leaving legitimate signals, which enter the mixer through the signal ports, unaffected. In particular, the β's selected can be thought of as steering, or spreading, the coherent LO noise so that it forms an equivalent spatial noise pattern similar to an antenna pattern. This noise is equivalent to a distribution of excess noise in space. As the receiving beam is steered through the use of the γ phase shifters, the coherent LO noise appearing at the beam output will vary.

The equivalent spatial noise distribution can be thought of as scanned by the signal antenna pattern. This suggests that the β phase shifters should be set to such values which minimize the amplitude of the noise pattern in the field of view of the array. This would occur if the noise beam were steered to endfire in the case of an array with ±45° scan from boresight. If the antenna elements were spaced 0.5λ apart, this would require $\beta_k = 0°$ for k odd and $\beta_k = 180°$ for k even.

The mixers in an actual array will probably not have equal phase lengths from the LO ports to the mixer crystals because of LO injection (coupling) screws which may be set differently for each mixer in order to compensate for variations in the crystals. Also, the LO path lengths from the LO source to the individual mixers may not be identical. The β phase shifts must be compensated for those errors.

If differential phase errors are introduced between the antennas and the signal ports of the mixers (which is especially likely if RF amplifiers are used) and these errors are compensated out at IF, then the coherent LO noise pattern will be modified.

In the usual array, the β phase shifters are not introduced. This would place the nose of the noise beam at boresight if there were no differential phase errors. However, it is to be expected that, due to the probable existence of errors such as those mentioned above, the actual noise pattern may have its main peak off-boresight with rather high sidelobes.

It is a simple matter to determine the actual noise pattern. A signal may be introduced together with the LO at the LO source. This signal will then simulate coherent LO noise (at a single frequency) and can be set to provide a convenient output level from the beam output. As the array is electronically scanned through the use of the γ phase shifters, the beam output due to the artificially introduced "noise" signal will vary in the same manner as the true coherent noise but at a higher, more convenient level. If the signal is then removed and the noise pattern

exhibits peaks in the same places as the signal, then the coherent LO noise is known to be significant. If the noise exhibits no apparent variation with scan, the coherent noise must be masked by independent, locally generated noise.

The experiment was performed on the 15-element test array. A 900-Mcps signal was added in with the 870-Mcps LO at the LO source, and the pattern sketched in Fig. 2-57 was observed as the array was electronically scanned. A subsequent search for a similar pattern due to noise alone revealed no noticeable variation in the noise pattern as the array was scanned. This indicates that coherent noise is not a problem in this particular array.

In an array which uses balanced mixers, an improvement of some 20 db in signal-to-LO-noise ratio is achieved over what would have obtained if single-ended mixers had been used. This is attributable to the balanced structure of the mixers which causes signals and noise that enter through the LO port to cancel at the IF output. The efficacy of the cancellation is dependent on the degree of balance in the mixers.

A "bonus" improvement in signal-to-common-LO-noise ratio can be realized if the LO inputs to all the mixers are adjusted to be in phase. Since the imbalance in the mixers is random, the IF outputs due to LO noise will be either in phase or out of phase with respect to each other. For 0.5λ element spacing, this will tend to form an endfire noise beam as discussed earlier. (In the case of balanced mixers, the β phase shifters are all equal to 0 for 0.5λ element spacing, provided care is taken with the LO corporate feed so that it does not introduce appreciable differential phase shifts.)

3. Conclusions

The noise in a phased array receiver can be divided into two categories. The first is incoherent and represents the effect of all the independent random noise sources. The effect of the incoherent noise can be included in an effective noise figure for the array, which is given by the average of the noise figures of the individual receiver channels (assuming a flat amplitude taper and equal receiver gains).

The second noise category comprises coherent noise or noise that is not independent from channel to channel in the array. This noise originates in a single source, the local oscillator, and is introduced into each channel via the LO corporate feed.

If coherent noise is significant, as it may be in certain frequency regions because of the types of local oscillators that are available, it can be controlled by controlling the LO phase applied to each mixer. In particular, the LO noise can be made to appear as a noise beam pointed at endfire of the array.

Balanced mixers can be used to provide a nominal 20 db additional rejection of the coherent noise. They are also attractive because any noise which does get through due to mixer imbalance will tend to appear at endfire if a few precautions are observed in building the array.

E. SOME IMPLICATIONS OF THE SYMMETRY PROPERTIES OF THE ELECTRON-BEAM PARAMETRIC AMPLIFIER FOR PHASED ARRAY APPLICATIONS

This section is based upon a discussion of the basic symmetry properties of the electron-beam parametric amplifier (EBPA) by Dr. Robert Adler.* An attempt is made here to outline some special implications of this device for phased array applications.

_____

*R. Adler, "Electron-Beam Parametric Amplifier with Synchronous Pumping," Proc. Symposium on the Application of Low Noise Receivers to Radar and Allied Equipment, Vol. III (U), Lincoln Laboratory, M.I.T. (November 1960), pp. 177-197, ASTIA 248692.

It is assumed that an EBPA has been included in each channel of a phased array to serve the function of a low-noise yet highly stable (gain and phase) amplifier. These EBPA's are to be followed by filters which separate the signal and idler components of the EBPA outputs.

The EBPA produces a signal output whose phase is independent of pump phase. In addition, an idler output is generated whose amplitude is within a decibel of the signal output[*] and whose phase is given by $\varphi_{idler} = \varphi_{pump} - \varphi_{signal}$. The pump frequency is ordinarily selected to provide enough frequency separation between the signal and the idler so that these can be separated from each other and only the signal outputs used.

A conventional array would utilize only the signal frequency outputs, combining these in some fashion to form the receiving beam or beams. It is proposed here to combine the idler outputs also, and then to observe what happens as synchronous operation of the EBPA's is approached ($f_{pump} = 2f_{signal}$, so $f_{signal} = f_{idler}$).

A block diagram of a phased array receiver using electron-beam parametric amplifiers is shown in Fig. 2-58. Channel 0 is not part of the array but is included as a phase reference in order to simplify the mathematics. The separation of the signal and idler components is depicted symbolically as occurring immediately after the EBPA's. This is a conceptual simplification; the actual separation could as well be performed at the output of a single beam-forming matrix such as the Butler matrix.[†] In such case, the α phase shifts encountered by the signal and idler components could differ slightly because of difference in frequency. The difference can be kept small, however, by keeping the frequency separation of the signal and the idler small.

Let the signal at antenna element 0 (the reference) be $e^{j0} = 1$; then at the kth element it is $e^{jk\sigma}$. The signal output of the kth EBPA will also be $e^{jk\sigma}$ if the amplifier gain is ignored. The idler output of the kth EBPA will be $e^{jk(\beta-\sigma)}$. Both signal and idler encounter the steering phase shift, which is $e^{jk\alpha}$ for the kth channel. The output of the signal beam combiner is thus

$$B_s = \sum_{k=1}^{n} e^{jk(\sigma+\alpha)} \quad \text{(beam pointed at } -\alpha) \quad ,$$

and that of the idler beam combiner is

$$B_i = \sum_{k=1}^{n} e^{jk(\beta+\alpha-\sigma)} \quad \text{(beam pointed at } \beta + \alpha) \quad ,$$

where a sum of the form $\sum_{k=1}^{n} e^{jkx}$ can be expressed in the familiar form

$$\frac{\sin nx}{n \sin x} \quad .$$

σ^* can be replaced in the above expressions by $(180°/\pi)(d/\lambda)\sin\xi$ (where ξ is the spatial scan angle).

The above expressions show that the idler beam can be positioned arbitrarily by introducing a suitable pump phase slope β. Once this is chosen, the signal and idler beams move in opposite directions in response to the steering phase slope α.

---

[*] For EBPA gain >10 db.

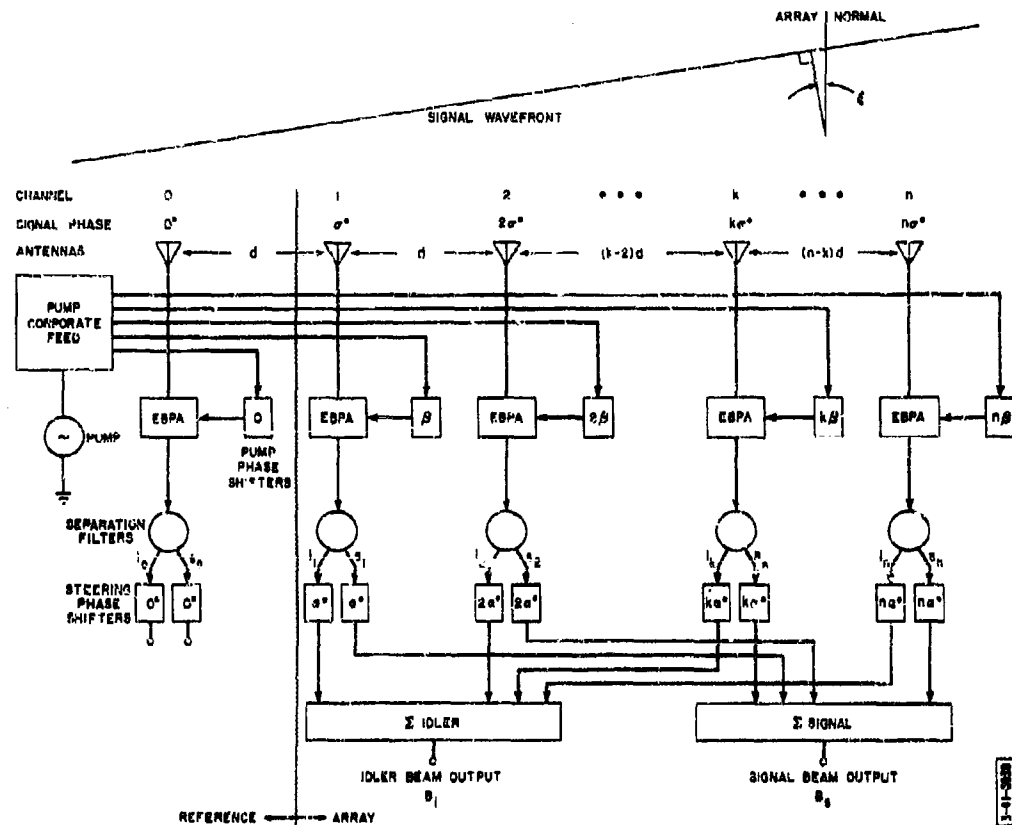[†] Discussed by Delaney in Part 2, Ch. 1.

Fig. 2-58. Block diagram of phased array receiver using electron-beam parametric amplifiers.

If a Butler matrix were used following the EBPA's and the matrix beam outputs were provided with separation filters to separate the signal and idler beams, a set of signal beams would be formed as usual. However, a set of idler beams would also be formed which could be positioned halfway between the signal beams through the choice of a suitable β phase slope. If the matrix output ports were denoted by $1\frac{1}{2}L$ ($1\frac{1}{2}$ beamwidths left), $\frac{1}{2}L$, $\frac{1}{2}R$, $1\frac{1}{2}R$, etc., to express the normal or signal beam positions, the idler beams formed at these ports would be $2R$, $1R$, boresight, $1L$, etc., respectively, when $\frac{1}{2}R$ is set to yield a boresight idler beam through proper setting of the β phase shifters.

Figure 2-59 shows the main-lobe locations of an 8 (signal) beam Butler matrix and the corresponding idler beam locations if $\frac{1}{2}R$ is caused to yield an idler beam at boresight. Whereas the signal beams cross over at the $2/\pi$ points permitting a possible signal loss of 4 db, the complete set of idler and signal beams crosses over at the 0.9 amplitude points corresponding to a loss of less than 1 db. The idler components also provide the Butler matrix with a boresight beam.

The preceding discussion has dealt with the case where the signal and idler outputs of the EBPA's are eventually separated from each other through the use of separation filters or branching filters. It is also possible to choose a pump frequency such that the signal and idler outputs are sufficiently close in frequency (or the following bandpass sufficiently wide) so that they remain unseparated from each other.

For a given pump phase slope β and steering phase slope α, the positions of the signal and idler beams are determined relative to the spatial scan angle ξ. The magnitude of the signal response due to an incident wavefront originating from a particular direction ξ is given by the height of the signal beam pattern at that angle. Let this magnitude be denoted by $S = S(\xi)$. Then the instantaneous signal output is $\mathrm{Re}(Se^{j\omega_s t})$, which may be represented by the vertical projection of a vector of length S which rotates at angular velocity ω_s (signal angular frequency). In a similar fashion, the instantaneous idler output is $\mathrm{Re}(Ie^{j\omega_i t})$, which may be represented by the vertical projection of a vector of length I which rotates at angular velocity ω_i (idler angular frequency). The actual instantaneous voltage output E_o is the sum of signal and idler or $\mathrm{Re}(Se^{j\omega_s t}) + \mathrm{Re}(Ie^{j\omega_i t}) = \mathrm{Re}(Se^{j\omega_s t} + Ie^{j\omega_i t})$. This may be represented as shown in Fig. 2-60, where Θ is the instantaneous angle between idler and signal vectors and is given by $\Theta = \Delta t$, where $\Delta = \omega_i - \omega_s$. R is the resultant of signal and idler as a function of Θ and is given by $R = (S^2 + I^2 + 2SI \cos \Theta)^{\frac{1}{2}} \approx S + I \cos \Theta$ for $S \gg I$.

For small Δ (signal and idler frequencies close together), the angle Θ varies slowly compared with ω_s or ω_i so that the resultant R can be thought of as the envelope of the combined signal plus idler output. If the variable $\Theta = \Delta t$ is replaced by d = distance from the load in a transmission line analogue (d is measured in units of 2π times the distance in wavelengths), then the signal response S becomes the incident wave and the idler response I becomes the reflected wave. In other words, the envelope of the signal plus idler output as a function of time has the form of a standing-wave pattern on a transmission line. If the received wavefront arrives at the array from such an angle that S is equal to I (an angle halfway between the signal and idler beams), then the envelope pattern will be the same as the standing-wave pattern on an open-circuited transmission line (i.e., maxima = $2I = 2S$, and minima = 0).

Operation of the array with signal and idler unseparated is thus seen to provide a form of automatic monopulse for pulses of sufficient duration to provide several minima in the output
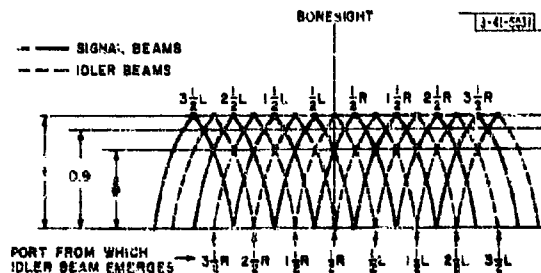
Fig. 2-59. Butler matrix beam outputs showing interlacing of idler and signal beams (main-lobe responses only).
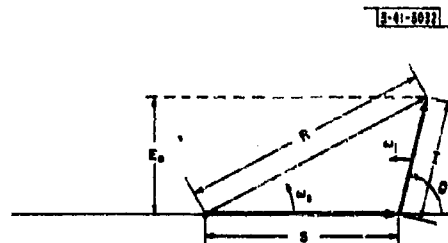

Fig. 2-60. Vector diagram showing relationship between signal and idler components of a Butler matrix beam output.

envelope. The period of the minima is $2\pi/\Delta$, where $\Delta = \omega_i - \omega_s$, or $1/(f_i - f_s)$, where $f_i =$ idler frequency and $f_s =$ signal frequency.

If the frequency separation between signal and idler is made smaller and smaller, the time scale of the envelope variation is stretched until finally for $f_i = f_s$ there can exist at most a fixed phase angle φ between the signal and idler vectors. This phase angle φ is dependent on the relative phase between the half pump frequency and the received signal at the reference or 0 channel of the array. (This non-time-dependent phase term was neglected up to now because it can be made zero by a suitable choice of the time reference t_0 implied in the time-varying expressions.)

The case where $f_i = f_s$ arises from synchronous pumping of the EBPA's ($f_p = 2f_s$). The combined signal plus idler output is now of constant amplitude corresponding to a fixed point on the "standing-wave" envelope of the asynchronous mode of operation. The location of this point is dependent on the fixed phase shift φ. Thus, anything from the sum to the difference of the signal and idler beam patterns can be obtained by varying φ.

If f_s is the transmitted signal frequency and f_p is made equal to $2f_s$, then the received signal may be of frequency $f_s + f_d$ because of a Doppler shift f_d. The EBPA's will then produce the "standing-wave pattern" of combined signal plus idler, but the period of the minima will now be $1/f_d$.

This discussion has been concerned with the properties of a receiving phased array with electron-beam parametric amplifiers in each channel. However, it applies as well if the EBPA's are replaced by any device which generates an idler frequency within its signal pass band.

88

CHAPTER IV
LOW-NOISE AMPLIFIERS

SUMMARY   W. J. Ince

Chapter IV presents the most recent work on the phased array project in the area of low-noise amplifiers. This work falls into two categories: an evaluation of the application of tunnel diodes to low-noise amplification and frequency conversion (Sec. A), and continuation of interest in the Adler electron-beam parametric amplifier (Sec. B). Although the electrical performance of the electron-beam parametric amplifier is extremely good, the package size leaves something to be desired; also, RF pump power is required for operation. Because of its simplicity and small power requirements, the tunnel diode may prove to be a powerful competitor despite inferior electrical performance, particularly with respect to noise figure. The development of an L-band tunnel diode amplifier is described, and the direction in which this effort will continue is indicated.

A. INTRODUCTION

The use of tunnel diodes in amplifiers and frequency converters for phased array radars has considerable attraction from the point of view of cost and simplicity. Semiconductor devices, operated within their specified ratings, are inherently long lived and would reduce down-time of the receiver. Power requirements are small; tunnel diodes typically used as amplifiers have peak currents in the order of 1 or 2 milliamperes. Gain is achieved by use of the negative-resistance portion of the diode I-V characteristic. Due to the high doping levels used in the manufacture of tunnel diodes, they are relatively insensitive to ambient temperature variations, and compared with transistors they are resistant to changes in electrical characteristics caused by nuclear radiation.

An evaluation of tunnel diode amplifiers is currently being made. The emphasis is on strip transmission line configurations because of the good reproducibility at reasonable cost which this type of fabrication allows. The design center frequency of 900 Mcps has been chosen so that completed designs may be installed in the linear array test facility for systems operation. Also, this frequency is sufficiently below the cutoff frequency of commercially available microwave tunnel diodes to obtain useful gain and noise figures.

Some diode parameter measurements have been made. The objective was to obtain diode admittance as a function of frequency for the purpose of amplifier design rather than for the establishment of an exact equivalent circuit. A bridge method was used, and the measurements were checked against admittance measurements by using a slotted-line technique. Complete, packaged tunnel diode amplifiers have been purchased from two commercial organizations and two of these amplifiers are undergoing evaluation in the laboratory.

A preliminary evaluation[*] showed that the electron-beam parametric amplifier warranted further interest and development. This work has been done on a subcontract basis. Attention has been paid to mechanical construction and reduction of the pump power requirement by improving the coupling arrangement. A number of these amplifiers will soon be installed and operated in the linear array test facility.

[*] J. L. Allen, et al., "Phased Array Radar Studies, 1 July 1959 to 1 July 1960," Technical Report No. 228 [U], Lincoln Laboratory, M. I. T. (12 August 1960), ASTIA 249470, H-335.
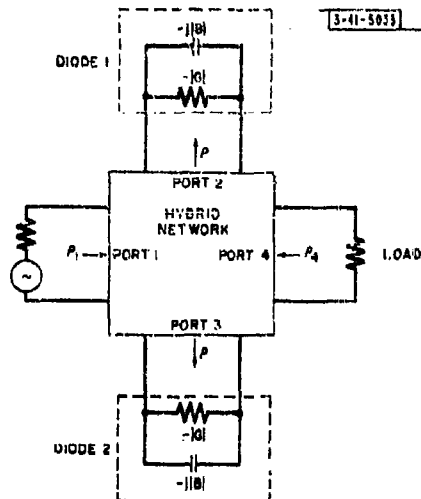
Fig. 2-61. Hybrid-coupled amplifier.
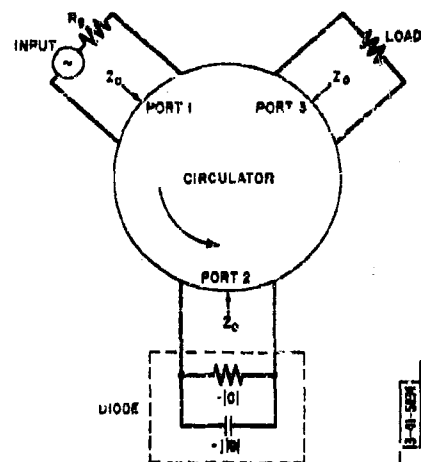

Fig. 2-62. Circulator-coupled amplifier.

Fig. 2-63. Circulator-coupled tunnel diode amplifier.

90

B. TUNNEL DIODES

Tunnel Diode Amplifiers:— Two possible configurations that have been considered are the two-diode hybrid-coupled amplifier and the single-diode circulator-coupled amplifier. Of these two reflection-type amplifiers, the circulator-coupled configuration has more desirable properties.

Hybrid-Coupled Amplifier[*]:— Figure 2-61 shows a hybrid-coupled amplifier which requires two matched diodes, connected at ports 2 and 3, respectively. Unfortunately, this arrangement is reciprocal, and enhanced gain is obtained if mismatches occur simultaneously at the load and input ports. For well-matched diodes, it can be shown[†] that the power gain is equal to

$$\left| \frac{|\rho|^2}{1 + |\rho|^2 \rho_1 \rho_4 e^{j4\theta}} \right|^2 \quad , \tag{1}$$

where $|\rho|^2$ is the power gain, ρ_1 and ρ_4 are the voltage reflection coefficients at the input and output ports, respectively, and θ is an arbitrary phase shift through the hybrid. It can be seen that the gain is very sensitive to the product $\rho_1 \rho_4$, particularly for large values of ρ. In order to ensure stability at all frequencies, the condition

$$|\rho|^2 \, |\rho_1| \, |\rho_4| < 1 \tag{2}$$

must be satisfied. In a receiving system, the input (antenna) VSWR could easily be as much as 2.1.[‡] Further, a gain of about 20 db is a reasonable requirement for an L-band amplifier. Hence, the load VSWR would have to be less than 1.01. This is a stringent demand in a phased array where relative phase and amplitude between receiver channels is important. Equally important is the fact that input and output mismatches have a detrimental effect on the noise figure. The effective input noise temperature T of the amplifier is given by[†] $T \approx T_n + |\rho_1|^2 \rho^2 (T_n + T_L)$, where T_n is the minimum effective input noise temperature, and T_L is the noise temperature of the load. From these considerations it is concluded that the hybrid-coupled amplifier is unsuitable for application as a low-noise L-band amplifier.

Circulator-Coupled Amplifier:— The circulator-coupled amplifier is shown in Figs. 2-62 and 2-63. A tunnel diode is connected to port 2 of a Y-circulator, and the generator and load are connected to ports 1 and 3, respectively. For this configuration, the condition for stability is

$$|\rho_1| \, |\rho_2| \, |\rho_3| < 1 \quad , \tag{3}$$

where ρ_1 and ρ_3 are the reflection coefficients at the respective circulator ports, and $|\rho_2|^2$ is the power gain of the tunnel diode.[§] This condition is much more easily met than the corresponding one for the hybrid amplifier expressed in Eq. (1). Also, the circulator-coupled amplifier is nonreciprocal. Isolation between output and input is provided by the circulator.

---

[*] J. J. Sie, "Absolutely Stable Hybrid Coupled Tunnel Diode Amplifier," Proc. IRE 48, 321 (1960).

[†] J.C. Greene, et al., "Eighth Quarterly Progress Report on the Application of Semiconductor Diodes to Low Noise Amplifiers, Harmonic Generators and Fast-Acting TR Switches," Report No. 4589-1-8, Airborne Instruments Laboratory, Inc. (June 1960).

[‡] See Part 3, Ch. I.

[§] M. E. Hines, "High Frequency Negative Resistance Circuit Principles for Esaki Diode Applications," Bell System Tech. J. (May 1960).
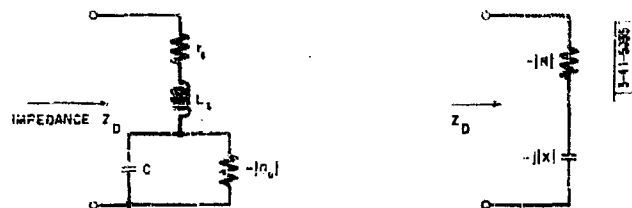
Fig. 2-64. Tunnel diode equivalent circuit transformation.

$$Z_D = r_s - \frac{|G_o|}{|G_o|^2 + \omega^2 C^2} + j\omega\left[L_s - \frac{C}{|G_o|^2 + \omega^2 C^2}\right] = -|R| - j|X|$$

Fig. 2-65. Breadboard of experimental tunnel diode amplifier.

Fig. 2-66. Strip line tunnel diode mount (note diodes at lower left).

Experimental Results:— The tunnel diodes used in the experimental work were Sylvania D4115A and General Electric ZJ62-2.2A types which are encapsulated in the pill-type package. These diodes are used well below their resistive cutoff and self-resonant frequencies, where the equivalent circuit transformation of Fig. 2-64 is applicable. $|G|$ is approximately equal to $|G_o|$, and $|B|$ is comparable to $|G|$ (see Fig. 2-71).

The power gain is given by[*]

$$\rho = \frac{(G_o + |G|)^2 + B^2}{(G_o - |G|)^2 + B^2} \quad .$$

Hence, for maximum gain it is necessary to tune out the diode susceptance. An amplifier experimental setup is shown in Fig. 2-65, and a circulator-coupled amplifier in Fig. 2-63. A close-up of the amplifier and its diode is shown in Fig. 2-66.

Since the characteristics of a circulator are very frequency-sensitive, it is preferable to use a 20-db coupler, which is usable within at least an octave bandwidth, to provide the necessary directionality during the initial testing of the strip transmission line circuit. The gain of the amplifier was about 16 db, the bandwidth was 14 Mcps and the best noise figure was 5 db. The amplifier saturates at approximately -40 dbm. A curve of the gain vs diode bias is shown in Fig. 2-67.

Two commercial amplifiers (Microstate NTAC 900) have been obtained for evaluation. Their specifications are:

Frequency	900 Mcps
Bandwidth (3 db)	50 Mcps
Gain	17 db
Noise figure	4 to $4\frac{1}{2}$ db
Saturation level	(1-db compression) -37 dbm
Bias voltage	110 mv
Relative phase stability	±2° instantaneous or long-term (24-hour period)

Figure 2-68 shows the swept frequency response taken for an input level of -40 dbm. A measurement of the gain and phase stability vs input VSWR was made with the arrangement of Fig. 2-69. Signal is fed to the amplifier under test through a 20-db coupler which maintains a constant amplitude input. The difference port is terminated via line stretcher 1 in 100 ohms. Thus, the input VSWR may be varied over a 2-to-1 range by changing the length of the line stretcher by $\lambda/2$.

The arrangement is balanced for a null indication at the IF amplifier by adjustment of line stretcher 2 and the variable attenuator, which are calibrated for direct reading of phase and amplitude changes. The amplifier was also tested for long-term stability over a period of 24 hours, and for temperature stability with the above setup. For these measurements the difference port of the 20-db coupler was terminated in 50 ohms. The results of the above tests are given in Table 2-V. The information gathered so far is encouraging.

Tunnel Diode Parameter Measurements:— In order to predict circuit performance closely, it was necessary to have a more detailed knowledge of tunnel diode parameters than the information

---

[*] C. Skalzried, "Interpretation of the Transmission Line Parameters with a Negative Conductance Load," Proc. IRE 49, 812 (1961).
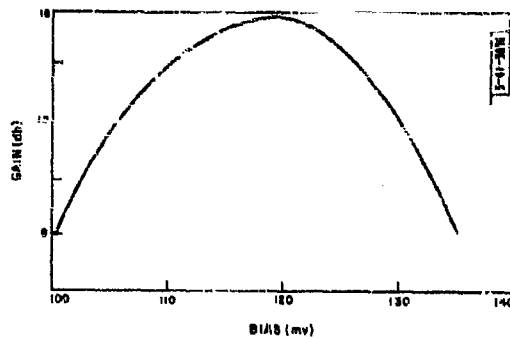
Fig. 2-67. Gain vs bias for tunnel diode amplifier.

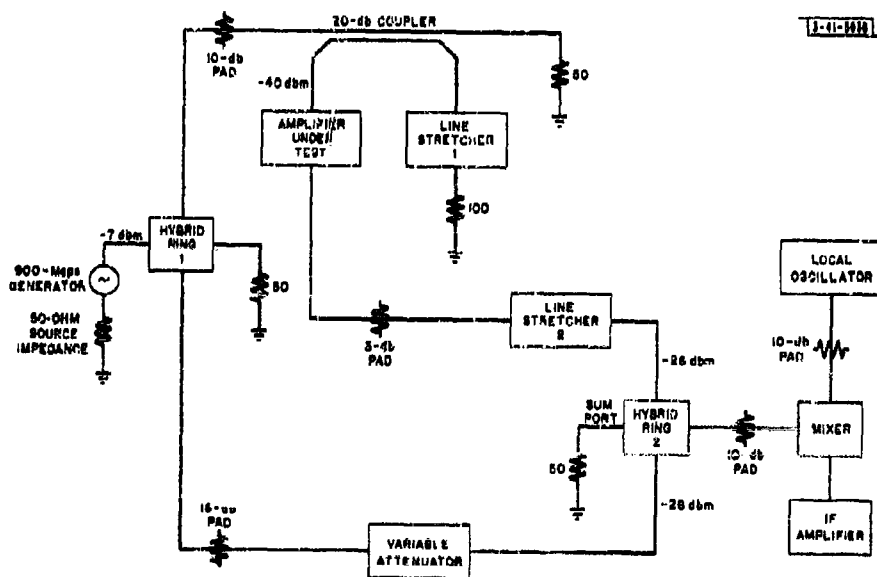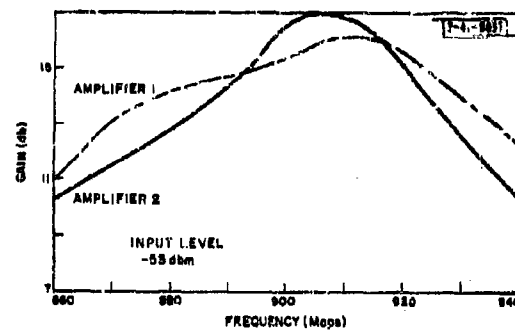Fig. 2-68. Gain vs frequency plot for tunnel diode amplifiers.

Fig. 2-69. Measurement of amplitude and phase vs input VSWR.

94

TABLE 2-V				
TUNNEL DIODE AMPLIFIER STABILITY MEASUREMENTS				
	Amplifier 1		Amplifier 2	
Test Condition	Gain Change (db)	Phase Change (degrees)	Gain Change (db)	Phase Change (degrees)
Variation of input VSWR by 2:1	0.1	1	0.1	1.6
24-hour stability	<0.1	2.5	0.1	1.6
Ambient temperature change 25° to 42°C	0.2	1.9	0.9	3

given in manufacturers' data sheets. Rather than establish the individual circuit components, it sufficed to measure the two-terminal admittance or impedance. Admittance measurements were found to be more convenient to make because less computation was involved.

A General Radio 1607A immittance bridge was used.* A special diode holder was constructed (Fig. 2-70) which is a 50-ohm coaxial structure. It is possible to introduce a disk resistor into the holder adjacent to the diode under test and in shunt with it. This enables the diode to be stabilized. Figure 2-71 shows an admittance plot vs frequency for a Sylvania diode. Results are given in terms of the equivalent circuits of Fig. 2-64. It can be seen that the real part of the admittance is relatively constant over a wide frequency range, while this is not true for the impedance plot.

Admittance measurements were also made by using a slotted-line method. This provided a check on the results obtained on the immittance bridge. However, because of the low signal levels used, VSWR's above 20 db could not be measured with accuracy.

Tunnel Diode Down-Converters:- A program for the testing of tunnel diode down-converters will soon be under way. The replacement of a conventional mixer by a tunnel diode down-converter does not seem to have significant advantages in a radar where a good low-noise front-end amplifier having reasonable gain is used. The possibility of replacing both the low-noise front-end amplifier and mixer with a single tunnel diode operated as a down-converter having conversion gain, although attractive, does not appear practical; hence, major effort has been given to the development of tunnel diode amplifiers. Consideration has been given, however, to the use of tunnel diode down-converters having unity gain and a noise figure of 2.5 db,† and the evaluation of two of these units is anticipated.

Conclusions:- The current evaluation of the use of tunnel diodes in a phased array receiver has been outlined. This evaluation, with particular emphasis on the measurement of noise figures, will continue. The particular difficulty encountered so far has been the suppression of undesirable oscillatory modes due to the frequency-sensitive characteristics of the associated circulator. So far it is felt that the tunnel diode is a promising competitor for use in a phased array radar.

---

*For a complete description of this method, see the General Radio Company "Experimenter," July 1960.
†F. Sterzer and A. Presser, "Stable Low-Noise Tunnel Diode Frequency Converters," 1961 WESCON Convention.

Fig. 2-70. Tunnel diode mount.
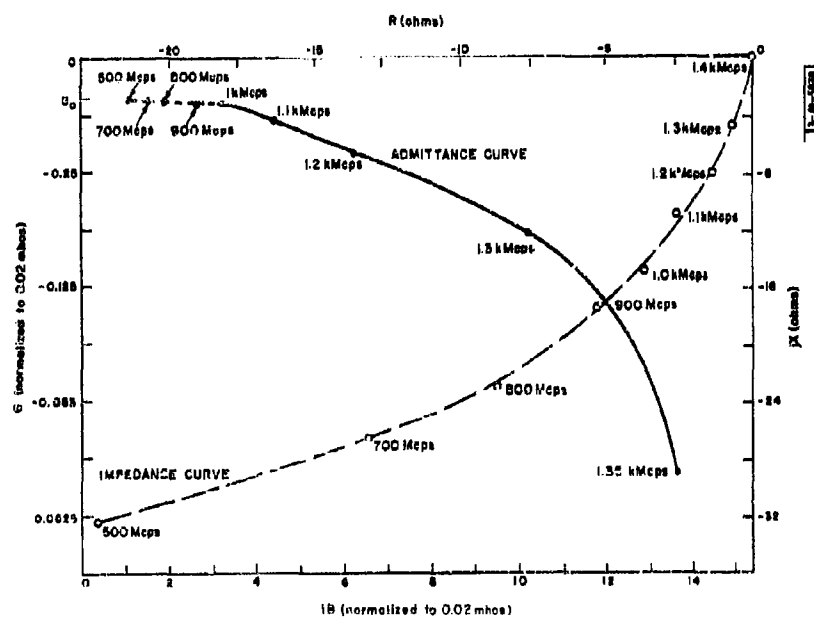
Fig. 2-71. Tunnel diode impedance and admittance vs frequency.

96

C. ELECTRON-BEAM PARAMETRIC AMPLIFIER

J. H. Teele

Preliminary tests on the Zenith/Adler fast-wave parametric amplifier[*] have been very encouraging. The results from these tests have confirmed the excellent gain and phase stability of the device. A contract for the delivery of sixteen of these low-noise amplifiers has been let. The contract completion date is 1 September 1961. The amplifiers will be installed in the linear test array, and a performance evaluation program will then be carried out.

It is desired to determine the performance of the sixteen amplifiers working together in a phased array. Although every effort has been made to insure uniform performance of the amplifiers, some operational problems are anticipated.

A second study program will measure the improved performance of the linear array radar system. The high noise figure (7 db) and low gain (13 db) of the present type 7077 vacuum tube front ends[†] have severely limited the number and kind of experiments that have been attempted with the linear array system.

---

[*] J. L. Allen, et al., op. cit., pp. 42-43.

[†] ibid., pp. 43-44.

CHAPTER V
INTERMEDIATE-FREQUENCY AMPLIFIERS

SUMMARY   J. DiBartolo, Jr.

This chapter describes the evolution of an inexpensive wideband IF amplifier which, because of its good phase and amplitude stability, is well suited for use in phased arrays. VHF transistors are used in grounded-base stages which are coupled with untuned transformers. Effects and limits of the transformers are discussed. Photographs are introduced to show the bandpass characteristic of the amplifier. Two graphs showing phase and amplitude stability for the duration of 150 hours are also included.

A. INTRODUCTION

A 30-Mcps IF strip with unilateralized grounded-emitter stages was presented in TR-228, together with amplitude and phase stability data taken during 40 hours of operation. To summarize, the rms phase error did not exceed 3°, and the amplitude rms error was less than 0.6 db.

The primary goal in the design of that amplifier was to stabilize the impedance and the gain and to extend the life of the transistors. Stability was achieved through unilateralization. The life of the transistors was extended by minimizing the dissipation. No interruptions due to transistor failure were logged in a full year's operation.

Stability is certainly of primary importance in amplifiers for a phased array radar but, if one considers a system using thousands of amplifiers, it is apparent that such a large number of amplifiers will make cost and maintainability important factors. In order to reduce this initial cost as well as maintenance difficulties, it was decided to try to eliminate all the variable (tuning) elements. A wideband amplifier was tried, based on a recent design,* with 50-db gain and 70-Mcps bandwidth. Phase and amplitude stability was scrutinized for several hours and, although the results were satisfactory, it was felt that the cost could be reduced considerably if a less expensive transistor were used.

In particular, it seemed that there might be advantages from the standpoint of transistor costs and stability in operating inexpensive VHF transistors in the grounded-base configuration. The nature of the grounded-base current gain parameter α, as contrasted to the characteristics of β, the grounded-emitter current gain, with regard to repeatability and frequency sensitivity suggests these possibilities.

A short investigation of available transistors showed that the 2N502 might suffice for such an amplifier, using untuned transformer coupling. Therefore, a toroid transformer was tailored to work in conjunction with this transistor in a grounded-base configuration.

B. TRANSFORMER EQUIVALENT CIRCUIT

The core used in the transformer is a 3/8-inch o.d., 3/16-inch i.d. toroid of Q-2 type ferrite ceramic material made by General Ceramics Corporation. Conventional transformer theory establishes the circuit of Fig. 2-72 as the equivalent of the transformer. In this figure,

---

* J.C. deBroekart and R.M. Scarlett, "Transistor Amplifier Has 100 Megacycle Bandwidth," Electronics 33, 73 (15 April 1960).

TABLE 2-VI

TYPICAL VALUES OF MUTUAL CAPACITANCE AND LEAKAGE INDUCTANCE
FOR TRANSFORMERS OF DIFFERENT TURNS RATIOS

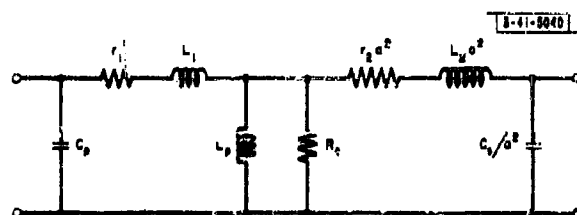| Turns Ratio	Mutual Capacitance (pf)	Total Leakage Inductance (μh)
36:9	9	1.2
36:6	5.2	2.1
36:5	4	2.5
36:4	3.7	3.5

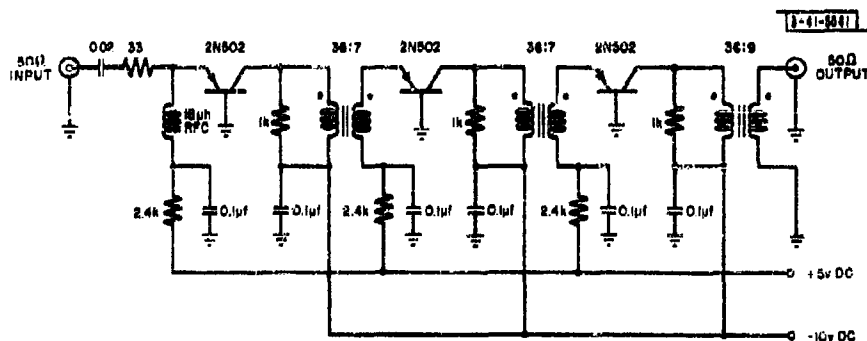Fig. 2-72. Transformer equivalent circuit.

Fig. 2-73. Circuit diagram of wideband IF amplifier.

100

C_p = distributed capacitance of primary winding,

r_1 = resistance of primary winding,

L_1 = leakage inductance of primary winding,

R_c = core loss,

$a = N_p/N_s$ (primary of secondary turn ratio),

L_p = primary inductance,

L_2 = secondary leakage inductance,

r_2 = resistance of secondary turns,

C_s = capacitance of secondary turns.

The parameters of the transistor are such that they add a capacitor of approximately 2 pf in parallel with 10 kilohms to the input side of the equivalent circuit of the transformer. The input impedance of the transistor, which is composed of an inductor L_T and a resistor R_2, is the load for the transformer and appears in series with the leakage inductance modified by the factor a^2.[*]

If the leakage inductance becomes very large, the high-frequency response will be limited severely. This, then, dictates limits for the highest transformer turns ratio that one can use. For a fixed number of primary turns, decreasing the number of turns of the secondary winding results in a greater leakage inductance. Therefore, although a given turns ratio might be ideal for matching transistors, this turns ratio has to be modified to restrict the values of L_1. Table 2-VI shows typical values of leakage inductance and mutual capacitance measured for transformers of different turns ratios.

The transformers have been wound simply by hand. The primary turns are wound in a single layer around the core, and the secondary turns are uniformly spaced over the primary. Obviously, the turns must be uniformly wound to assure repeatability.

C. AMPLIFIER CIRCUIT

The circuit diagram of the amplifier is shown in Fig. 2-73 and, except for the restriction placed on the transformer, the circuit is conventional. The biasing current must be held within 10 per cent of 2 ma because the input and output parameters of the transistor are current sensitive. Therefore, a 2.4-kilohm resistor has been inserted in series with each emitter in order to minimize any variation in this current. A 33-ohm resistor has also been placed in series with the signal voltage to raise and stabilize the input impedance. The noise figure for the system where this IF amplifier will be used is determined by the RF amplifier. Therefore, the loss of sensitivity caused by this small series resistor is negligible. However, for the system where the loss can not be tolerated, other means should be used to obtain the desired impedance. Wherever an optimum noise figure is desired, it will be necessary to mismatch the amplifier by increasing the impedance of the source.[†] The response of the amplifier is presented in Fig. 2-74. No initial selection of transistors has been made.

---

[*] For a discussion of transformers of amplifiers in general, see R. Lee, Electric Transformers and Circuits (Wiley, New York, 1947).

[†] R.B. Hurley, Junction Transistor Electronics (Wiley, New York, 1958), pp. 103-118.

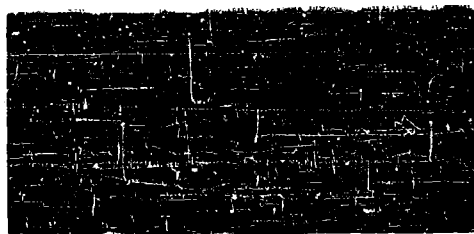Fig. 2-74. Typical IF amplifier response. Marker at 30 Mcps; 3-db points at about 5 and 45 Mcps.
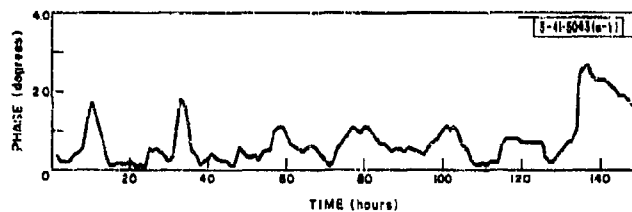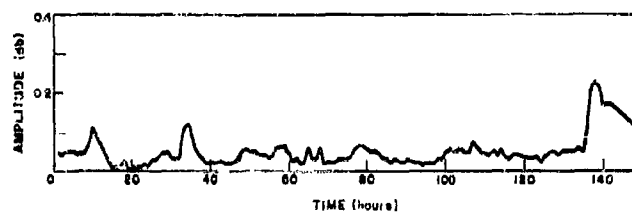

Fig. 2-75(a). Rms phase error.

Fig. 2-75(b). Rms amplitude error.

Fig. 2-76(a). Top trace: 30-mμsec input pulse (below limiting level). Bottom trace: output waveform. Scale: 50×10^{-9} sec/cm.

Fig. 2-76(b). Response of amplifier to 30-mμsec input pulse 20 db above limiting level. Scale: 0.4 volt/cm, 0.1 μsec/cm.

One practical word of caution is in order: It was found that the corresponding ends of the coupling transformer must be connected to the collector and emitter as shown in Fig. 2-73. Otherwise, the mutual capacitance C_m will take a higher value. This will lower the frequency at which it resonates with the leakage inductance, therefore limiting the high-frequency response.

A 1000-ohm resistor is placed across the primary winding of the coupling transformers to reduce the gain of the amplifier in the vicinity of the high-frequency peak caused by coupling circuit resonance.

The amplifier specifications are listed below.

Input impedance	50 ohms
Output impedance	50 ohms
Bandpass (3 db)	5 to 45 Mcps
Gain	30 db
Linear dynamic range	70 db (-30 to -100 dbm)
Noise figure	7 db

D. EXPERIMENTAL RESULTS

Phase and amplitude stability measurements of seven amplifiers were made for a period of 150 hours. Information was printed automatically every half hour. From the data obtained, rms errors were calculated; these results are depicted in Figs. 2-75(a) and (b). A coherent 30-Mcps signal was used to make this test in conjunction with the equipment described in Part 2, Ch. VII.

Another test was performed to observe the behavior of two amplifiers — one used at room temperature as a standard, the other enclosed in an oven where the temperature was varied from 25° to 50°C. Differential phase shift was less than 2°, and the gain remained constant within ±0.5 db.

Overload recovery of one of the amplifiers was also tested using 50-μsec pulses for the saturating signal. The amplifier recovered completely from a +17-dbm input signal in less than 20 μsec. It recovered completely from a 0-dbm signal in less than 5 μsec.

Noise figure was measured by using a similar amplifier as a postamplifier, a bolometer as a detector, and the AIL noise generator model 70C. The noise figures of the several amplifiers tested fell within the range from 7 to 8 db.

Finally, the transient response was tested by feeding the amplifier 30-mμsec video pulses and observing the output on a sampling oscilloscope. The amplitude of the input pulse was varied from a value below limiting to one some 20 db above limiting. The results are shown in Figs. 2-76(a) and (b).

Eight receivers in the presently existing 16-element phased array system have been equipped with these new amplifiers in order to check their performance relative to the older IF strips. Eight others are mounted in a test rack for continuing long-term stability measurements.

E. CONCLUSIONS

Reproduction of this amplifier is made easy and uniform by the use of a printed-circuit board (Fig. 2-77). A careful examination of more than twenty units already built has demonstrated that it is indeed possible to build stable amplifiers economically and to obtain virtually identical transmission characteristics with no adjustable circuit elements.

Fig. 2-77. Use of printed circuitry in IF amplifier.

CHAPTER VI
TRANSMITTER STUDIES

SUMMARY   L. Cartledge

This chapter describes the results of efforts directed toward making a very high power phased array transmitter composed of large numbers of moderately powerful plug-in elements practical. The first part of the chapter outlines a tube development and some design studies aimed at producing 1300-Mcps plug-in elements and a system for using them. The individual elements should produce 200 kw of peak power and up to 2 kw of average power. Plug-in elements are to include the actual radiating elements and be usable with these radiators spaced 0.58 wavelength apart to form a planar array. The cabling problems inherent in such an array were studied.

The second part of the chapter discusses the development of low-power, 900-Mcps plug-in elements for use in the linear test array. These elements will operate at 5 kw peak power and consist of a phase shifter, two tetrode amplifier stages, a plate modulator, and control and monitoring circuitry. The units are to be arranged in packages a few feet long and 6 inches square. All excess heat is removed by cooling water.

A. INTRODUCTION

A large part of the transmitter techniques effort over the past year has been devoted to studies of possible array system configurations for various tasks. Some qualitative conclusions are presented. Two sets of components are being developed into hardware; namely, parts for a high-power (200 kw peak and 2 kw average per element), 1300-Mcps transmitting array and for a much lower-power (50 to 100 watts average at 5 kw peak per element) array at 900 Mcps. With the possible exception of stability and reliability, the electrical requirements for these transmitter elements are within the existing state of the art. Development work in the areas of reliability and packaging for the close spacings is described.

B. 1300-Mcps TRANSMITTER

1. Tube Development

No microwave amplifying device suitable for use as an output amplifier in the 1300-Mcps transmitter package exists. Hence, a development contract is under way on a 100-kw peak, 1-kw average device small enough to fit in a half-wavelength square package. Detailed specifications for the device to be developed are listed below.

Requirements for Phased Array Output Amplifier

Frequency   The center frequency is to be 1290 Mcps.

Power output   The device must produce an RF power output over the specified bandwidth
                   of 100 kw peak and 1 kw average.

Gain   The device shall have a small signal gain of 16 db and shall meet the power
                   output and other requirements when excited by RF pulses having a peak
                   power of 5 kw.

Pulsewidths   The device must be able to transmit pulses at its rated peak power with
                   any pulsewidth from 0.1 to 100 μsec. Pulsewidth is defined as the time be-
                   tween the 50 per cent voltage points.

Bandwidth	Instantaneous 1-db bandwidth must be at least 100 Mcps. More bandwidth is desirable if other requirements are not jeopardized.
Rise time	The rise time of an RF output pulse shall not be more than 15 mμsec greater than the rise time of the input RF pulse.
Burst modes	The amplifier must be capable of transmitting a burst of a number of short pulses, each separated from the other by 10 μsec or less. The burst length may be as long as 300 μsec, and the "on time" inside a single burst may be as much as 100 μsec.
VSWR	The device must be capable of operating into a VSWR of 2:1 at any phase angle (50-ohm nominal impedance).
Efficiency	Over-all efficiency, including heater power, magnetic focusing power and plate efficiency must be at least 30 per cent.
Short-term phase stability	Output phase must not vary more than 2° as a result of a 1 per cent change in the most critical input voltage. Similarly, output phase must not change more than 2° for a 1-db change in input power.
Long-term stability	At a fixed set of input voltages, the drift in absolute phase change through the amplifier shall not exceed 6.5° over the life of the device. Similarly, the change in saturated output amplitude shall not exceed 1 db over the life of the device.
Spurious radiations	All spurious radiations during transmitter "on time" must be at least 25 db below the peak power output.
Interpulse noise	Noise power out of the device between pulses shall be less than 1.4×10^{-20} watt per cycle.
Uniformity	Differential phase differences between devices as a function of frequency shall not exceed 2° over the pass band when the devices are operating into identical VSWR's which may be as high as 2:1 at any phase angle.
Size and shape	The device must be less than 12 inches long and must fit into a square tube 4.5 inches on a side with enough room for six cables $\frac{1}{2}$ inch in diameter to be run inside the square tube and past the amplifier.
Spacing	Design must be such that the device can be operated without difficulty due to mutual interaction with no external shielding and 5.32 inches spacing between the centers of adjacent units.
Plug-in features	The complete transmitter package must be replaceable while the array is operating normally.
Modulation	Low-level modulation capable of producing single or multiple pulses with widths varying from 0.1 to 100 μsec is desired.
Life	The device must be designed for a minimum operating life of 5000 hours. End of life is defined as a 1-db change in saturated output amplitude or a $6\frac{1}{4}°$ change in the absolute phase shift through the device.

| Cooling | The device shall be designed for water cooling. |
| Producibility | Maximum attention is to be given in the design to economy of future mass production of such devices. |

2. System Considerations

System studies in the area of phased array transmitters have led to some qualitative conclusions. The first of these is that every element should be driven at the same power level in order that the highest possible peak and average powers can be obtained. Every effort should be made to obtain acceptable sidelobe performance by means other than amplitude tapering the transmitting array such as density tapering[*] or staggering transmit and receive sidelobe peaks and nulls for low two-way sidelobes.[†]

A second conclusion is that the final phase-shifting operation should be done at as high a power level as components will permit in order to reduce the gain required from the final RF amplifier. The amount of variation in phase shift through an amplifier due to changes in voltage, etc., is usually proportional to the gain of the device. Hence, making the high-power output amplifiers operate at high gain adds to the problems of adequate power supply and temperature control.[‡]

Lastly, it seems that the best system reliability, as well as economy in weight, volume and money, may well be obtained by generating RF power in large numbers of relatively low-power modules. The power level of the individual module should be low enough to permit low-level modulation, energy storage in the module, air or solid insulation and freedom from problems due to hard x-rays. Obviously, the design must be such that individual modules can be removed from service and replaced without interrupting the system operation.

3. Integrated Transmitter System Design

It becomes apparent that if a phased array transmitter is to become economically feasible, the design of the electronics and of the support structure must take full advantage of the production economies inherent in very large numbers of identical elements. Also, because of the very high density of components, the electronic design must be carefully integrated from the start with the design of the support structure and with that of the cooling system. Such an integrated design has been started at 1300 Mcps. The device development mentioned above is one part of this design effort.

Another step in the development of a 1300-Mcps transmitter is the design of the cabling and coolant distribution systems. A full-scale wooden mock-up of an 8 × 16 element transmitting array at 1300 Mcps has been built. This mock-up, which is shown in Figs. 2-78, 2-79 and 2-80, is used for testing cable routing schemes. The individual plug-in elements (Fig. 2-81) are approximately 0.5 wavelength square and are spaced 0.58 wavelength center-to-center for ±45° scan in the principal planes. All connections are brought in at one end, and the actual radiating elements are mounted on the pluggable module at the other end. The radiator is removed with the element so that the only electrical connection that is not readily accessible is a break in

---

[*] See Part 3, Ch. III, Sec. G.

[†] J.L. Allen, et al., "Phased Array Radar Studies, 1 July 1959 to 1 July 1960," Technical Report No. 228 (U), Lincoln Laboratory, M.I.T. (12 August 1960), pp. 179-180, ASTIA 249470, H-335.

[‡] See Part 2, Ch. II, Sec. F-2.

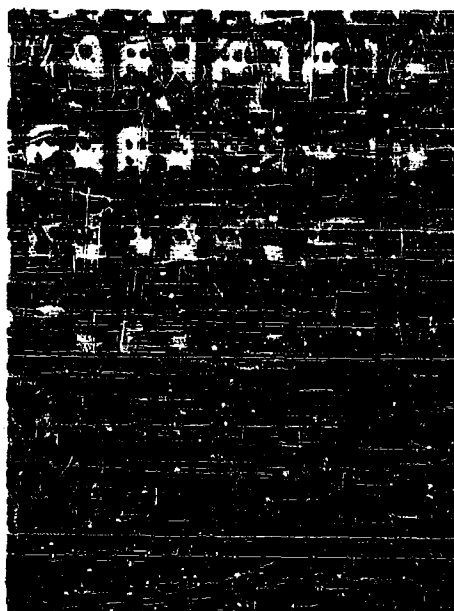Fig. 2-78. Section of phased array transmitter mock-up
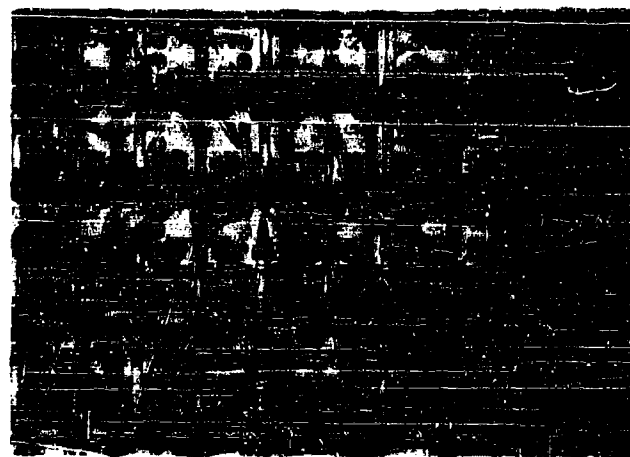with water and power connections installed.

Fig. 2-79. Section of phased array
transmitter mock-up with all con-
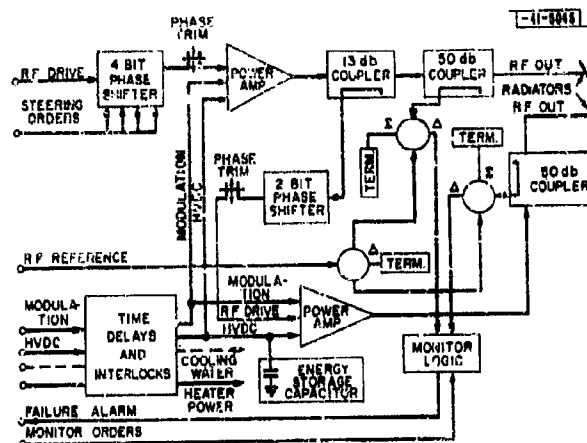nections installed.
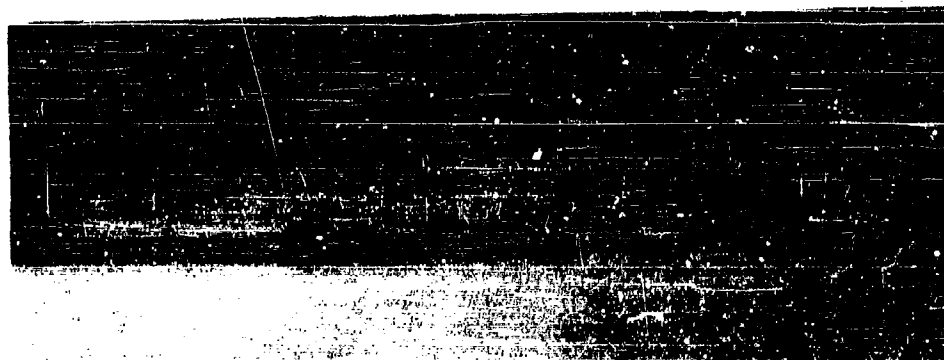
Fig. 2-80. 200-kw L-band transmitter plug-in module.

Fig. 2-81. Phased array transmitter mock-up plug-in unit.
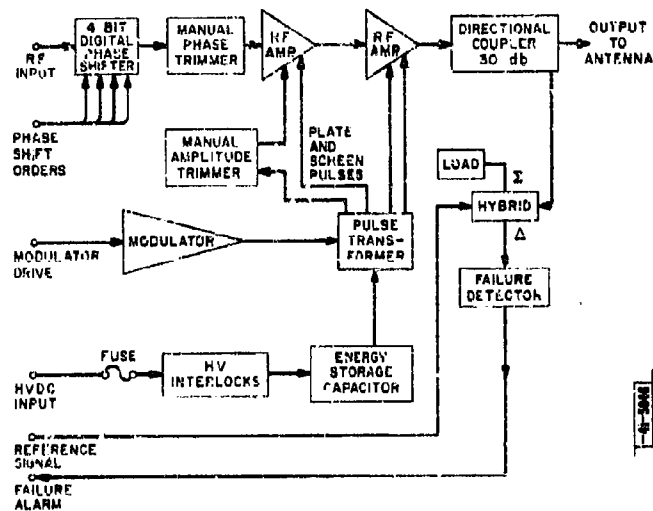
109

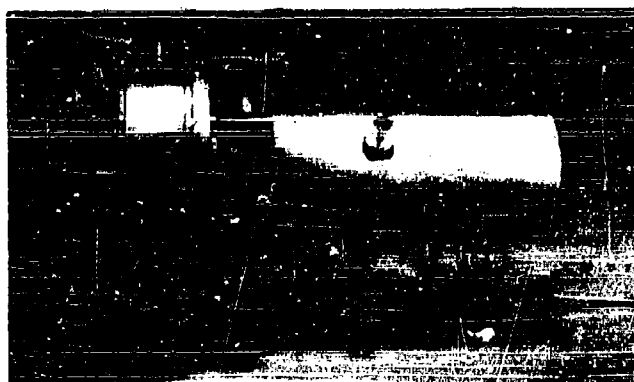Fig. 2-82. Block diagram of 900-Mcps transmitter unit.

Fig. 2-83. Single amplifier stage.

the ground plane behind the radiators. A brief test was run to check the feasibility of this arrangement.

In addition to supply and return lines for 3 gallons per minute of cooling water, connections are provided for 5 to 7 kw of DC power at between 8 and 20 kv (these parameters to be determined exactly by the outcome of the tube development), 10-kw peak-power RF drive pulses, some twenty low-voltage low-frequency control leads, a phase-stable RF cable for performance monitoring and a small coaxial cable for modulator drive. Since a suitable high-voltage connector does not exist at present, development of such a connector outside Lincoln Laboratory has been initiated as has development of some specialized RF connectors for the various corporate feeds

Each element will contain two final amplifiers, a phase shifter, an energy storage capacitor, modulating circuitry, a polarization switch, and monitoring and protective circuitry. Each element package will operate at 200 kw peak and 2 kw average power and can be built from available parts, or from parts presently under development, to weigh less than 100 pounds. This weight is made up as follows:

	Pounds
Power amplifier tubes	≤50
Energy storage capacitor (0.25 μf, 20 kv)	≤20
Modulator circuitry	≤5
Monitoring circuitry	≤5
Support and miscellaneous	10

4. Planar Array Ground-Plane Tests   W. P. Delaney

Tests were made on a small planar array of dipoles to investigate the effect of small grooves in the array ground plane. These grooves appear when the individual ground planes of the array modules are separated by a short distance for mechanical considerations.

Antenna patterns were taken on a 4 × 4 array of dipoles which had grooves between 2 × 2 dipole "modules." Groove widths of 0, 1/32 and 1/16 inches were tried, and groove depth was kept constant at 1/4 inch. The shape of the antenna patterns did not change significantly with groove width. Relative gain measurements indicated a 0.5- to 1.0-db increase in gain as the groove width was changed from 0 to 1/16 inch. This gain increase is not enough to be concerned about in view of the possibilities for errors in the measurement. For example, patterns for each groove width were taken on different days; the accuracy of the pattern recorder is ±0.25 db.

C. 900-Mcps TRANSMITTER   L. Cartledge

1. General

A series of 900-Mcps transmitting elements is being designed and built for inclusion in the test array. Since this effort was started rather late, the elements are presently at the breadboard stage. Hence, only preliminary results can be presented at this writing. In the paragraphs that follow, the design objectives will be outlined and the units will be described as fully as possible.

The 900-Mcps units are a half-wavelength (6 inches) square in cross section to be usable in a full power density transmitter array. Each unit is pluggable and contains the cooling and monitoring necessary for operation in a full density array. A block diagram of one unit is shown in Fig. 2-82. Figures 2-83, 2-84 and 2-85 are photographs of various parts of a unit and of a two-stage breadboard. These units are to operate under the following specifications:
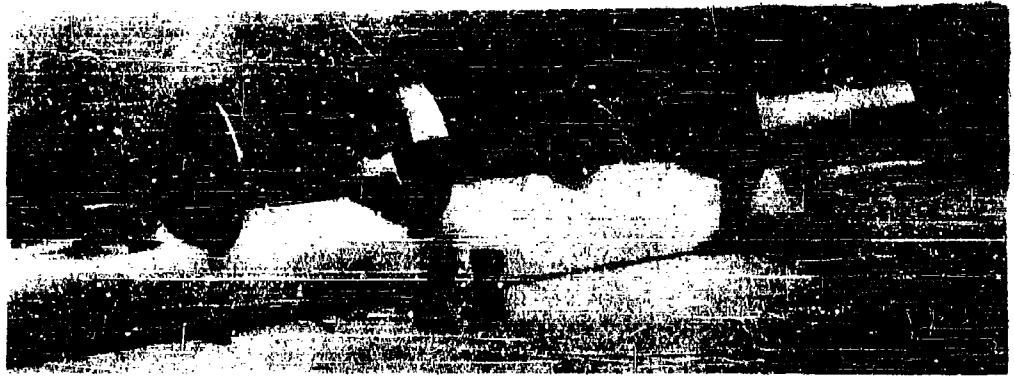
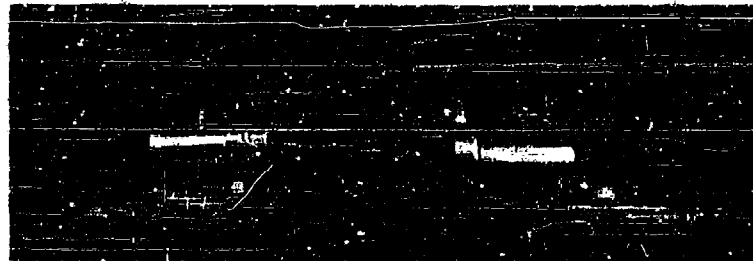Fig. 2-84. Exploded view of amplifier stage.

Fig. 2-85. Breadboarded unit.

Power output	$\geq$50 watts (average)
	$\geq$5000 watts (peak)
Center frequency	900 $\pm$ 40 Mcps
Signal bandwidth	10 Mcps
Pulsewidth	0.1 to 10 μsec
Phase quantum	$\frac{1}{16}$ wavelength

Since the elements are to be packed on half-wavelength centers, there is no room for convection cooling. All heat dissipated in the elements is removed by water cooling. This requires about 10 cc of water per second. Cool water is used for stabilizing temperature-sensitive components where necessary.

The components in the RF chain include the phase shifter, two amplifier stages and the monitoring directional coupler. The 4-bit digital phase shifter is a type that operates at a peak power level of few watts and is based on the work described in Part 2, Ch. II. The following paragraphs describe the work that has been done on these transmitting elements to date.

2. RF Amplifiers

The RF amplifiers are conventional, coaxial-cavity, tetrode amplifiers. All the amplifiers built so far have used tubes similar to type 7649 tetrodes which were modified for water cooling. These tubes are used with a three-quarter wavelength cathode cavity and a quarter-wavelength plate cavity. The grid-screen bypassing is accomplished with mica washers some 4 inches in diameter. Similar mica washers provide DC blocking at either end of the plate cavity. The tubes are operated as zero-grid-bias, cathode-driven, plate and screen pulsed amplifiers with capacitance coupling to both the input and output cavities. When used as a low-level stage of the two-stage chain, the amplifier is operated with a single-tuned output circuit and can provide about 17 db of gain and 350 watts peak output at about 15 per cent plate efficiency. The bandwidth of this stage is about 20 Mcps.

The output stage is operated with the plate circuit single-tuned and produces some 12 db of power gain at 50 per cent plate efficiency. The over-all bandwidth of the two stages is 15 Mcps.

These amplifiers exist presently in breadboard form. The next step in the transmitter development will be to manufacture some 25 two-stage amplifiers and assemble them into complete units for life testing and use in the test array.

3. Pulse Modulator for 900-Mcps Transmitter   M. Siegel

As described in the previous paragraphs, it was decided to build 900-Mcps transmitter modules as a first approach in the phased array transmitter program, each module containing a final amplifier, a driver amplifier, a phase shifter, monitoring equipment and its own individual modulator. Since it was desired to obtain 5 kw of peak power output at 900 Mcps using a 10-μsec pulse and a 0.01 duty cycle from tetrodes in cavities operating class B, each modulator is required to produce at least 10 kw of peak power for the plate circuit of the final amplifier, plus the plate power for the driver stage.

Two ways of achieving plate and screen modulation present themselves. The first way is to provide a common bus modulator and feed all the sixteen modules in the linear array through individual pulse cables carrying large pulse currents from one or a few large modulators capable of providing 160 kw of peak power at 1.6 kw of average power. However, the screen circuits

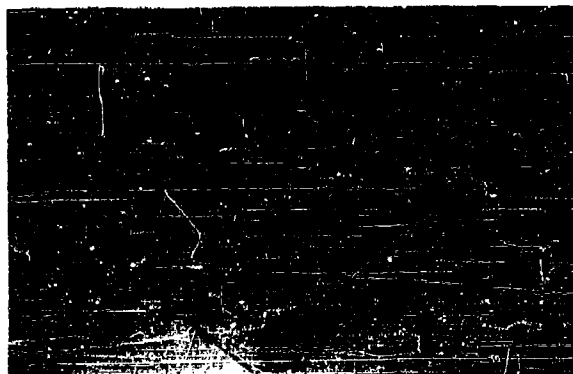Fig. 2-86.   Schematic diagram of pulse modulator.

Fig. 2-87.   Pulse modulator.

must operate at pulse voltages different from the plate voltage; also, the driver stage might operate optimally at a plate voltage different from the final amplifier plate voltage. This would entail either throwing pulse power away in dropping resistors, decreasing the efficiency and increasing the heat load, or providing many pulse cables to each module, one for each different voltage.

The other alternative, and the one that was followed, was to make each module a complete transmitter, and provide an individual modulator plus sufficient energy storage (to supply power for each pulse) for each module.

Two advantages immediately accrued from doing this. First, it is now practical to use a pulse transformer, since the maximum pulsewidth needed is $10\,\mu sec$ and the minimum video pulsewidth most likely needed would be $1\,\mu sec$. A pulse transformer with several taps can provide all the various output voltages required by the tubes over these pulsewidths. As many as four voltages can be provided from one transformer simultaneously without seriously degrading the pulse shape. Second, since the peak power required is now of the magnitude of only 10 to 20 kw, a hard-tube modulator can be used with the advantage that any pulsewidth between .1 and $10\,\mu sec$ can be provided and the pulse repetition frequency can be adjusted so that a 0.01 duty ratio is maintained. (The modulator acts only as a pulse amplifier and does not determine the pulsewidth.) This provides a more flexible modulation arrangement. In addition, none of the large pulse currents have to be carried around from module to module, and pulse current to charge cable capacitances need not be provided.

For the prototype, it was therefore decided to design a 10- to 15-kw hard-tube modulator capable of providing pulses of 1 to $10\,\mu sec$ and voltages of 4, 2.5, 2.0, 1.5, 1.0 and 0.5 kv. These voltages would be capable of driving a primarily resistive load of approximately 1 kilohm. (The 7649 tetrode when pulsed to 3 kv draws approximately 3 amperes of peak current.)

Since pulse voltages as great as 4 kv were desired, the 3E29 pentode which is capable of 5-kv operation was used. It was determined that, to obtain the 10 to 15 kw desired, the tube's rated plate dissipation would not be exceeded, but the screen dissipation rating would. It was therefore decided to parallel two 3E29's to obtain the necessary power out with a good margin of safety.

More than 20 kw of peak power have been obtained from one modulator without adversely affecting the pulse shape or exceeding dissipation ratings. The size of the final modulator package is $6 \times 6 \times 6$ inches. Each modulator contains its own energy storage capacitor ($0.5\,\mu f$ at 5 kv) which is sufficient to hold up a $10\,\mu sec$ pulse with maximum droop across the capacitor of approximately 2 per cent during the pulse. In addition, in series with the high voltage to each modulator will be a fuse capable of interrupting 5 kv if the average current becomes excessive. In this way, each module will have its own energy storage and its own protective device.

Figure 2-86 is a schematic of the pulse modulator. Figure 2-89 shows the latest assembled version of this modulator, and Fig. 2-88 shows the modulator output pulses when operating into an RC load (1 kilohm in parallel with $50\,\mu\mu f$). Figure 2-87 shows the water tubing or channeling used to cool the chassis.

In order to provide video drive power for the sixteen modulators, a driver modulator was built that is capable of taking a pulse of 1 to $10\,\mu sec$ from the timing circuitry in the data-processing equipment and amplifying this to provide pulses for as many as twenty modulators through a 20-foot length of cable attached to each modulator.
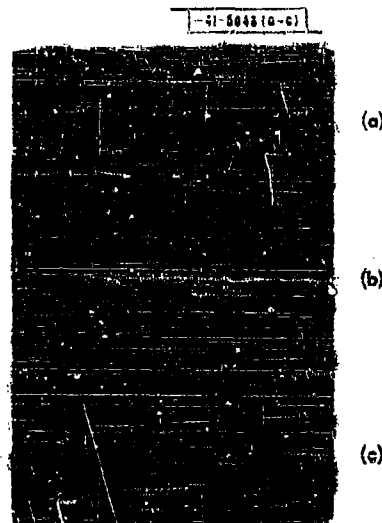
(a)

(b)

(c)

Fig. 2-88. Output of pulse modulator (load impedance 1 kilohm in
parallel with 50 µµf).
Amplitude scale (per major division): 2000 volts.
Time scale (per major division): (a) 200 µsec; (b) 2 µsec; (c) 0.1 µsec.

Fig. 2-89. Bottom view of pulse modulator.

To evaluate how much cooling would be required by the modulator, the following estimation of heat generation was made.

	Watts
Filament power	36
Plate dissipation	20
Screen dissipation	5
Screen dropping resistor	5
Transformer losses	10
	76

Tests were run with the modulator completely enclosed in a heat-insulating medium and producing 16 kw peak power and 160 watts average power output at water flow rates of only 1.5 cc/sec through the entire modulator. Temperatures were measured continuously at suspected hot spots which were electrically at ground potential, and temperature-sensitive paints were placed on hot areas that were at high voltage. The hottest temperature measured (excluding the glass of the tube) after an 8-hour period was 190°F. In addition, no component manufacturer's maximum allowable temperatures were exceeded nor was any component adversely affected after two 8-hour periods of continuous operation. The final modulator will be cooled by much larger flow rates (at least 10 cc/sec) and will be life-tested over much longer periods of operation time.

It might be mentioned that subsequent to this test, when a destruct test was performed on this modulator, no water was allowed to flow; the first component failure occurred in the high-voltage section after 1½ hours of operation.

Figure 2-90 is a graph of average temperature vs time for an 8-hour run with water flow rates of 1.5 cc/sec. On the average, a 12°F temperature differential from inlet to outlet of the water was obtained. As mentioned before, approximately 76 watts were dissipated within the modulator. The water required to remove 76 watts if the cooling system were 100 per cent efficient would be $Q(gal/min) = P(watts)/264(T_2 - T_1)°K$. Upon adjusting the units and substituting in $P = 76$ watts, $\Delta T = 20°F$. Therefore, the flow rate $Q = 1.62$ cc/sec. It was also decided that the large heat-producing elements should rest securely on a heat sink or slab directly connected to the water-cooling channeling.

Since it is hoped to be able to plug in and remove each module while the other modules are in operation, investigation into appropriate cabling and connectors for the modules is being conducted. Such problems as locating and providing suitable quick disconnects for the water lines, disconnecting high-voltage cables with complete operator safety, and proper protective devices for both personnel and equipment while in operation and being serviced are being examined in detail.

4. Water Cooling

One of the primary problems in the design and construction of any planar transmitting phased array is that of cooling the component parts and maintaining the temperature of the array at some reasonable value.

Until the time of this writing, the approach of most of the array designers has been to use air cooling as the main, if not only, cooling means. In a high-power planar phased array, however, the individual modules are usually spaced about one half-wavelength apart, hence there is
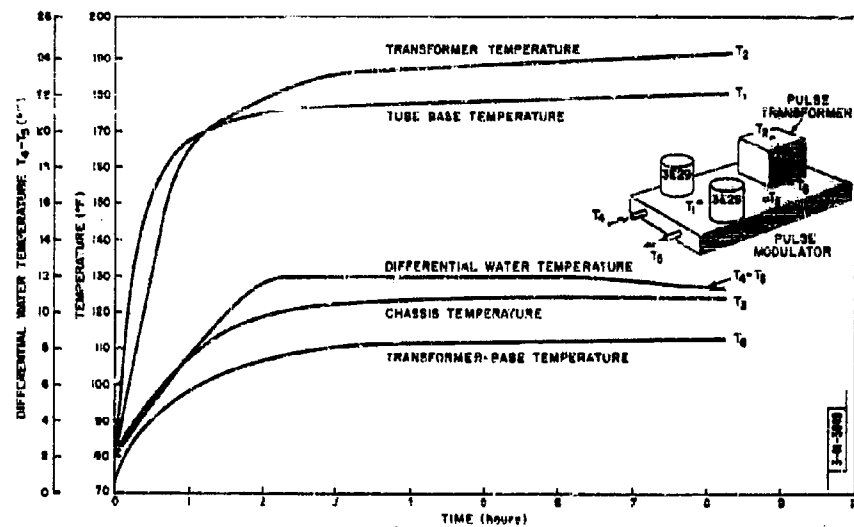
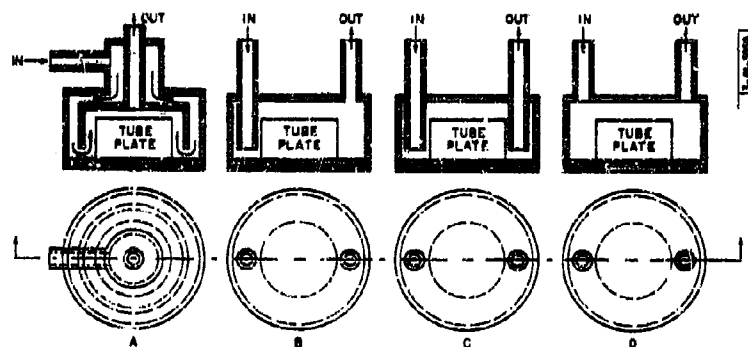Fig. 2-90. Temperature vs time for pulse modulator.

Fig. 2-91. Experimental water jackets for transmitter tubes.

no practical way of ducting the large volume of air required to cool the densely packed amplifier modules. In the design of the final amplifier modules to be used in the 16-element 900-Mcps linear array, provision was made to cool these modules entirely by water.

A water purifier (ion and oxygen remover) and a temperature stabilizer (which maintains constant array water temperature either by heating or cooling the water) were assembled as a unit with sufficient capacity to provide ion-free temperature-stabilized water to all the modules. Provision was made to connect and disconnect the individual modules from this unit by means of quick-disconnect connectors.

The actual design of the cooling system within a module was done in two steps. First, it was decided to provide water jackets for the main heat-producing components such as the final amplifier tube and the driver tube preceding it. Second, it was decided to cool the chassis itself by running an extruded channel or pipe along the walls of the chassis and thermally connecting all hot components to generous slabs of aluminum which were connected thermally to the chassis. By cooling the chassis, the ambient temperature in the module is held to some reasonable value.

Since no water-cooling jacket was available at the time for the amplifier tubes that were to be used in the 900-Mcps array, it was decided to design a few different types of water jackets and measure their relative performance. Two major factors were utilized in determining the optimum design for a water jacket for the phased array tubes:

(a) The minimum amount of water to adequately cool the tube with a margin of safety is to be provided.

(b) The jacket should have low manufacturing cost.

Both of these restrictions were placed on the choice of the water jacket, since large numbers of cooling jackets would be required for any phased array, and factors of this nature affect the cost of a large system.

After consideration of the tube dimensions, the quantity of water necessary to carry off the heat, and the flow conditions necessary to establish turbulent rather than laminar flow at the heat generating surface, four types of water jackets were assembled (Fig. 2-91).

It was assumed that the most effective cooler was jacket A because of the nature of the water-flow path, and the least effective was D, efficiency of cooling decreasing from A to D.

A detailed analysis was performed on water jacket A to ascertain the proper water flow and the dimensions and location of the concentric cylinders to provide sufficient cooling and turbulent flow conditions. Analytical results were then compared with experimental data obtained using these water jackets on tubes that were dissipating 100 watts of average power. All the tube seals (ceramic to metal) were coated with temperature-sensitive paint to ensure that no manufacturer's maximum seal temperatures were exceeded. In addition, thermocouples were mounted at various suspected hot spots on the tubes and continuously monitored. It was assumed that the ambient water temperature would be from 100° to 120°F and that allowable temperature rises in water would be 20°F. Flow rates per water jacket were calculated to be about 3 cc/sec to remove the 100 watts of heat generated.

Water jacket A was assumed to provide the optimum in cooling and was to be established as a standard with which to compare other designs. Its chief disadvantage was that it would be considerably more expensive to mass produce than other designs.

Figure 2-92 shows curves of tube temperature and water temperature change vs water flow rate. These data were obtained with the tube dissipating 100 watts into water jacket D and allowing the temperature to stabilize at each of the measured flow rates.
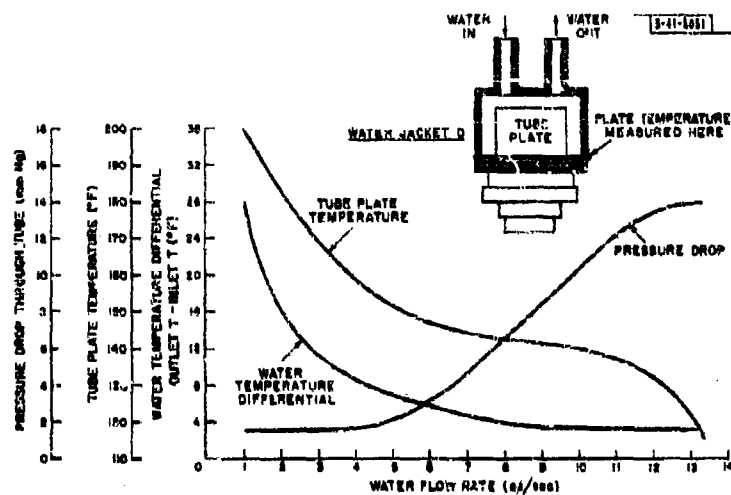
Fig. 2-92. Tube plate temperature, output minus inlet water temperature, and pressure drop vs water flow rate.
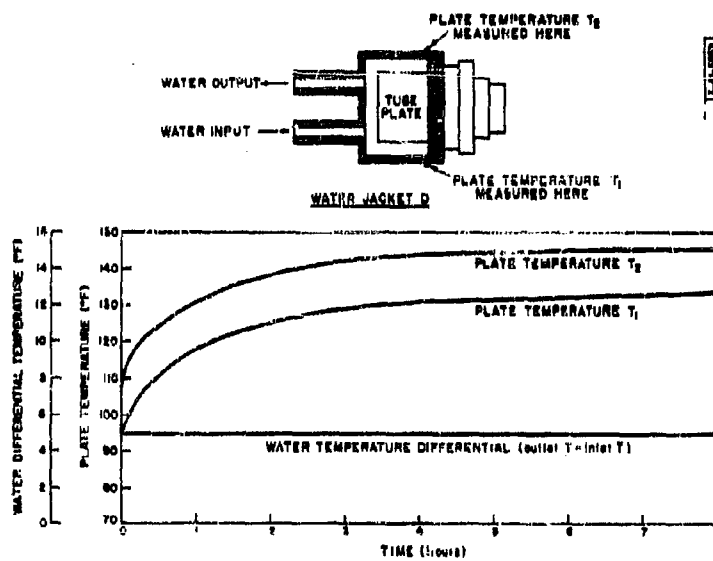
Fig. 2-93. Temperature vs time for water jacket D.

The difference in performance from tube jacket A through tube jacket D was not considerable. In addition, at no time during the test was the manufacturer's maximum seal temperature approached with any of the water jackets.

As a result of these tests, it was decided to use in the array the simplest water jacket to manufacture (water jacket D) and to provide a flow rate that was more than double the test flow rates. Water jacket D was then tested for periods of 8 hours at a time at flow rates of 10 cc/sec removing 100 watts of plate dissipation from the tubes (Fig. 2-93).

It should be mentioned that, for the purposes of the water-jacket experimentation, the water jackets were machined from brass and cemented to the copper coaxial plate caps of the power tetrodes. These tubes were originally available with fins for air cooling; however, the manufacturer provided several developmental tubes without radiators. Henceforth, the tube manufacturer will provide these tetrodes with water-cooling jackets similar to water jacket D attached to the plates by a shrink-fit process.

It is expected that sixteen modules will be assembled, each module containing at least two tubes. Therefore, 32 tubes with water jackets will be assembled and placed in cavities. Since no air cooling or convection cooling whatever is to be provided, wherever excessive heat is generated, this heat will be removed by copper tubing or water jackets wrapped around or nearby the heat-producing elements. It is expected that all the water entering a module will flow past or around the major heat-producing components in addition to flowing along chassis sides. Each transmitter module thus has one water inlet and one water outlet.

CHAPTER VII
ARRAY CONTROL AND DATA PROCESSING

SUMMARY   J. H. Teele

This chapter deals with certain problems of the array radar-computer interface. Part A presents the guiding philosophy of the phased array data-processing effort, along with some remarks on possible future investigations. In Part B, a method of precise beam-position control is considered. Use of this technique may well result in large cost reductions for phased array systems where digital phase shifters are employed to form and steer the beams. In Part C, an accurate time-variable gain control circuit is discussed. Use of this control permits measurement of target cross section with automatic compensation for target range. Part D presents a discussion of a flexible, programmable, pulse-train synthesizer. This device has application to the general target parameter measurement problem in conventional, as well as in electronically scanned, radar systems.

A. INTRODUCTION AND DATA-PROCESSING PHILOSOPHY

Effort in the area of array control and data processing is being concentrated on two general problems. The first involves studies of various schemes to precisely control the position of receiving and transmitting beams in electronically scanned radar systems. The second area of investigation embraces the general analog-digital system problems connected with the operation of a high-data-rate, electronically scanned array in a dense-target environment.

The effort in these areas is expanding, with the realization that many proposed control and data-processing systems (for arrays) are inadequate in both speed and sophistication. The previous statement arises from consideration of some of the ultimate applications of array radar systems.

Most proposed array data-processing systems consist of a large central computer with associated input/output equipment. It is felt that the computer itself will be available, when needed, from one of several sources. The requirements on this computer are simply speed, flexibility, and size.

There is, however, an area that has been largely neglected. This area embraces all the problems that might be lumped under the general heading "input/output equipment." It is clear, however, that the term "input/output" hardly does the problem justice.

Electronically scanned arrays operating in a dense-target environment, transmitting many varied sophisticated waveforms, will have a high information-gathering capability. The information on target position and target parameters will arrive in real time at data rates hitherto not experienced in operating radar systems. A few present-day computers could conceivably handle the data-processing problems associated with such systems if the wide-bandwidth analog information could be presented in a format suitable for direct storage or computation. The "black box" that accepts high-bandwidth analog data in real time and delivers compact, ordered, digital data to the control and central processing system is largely a gray area.

We are faced with a situation where the problem of waveform generation may be easier than the problem of waveform analysis. Much attention is being given to the problem of waveform design in certain situations. Many waveform designers seem to feel that the reception (matched filtering) of the received data is nothing more than a conjugate process. This view is satisfactory as far as it goes; however, it is clear that it does not represent a complete solution to the problem.

During the next year, more effort will be concentrated in the area of analog/digital conversion in the widest sense. It is the view of this writer that this area represents a major challenge to digital system designers and that it represents a major bottleneck to the realization of some of the more sophisticated, electronically scanned array systems that have been proposed.

B. A METHOD OF PRECISE BEAM-POSITION CONTROL WITH COARSE PHASE QUANTIZATION

This section describes a simple technique whereby the beam in a phase-scanned array may be precisely positioned without resort to fine quantization. In this technique, there is an inequality between the length of the computer control word and the number of phase-weighted bits in the phase shifters. The bits of the phase shifter are connected to the higher-order bits of the computer control word. The lower-order bits of the control word are discarded.

This technique has applicability to beam-positioning systems where the bits of the computer control word have fixed weights in phase or time delay, and where discrete rather than continuous values of phase shift are available. Hence, it is ideally suited to systems where the phase-control medium is a direct digital phase shifter.*

1. Basic Considerations

Figure 2-94 shows an application of this technique in a phantom-bit beam-steering system. The computer control word α is of sufficient size to uniquely specify the required number of discrete beam positions.

Let N be the number of elements in a linear array, n be the number of control bits, and f be the fraction of the $2/\pi$ (voltage) beamwidth that the desired beam-position step size represents. Then

$$n \approx \log_2 N/f \quad .$$

Let m be the number of phase-shifting bits; then the phase quantization (radians) is defined as Q, where $Q = 2\pi/2^m$. The number of phase-shifting bits will depend on several factors. For instance, the cost of each bit may well vary inversely as the weight of that particular bit. At 1300 Mcps (L-band), phase quantization to, say, 5.625° may be prohibitively expensive if not technically infeasible.

The utility of what has been called "the phantom-bit technique," lies in the fact that one need not quantize phase to an accuracy of $2\pi(f/N)$ radian steps to obtain N/f beam positions. In other words, we make n greater than m. The nature and limitations of this technique can be shown by considering a specific example.

2. Application of Phantom-Bit Technique

Consider the problem of precise control of the beam-pointing angle for a linear array of 64 uniformly driven elements, where the interelement spacing can assume two values: $D = 0.586\lambda$, $D = 0.8\lambda$.

---

* J.L. Allen, et al., "Phased Array Radar Studies, 1 July 1959 to 1 July 1960," Technical Report No. 228 (U), Lincoln Laboratory, M.I.T. (12 August 1960), pp. 81-101, ASTIA 249470, H-335.

For this example, we assume that beam-position control to half of the $2/\pi$ voltage beam-width will be satisfactory.* This control precision would be adequate where the array is to be a transmitting array with a function as an all-sky illuminator (i.e., to illuminate all of a scanned sector with a certain maximum permissible amplitude ripple).

The number of control bits required is 7, which value of n yields a total of 128 beam positions. Figure 2-95 shows the linear array geometry. Half of these 128 positions are in the first quadrant, and half are in the second. Some of the positions will form grating lobes.

We assume phase quantization to $22.5°$. (Hence, m = 4, the weights of the phase-shifting bits being $180°$, $90°$, $45°$ and $22.5°$.)

There is, therefore, an inequality of 3 bits (n − m = b = 3) between the computer control word and the phase-shifter word. Assume the connection of Fig. 2-94 and consider the phase fronts that will be distributed as the beam of the array moves clockwise from the boresight position.

The computer control word (α) which specifies boresight is 0000000. A little thought will show that this control word produces an error-free phase front across the array. The 4-bit phase shifter in each channel will be set to the condition 0000 by the $\times\alpha$ computation and distribution system. The three additional phase-shifting bits are always considered to have the value $0 \times 11.25° + 0 \times 5.625° + 0 \times 2.8125° = 0°$. Hence, for the boresight position, there exists an effective match between the length of the computer word and the phase-shifting word. The total number of error-free pointing positions is a function of b, the measure of inequality between the computer control word and the phase-shifting word (n − m = b), and is simply 2^{n-b}. For the case under consideration, every eighth position is free from pointing error.

What about the intermediate positions (i.e., positions 1-7, 9-15, 17-23, etc.)? We will simply state that, associated with an inequality of b bits, there exist $2^b − 1$ different phase-front error distributions. Error distribution 1 applies to off-boresight positions: 1, 9, 17, 25, etc. Similarly, error distribution 2 applies to positions 2, 10, 18, etc.

The phase fronts distributed for these intermediate positions are not linear. The form of the phase front for any intermediate position can be obtained by subtracting the proper phase-front error functions from the phase front that would have been distributed had there been as many phase bits as computer bits.

The seven phase-front error distributions for the case b = 3 are given in Figs. 2-96(a) through (g). The term LSB_c refers to the least significant bit of the computer control word (i.e., computer word, phase quantization).

Error distributions are certainly of academic interest. However, the real questions are:

    (a) If one attempts to obtain precise control through the medium of the phantom-bit technique, how closely does the beam point to the computer-initiated direction?

    (b) What, if any, effect has the use of this technique on the envelope of the sidelobes of the array function?

3. The Worst Case Pointing Error

Consider the first beam position off-boresight (α = 0000001; i.e., $\alpha = LSB_c$). We assume that this position is the worst case as far as relative percentage pointing error is concerned.

---

* The constant reference to the "$2/\pi$ beamwidth" may be confusing. This particular beamwidth comes from the discussion in Part 2, Ch. I, where Delaney points out that the flat illumination beams out of the RF beam-forming matrix cross over at the $2/\pi$ points in voltage. We are tacitly assuming a system where the transmitter beam is steered through the use of phantom bits, while the receiving system uses the beams from the aforementioned matrix.

4-BIT DIGITAL PHASE SHIFTER

INPUT SIGNAL

180° | 90° | 45° | 22.5° | 11.25° | 5.625° | 2.8125°

PHASE-SHIFTED OUTPUT SIGNAL

n − m = 3

Ka DISTRIBUTION

a REGISTER

7 LINES

FROM CONTROL COMPUTER
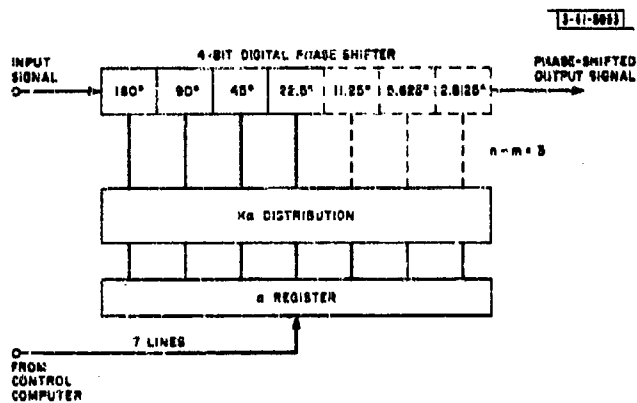
Fig. 2-94. Phantom-bit beam-steering system.

ARRAY BORESIGHT

SECOND QUADRANT

FIRST QUADRANT

φ

θ

ARRAY AXIS
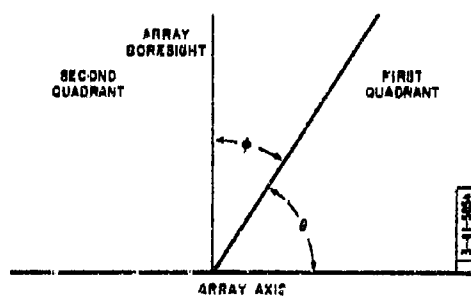
Fig. 2-95. Linear array geometry.

(a) First position off-boresight.
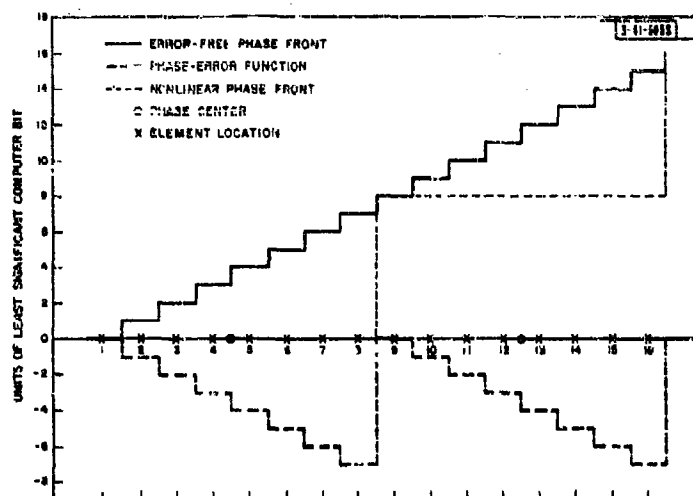
(b) Second position off-boresight.
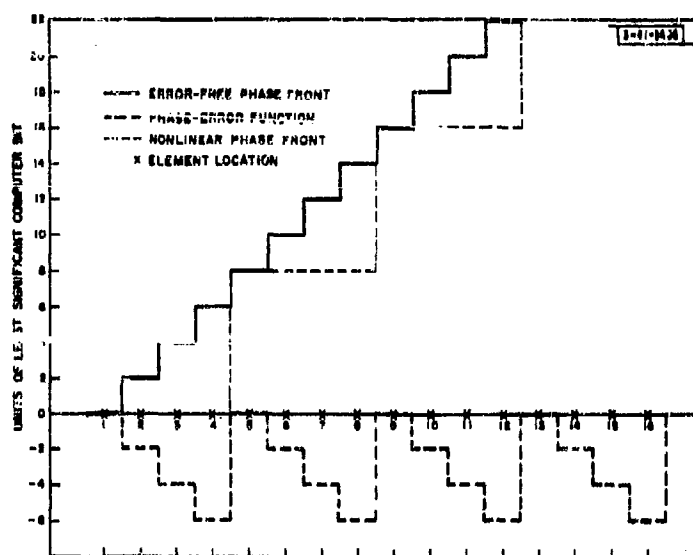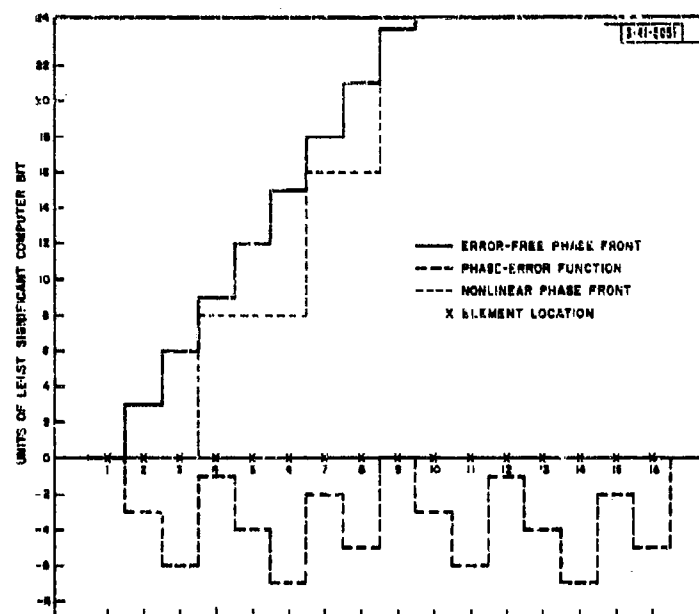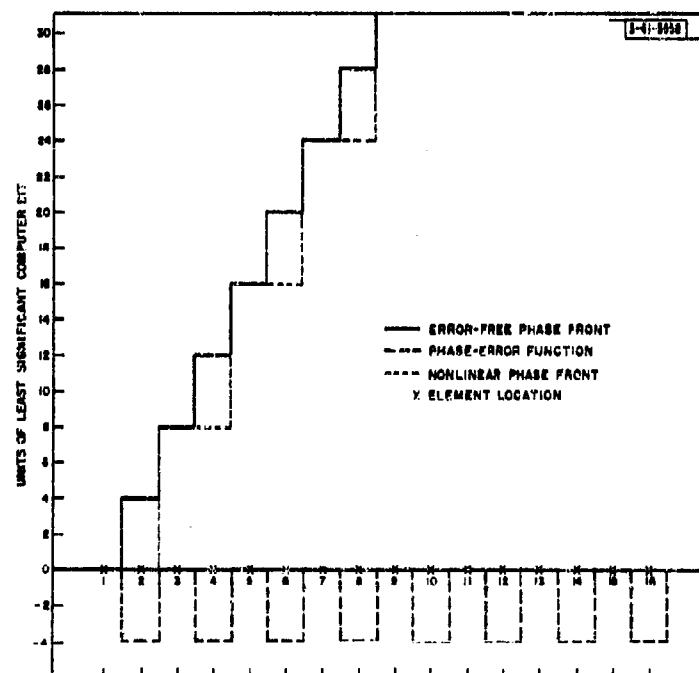
Fig. 2-96. Phantom-bit phase fronts.
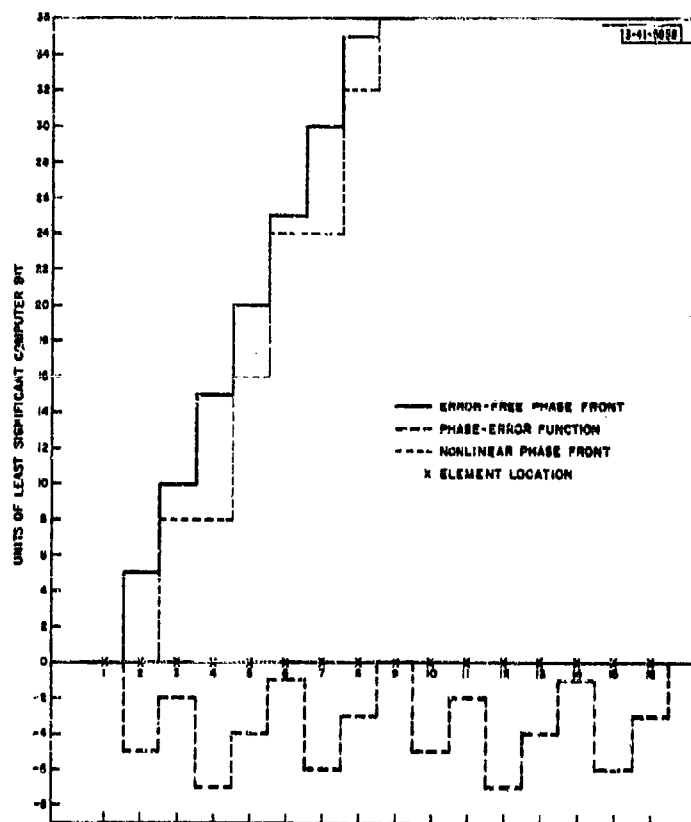
(c) Third position off-boresight.

(d) Fourth position off-boresight.

Fig. 2-96. Continued.

128

(e) Fifth position off-boresight.

Fig. 2-96. Continued.

129
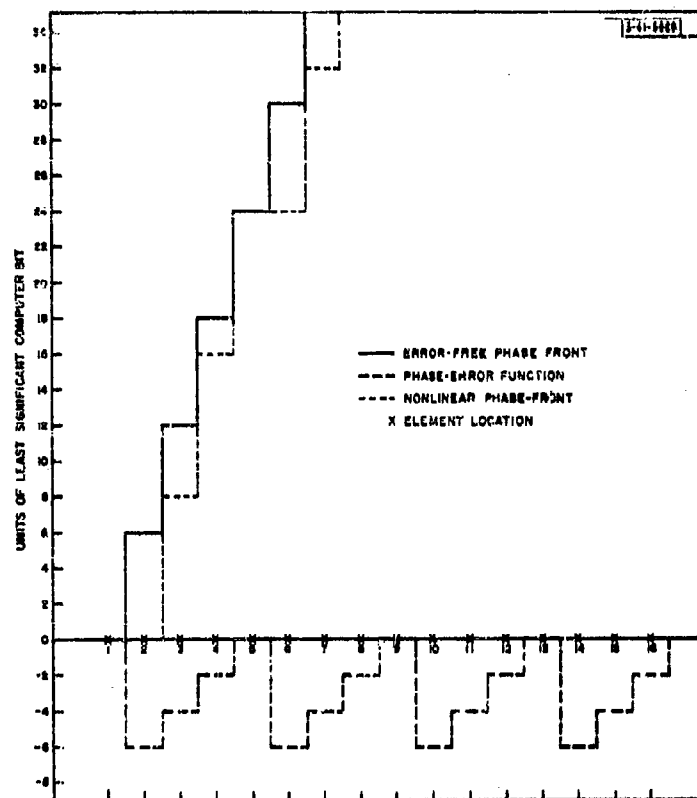
(f) Sixth position off-boresight.
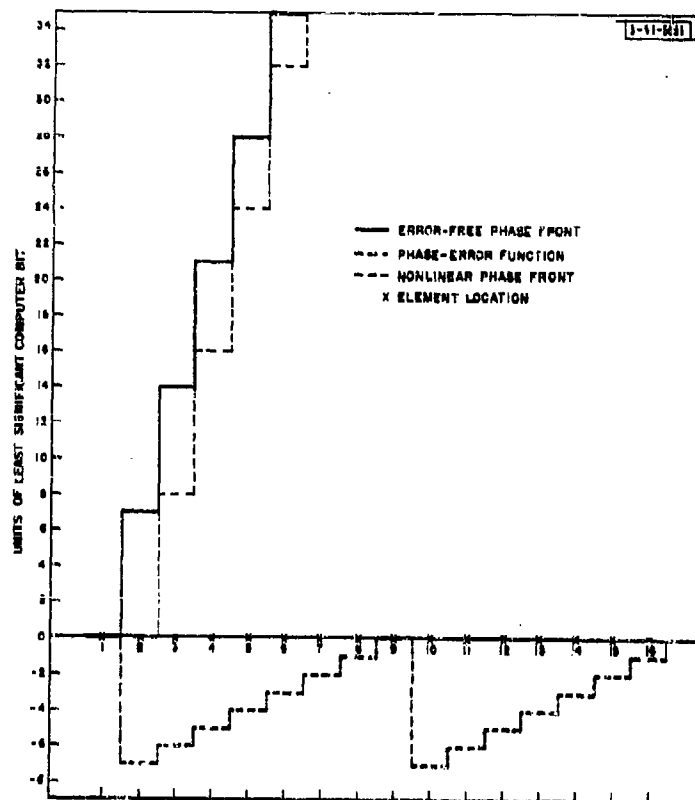
Fig. 2-96. Continued.

(g) Seventh position off-boresight.

Fig. 2-96. Continued.

131

There are three qualitative reasons for this assumption. The phase-front error function for this position represents the largest percentage error in phase. The nonuniform stepped phase front for this position is one of the most systematic in appearance. The number of elements in the subarray set is maximum for this position, and the subarray set has its maximum in an error direction. These three reasons do not in themselves constitute conclusive proof of the worst case. However, the assumption that the first position off-boresight is the worst case has been borne out by the results of a computer program.*

The normalized far-field pattern for the first position off array boresight has the form

$$|E_t| = \left| 1/2^b \left[\frac{\sin 2^b (\psi_1/2)}{\sin (\psi_1/2)} \right] \cdot 2^b/N \left[\frac{\sin N/2^b (\psi_2/2)}{\sin (\psi_2/2)} \right] \right| ,$$

where

$$\psi_1 = \frac{2\pi D}{\lambda} \cos \Theta ,$$

and

$$\psi_2 = 2^b (\frac{2\pi D}{\lambda} \cos \Theta + LSB_c) .$$

In theory, it is perfectly possible to differentiate $|E_t|$ with respect to $\cos \Theta$, find the singular points, and eventually find the angle Θ at which the maximum value of E_t occurs. An exact calculation of beam-pointing angle error by this method is, at best, very involved.

A useful approximate expression for the worst case pointing angle error is derived below.

4. Derivation of Pointing Angle Error Function

Let

        D = element spacing in wavelengths,
        N = number of elements in array,
        φ = angle off array boresight,
        $2^b = \frac{Q}{\alpha} = \frac{\text{Actual Phase Quantization}}{\text{Computer Phase Quantization}}$,
        b = n − m as before.

Then the normalized far-field pattern amplitude of an N-element linear array is E_t, where

$$|E_t| = \left| 1/2^b \left[\frac{\sin 2^b (\psi_1/2)}{\sin (\psi_1/2)} \right] \cdot 2^b/N \left[\frac{\sin N/2^b (\psi_2/2)}{\sin (\psi_2/2)} \right] \right| , \tag{1}$$

and

$$\psi_1 = \frac{2\pi D}{\lambda} \sin \varphi ,$$

$$\psi_2 = 2^b (\frac{2\pi D}{\lambda} \sin \varphi + \alpha) .$$

Equation (1) is of the form

$$E_t = (\frac{\sin mx}{m \sin x})(\frac{\sin ny}{n \sin y}) \tag{2}$$

---

* See Sec. B-5.

where

$$m = 2^b \quad ,$$

$$n = \frac{N}{2^b} \quad ,$$

$$x = \frac{\psi_1}{2} \quad ,$$

$$y = \frac{\psi_1}{2} \quad .$$

We may expand $\sin mx$ as

$$\sin mx \approx mx - \frac{m^3 x^3}{3!} + \frac{m^5 x^5}{5!} - \frac{m^7 x^7}{7!} + \dots \quad ,$$

and $m \sin x$ as

$$m \sin x \approx mx - \frac{mx^3}{3!} + \frac{mx^5}{5!} - \frac{mx^7}{7!} + \dots \quad .$$

We first multiply the numerators and denominators of the two factors of Eq. (2) together and then divide. Neglecting second-order terms, we obtain

$$E_t \approx 1 + x^2 \left(\frac{1 - m^2}{6} \right) + y^2 \left(\frac{1 - n^2}{6} \right) + x^2 y^2 \left(\frac{1 - n^2 - m^2 + m^2 n^2}{36} \right) \quad .$$

We then consider the first three terms alone, take

$$\frac{\partial E_t}{\partial \sin \varphi} \quad ,$$

and set this partial derivative $= 0$.

We obtain

$$\sin \varphi_{max} \approx \frac{(N^2 - 2^{2b}) \lambda \alpha}{2\pi D (1 - N^2)} \quad .$$

Let

$$\nu \approx \frac{2\pi D}{\lambda} \quad .$$

Then the pointing angle error function is

$$\epsilon (\%) \approx \frac{\dfrac{\alpha}{\nu} + \left(\dfrac{N^2 - 2^{2b}}{1 - N^2} \right) \dfrac{\alpha}{\nu}}{\dfrac{\alpha}{\nu}} \times 100\% \quad .$$

$$\therefore \quad \epsilon (\%) \approx \left(\frac{1 - 2^{2b}}{1 - N^2} \right) \times 100\% \quad ,$$

where ϵ is the absolute value of the percentage error in pointing angle for the first position off array boresight.

If N is large, we may make further approximations, and obtain

$$E_t \approx \frac{2^{2b}}{N^2} \times 100\% \quad .$$

133
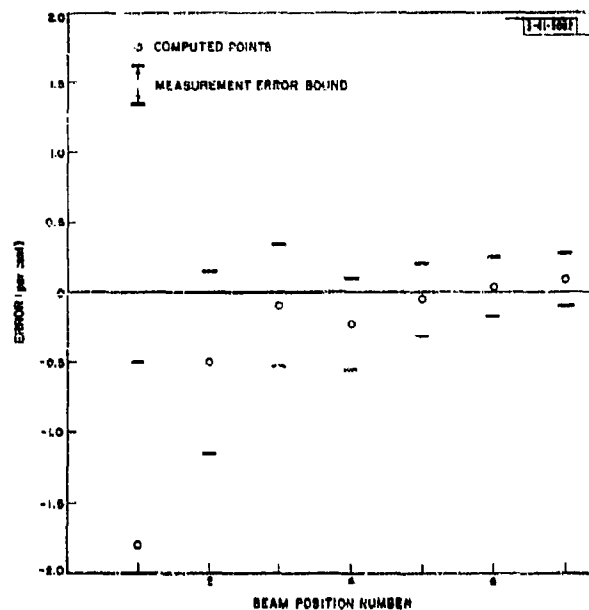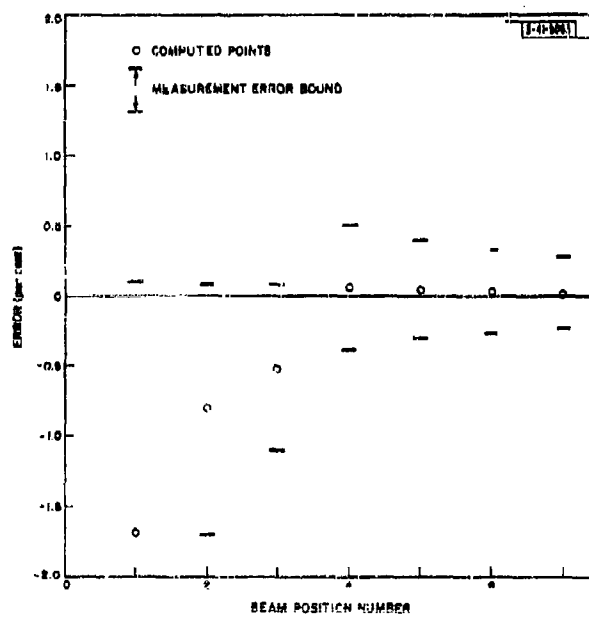
Fig. 2-97. Computer beam-pointing angle error, 64-element array.

(a) D/λ = 0.586.

(b) D/λ = 0.8.

The error can be expressed in other ways, one of the more interesting being in terms of the $2/\pi$ beamwidths of a uniformly illuminated array (bw = λ/ND).

$$E_t \approx \frac{\alpha 2^{2b}}{2\pi N} \times 100\% \quad ,$$

where E_t is the worst case error expressed as a percentage of the $2/\pi$ beamwidth.

5. Computer Prediction

A computer program, written by W. C. Danforth, Jr. of Group 315, was used to calculate the far-field patterns of a 64-element array composed of uniformly illuminated isotropic elements. The program was run for two element spacings (D = 0.586λ and D = 0.8λ) for the seven different error distributions (b = 3) for the first seven positions off-boresight.

The computed pointing angles for the phantom-bit, nonlinear phase case were then compared to the pointing angles produced by an error-free, uniform, phase-front distribution. The percentage error between the two sets of seven pointing angles is plotted in Figs. 2-97(a) and (b). It is interesting to contrast the worst case pointing angle error predicted by the approximate expression to the computer-predicted pointing error.

The computer-calculated results for the first position off-boresight are given in Table 2-VII. The approximate expression does a fair job of predicting the beam-pointing errors in this case.

TABLE 2-VII POINTING ANGLE ERROR		
	D = 0.586λ (per cent)	D = 0.8λ (per cent)
Approximate expression	1.54	1.54
Computed value	1.8 ± 1.31	1.69 ± 1.79

Returning to Figs. 2-97(a) and (b), we see that a smooth curve may be drawn through the error bound points. (The large error bound is a function of the angle step size in the computer program, 0.01°.) This error envelope contains the true values of the pointing angle errors. As regards the actual shape of the error curve, we might well be able to fit anything from a straight line to a decaying exponential into the error envelope.

One statement may be made, however. The beam-pointing error is a strong function of beam position off-boresight. Positions 1 to 7 contain the maximum relative pointing error. The truth of this statement appears when one considers that the error functions are periodic with period $2^b - 1$ and that they are fixed in amplitude. As the beam moves clockwise from boresight, the error functions modulate the normal phase fronts less strongly.

6. Sidelobe Structure

The effect of nonuniform phase fronts on the envelope of the array sidelobes is of considerable importance. Allen[*] has studied the effect of stepped phase, where the steps are either uniform

---

[*] J. L. Allen, et al., op. cit., pp. 207-216.

or nonuniform, in height and width. He derives an expression for the levels of the high sidelobes that occur as the beam is moved off-boresight. This expression is approximate and states that the jth near-in sidelobes have an amplitude, down $20 \log_{10} jn$(db), from the main beam, and that they approach (in our notation) $20 \log_{10} 2/\alpha$, as an asymptote.

A relatively coarse antenna pattern was run with the same nonlinear phase fronts used in the fine structure pointing error computations. This was done for two reasons. A qualitative notion of the structure of the array pattern and a check on the utility of the sidelobe level formula were desired.

Figures 2-98(a) through (p) present a collection of computed antenna patterns for an array of 64 uniformly illuminated, uniformly spaced, isotropic elements. The horizontal point spacing is 0.45°. The quantization in angle in the computer program causes the maximum of the beam to be slightly displaced vertically downward from its correct position. The decimal figure at the top of each pattern gives the correction in db needed to place the maximum of the beam at the proper level.

The two heavy vertical lines at $+45°$ and $-45°$ show the approximate field of view of individual antenna elements that might be used in the array. It should be remembered, of course, that elements with a narrower field of view might be used for array spacing, $D/\lambda = 0.8$. The phrase "0 shifts" or "2 shifts" refers to the value of b for that particular pattern (i.e., for "0 shifts" read "b = 0," etc.). The patterns for $D/\lambda = 0.8$ are alternated with those for $D = 0.586\lambda$ for the purpose of easy comparison.

It is difficult to make any meaningful general statements about the patterns. All seven nonlinear phase fronts give rise to one or more high sidelobes either side of boresight. The height of these sidelobes is generally below -20 db with respect to the main beam. The sidelobe levels seem to follow the $(20 \log_{10} jn)$ rule fairly well when the phase steps are of equal width. However, there are certainly cases ($\alpha \sim 3$, $D/\lambda = 0.586$) where near-in sidelobes are not the highest sidelobes within the field of view.

The high sidelobes caused by the nonlinear phase front control will degrade the over-all system noise temperature, especially if they point at the ground. In some systems, they might also cause deghosting problems, especially if the phantom-bit pointing system controls both transmitting and receiving arrays.

7. Conclusions

This brief investigation has by no means exhausted the possibilities in this technique, or in its many possible variations.

Rather than simply discard the lower-order control bits, one might well implement some sort of a round-off technique, where an effort would be made to minimize the integrated squared error between the distributed nonlinear phase front and a true stepped phase front.

The nonequivalence beam-steering technique can be applied to many different array systems. It may be profitably employed wherever phase-shifter fabrication problems have heretofore prevented precise control over the fine beam position in electronically scanned arrays. It is most useful in the control of large arrays in surveillance systems, where the array beamwidth is small enough to require precise control, and where a small, predictable, pointing error is tolerable.

C. TRANSISTORIZED TIME-VARIABLE GAIN CONTROL

The function of the transistorized time-variable gain control (TTVGC) is to accurately compensate for the change in IF signal level that would be observed on a target of constant cross

Fig. 2-98(a-p). Computed antenna patterns.
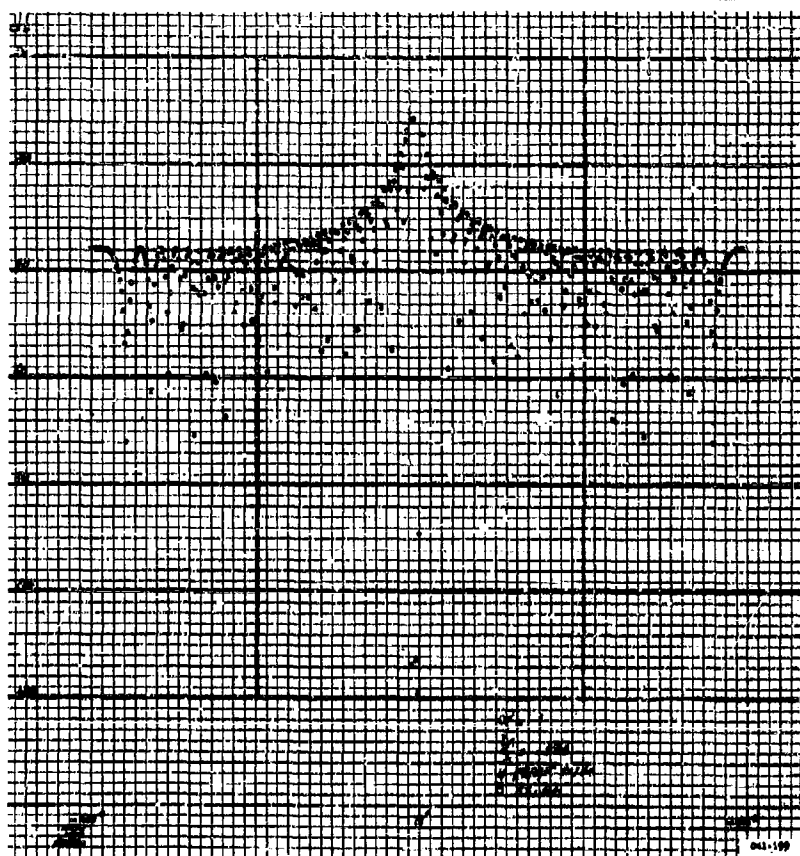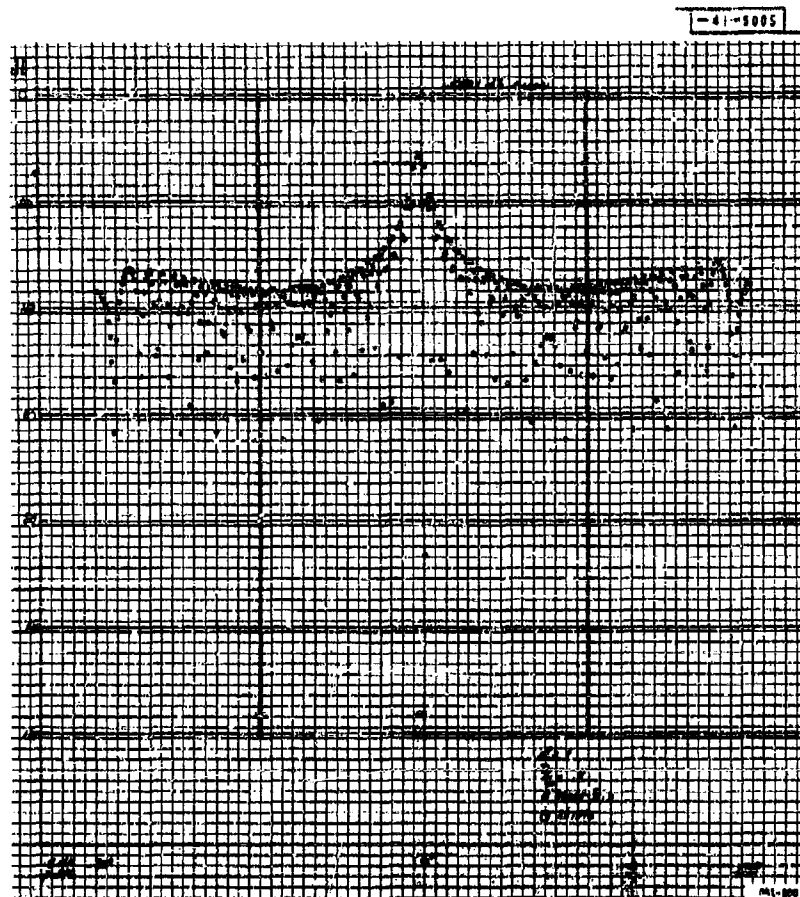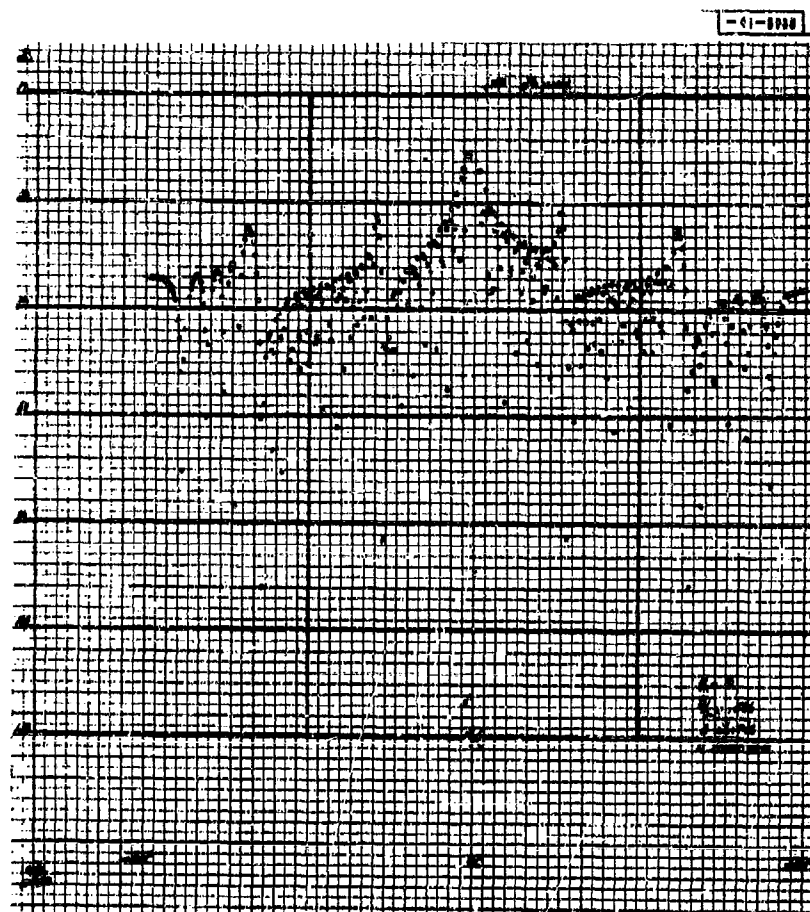
Fig. 2-98(b).

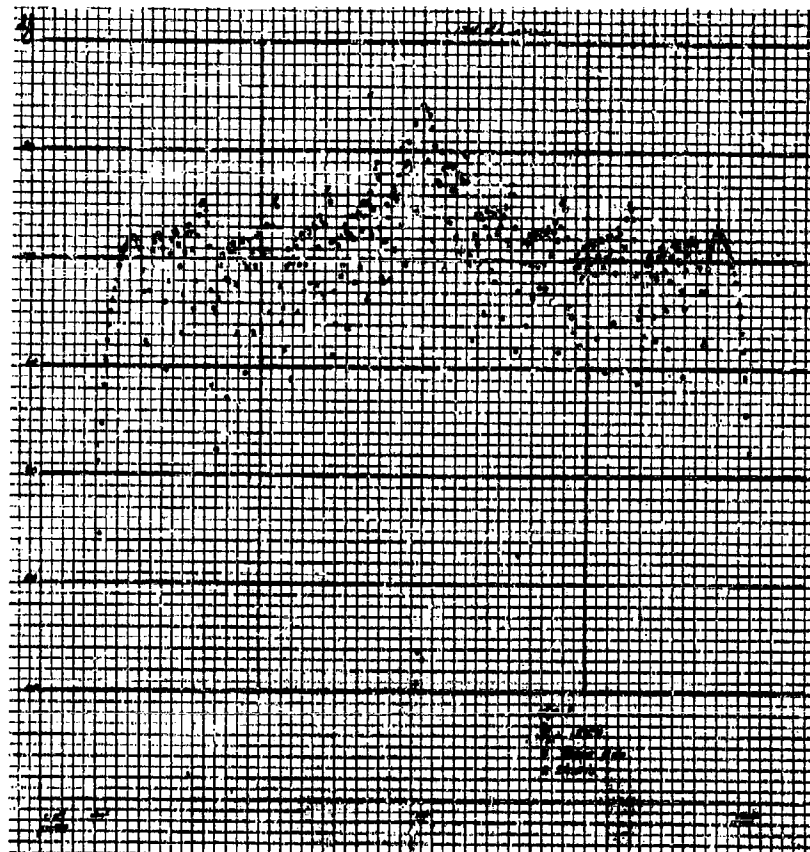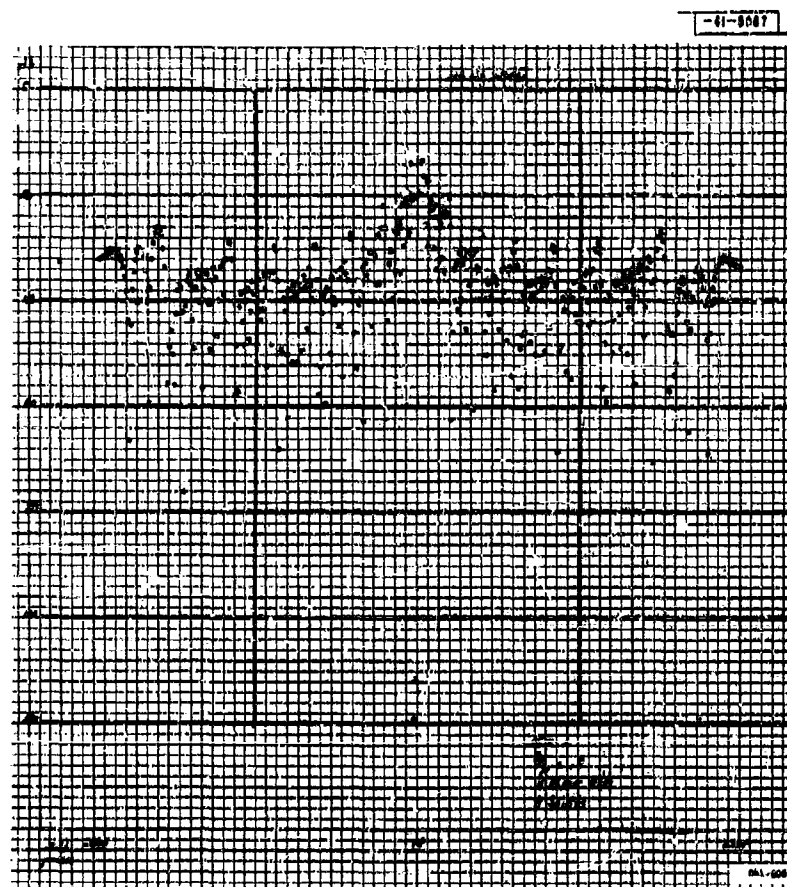138

Fig. 2-98(c).

Fig. 2-98(d).

Fig. 2-98(e).
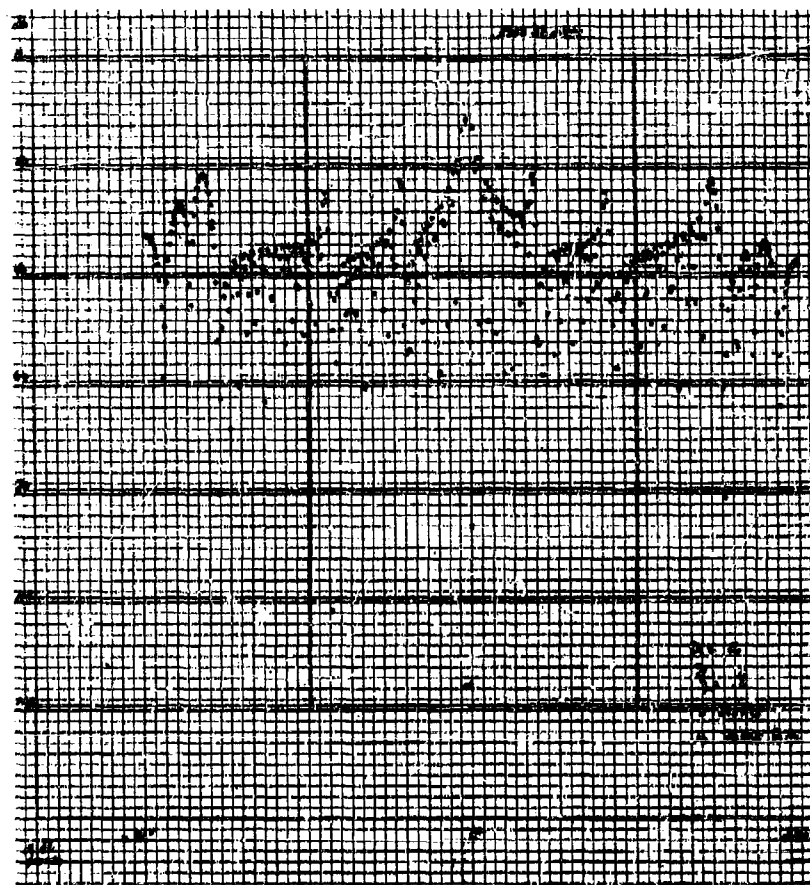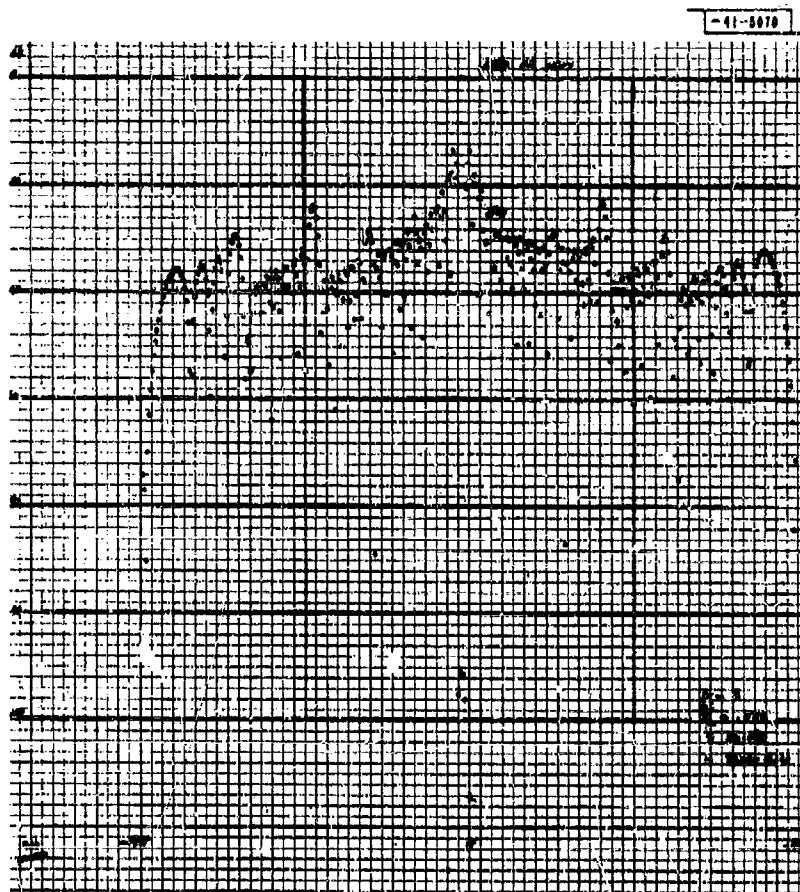
Fig. 2-98(f).

Fig. 2-96(g).
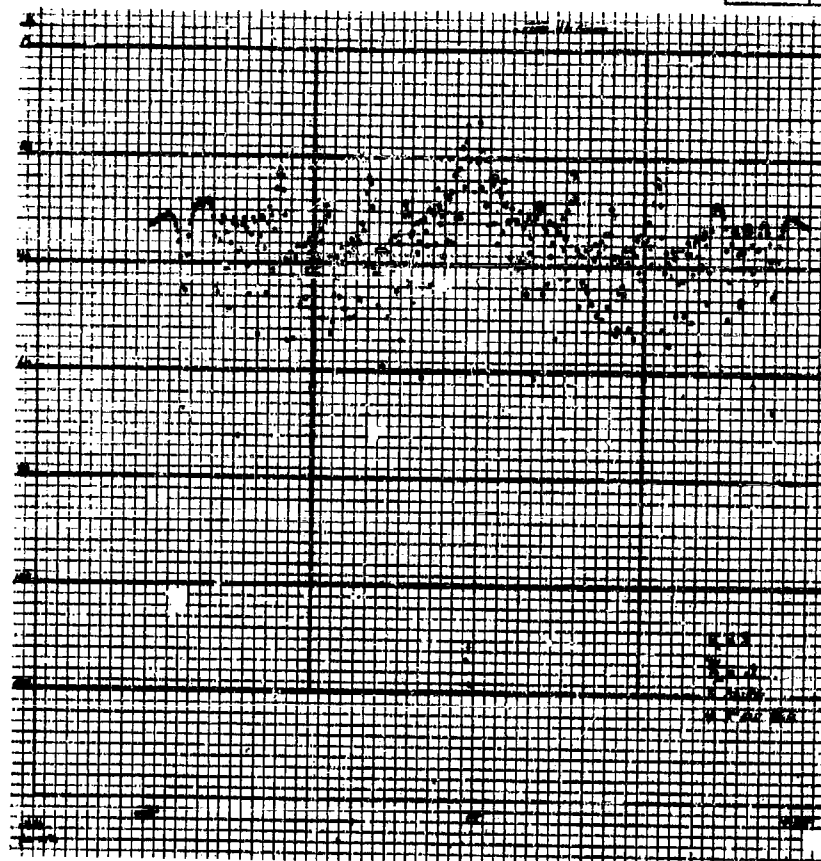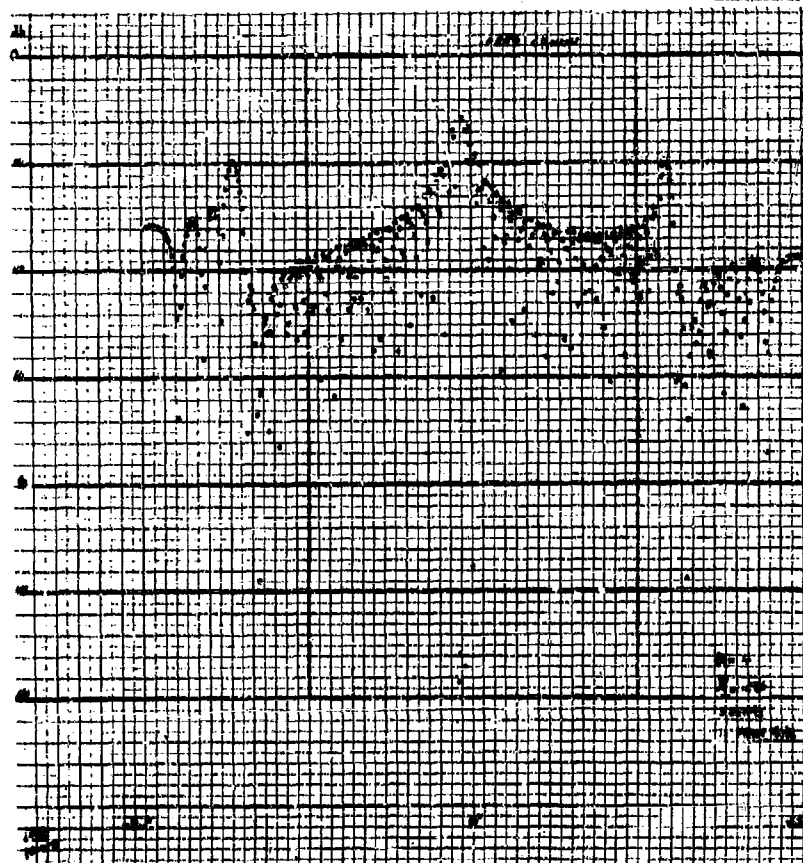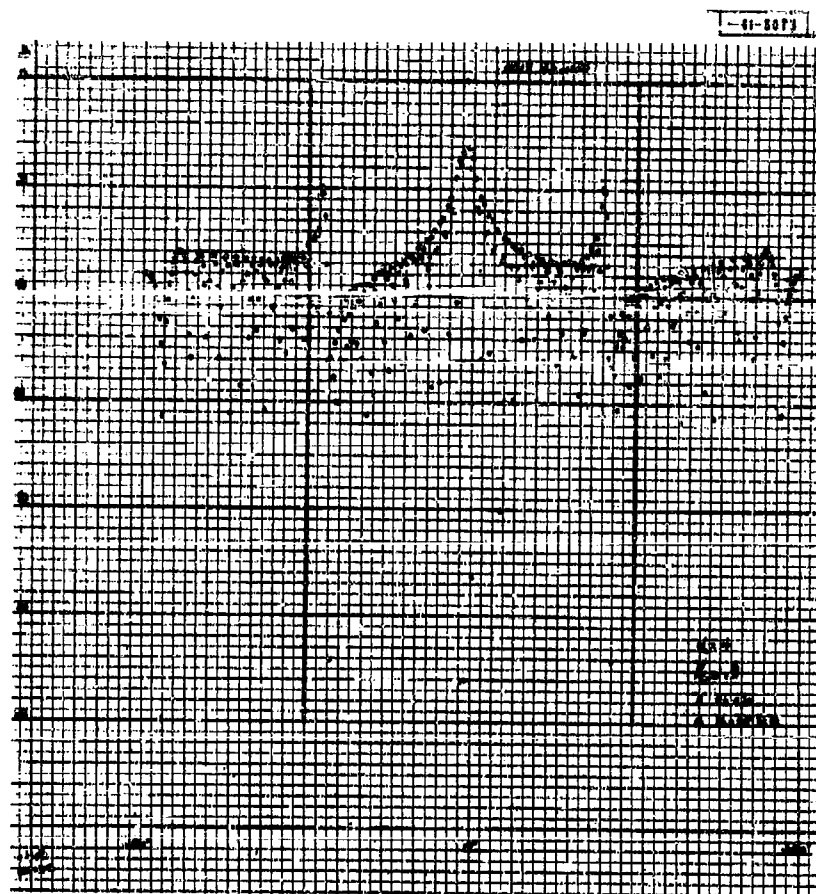
Fig. 2-98(h).

Fig. 2-98(i).
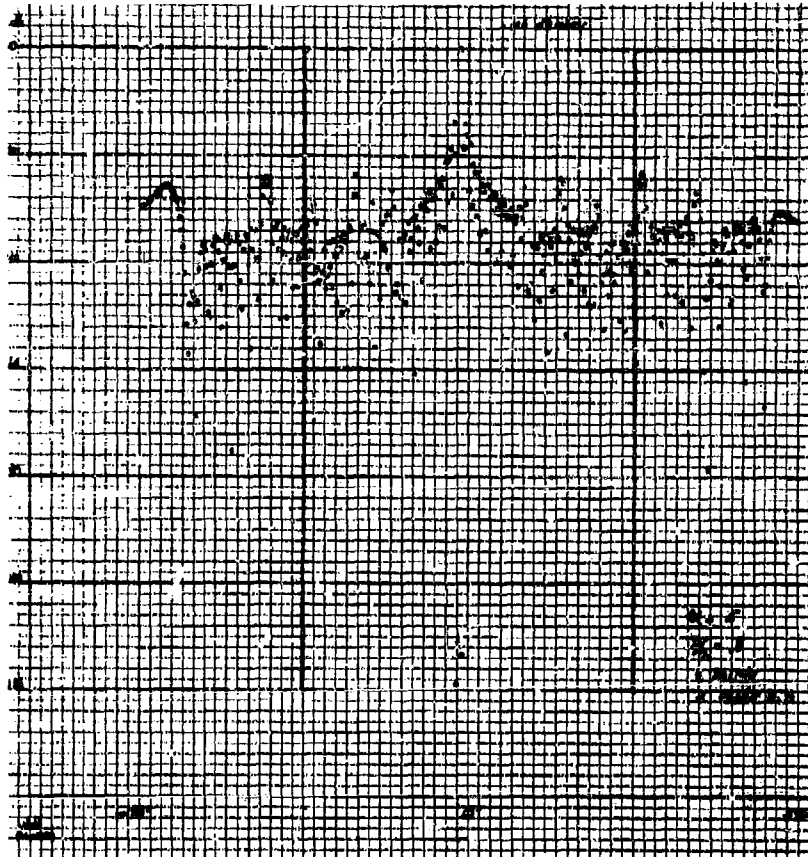
Fig. 2-98(j).
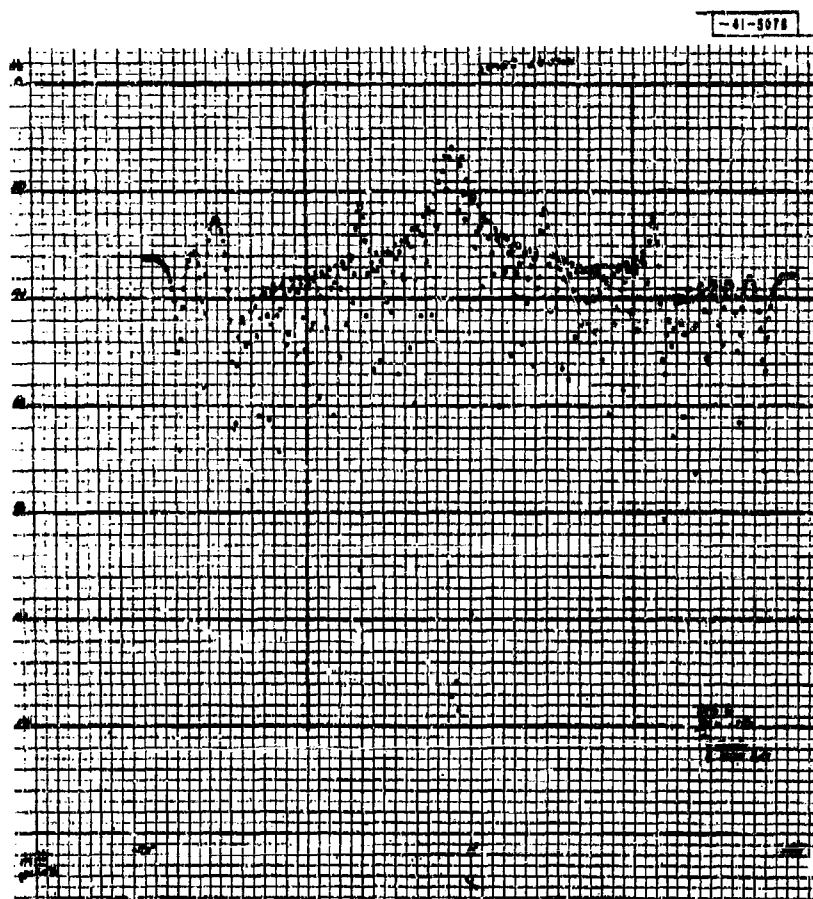
Fig. 2-98(k).
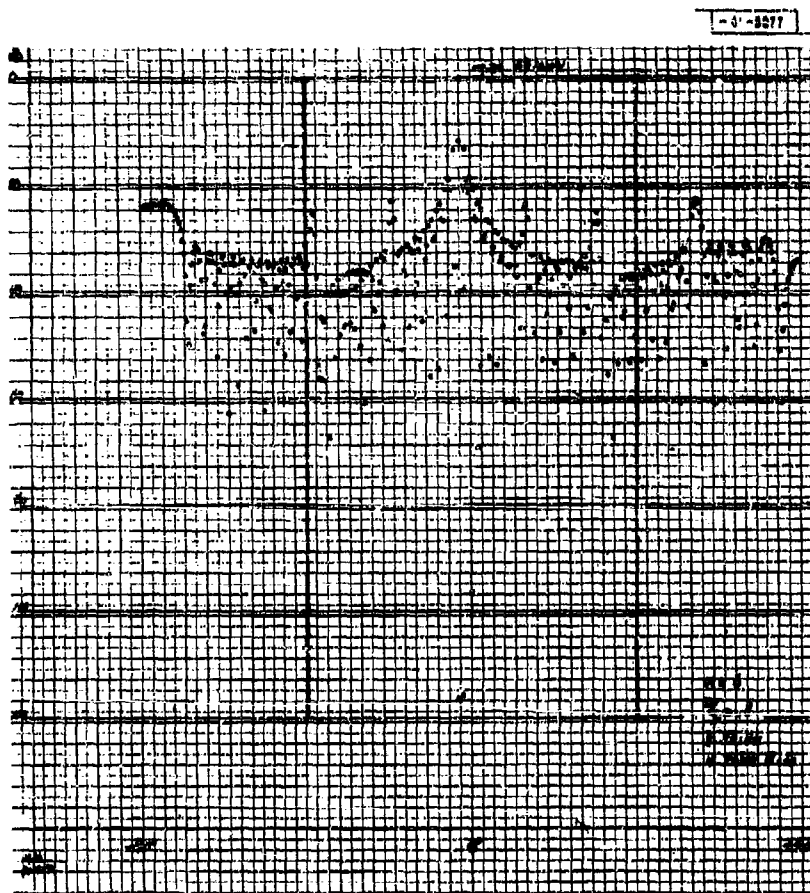
Fig. 2-98(I).
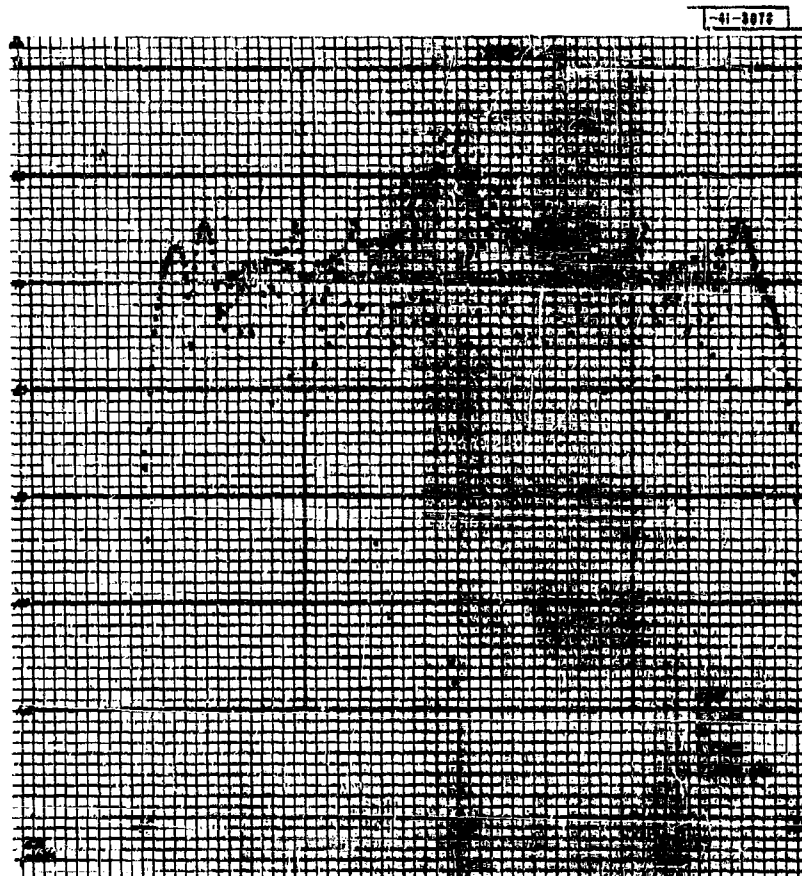
Fig. 2-98(m).

Fig. 2-98(n).

Fig. 2-98(c).
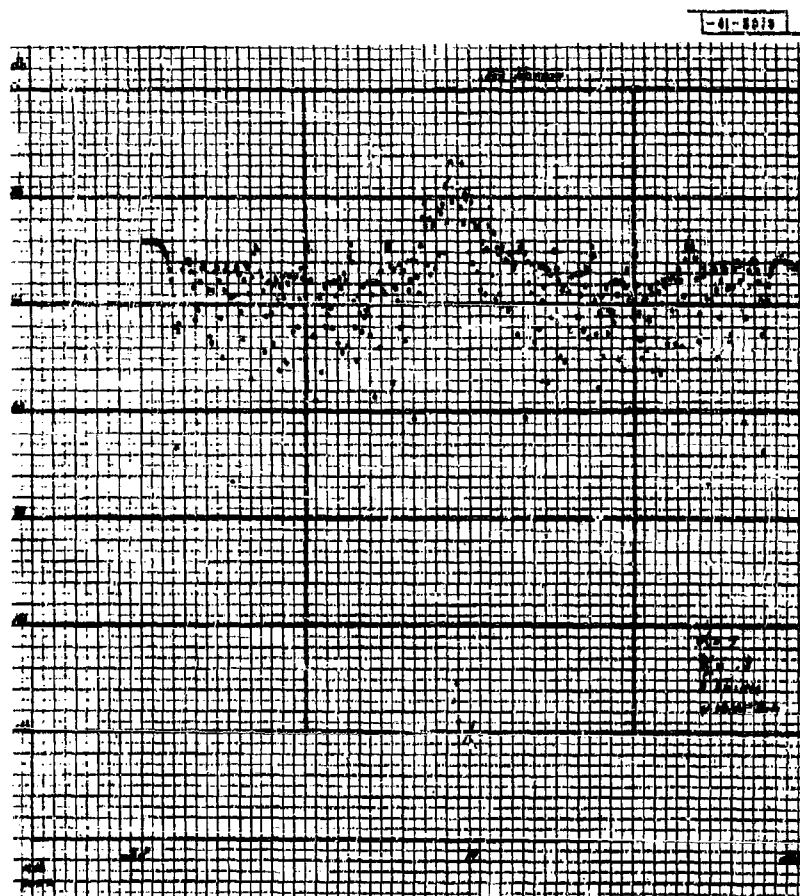
Fig. 2-98(p).

section at varying ranges. With the TTVGC in operation, a signal measurement made at IF is truly indicative of target cross section (provided the receiver is not saturated).

1. Introduction and Basic Design

The gross signal variation at any point in the IF consists in variations due to changes in instantaneous target cross section, as well as a predictable signal power variation as the fourth power of range (signal voltage as the second power of range).

The design of the TTVGC is straightforward. It consists of two series-connected linear attenuators with associated buffer amplifiers. A block diagram of the TTVGC is shown in Fig. 2-99; Fig. 2-100 is a circuit schematic of the device.

The open-circuit driving voltage to the TTVGC is of the form

$$E_{oc} = \frac{kR_{max}^2}{R^2}$$

where R_{max} is some maximum range and k is the open-circuit source voltage when $R = R_{max}$.

For perfect range compensation, the series resistance of each attenuator should follow the relation

$$r_1 = \left(\frac{50\,R_{max}}{B^{1/2}R} - 100\right) \text{ (ohms)}$$

where B is a minimum attenuation factor.

$$B = \frac{E_{out}}{k} \quad (R = R_{max})$$

The actual resistance of the attenuator is always positive and can be made equal to

$$r_2 = \frac{50\,R_{max}}{B^{1/2}R}$$

Power limitations in the 2N502 determine the minimum value of series resistance. Duty cycle considerations help a little and allow a minimum series resistance of about 180 ohms. At $R = R_{max}$, the loss through the TTVGC is about 30 db, increasing to about 100 db at $R = 1/50\,R_{max}$. The worst case for range compensation occurs at $R = R_{max}$, where the compensation error amounts to about +0.4 db for a minimum resistance value of 180 ohms.

Two points have not been considered. The first concerns the effect of the TTVGC on system signal-to-noise ratios. The double emitter follower — video amplifier combination has an input impedance of over 100 kilohms, a gain of about 20 db, and a noise figure of 8 db. Two of these amplifiers in combination with the series attenuators degrade the system signal-to-noise ratio less than 1.5 db at $R = 1/50\,R_{max}$.

The use of the TTVGC by no means solves the problem of keeping the system from saturating on strong targets. Assume a system dynamic range of 75 db (proposed modifications on the existing system). This dynamic range is measured up to the input to the TTVGC. It is clear that a range variation of 50 to 1 can absorb almost the entire dynamic range of the system. The TTVGC does not, therefore, increase the dynamic range of the system per se. Rather, it should be used in combination with a series of perhaps two or three pads in the input to each receiver RF amplifier. These pads would, of course, degrade the system signal-to-noise ratio in exchange for this increased dynamic range.
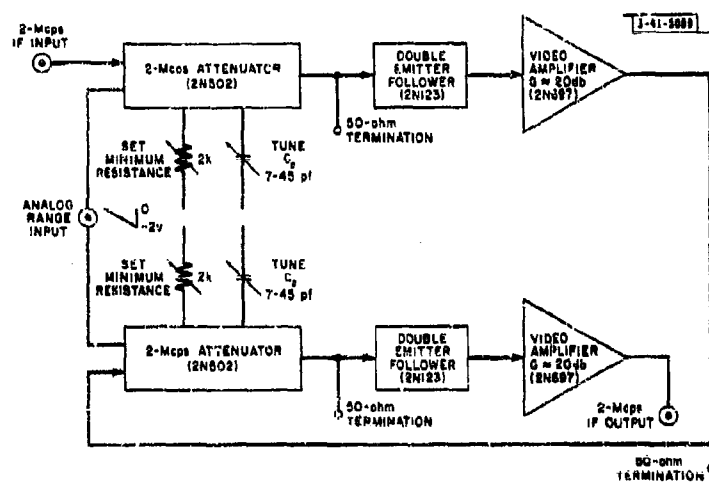
Fig. 2-99. Block diagram of transistorized time-variable gain control.
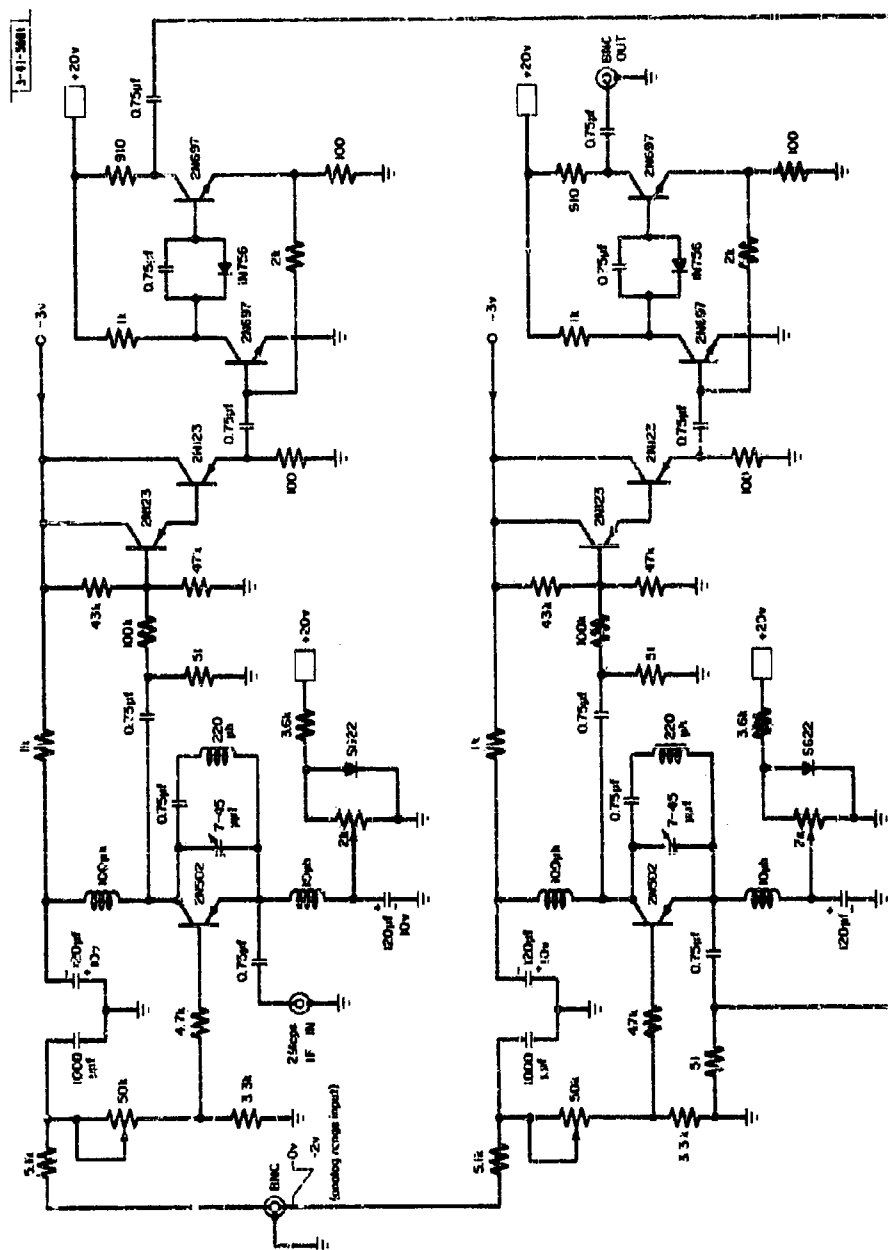
Fig. 2-10f. Circuit schematic of transistorized time-variable gain control.

The ideal time-variable gain control would be operated at RF frequency in the low-impedance input line to the receiver. Conductivity modulation of a tuned varactor diode for a purely resistive change in series-impedance might well be employed.

D. HIGH-SPEED PULSE-TRAIN SYNTHESIZER

This section describes a flexible, programmable, video-waveform synthesizer. This generator is capable of generating a great variety of pulse wave trains under external digital computer control. The pertinent characteristics of the device are listed below.

Maximum burst length	10 µsec (expandable)
Minimum pulse width	0.1 µsec
Output pulse rise time	<5 nsec (10% to 90%)
Output pulse fall time	<5 nsec (10% to 90%)
Coding	NRZ*
Amplitude tapers	Cosine or triangular
BRF†	Up to 83 kcps

The utility and need for the generator is considered in Sec. D-1. Succeeding parts of this section briefly outline the method of waveform synthesis and some of the problems involved in realization of the device.

1. Introduction

In the past, most radar systems have been used to obtain a limited amount of information about the targets observed. Typically, a short pulse of 1 to 100 µsec, of sufficient energy to detect the target and measure its range, was transmitted. It is not our aim to review the various changes, additions and improvements that have taken place in radar systems since World War II. However, one change is important. Radar systems are being required to obtain more information on target parameters, to a greater precision and in more difficult target situations than ever before. Much attention has been focused on the subject of object resolution and parameter estimation as it affects the choice of waveforms to be transmitted in a particular situation.[‡]

Most system specifications require simultaneous measurement of target radial velocity and target range. Two signals come to mind when one considers the simultaneous measurement of range and velocity. The first of these is the so-called "chirp" or pulse-compression scheme which involves either linear or nonlinear frequency modulation in the transmitted envelope.[§¶]

The second useful waveform consists of a train of pulses of appropriate spacing and width.[‡] With proper choice of four parameters, a pulse train can be used to measure range and radial velocity. These four parameters are pulse width, pulse spacing, pulse train length (number of pulses) and amplitude taper over the length of the pulse train. (Pulse-to-pulse phase shifts and jittered prf's are useful in certain situations but are not considered here.)

---

* Non-return to zero.

† Burst repetition frequency.

‡ E.N. Fowle, E.J. Kelly and J.A. Sheehan, "Radar System Performance in a Dense-Target Environment," 1961 IRE International Convention Record, Part 4, pp. 136-145.

§ E.L. Key, E.N. Fowle and R.D. Haggarty, "A Method of Designing Signals of Large Time-Bandwidth Product," 1961 IRE International Convention Record, Part 4, pp. 146-154.

¶ C.E. Cook, "Pulse Compression -- Key to More Efficient Radar Transmission," Proc. IRE 48, 310 (1960).

In the interest of brevity, we will merely state a few of the constraints on these four parameters. (The reader is referred to the work of Resnick[*] and Manasse[†‡] for further discussion of the effects of signal parameter variations.)

Call the width of the individual pulses t_1, and the spacing between pulses t_2. Let d_u be the desired range resolution. Then

$$t_1 < \frac{2d_u}{c} \quad ,$$

and

$$t_2 > t_1 \quad .$$

Consider the first ambiguity in velocity, which ambiguity occurs at V_{a1}:

$$V_{a1} = \frac{c}{2t_2 f} > V_{max} \quad .$$

hence,

$$t_2 < \frac{c}{2V_{max} f} \quad .$$

Consider the effect of overlapping ground clutter. Assume the ground clutter to have an extent R_o in range. The target minimum range is R_{min}. The constraint on the burst length T is

$$T < \frac{2(R_{min} - R_o)}{c} \quad .$$

The number of pulses in a uniform burst is n, where

$$n = \frac{(T + t_2 - t_1)}{t_2} \quad .$$

The pulse-train generator should have provision for implementing an amplitude taper over all or part of the burst. There are many different possible tapers, including linear, cosine, cosine^2, triangular, Taylor, etc. In general, an amplitude taper has the effect of reducing the sidelobe levels in the waveform ambiguity function at the expense of a slightly fatter main response. The amplitude taper in the high-speed pulse-train synthesizer is implemented by changing the gain of the Hewlett-Packard distributed amplifiers, which act as buffer-drivers between the high-speed flip-flop and the low-level bridge modulators.

2. System Description

Figure 2-104 is a system block diagram for the pulse-train modulator programmer. The following brief description should be referenced to this figure. A control computer is assumed to have supplied the modulator programmer with a 5-bit control word, which control word specifies one of 32 possible wave trains. The code-word/wave-train format is under control of the "patchboard circuit" which is simply a pluggable patch panel.

* J.B. Resnick, "A Class of Pulse-Train Waveforms Suitable for Use in a Multiple-Target Environment," to be published.

† R. Manasse, "Range and Velocity Accuracy from Radar Measurements," Group Report 312-26 [U], Lincoln Laboratory, M.I.T. (3 February 1955), ASTIA 236236, H-78.

‡ R. Manasse, "Summary of Maximum Theoretical Accuracy of Radar Measurements," Technical Report No. 2 [U], MITRE Corporation, Bedford, Massachusetts (1 April 1960).

Fig. 2-101. High-speed pulse-train synthesizer.

Assume the control flip-flop to be "on." The next burst repetition trigger (BRF) pulse from the BRF generator will pass through the fast gate. (A "fast gate" is a simple transistor AND circuit with very small delay time, say, 0.015 μsec and fast rise time, say, 0.005 μsec.) The 1-μsec pulse is sent immediately to the high-level modulators in the transmitter final amplifier. The overlap delay allows for the rise time of the modulator. This same pulse also starts the taper control which controls the gain of the video amplifiers (during the pulse train) according to a preset specification. The 1-μsec pulse also passes down the delay line (terminated in its characteristic impedance, Z_0 = 250 ohms). A high-impedance pulse-pickoff amplifier (Fig. 2-102) is connected to each of the taps of the delay line. These amplifiers are required for several reasons. The so-called "taps" on the delay line are simply wires soldered between sections of the line. Any load, whether resistive or reactive, will upset the proper operation of the line. The input impedance of the pickoff amplifiers is over 100 kilohms, and the signal pickoff has negligible effect on tap-to-tap phase shift.

The noninfinite delay to-rise-time ratio of the lumped-parameter delay line means that the pulse rise time is different at all the 100 taps. The delay-to-rise-time ratio of the delay line used is about 75.

The 2N697 video-amplifier doublet has a gain of about 20 db and a 3-db bandwidth of approximately 5 Mcps. This high-gain amplifier, together with the 1N625 limiter pair, effectively normalizes the rise time of the blocking oscillator trigger signal to about 0.1 μsec.

The blocking oscillator section of the pickoff amplifier package produces a nominal 0.5-μsec pulse with a rise time of 5 mμsec into a 1-kilohm, 50-pf load. The field of one hundred 0.5-μsec pulses is gated under control of the computer control word and the patch panel wiring. The encoded set of triggering pulses for the high-speed flip-flop are differentiated by passing the fast-rise 0.5-μsec pulses through a high-pass filter.

The coding of the triggering pulses is NRZ in that they are applied to the complement input of the flip-flop. The main advantage of this type of coding is that it minimizes the number of fast gate circuits that computer-word, decoding-matrix, buffer amplifiers need drive. Figure 2-103(a) shows one possible set of flip-flop triggering pulses, Fig. 2-103(b) shows the resulting video waveform, and Fig. 2-103(c) demonstrates how long, multiple-burst wave trains are formed through an appropriate choice of burst repetition frequency.

The system will track for small changes in the level of the 1-μsec BRF pulse. The leading edge of the pulse train may shift slightly with respect to t_0, but the pulse train will hang together. Amplitude regulation of the BRF pulse may be employed in systems where absolute burst-to-burst registration is required.

Relative registration tests have shown that two buffer-amplifier – blocking oscillator units will track to within 5 mμsec for constant input pulse level. Part of this jitter was probably due to oscilloscope synchronizing difficulties.

The high-speed flip-flop deserves some comment. The schematic diagram of the flip-flop is given in Fig. 2-104, which shows the flip-flop complete with all gating circuits and with its cascode output amplifiers. The configuration has a 200-ohm output impedance in either state and a waveform rise and fall time of 5 mμsec. Figure 2-105 shows some flip-flop performance photographs taken on a Hewlett-Packard 185B sampling oscilloscope. It is clear that a simplified version of the same basic internal flip-flop could be employed where system requirements are less severe.

159
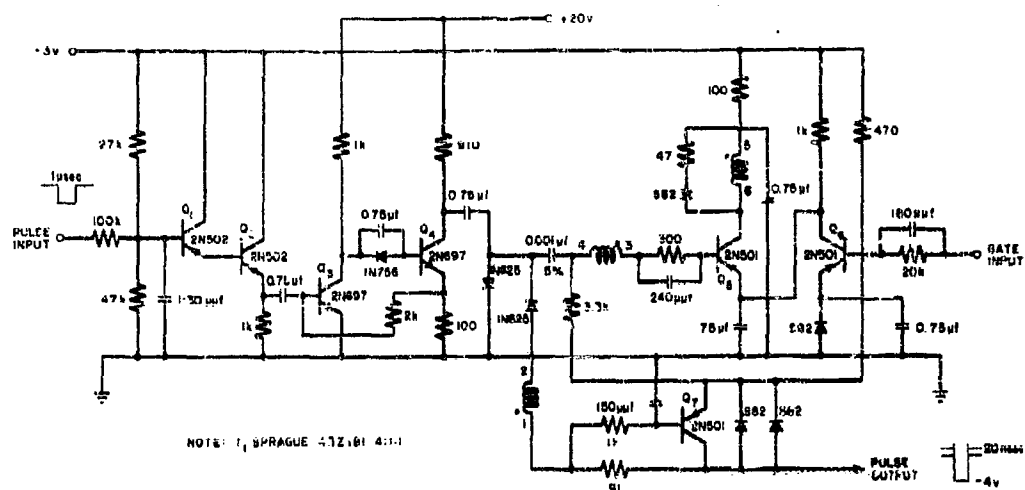
Fig. 2-102. Delay-line pickoff pulse generator.
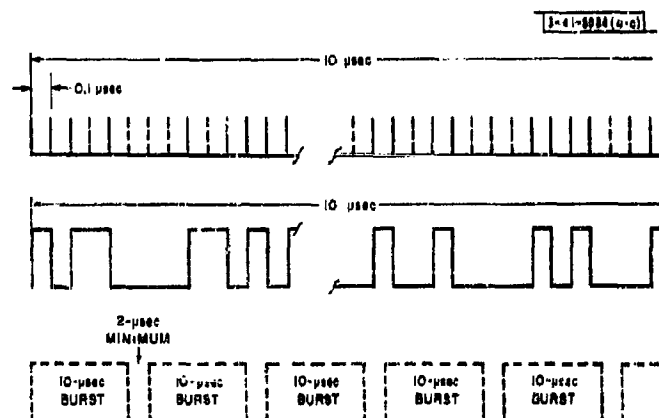
Fig. 2-103. Pulse-burst coding.

Fig. 2-104. Schematic diagram of 20-Mcps flip-flop.
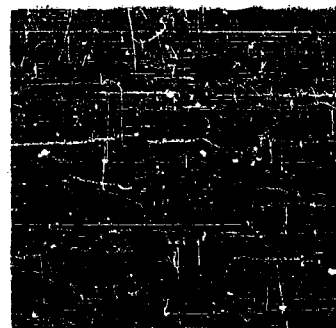
(a) Upper trace: "1" side, output
Lower trace: trigger pulses
Vertical scale: 1 v/cm
Horizontal scale: 50 mμsec/cm

(b) Upper trace: "1" side, output
Lower trace: 50-Mcps sine-wave
trigger input
V_U: 1 v/cm, H_U: 20 mμsec/cm
V_ℓ: 2 v/cm, H_ℓ: 20 mμsec/cm

(c) Upper trace: "1" side, flip-flop
rise time
Lower trace: trigger pulse
V_U: 0.5 v/cm, H_U: 10 mμsec/cm
V_ℓ: 2 v/cm, H_ℓ: 10 mμsec/cm

(d) Upper trace: "1" side, flip-flop
fall time
Lower trace: trigger pulse
V_U: 0.5 v/cm, H_U: 10 mμsec/cm
V_ℓ: 2 v/cm, H_ℓ: 10 mμsec/cm

Fig. 2-105. High-speed flip-flop performance photographs.

162

CHAPTER VIII
TEST EQUIPMENT

SUMMARY   S. Spoerri

This chapter deals with the various types of special-purpose test equipment which were
developed to simplify the testing and monitoring of phased array systems and their components.
The test equipment consists of four basic test units: an IF sampler, an automatic phase meter,
a coherent frequency synthesizer and an automatic data printer. One combination of these test
units, used to monitor the phase and amplitude stability of eight receiver strips, is described
as a test system. This is followed by a more detailed description of the test units themselves,
as well as the auxiliary equipment used in conjunction with them.

A. INTRODUCTION

The test equipment concept and the basic types of test equipment were discussed in a pre-
vious report.* Since that time, the prototype test equipment has been improved and rebuilt in
more permanent form.

This chapter describes the test equipment in its present form. The individual test units
may be used singly or in combination, depending on the test requirements. One combination.
the test system which is used to monitor the phase and amplitude stability of eight receiver
strips, is described first. This is followed by a detailed description of the individual test units.
Two of these, the IF sampler and the automatic phase meter, were built from special-purpose
printed-circuit boards which were designed for mixed (part analog, part digital) system applica-
tions. Accordingly, one section is devoted to a brief description of these boards and their more
important characteristics. The last section covers the auxiliary equipment used in conjunction
with the basic test units.

B. DESCRIPTION OF TEST SYSTEM

The test system described in this section consists of four basic test units[†] interconnected
in a particular way. This arrangement is used to monitor the outputs of eight receiver strips,
or portions thereof. The amplitude and relative phase shift of each channel output are recorded
as a function of time. Figure 2-106 shows the test units that make up the test system.

A block diagram of the test system is shown in Fig. 2-107. The coherent frequency synthe-
sizer supplies a set of test and local oscillator signals to the receiver test rack. The test rack
is provided with two hybrid corporate feeds to distribute 870- and 900-Mcps signals to each of
the eight receiver strips.

Two eight-way resistive power dividers are provided for distribution of lower-frequency
signals. The eight receiver strip outputs are fed to a set of auxiliary mixers, where they are
converted to a 200-kcps intermediate frequency and fed to the IF sampler. The IF sampler
serves as an electronic switch for the phase meter and the diode (amplitude) detector.

The automatic data printer provides the master control for the system. It initiates a read-
ing cycle, prints an amplitude reading, and advances the IF sampler to the next channel. After

---

* J.L. Allen, et al., "Phased Array Radar Studies, 1 July 1959 to 1 July 1960," Technical Report No. 228 [U],
Lincoln Laboratory, M.I.T. (12 August 1960), Part 2, Ch. VIII, ASTIA 249470, H-335.

† Coherent frequency synthesizer, IF sampler, automatic phase meter and automatic data printer.
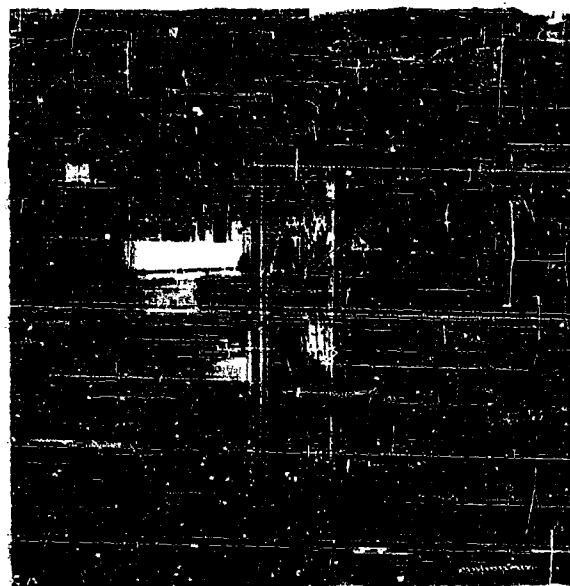
Fig. 2-106. Test system.
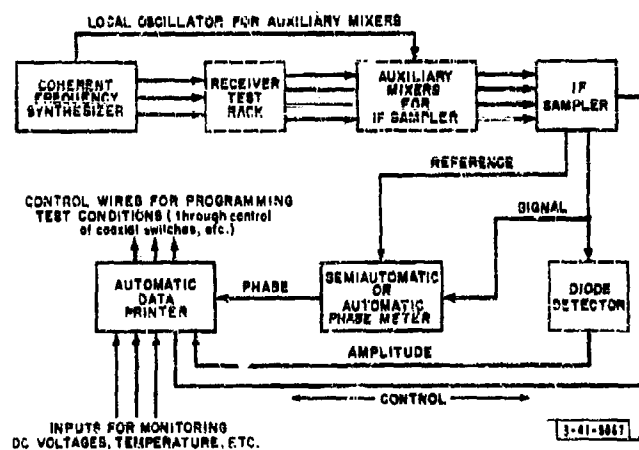
Fig. 2-107. Block diagram of rest system.

164

all the channel amplitudes have been printed, it resets the sampler and repeats the cycle to pro-
vide a set of phase readings. Provision is made to monitor additional variables, and the auto-
matic data printer may also be used to make programmed changes in the test conditions at se-
lected points in the reading sequence.

A variation of the test system, in which the automatic data printer is replaced by a monitor-
oscilloscope, is used with the 16-element receiving array. The dual-channel oscilloscope pro-
vides a visual display of the phase and amplitude of the IF sampler output. The IF sampler trig-
gers the scope sweep when it switches to channel 1 so that all sixteen channels are displayed in
sequence. The display can be used for monitoring the performance of the receiving array and
for periodic adjustment of the channel phase and amplitude controls. The system is capable of
being expanded to handle larger receiving arrays (see Sec. F-3 on IF sampler serial connection).

C. COHERENT FREQUENCY SYNTHESIZER

1. Function

The coherent frequency synthesizer supplies the test and local oscillator frequencies re-
quired for the operation and testing of the 16-element linear receiving array. All frequencies
are derived from a single oscillator through multiplicative and additive (heterodyne) operations.
This arrangement makes it possible to use an external low-frequency sync for an oscilloscope
while observing signals anywhere in the system.* All output frequencies can be maintained with
a high degree of accuracy by using a frequency standard as the basic oscillator.

2. Design Requirements

Experience has shown that a stable source of test frequencies is a necessity for the efficient
maintenance of a phased array receiver and the testing of phased array components. The large
number of components involved in a phased array system requires that test and alignment pro-
cedures be standardized and as simple as possible. To this end, a test frequency source should
have the following characteristics:

(a) It should provide a number of well isolated outputs at each frequency
of interest. The output impedance should be compatible with a standard
type of coaxial cable.

(b) The frequency and amplitude of the outputs should be stable and well
known (preferably standardized at a convenient power level). All out-
puts of the same frequency should be phase stable with respect to each
other.

(c) Spurious outputs should have negligible effect on the accuracy of the
majority of tests to be performed. A level of −60 db relative to the de-
sired output should be adequate. (Additional filtering can be supplied
for critical tests.)

(d) RF radiation should be minimized, and adequate power line filtering
should be provided.

(e) The system should be readily expandable to meet changing requirements.

(f) Outputs should be immune to abuses such as being improperly loaded.
Oscillations should not occur under any load condition (e.g., unterminated
coaxial cable).

---

*A sampling oscilloscope can be used for frequencies above 30 Mcps without encountering the usual problem of
providing a suitable triggering signal.
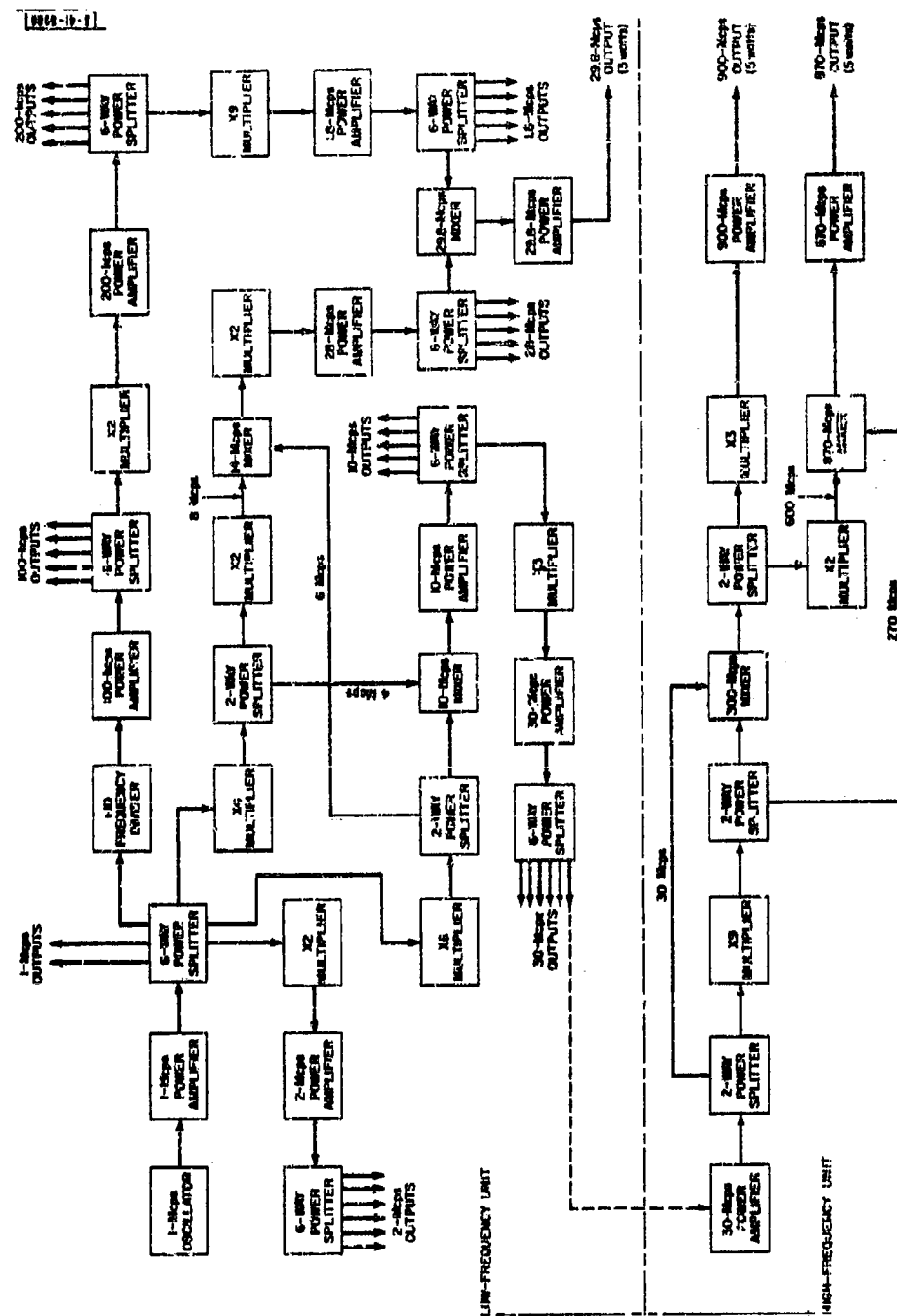
Fig. 2-168. Block diagram of coherent frequency synthesizer.

3. Block Diagram and Packaging

Figure 2-108 is a block diagram of the synthesizer in its present form. Because of the modular construction, it is possible to add new frequency outputs as the need for them arises. The block diagram is divided into two sections corresponding to the physical separation of the synthesizer into two units.

The low-frequency unit [Fig. 2-109(a)] provides output frequencies up to 30 Mcps. It consists of a Manson RD140A 1-Mcps stable oscillator, a Manson RD125 regenerative frequency divider, and a number of forced-air-cooled plug-in modules [Figs. 2-109(b) and (c)]. A three-tube configuration is used for mixing and frequency multiplication, whereas the output power amplifier modules contain two tubes. Air is forced through the chimney formed by the tube compartments of the plug-in modules by a blower unit located just below the module subracks. The blower unit also functions as the power control and distribution panel.

The high-frequency unit, which provides outputs at 870 and 900 Mcps, is not shown in its entirety, but several of the plug-in modules are displayed in Fig. 2-110.

4. Characteristics

Low-Frequency Synthesizer Unit:— The low-frequency synthesizer unit provides output frequencies at 100 and 200 kcps, and 1, 1.8, 2, 10, 28, 29.8 and 30 Mcps. The frequency stability of these outputs is determined by the 1-Mcps basic oscillator which is quoted to be 1 part in 10^8 per day and 5 parts in 10^9 per minute at 25°C.

The mixer and frequency-multiplier modules have a nominal output of 3 volts peak-to-peak into 50 ohms. The power amplifier modules provide an output of 4 watts (40v p-p into 50 ohms) and have protective AGC to prevent screen grid damage in the output tube if the load is removed. Spurious outputs are less than −60 db (relative to the 4-watt output level).

Forced-air cooling insures cool operation of the tubes and other components at a relatively high vacuum tube packing density.

Six-way resistive power splitters are employed to provide multiple outputs at each frequency, with excellent relative phase and amplitude stability. These can handle 10 watts of input power and have an attenuation of 19.3 db ± 0.5 db from the input to any one of the six outputs. Output impedance is 50 ohms, and the isolation between outputs is 48 db at 30 Mcps (when the input is connected to a power amplifier).

The absolute amplitude of the outputs up to 30 Mcps was monitored for a period of several days and found to vary less than 0.25 db.

High-Frequency Synthesizer Unit:— The high-frequency power amplifier modules provide 5 watts of output at 870 and 900 Mcps. A Microlab signal sampler tee extracts and rectifies a small portion of the output power to provide an output level monitor (a 0-1 ma meter) on the front panel.

D. AUTOMATIC DATA PRINTER

1. Introduction

The process of testing phased array systems and components involves the accumulation and evaluation of a large amount of phase and amplitude stability data. Both short-term and long-term effects are of interest, since equipment must first be made stable over the short term although, ultimately, long-term stability is very important. Short-term data present the least

Fig. 2-109. Low-frequency synthesizer unit: (a) front view of rack; (b) and (c) low-frequency plug-in modules.
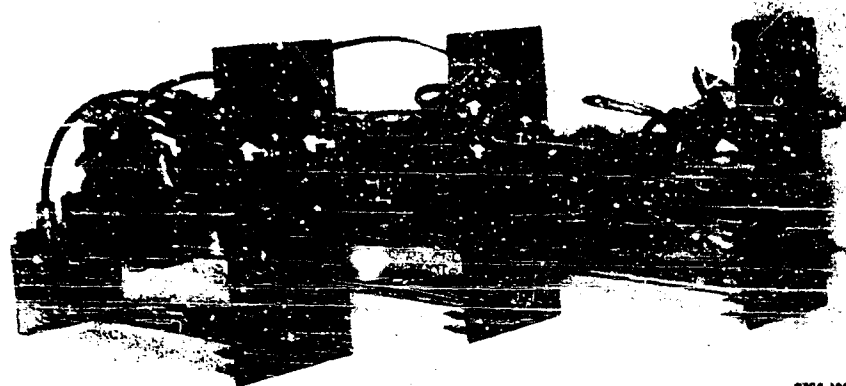
Fig. 2-110. High-frequency plug-in modules for coherent frequency synthesizer.

difficulty because of the short time spans involved. The long-term data, on the other hand, can present a tremendous correlation and reduction problem, to say nothing of the initial recording task.

A digital data recording system simplifies the recording and processing of long-term data for several reasons. A single system can be made to handle a large amount of data automatically. The data are recorded in a compact form, since readings are taken only when desired. In addition, data can be recorded in a specific time sequence to simplify the correlation of cause and effect when the data are processed. Finally, the digital form of the output record is the most convenient one for subsequent data reduction.

The application of digital recording techniques to a phased array testing program requires a particular type of digital data system in order to make full use of the potential of the resulting test system. A special-purpose machine is required which can serve as the master control element in the test system and which makes full use of the capabilities of the other test equipment. The format of the output record is of prime importance, since it determines how easily the data can be processed.

2. Function

The automatic data printer was developed to serve as a special-purpose control and digital data recording system for phased array monitoring and component testing. It is a versatile, self-contained unit which can be used independently as a digital voltmeter/data recorder, or it can be tied in with other units to form a test system such as the one described in Sec. B.

3. Over-All Description

The automatic data printer is an aggregate of six separate units which share a single 5-foot relay rack. A front view of this rack is shown in Fig. 2-111. Three of the units (the digital clock, digital voltmeter, and relay-controlled typewriter) are standard commercial items. The timer, control unit, and pulser are special-purpose units which perform the system control functions.

The timer controls the interval between reading cycles. It is interlocked with the digital clock so that the control unit is not started until the digital clock readout changes. This prevents time indication change while the clock time is being printed (at the beginning of a reading cycle) and provides consistent synchronization of the reading cycle with the minutes' digit of the clock. The reading interval may be set in one-minute steps from one minute to one hour. The timer also determines the allowable voltmeter cycling time. If the voltmeter should fail to stop cycling within a preset time (up to 60 seconds) due to noise on the input, the timer will stop the voltmeter (via the hold line) and cause the typewriter to print the reading preceded by a symbol for error.

The digital voltmeter that was selected is of the "bracketing" type. The most significant digits settle first, followed by the least significant. Although not quite so fast as some other logic, this arrangement offers better accuracy in the presence of noise. If the voltmeter is caused to lock up while the least significant digits are still cycling, the reading may still be approximately correct, whereas a voltmeter of the "non-bracketing" type may give completely erroneous results. A second feature that was felt to be essential is decimal lock-up, or fixed-decimal operation. This allows the sensitivity of the voltmeter to be set just high enough for the test requirements, thus reducing the cycling time. The sensitivity can also be kept below the ripple and noise level of the DC voltages being monitored, thus preventing excessive meter cycling.

169
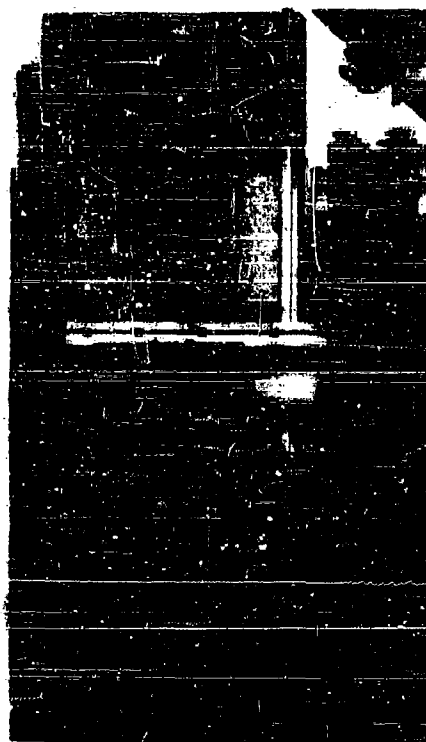
Fig. 2-111. Automatic data printer.

The control unit has three functions: it serves as an input scanner for the digital voltmeter, it provides parallel-to-serial conversion for the typewriter, and it determines the operating cycle of the automatic data printer and any auxiliary equipment that may be used. Although the basic operating program of the control unit is fixed, the program details can be tailored to the test situation through the use of the patch panel.

The stepping switches in the control unit and the relay-controlled typewriter are powered by the pulser which supplies 24-volt, 80-msec pulses at a repetition rate of 6 pulses per second. Since all stepping switches are of the type which cock when energized and advance when de-energized, no (inductive) circuits are broken during the duration of the pulse; thus arcing is minimized. The pulser output transistor serves as a damper for the inductive transients.

4. Control Unit Details and Operating Cycle

The circuit diagram of the control unit is shown in Fig. 2-112. Only one deck of each stepping switch is shown; the rest are wired to the patch panel and to the signal inputs. The stepping switch wiper arms are grounded for uniformity.

Stepping switch 1 serializes the clock time and makes one revolution at the beginning of a reading cycle. Operation is then transferred to stepping switch 2 which serializes the digital voltmeter reading. Every revolution of SS (stepping switch) 2 advances SS 3 (the input selector) one step. SS 3 has three decks brought up to the patch panel so that a three-character code can be assigned to each input position. When the input selector reaches the same position as the reset selector, the control unit is reset and is ready for a new reading cycle.

Stepping switch 2 triggers the digital voltmeter through the PP (patch panel) start line. Once triggered, the voltmeter cycles until it completes a reading. Meanwhile, SS 2 is allowed to continue to the PP stop position which immediately precedes the contacts used to serialize (and print) the digital voltmeter reading. It can not continue past this point while the voltmeter is cycling.

5. Special Features

The revolutions of SS 2 can be used to advance SS 3 directly (internal advance) or they can be used to provide advance pulses for an external switch (such as the IF sampler). The external switch then advances SS 3 every time it resets (external advance). This mode of operation is used to take a line of amplitude readings followed by a line of phase readings (data group).

The patch panel contacts of SS 1, SS 2 and SS 3 are used to print the clock reading, the digital voltmeter reading, and the three-character input code, respectively. The grounded wiper operation of these stepping switches permits the convenient use of unused contacts for the control of external relays (such as coaxial relays) to provide programmed changes in the test conditions at selected points in the reading sequence.

6. Alternate Controller

An alternate control unit for the automatic data printer is shown in Fig. 2-113. The sequence of operation is completely controlled by stepping switches and mechanical latching relays to prevent "memory loss" in the event of power failure during the operating cycle. A fourth stepping switch has been added to permit "one-way" control of the IF sampler by the printer (IF sampler advance and reset pulses provided by the automatic data printer). This arrangement permits the printing of data groups with nonuniform subdivisions. For example, five inputs might be
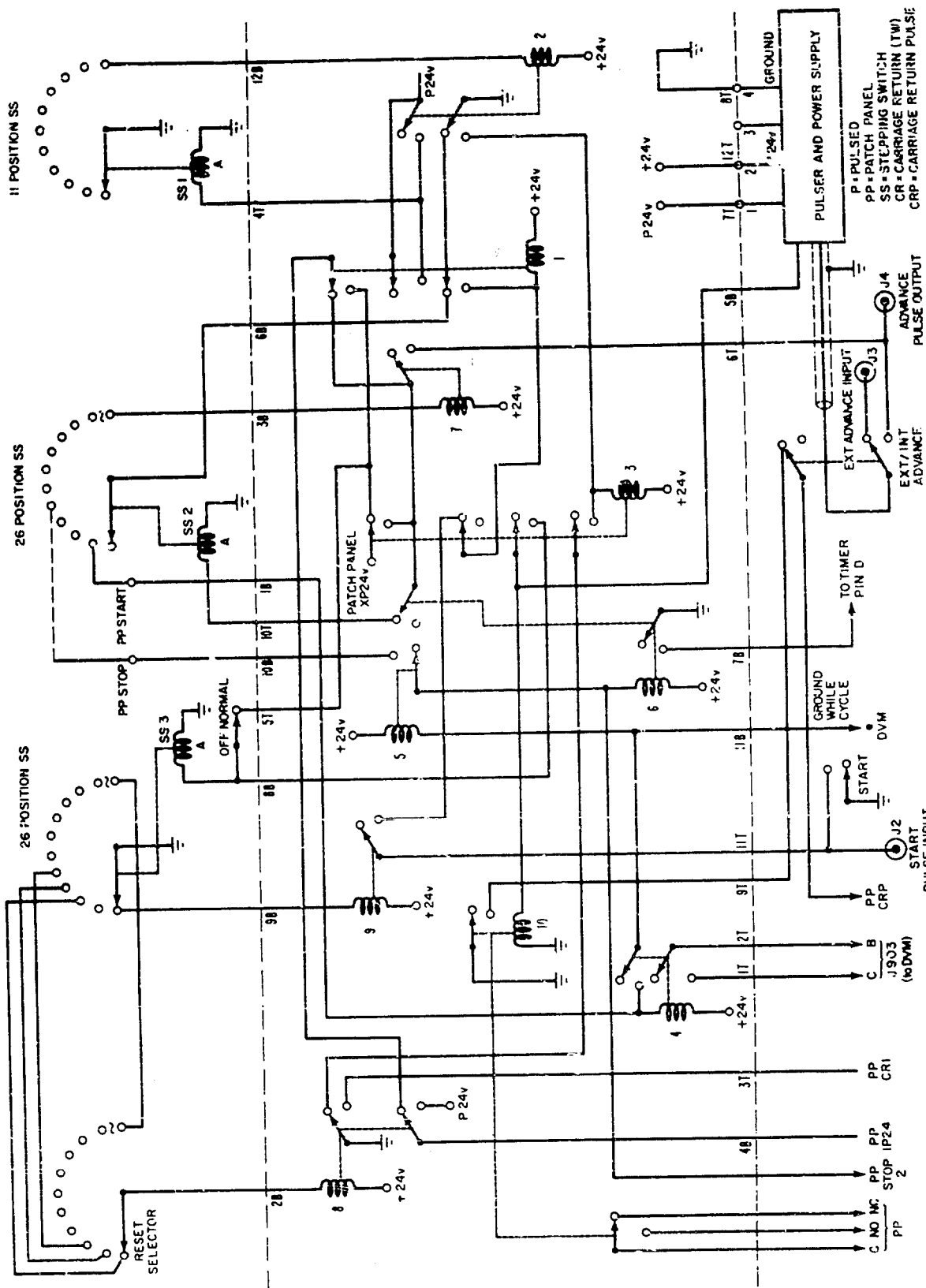
Fig. 2-112. Circuit diagram of automatic data printer control.
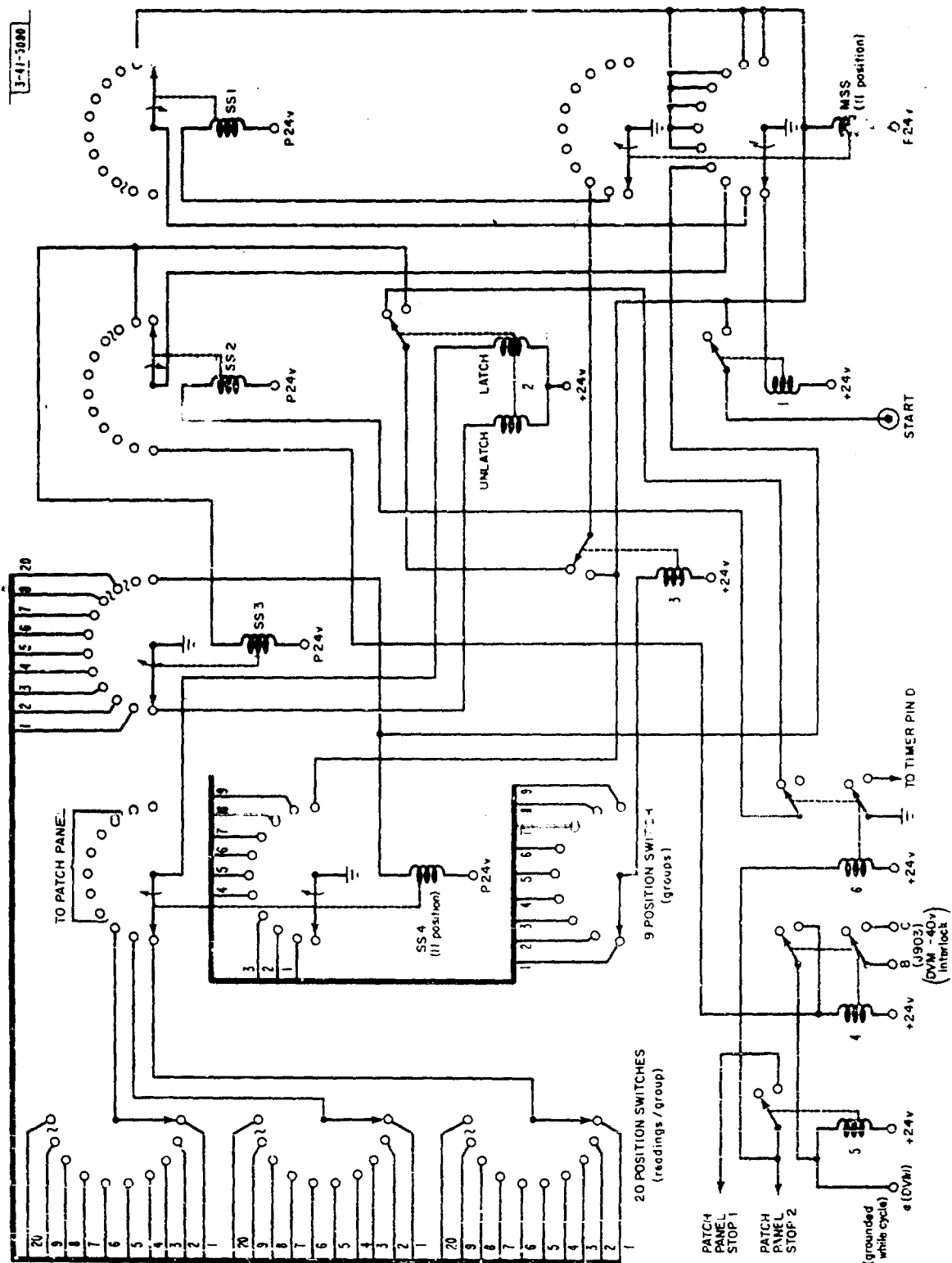
Fig. 2-113. Alternate control for automatic data printer.
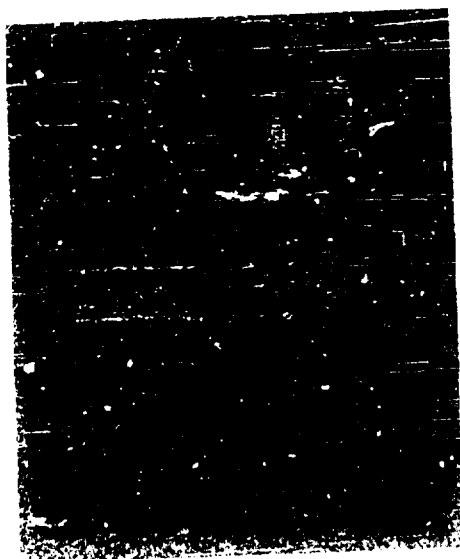
(a) Delay-line gate.
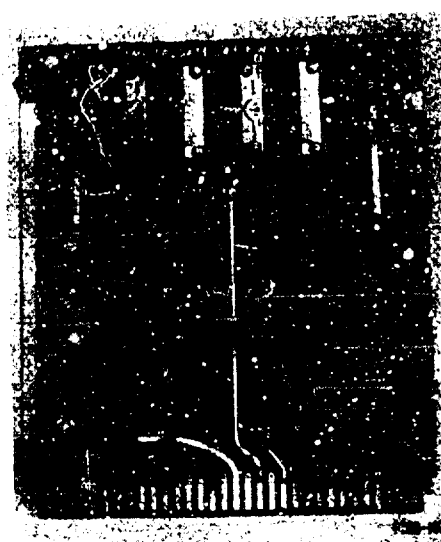
(b) Signal (IF sampler) gate.

Fig. 2-114. IF signal gates.

scanned first, corresponding to selected system test points, follows by eight amplitude and eight phase readings.

E. SPECIAL-PURPOSE PRINTED-CIRCUIT BOARDS

1. Introduction and Function

A number of special-purpose printed-circuit boards were developed to serve as building blocks for test systems of a mixed (analog and digital) nature. Two test units were designed using these boards and are described in the next two sections. These are the IF sampler and the automatic phase meter. This section provides a brief description of the most commonly used special-purpose boards.

2. Basic Digital Gates

A printed-circuit board containing four 3-input NOR gates serves as the primary logic element. Two of the three inputs are direct and are symbolized by arrows touching unshaded sides of the gate symbol. The third (inverting) input is symbolized by an arrow touching the shaded side of the symbol. Four inverters are also provided. These can be used to transform the basic NOR gates into AND gates or OR gates.

The logic levels are −10 volts for a zero and +4.5 volts for a one. Complete transition of gate or inverter outputs occurs with an input swing of (less than) −4 volts to +0.5 volt. One gate or one inverter will drive six other gates or inverters.

A diode (OR) gate board with three 3-input and four 2-input diode OR gates is used in conjunction with the NOR gate boards to provide more efficient transistor and space utilization when more than a few gate boards are required. Each diode gate is capable of driving one inverting and one direct NOR gate input. (The NOR gate restores the logic levels.)

3. Remote Control Gates

The remote control gates utilize special 24-volt relays which are designed for printed-circuit board use. These relays have 5-msec pickup and dropout times and require 15 ma of control current. The use of these relays simplifies the remote control of solid state logic circuits (such as the NOR gates).

The Control Relay Board is a relay logic board which provides the mode control for the IF sampler.

The Reset and One Pulse Gate provides remote control (through relays) of the binary counter state (count) which will provide a reset pulse. It also provides a separate output pulse on the count of one. The use of relays removes the necessity for transmitting pulsed waveforms over long cable runs.

4. IF Gates

Two types of digitally controlled analog signal gates (200 kcps) were developed for special applications. Both types are controlled by a 5-bit binary word. Figures 2-114(a) and (b) are photographs of the gates.

The Signal Gate Board (IF sampler gate) contains two gates with separate signal inputs and a common signal output. The input impedance is 8 kilohms at 200 kcps, and the output is designed to work into a 2-kilohm resistor to ground. The (gate on) gain is constant at 0.45 from 100 to

175

300 kcps, and the (gate off) leakage is down 60 db. The maximum signal input is 2 volts peak-to-peak. Amplitude and phase trimmers are provided so that all gates can be adjusted for identical characteristics.

The Delay Line Gate Board (for the automatic phase meter) contains two gates with common signal input and signal output connections. Provision is made for up to two delay lines in each gate's signal path. These delay lines are chosen to provide phase shift multiples of 20° at a 200-kcps signal frequency. A set of five gate boards (ten gates) will provide 20° phase increments from 0° to 160°. The gates should be fed from a 2-kilohm source, and the output line should be terminated in 2 kilohms (to match the 2-kilohm characteristic impedance of the delay lines).

Both the signal and delay line gates were tested over the temperature range 25° to 50°C. The amplitude and phase changes were less than 0.1 db and 1°, respectively.

5. Other Printed-Circuit Boards

The Delayed AND Gate Board contains two 4-input AND gates. Two of the inputs are direct and two are inverting. The gate output is delayed 0.5 to 6 μsec, depending on the delay line used.

The Dual Driver Board contains two cable driving amplifiers capable of 4 volts peak-to-peak into 50 ohms. The gain is 2 at 200 kcps, and the 3-db points occur at 55 and 600 kcps.

The Fast Trigger Board contains two shaping circuits with a gain (slope multiplication) of 1000. The inputs are designed for 2-kcps to 2-Mcps sine-wave signals with a minimum amplitude of 2 volts p-p. The output waveform is a −10 to +8 volt square wave with 50-nsec rise time and 1-μsec fall time (with an input frequency of 200 kcps and an output load of 50 pf).

The Sine Trigger Flip-Flop Board utilizes one of the shaping circuits used on the fast trigger board. The shaper permits triggering of a flip-flop (located on the other half of the board) with a sine-wave input of greater than 4 volts p-p. The frequency range is 10 kcps to 1 Mcps.

The Forward-Backward Counter Board contains a flip-flop with gated carry output. When the add (gate) line is energized, the output pulse occurs on the flip-flop transition to a zero, whereas the subtract (gate) line causes an output pulse to occur on the transition to a one.

The Dual Voltage Comparator Board consists of two separate comparing circuits. Each circuit provides an output ("one") when the input voltage exceeds a reference threshold. The sensitivity for a complete switch is 10 mv.

The Integrate and Store Board provides a voltage output proportional to the integral of the input current (rise input) when the dump circuit is released. The dump circuit returns the output voltage to zero when it is energized.

The Multiple Differentiator/Adder Board has ten inputs and one output. A 5-volt (min), 200-volt/μsec (rise slope), positive-going step at any one of the inputs will produce a 0.5-μsec pulse in the output.

F. IF SAMPLER

1. Function

The IF sampler serves as an electronic switch for low-frequency (100 to 300 kcps) signals. It finds its primary application in the monitoring of a number of receiver channel outputs. Each channel output is sampled in sequence and fed to a common output line. The output line provides a composite IF signal (the receiver channel outputs in sequence) from which phase and amplitude information may be extracted. The phase and amplitude detectors may be made quite complex, since only one of each is required.

176

2. Construction

The IF sampler rack is shown in Fig. 2-115. The sampler itself consists of the printed card subrack (near the bottom of the rack) and the control box located just above it. A remote control box is not shown. The panel below the printed card subrack contains the auxiliary mixers for the IF sampler. These mixers (described in Sec. H-1) extend the range of the sampler inputs to cover frequencies up to 30 Mcps.

The IF sampler circuitry can be conveniently separated into two functional categories. One category includes the signal gates (see Sec. E-4); the other encompasses all the control circuitry.

The signal gates were designed for uniform transfer functions when conducting and high loss when nonconducting (low leakage). In addition, it was desired that the switching transients be held to a minimum.

The primary concern, however, was the IF sampler control circuitry. A versatile control with a variety of operating modes was desired which would enable the sampler to be used in conjunction with other test units. Figure 2-116 is a block diagram of the IF sampler control circuitry. Figure 2-117 shows the local and remote control box connections.

3. Modes of Operation and Performance

The IF sampler signal gates are divided into two groups. These groups, the A gates and the B gates, are operated either singly in sequence or concurrently in pairs. The SINGLE/DUAL switch determines whether the sampler functions as a single-pole, 16-position electronic switch or as a double-pole, 8-position switch. The double-pole (DUAL) operation allows switching of both the signal and reference inputs of a phase meter to permit time-shared monitoring of independent test setups.

The gates are controlled by a binary counter. The A gates are set so that one gate opens on each of the following counts: 0, 1, 2, 3, 4, 5, 6, 7, 8-15, 16-31. The B gates open on the counts 8, 9, 10, 11, 12, 13, 14, 15, 16-31, 0-7 on SINGLE, and on the counts 0, 1, 2, 3, 4, 5, 6, 7, 8-15, 16-31 on DUAL.

The pertinent gate characteristics are:

Transient disturbance	1 v peak, 5 μsec max
Signal output	2 v p-p max into 50 ohms
Leakage	−40 db (at 200 kcps; all channels fed in phase except for selected channel which is terminated in 50 ohms)
Gate input impedance	8 kilohms at 200 kcps
Channel voltage transfer ratio	0.9 from 100 to 300 kcps

The binary counter which controls the sampler gates is controlled in turn by the CHANNEL SELECTOR (binary switches) and the MODE switch. On the MANUAL mode, the CHANNEL SELECTOR stops the counter on the selected count. On all other modes, the CHANNEL SELECTOR functions as a reset selector and resets the counter on the selected count.

On the CONTINUOUS mode, the counter is triggered by an external sine-wave input (SINE INPUT) with 1 volt p-p minimum amplitude and a frequency range of 2 kcps to 1 Mcps. The SAMPLE TIME switches control the number of binary countdowns that occur before the triggers are applied to the gate-controlling counter. Sample times of 4, 8, 16, 32, 64, 128, 256 and 512 times the sine-wave input period may thus be obtained.

177
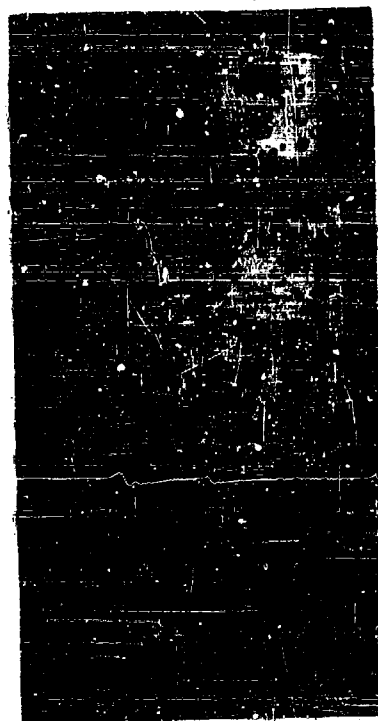
Fig. 2-115. IF sampler rack.

Fig. 2-116. Block diagram of IF sampler.
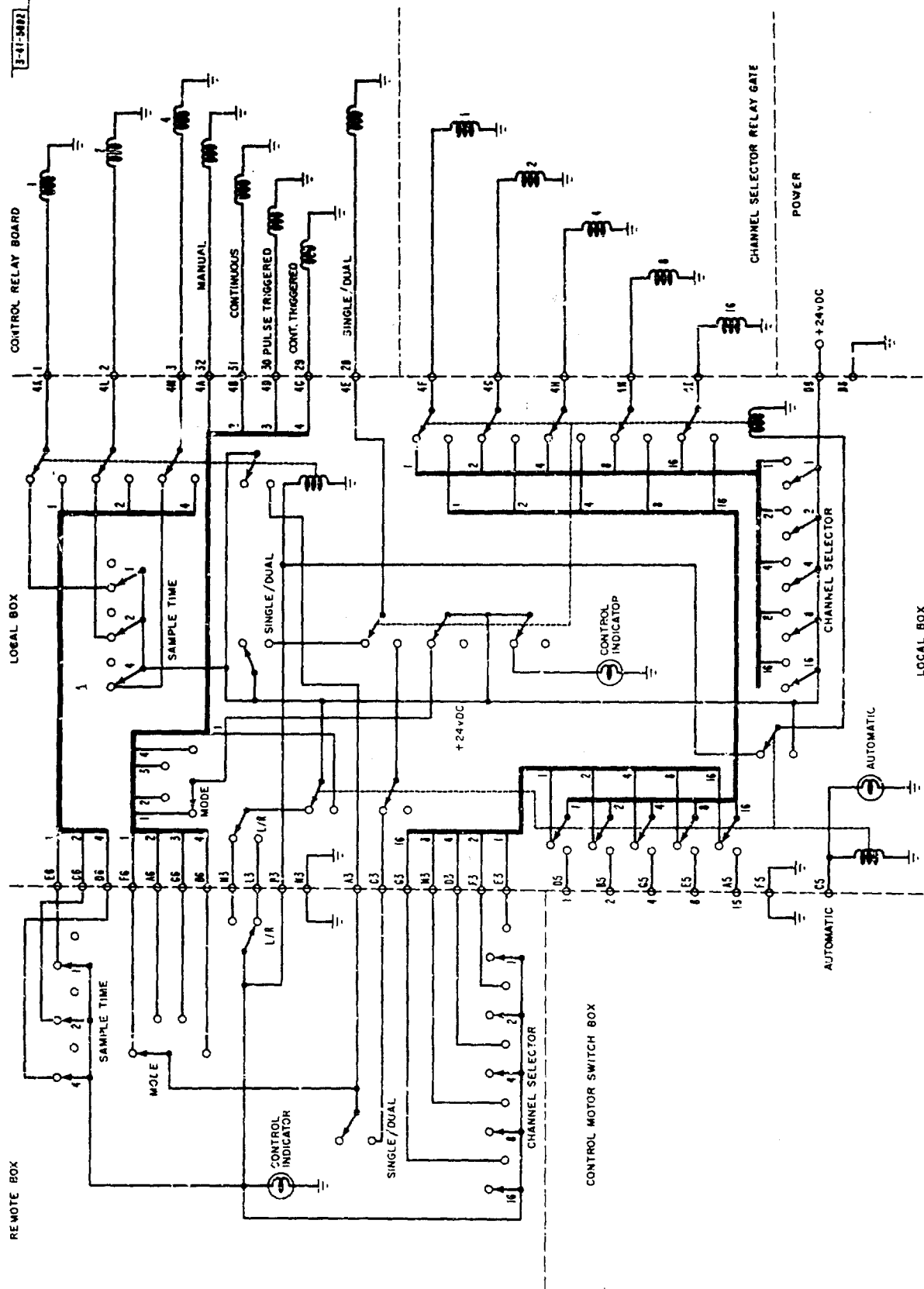
Fig. 2-117. IF sampler control wiring.

The CONTINUOUS TRIGGERED mode is similar to the CONTINUOUS mode except that the gate-controlling counter is advanced by pulses applied to the TRIGGER INPUT.

On the PULSE TRIGGERED mode, the counter is also advanced by pulses applied to the TRIGGER INPUT, provided an arming pulse has first been applied to the START PULSE INPUT. When the counter reaches the same state as the CHANNEL SELECTOR, the counter is reset to zero and all subsequent trigger pulses are steered to the TRIGGER OUTPUT (until the application of another start pulse).

The counter may be reset at any time through the EXTERNAL RESET INPUT. The sampler provides an output pulse when it resets (RESET OUT) and while it is on channel 1 (ONE PULSE OUT).

Figure 2-118 shows the interconnections for cascading a number of IF sampler units to handle more channels than a single sampler is capable of handling. Each sampler scans in turn until all have done so; then the cycle is repeated.

G. AUTOMATIC PHASE METER

1. Function

The automatic phase meter is a fully automatic, nonambiguous, 0-360° phase meter with a digital readout. It is designed to read the phase between two 200-kcps signals with an average reading time of 1 msec.

The automatic phase meter (Fig. 2-119) can be used independently (as a 200-kcps phase meter) or it can be used in conjunction with the IF sampler and the automatic data printer (see test system description in Sec. B).

2. Design Philosophy and Over-All Operation

The design of the automatic phase meter is based upon a "two-step" measuring technique. A coarse estimate of phase (to the nearest 20°) is made first. A precision, digitally controlled, phase shifter is then used to insert the nearest multiple of 20° in the reference circuit of a phase detector which provides a DC output essentially proportional to the remaining phase shift. The complete phase reading can then be obtained by taking the sum of the coarse and fine phase readings. The "two-step" measuring technique offers several significant advantages in a phase measuring system.

Phase shift modulo 2π is a discontinuous function at multiples of 2π. This presents a real problem in the design of a nonambiguous phase meter. Excessive reading errors in the neighborhood of 2π can best be prevented in a dynamic (null-seeking) system. The coarse phase estimating (tracking) circuit provides a coarse phase reading which is always correct to within a nominal ±10° even near 360°.

The fine phase meter is a simple, all solid state, digital voltmeter which reads the DC output of the phase detector. High-speed, relatively high accuracy operation (1°) can be obtained with a simple circuit because it is only required to operate over a small phase range (±15° is provided to allow some overlap of the fine and coarse readings).

The combination of the fine and coarse circuits provides a higher-speed circuit (with simpler circuit elements) than a "one-step," null-seeking, digital phase meter with the same phase resolution (1°) would require.
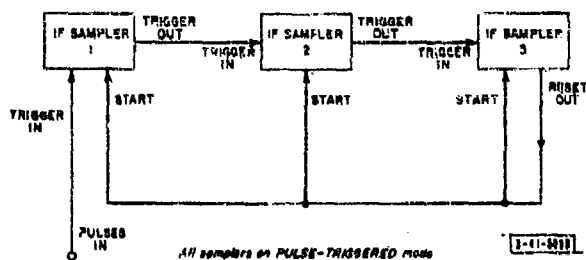
Fig. 2-118. If sampler serial connection.

Fin. 2-119. Automatic phase meter.

Fig. 2-120. Limiter strip and filter.

3. Circuit Details

Both input channels (signal and reference) of the automatic phase meter contain a limiter strip and filter (Fig. 2-120) combination which eliminates amplitude variations while preserving phase (zero crossings). The limiter strips were designed for minimum zero-crossing shift over a 50-db input dynamic range (60 mv to 18 v p p). The low-pass filters ($f_c = 300$ kcps) convert the limiter strip 200-kcps square-wave outputs back to 200-kcps sine waves.

The block diagram of the coarse phase tracker is shown in Fig. 2-121. The delay line gates (see Sec. E-4) are controlled by a forward-backward counter. Associated control circuitry steps the counter until the phase detector DC voltage is within limits corresponding to ±10° of phase. To eliminate the phase detector ambiguity, a second phase detector (auxiliary phase detector) is offset 90° from the first. If the first phase detector is near the correct null, the second phase detector output will be near its maximum (positive) value.

The coarse phase tracker has two modes of operation. In the TRACK mode, the tracker will restart whenever the phase changes by more than ±10°. The READ mode requires a starting pulse at the COARSE READ PULSE input. The tracker will then run until it matches the input phase within ±10°. It can not be restarted except by another coarse read pulse.

A FINE READ PULSE output is provided for the fine phase meter. This pulse is coincident with the completion of the coarse phase track cycle except for an adjustable delay (nominally 100 µsec). The delay is provided to allow the phase detector transients to die down before a fine phase reading is made.

The fine phase meter block diagram is shown in Fig. 2-122. A binary-coded decimal (BCD) counter is coupled to a digital-to-analog converter which provides thirty possible reference voltages for a voltage comparator. The counter is stepped until the reference voltage level is within one step of the phase detector DC output level. The state of the individual counter stages is then an expression of the phase detector DC level in binary-coded decimal form. The fine phase meter may be operated in a TRACK or a READ mode in the same way as the coarse phase tracker.

The digital outputs of the coarse phase tracker and the fine phase meter are connected to the readout gates shown in Fig. 2-123. These gates sum the overlapping portion of the two readings and convert the complete phase reading to straight BCD form for the readout lights.

H. AUXILIARY EQUIPMENT

1. Introduction

The test equipment described in the preceding sections forms the nucleus of special-purpose test units required for phased array system and component testing. Some of the auxiliary equipment used with the basic test units is described in this section.

2. Auxiliary Mixers for IF Sampler

The useful frequency range of the IF sampler is 100 to 300 kcps. A simple, stable mixer is required which can convert frequencies of up to 30 Mcps (frequencies above 30 Mcps can be converted to a 30-Mcps IF) to the 200-kcps sampler IF frequency. The mixer should be compact, since one is required for each input channel of the IF sampler.

Diode-mixer, low-pass filter ($f_c = 300$ kcps) packages are shown in Figs. 2-124(a) and (b). The signal and local oscillator inputs are coupled to the mixer diode through a resistive adder so that any signal frequency up to 30 Mcps may be used. The LO must be 200 kcps away from the signal frequency and must be well isolated from the LO inputs to other mixer units.

183
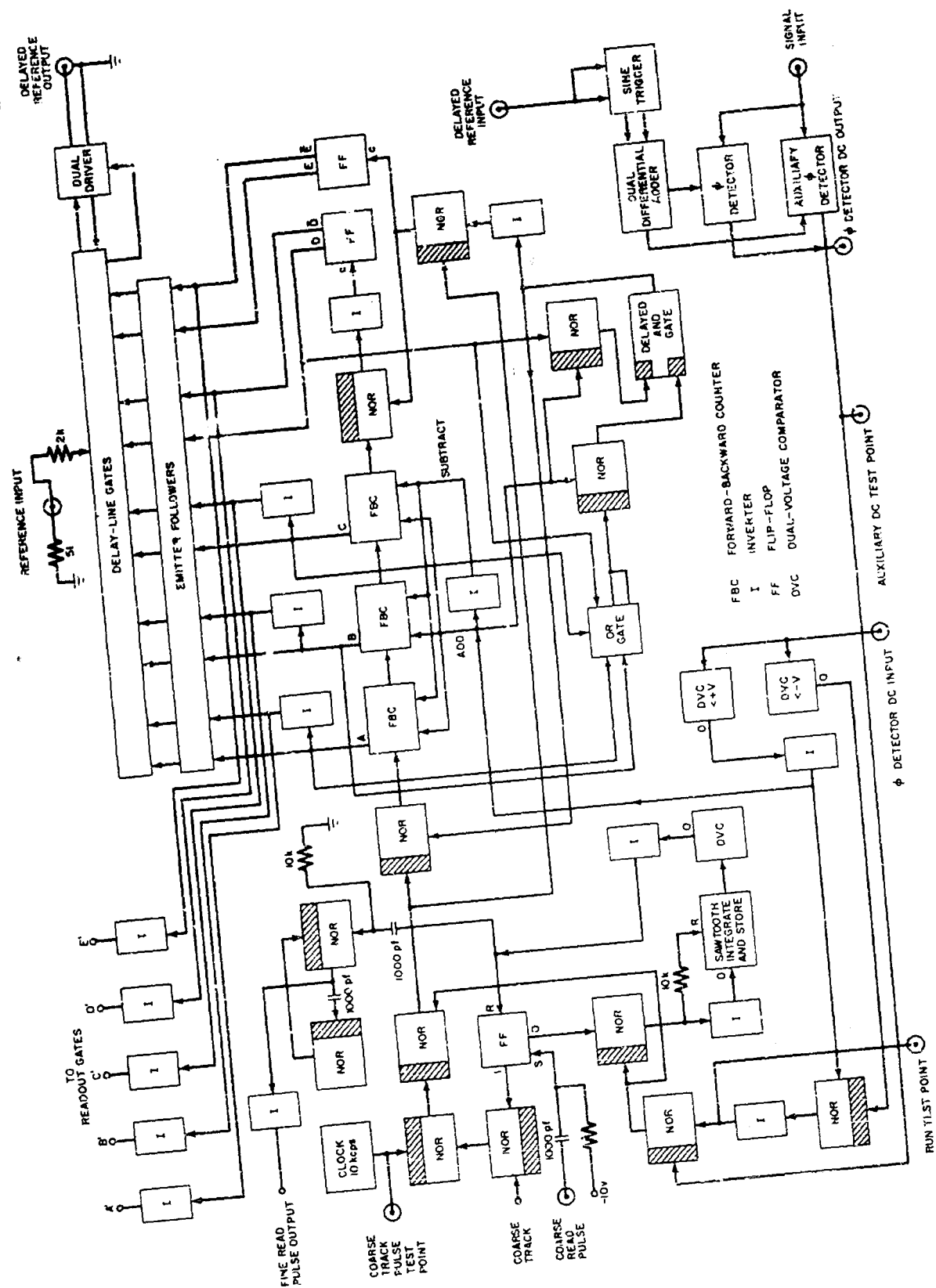
Fig. 2-121. Coarse phase tracker.

FBC   FORWARD-BACKWARD COUNTER
I   INVERTER
FF   FLIP-FLOP
DVC   DUAL-VOLTAGE COMPARATOR

184
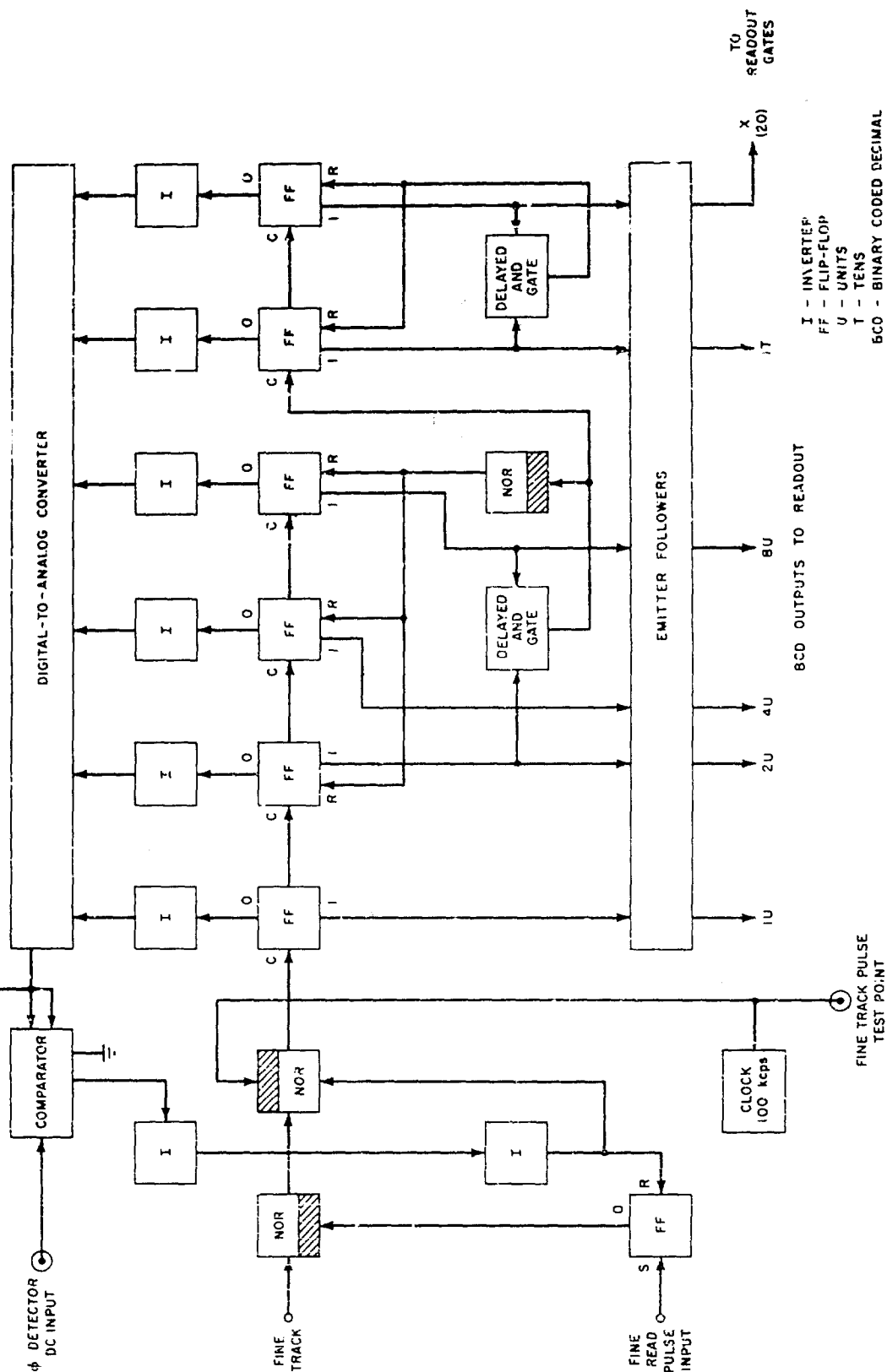
Fig. 2-122. Fine phase meter (digital).
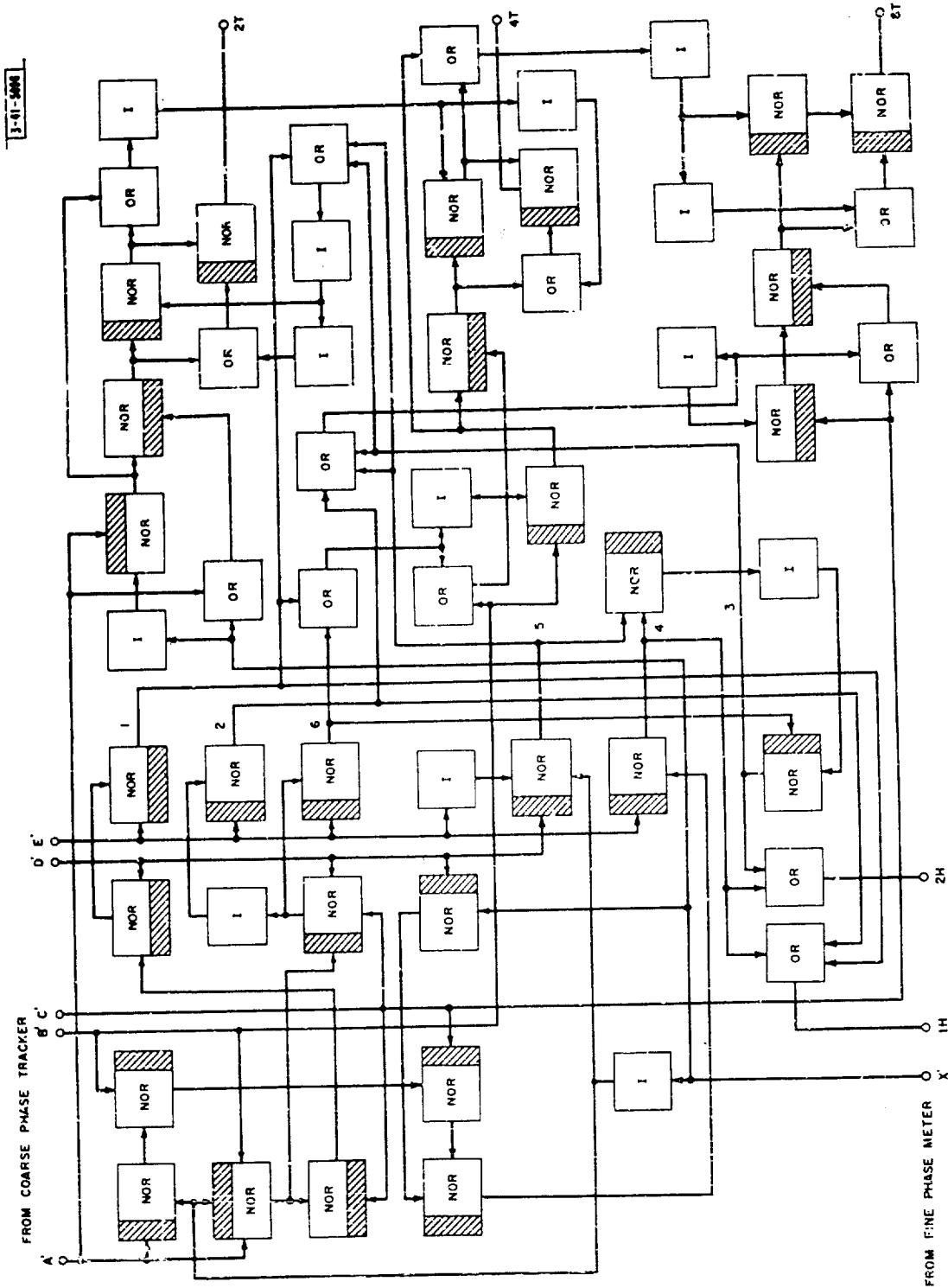
Fig. 2-123. Readout gates.

Fig. 2-124. Auxiliary mixers for IF sampler.

Fig. 2-125. Receiver test rack.

Fig. 2-126. Phase and amplitude controller.
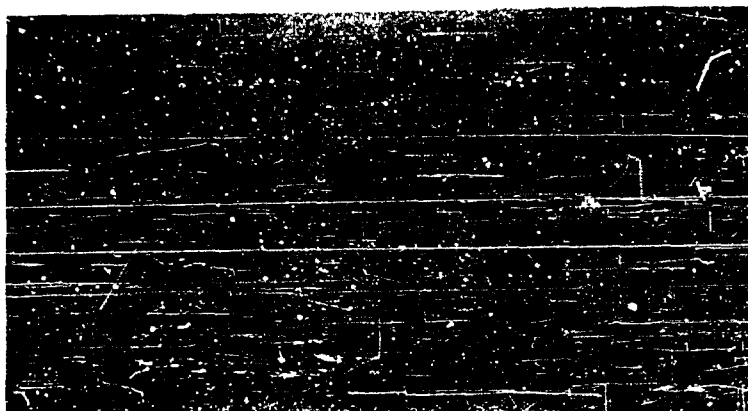
Fig. 2-127. Schematic of phase and amplitude controller.

Best Available Copy

The performance of eight mixer units was checked, and the stability results are given below.

Test conditions

Signal input	0.5 v p-p at 30 Mcps
Local oscillator	3 v p-p at 29.8 Mcps

Peak output phase and amplitude variations

0.5° and 0.5 db	for −6 db LO change
1° and 2 db	for −12 db LO change
1° and 0.1 db	from 25° to 50°C
1° and 0.3 db	differential stability over 3 days

3. Receiver Test Rack

Figure 2-125 is a photograph of the receiver test rack which is used to test the phase and amplitude stability of eight receiver strips at a time. It was found that the use of the 16-element receiving array as part of an experimental radar made it difficult to gather detailed stability data on receiver strips located therein. The receiver test rack provides an independent test setup in a less confusing environment. It is provided with the power supply, local oscillator, and test signal distribution system necessary for the operation and testing of eight receiver strips.

The receiver strips are divided into two sections. One RF and eight IF sections are shown in Fig. 2-125. Frequencies below 30 Mcps are divided eight ways in special resistive power dividers which will handle 10 watts input and provide 50 db isolation between outputs. One hybrid corporate feed distributes the 870-Mcps LO to the receiver strip RF sections. Another is used to provide 900-Mcps test signals for the RF sections.

4. Channel Phase and Amplitude Control

The sixteen receiver channels of the linear test array were provided with motor-driven phase and amplitude controls. This was done to permit rapid, convenient adjustment of the receiver amplitude and phase from a central point. Figure 2-126 is a photograph of the phase and amplitude controller used to operate the motor-driven adjustments. Figure 2-127 shows a circuit diagram of the controller.

The controller supplies 24-volt pulses to a stepping switch located in the receiving array equipment box. This stepping switch is used to switch the phase and amplitude control lines to any one of the sixteen receiver channels. The stepping switch is pulsed until its position matches the setting of the decimal channel selector switch (or the binary channel selector switches, when the decimal channel selector is on B).

Three operating modes are provided. On PULSED, the remote stepping switch is advanced one step at a time by the channel advance pushbutton on the controller. Indicator lights show the stepping switch position in binary form. A DISPARITY light is lit whenever the channel selector switches and the remote stepping switch are in disagreement. The PARITY pushbutton may be depressed to bring the remote stepping switch into agreement with the channel selector.

The MANUAL mode provides automatic tracking of the remote stepping switch with the channel selector. It is used to switch directly to a particular channel.

The AUTOMATIC mode requires a servoamplifier unit and an IF sampler – phase detector combination. The IF sampler is slaved to the controller so that the servoamplifier can be provided with phase and amplitude error voltages corresponding to the channel whose motors are

under control. When the phase and amplitude of a particular channel have been adjusted to desired reference levels, the controller advances the remote stepping switch (and the IF sampler) to the next channel. This process continues automatically until all the channels have been adjusted.

5. Thermistors for Temperature Measurement

Thermistors are used for the measurement and recording (on the automatic data printer) of temperature because extreme accuracy is not required. The use of thermistors instead of thermocouples eliminates the need for cold junction correction and special leads.

It was found that the nonlinear characteristic of voltage divider output vs resistance (of one resistor in the divider) could be used to compensate somewhat for the nonlinear resistance vs temperature characteristic of the thermistor. The optimum resistor for use with the Bendix Friez 523391-3 thermistor is 12.2 k ohms. The maximum temperature error obtained over the temperature range −30° to +40°? was less than 1°C.

6. Diode Detectors for Gain and Amplitude Measurement

The measurement of receiver gain is complicated whenever frequency conversions are involved. Calibrated signal sources at the receiver RF input and intermediate frequencies are normally required, and the calibration accuracy is typically ±1 db.

The Telonic XD-3E RF detector has a response vs frequency characteristic that is flat within 2 db from 200 kcps to 900 Mcps. The use of such a detector enables gain measurements to be made conveniently with a calibrated attenuator and a DC indicator. Uncalibrated signal sources may be used, and the measurement accuracy is comparable to that obtained with calibrated signal generators (±1 db).

Although a diode detector has a nonlinear amplitude characteristic, its behavior may be approximated by a linear characteristic over a small region. Ten detectors were tested for DC output vs RF input. Although the absolute DC output for a given input varied from unit to unit, the incremental output change for a given input change was found to be uniform, provided the detector inputs were padded to give the same DC output for one input level. Therefore, a single calibration chart can be used for incremental sensitivity (DC output change in millivolts for a 1-db input change in RF level). The detectors are thus useful for measuring amplitude stability.

An output DC change corresponding to less than 0.1 db input change was observed over a temperature range of 25° to 50°C (1 and 0.1 v rms input levels at 2 and 30 Mcps).

7. UHF Mixers for Phase Measurement

The use of the automatic phase meter for phase measurements at frequencies other than 200 kcps requires two mixers — one for the signal channel and one for the reference. The auxiliary IF sampler mixers may be used up to 30 Mcps. Empire Devices CM107B single-ended mixers are used at 900 Mcps. It was found that the insertion of a 10-db pad at the mixer signal input provides a great improvement in the phase and amplitude stability vs LO drive level. Two mixers tracked within 1° phase and 0.2 db amplitude over a 6-db LO range (crystal current from 0.1 to 0.6 ma). The absolute change of one mixer was 6° phase and 4 db amplitude. If the mixer crystal currents initially differ by 0.2 ma, two mixers track within 2° and 0.5 db for a 6-db LO change.

8. Sideband Separator

The sideband separator consists of three double-tuned filters which are driven from a common input. The filters are centered at 150, 200 and 250 kcps, and each has its own 50-ohm output driver.

If the RF test signal for a phased array receiver is modulated at a 50-kcps rate (a diode modulator will suffice), then the sideband separator can be used to separate the IF sampler output into the three frequency components corresponding to the carrier (200 kcps) and the two sidebands. The phase and amplitude tracking of the array can thus be checked at three frequencies simultaneously

9. Standard Power Control

A standard power control box was designed to control both high- and low-voltage commercial regulated power supplies. The control system utilizes 24-volt DC relays to permit remote control operation of a number of relay racks of equipment. All equipment may be shut off with a single master switch by shutting off the 24-volt control power. The 24-volt relays were chosen for compatibility with the other special-purpose test equipment as well as their quiet operation and reduced shock hazard (over 110 v AC relays).

Relay-switched AC outlets are provided for rack-mounting commercial test equipment. A jumper plug may be removed and replaced with a special unit which senses power supply failure. This unit will shut off all power if any power supply voltage drifts out of tolerance. Turn-on time delays can also be provided.

CHAPTER IX
PHASED ARRAY SUPPORT STRUCTURES

SUMMARY   E. A. Davidson

This chapter describes some preliminary design studies of support structures for transmitting arrays. Two arrays are considered: a low-power 900-Mcps array and a higher-power 1300-Mcps array. In both cases, the structure was designed to allow most of the electronic equipment to be mounted in plug-in modules directly behind the radiating elements.

A. INTRODUCTION

No study of phased array techniques is complete with a thorough consideration of the mechanical design of the array support structure. In a phased array, the sidelobe level of the antenna pattern is dependent upon both electrical and mechanical errors; hence, the mechanical tolerances are more stringent than in a conventional antenna designed for the same sidelobe level, since some of the allowable rms phase error must be allocated to the electronic equipment in the phased array.

The problem is further complicated by the fact that the space immediately behind each radiating element contains an electronic module. This equipment is heavy and leaves very little room for the actual support structure. The structure must be designed to accommodate all the cabling and to support the individual electronic modules in such a way that they can be replaced easily.

B. PRELIMINARY STUDIES

In considering the mechanical design for phased arrays, many discussions were held with representatives of the electronics section to ascertain basic design parameters. At that stage, however, there were many unknowns in the electronic requirements which made it difficult to set forth definite mechanical design criteria. The design described below, although very general in nature, was agreed upon as a basic configuration, and preliminary investigation was initiated.

It was decided that two arrays would be required: one would be a transmitting array and the other a receiving array. As the transmitter appeared to be the greater problem from a mechanical viewpoint, the major effort was expended on this unit. The array would require a large billboard-type ground plane, tipped back at approximately 45° from the vertical, to the rear of which would be mounted several boxes arranged rectilinearly. Each of these boxes would contain a removable electronic package complete with radiators (dipoles were taken as an example) that would protrude through the ground plane when in the installed position. All cabling and cooling hoses would be attached at the rear of the packages to facilitate maintenance and permit servicing during operation of the array. A suitable structure would be required to support this array in its inclined position.

With the general configuration in mind, it was decided to evolve an initial concept based on a 32×32 element stationary array at 900 Mcps. An element-to-element spacing of approximately 0.58λ (7.7 inches) was assumed. Figure 2-128 shows a model of a partial section of this preliminary design. The ground plane consisted of a series of $\frac{1}{4}$-inch thick square aluminum plates, with openings for dipoles, butted together and attached to an adjustable, welded-aluminum tubular frame. Aluminum extrusions, approximately 7 inches square and 40 inches long, were

Fig. 2-128. Model of partial section of phased array antenna.

attached to the back of these plates to house the removable electronic packages and their dipoles. Initial estimates of the weight of these packages ranged from 15 to 20 pounds. Trusses made of rectangular aluminum tubing, spaced at every fourth row, supported the ground plane -- module complex from a sturdy base structure made up of structural beams. The trusses were necessarily of sufficient depth to permit removal of the electronic packages from the extruded boxes without interference with the base structure. Adequate catwalks and ladders would be provided on the base structure for servicing and maintenance. Since each of the packages would have five connectors for electronic cables and two connectors for water cooling, it became evident that considerable thought should be given to the routing of these services. Space between the housings would have to be utilized for cable runs in order to permit unhampered removal of the packages. The use of the trusswork tubes as water manifolds was considered, and efforts were made to combine common electronic circuits. Weight estimates on this preliminary design, with aluminum structure, were as follows:

		Pounds
Ground plane		1,370
Extruded boxes		13,312
Internal electronics (1024 units at 15 pounds each)		15,360
Trusses		2,200
Adjustable frame		1,100
Base structure		4,600
	Subtotal	37,942
Miscellaneous connectors, adjacent devices, etc.		8,000
	Total	45,942

The above weight did not include any of the cabling or cooling hose.

The preliminary design was based on the assumption that the array would be a low-power 900-Mcps radar. Further investigation by members of the electronics section indicated that a higher-power 1300-Mcps radar would prove more useful from their standpoint and that other preliminary studies should be made.

A shipboard application that involved mounting different array sizes aboard a vessel of the C-4 class was also investigated. The problems connected with shipboard mounting were necessarily compounded not only by the major physical modifications to the superstructure of the ship but also the resultant effect that these large, heavy structures would have on the center of gravity, center of buoyancy, and the metacenter of the ship. Other problems were the pitch, yaw and roll of the vessel. An investigation was made into the necessary bearing for azimuth rotation of the array, and it appeared that an 8-inch gun turret bearing would be adequate.

It was later decided, however, that the most useful tool for immediate needs would be a stationary land-based radar with 0.58λ spacing (5.26 inches). It was also assumed that the array would be radome-housed, thereby eliminating wind loading. The number of elements had been established as 4096 (64 × 64).

In order to more realistically determine loading on the structure, the electronic package was reviewed, and its size and weight were re-estimated according to latest component development. The new estimate shows a weight of approximately 100 pounds per unit, and the
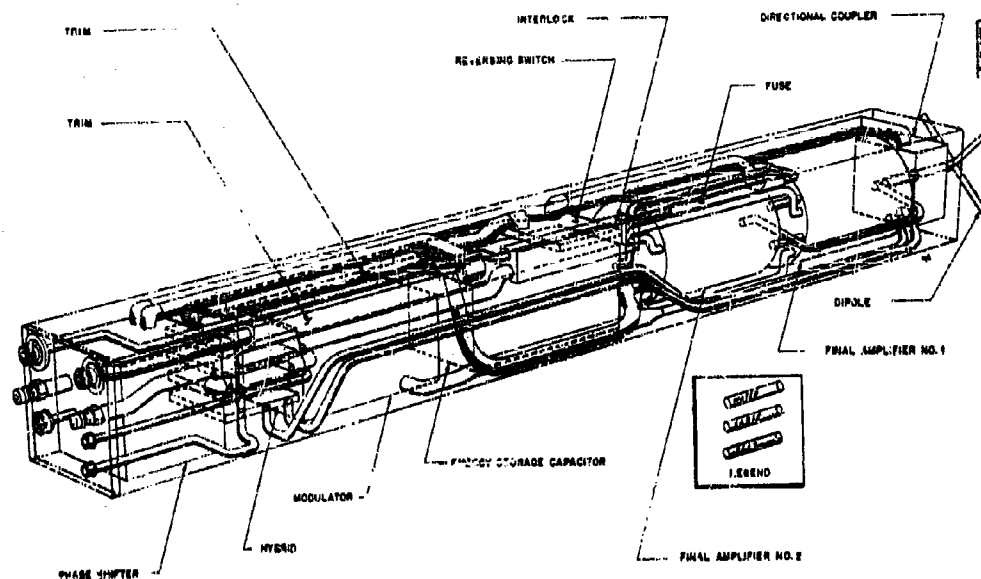
Fig. 2-129. Phased array transmitter module.

minimum external dimensions appear to be $4\frac{1}{2} \times 4\frac{1}{2} \times 42$ inches plus, of course, the protruding dipoles. Figure 2-129 shows a sketch of a proposed package.[*] The dipoles have been rotated to 45° to be within the cross section of the package.

Since the package dimension was 4.5 inches with an element-to-element spacing of 5.26 inches, the remaining space of 0.76 inch was available for housing and support structure. An initial approach employing interlocking stacked extrusions, behind the ground plane, with a confining band around the periphery of the 28-foot square array was investigated. Since the average thickness of the extrusions was $\frac{3}{8}$ inch, it was found that the weight of the extrusions themselves amounted to 144,000 pounds. Also, when each of the boxes was loaded with the 100-pound package and unsupported across the entire span, the deflection would exceed the allowable $1/64\lambda$ or 0.142 inch. Shear between boxes was difficult to overcome without precise machining on shear bars and slots.

An approach that appears feasible is one that employs jig-welded grids of $\frac{1}{2}$-inch aluminum bar stock at the front and rear of the array which are interconnected with thin-wall (0.1 inch) extrusions. Units of 4×8 elements can be shop-fabricated for precision and erected on posts supporting common corners. The posts stand off from a concrete foundation having access stairs for servicing. The bottom row and one side row can be precisely located by means of accurate base rails. As the units are stacked, clips interlock adjacent units and the supporting post. The front ground plane can be attached directly by screws to the forward grid. Figure 2-130 shows a cut-away sketch of the configuration.

Assuming this type of construction, with 0.1-inch wall thickness of extrusion, the weight of the grid and extrusion combination would be 44,000 pounds. By decreasing the wall thickness to 0.0625 inch, the weight would drop to 28,300 pounds; however, this latter thickness appears to be slightly marginal for extrusion tolerances. Preliminary calculations indicate this type of construction to be capable of supporting the present assumed loads.

The receiving array will be similar to the transmitting array in over-all size and will employ a like amount of elements. However, unlike the heavy transmitting elements, it is estimated that each receiving element will consist of lightweight printed circuitry, which will minimize the problem of support structure. Therefore, the details of this design have not been pursued.

C. DETAILED STUDY PLANS

Further studies will be undertaken on the support structures described above and on other configurations, which will be directed toward an ultimate design encompassing more efficient use of materials combined with ease of fabrication and erection.

---

[*] See Part 2, Ch. VI, Sec. B.
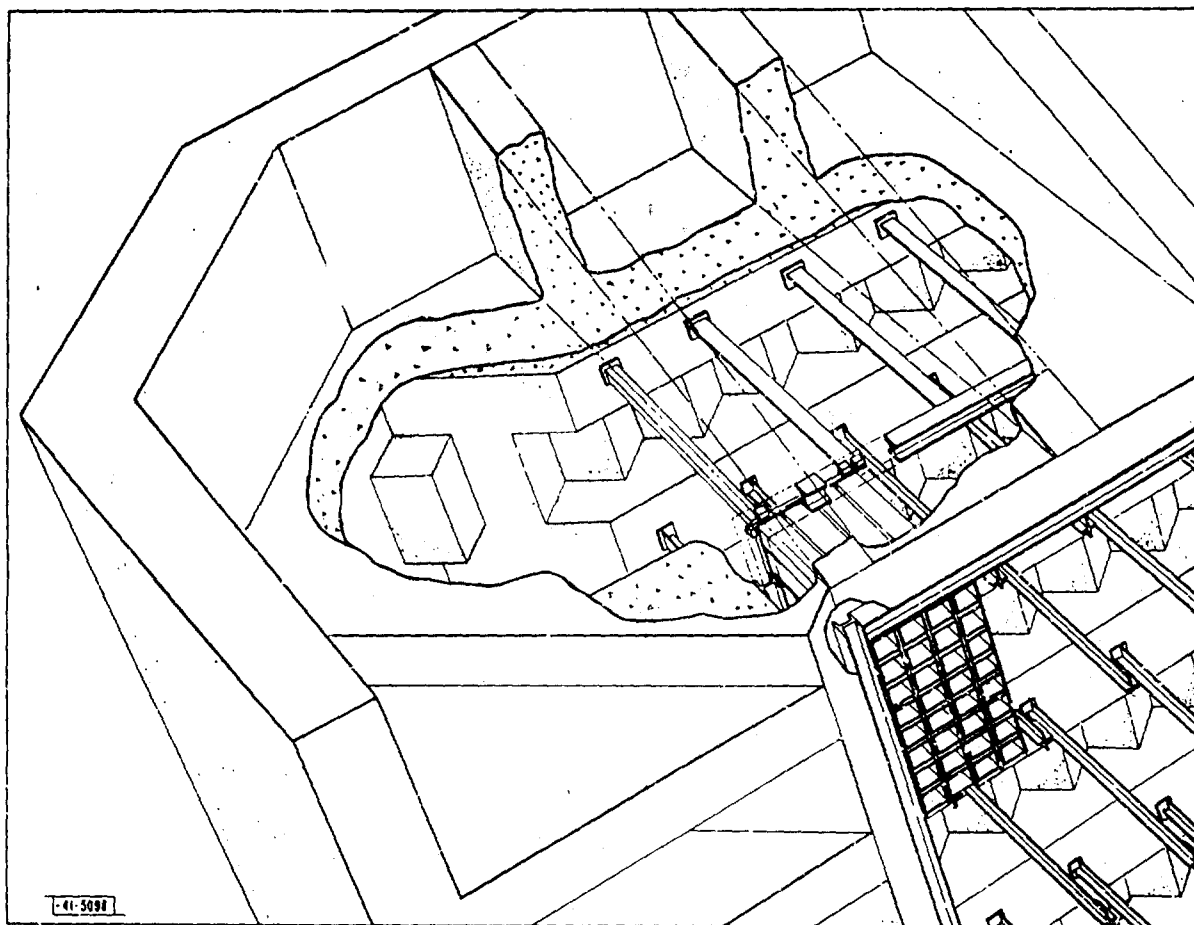
Fig. 2-130. Proposed phased array structure.

PART 3

SUPPORTING STUDIES

Introduction and Abstract

Part 3 reports the work of various basic investigations into the fundamentals of array antennas and array radar systems. The studies are grouped into three chapters, and a summary can be found at the start of each chapter except Chapter III. Because of the length of that chapter and a diversity of topics taken up therein, the summaries will be found at the beginning of the appropriate sections [indicated by capital letters (A, B, C, etc.) in the Table of Contents].

Chapter I reports the results of investigation into the effect of mutual coupling on the gain and the impedance as a function of angle of scan of dipoles in planar arrays, for various element spacings and heights of the dipoles above the ground plane. This work is a continuation of work reported in the previous technical report, and will undoubtedly be continued in the future, branching out into elements not so easily analyzed as dipoles.

Chapter II deals with the limitations of phased arrays from the bandwidth standpoint. In particular, the effects of an array antenna on range resolution and range measurement accuracy of the received waveform are reported. Detailed results are given for the case where the transmitted signal is a rectangular pulse.

Lastly, Chapter III deals extensively with the effect of random "errors," both unintentional and intentional, in array antennas. The previous "small error" theory is extended to account for large phase errors which may be deliberately introduced for reasons brought out in the chapter, and several topics are investigated using this development. Among these are (1) grating lobe suppression by element position randomization, (2) far-field shaping by varying the density of the elements of an array rather than their amplitude, and (3) a review of the effects of errors on sidelobe levels, including a new and simpler result for the gain degradation arising therefrom. Finally, the effects of random errors on pointing error are examined, and formulas useful for the effects of both the sum and difference patterns of monopulse arrays are presented.

CHAPTER I
THE EFFECTS OF MUTUAL COUPLING ON THE GAIN AND IMPEDANCE
OF SCANNING DIPOLE ARRAYS

SUMMARY   J. L. Allen

This section is devoted to the results obtained during the past year from the continued investigation of the effects of mutual coupling in arrays. In the previous technical report[*] of this project, an approach to the evaluation of mutual coupling effects through the use of the element pattern concept was outlined, and some results were given for linear arrays of dipoles. Although this concept is not restricted to dipole arrays, at least as an experimental tool, it is amenable to analysis only for such simple elements. Therefore, prior to attempting to get a better understanding of more "exotic" elements (such as log-periodics), we have attempted to thoroughly investigate coupling in dipole arrays, particularly in planar dipole arrays. The results of this investigation are reported in the following section.

[*] J. L. Allen, et al., "Phased Array Radar Studies, 1 July 1959 to 1 July 1960," Technical Report No. 228 [U], Lincoln Laboratory, M.I.T. (12 August 1960), ASTIA 249470, H-335.

To get a sufficiently broad picture of the effects of mutual coupling on dipole array gain and element impedance as a function of scan angle, an analysis of these effects has been carried out with the aid of a digital computer and a small test array. In order to maximize the "insight content" of the results, wide ranges of parameters were used. For example, element spacings ranging from 0.5 to 0.8 wavelength were used, and the height of the dipoles above the ground plane was varied from $\lambda/8$ to $3\lambda/8$ in steps of $\lambda/16$.

In order to simplify the computation, results were obtained for the characteristics of the center element of two different small arrays of 63 and 25 elements. The comparison of these results with known results for "infinite" arrays confirms the validity of this approach, both analytically and experimentally, but with certain reservations as pointed out in the text.

It is shown that the gain of the array as a function of scan angle depends primarily upon the element-to-element spacing alone and is quite insensitive to other parameters, such as the height of the dipoles above the ground plane. The gain variation of the array when the elements are fed from constant impedance sources is shown to be very nearly that predictable on a directivity basis from the well-known gain vs area relationship, modified to account for the grating lobe formation with scan. On the other hand, it is seen that the change in element impedance is considerably affected by parameters which have little effect on the array gain behavior, and possibilities for minimizing mismatch caused by scanning are pointed out making use of this result.

A. INTRODUCTION

Although the phenomenon of mutual coupling between dipole antennas was long ago reduced to mathematical formulation,[*][†][‡] the recent upsurge of interest in phased array antennas of large numbers of radiators has served to emphasize the fact that the effects of mutual coupling on the various aspects of array performance are not, as yet, reduced to "handbook engineering" levels. Although several recent papers have been published on the subject of mutual impedance effects in dipole arrays, attention has usually been restricted to half-wavelength spacing between elements and quarter-wavelength spacing from dipole to ground plane. Further, explicit attention has been concentrated almost exclusively on the effect of the mutual coupling on the variation of element driving impedance with scan angle, ignoring explicitly the important question of the effect on array gain with scan angle.

The primary purpose of the investigation reported here was to examine both these effects in planar arrays of regularly spaced dipoles, over a range of element spacings and a range of dipole-to-ground-plane spacings, in order to facilitate more enlightened design of scanning dipole arrays. Secondarily, some information about the effects of array size on mutual coupling phenomena was obtained indirectly by calculating relevant data for two different sized arrays.

As outlined in the text, the array element impedance variation was calculated by the usual mesh equation approach, making use of certain approximations appropriate to large arrays. To investigate the effects of coupling on the array gain, the concept of an "element gain function" (the gain vs angle of a typical element in a passive array) is used, and its relation to the variation of array gain with scan angle is pointed out.

[*] A. A. Pistolkors, "The Radiation Resistance of Beam Antennas," Proc. IRE 17, 562 (1929).

[†] P. S. Carter, "Circuit Relations in Radiating Systems and Applications to Antenna Problems," Proc. IRE 20, 1004 (1932).

[‡] R. W. P. King, The Theory of Linear Antennas (Harvard University Press, 1949).

Computed data for the center element of planar arrays of 63 and 25 elements are compared in order to estimate the effects of finite size on results obtained from both formulations, and experimental checks of the results for the smaller size will be presented. Comparisons of the results of this study with the results of other writers will be made.

It will be seen that there is a consistent trend in the results indicating that the effects of mutual impedance on array gain are essentially dependent only upon element spacing and produce results easily predictable from array directivity considerations. The good agreement of the experimental results with the computed data, despite the use of dipoles that were poor approximations to the dipoles theoretically considered, emphasizes this fact.

It is also pointed out that even though the gain as a function of scan results depends essentially only on element spacing, other variables have a significant effect upon the element VSWR variation with scan, and that the VSWR can be held to quite reasonable limits by judicious choice of such parameters as the height of the dipoles above the ground plane.

No explicit consideration will be given in this report to edge effects. Rather, attention is solely directed toward the questions of the effects of mutual impedance on the interior elements of large arrays, and the ability to predict these effects by the use of data taken on the center element of a small array. Some examples of edge effects on dipole gain functions can be found in another report[*] (for linear arrays only), and data on the impedance variation of edge elements for one particular array configuration are given by P. S. Carter, Jr.[†]

B. MATHEMATICAL DESCRIPTION OF MUTUAL IMPEDANCE EFFECTS

1. Basic Concepts and Definitions

It is well known that the currents and voltages existing at the terminals of the elements of a dipole array can be expressed by circuit equations. For a two-dipole array, as shown in Fig. 3-1, these equations are of the form

$$
\left.
\begin{aligned}
V_{mn} &= Z_{mn,mn} I_{mn} + Z_{mn,pq} I_{pq} \\
V_{pq} &= Z_{pq,mn} I_{mn} + Z_{pq,pq} I_{pq}
\end{aligned}
\right\}
\tag{1}
$$

where the notation is indicated in the figure (double subscripting is used in anticipation of application to planar arrays). The quantities $Z_{mn,mn}$ and $Z_{pq,pq}$ are the self-impedance of the two dipoles, while $Z_{mn,pq}$ and $Z_{pq,mn}$ are the mutual impedances between the two dipoles and are equal for reciprocal dipoles and media, as will be assumed throughout this section. If the two dipoles are completely isolated from other antennas and other reflecting surfaces, the self-impedances will be the normal radiation impedance, Z_r, of a dipole in free space.

The mutual coupling between dipoles acts in the manner of a generator of open-circuit voltage, $V'_{mn} = Z_{mn,pq} I_{pq}$, as indicated in the equivalent circuits of Fig. 3-2, and either increases or decreases the current through the antenna (in comparison to the current in the absence of mutual effects), depending upon the induced polarity.

To an observer looking into the terminals of the antenna, the presence of the generator leads to an alteration of the antenna impedance. This impedance will be referred to as the element driving impedance, Z_D, which depends upon the relative current flowing in the two dipoles:

[*] J.L. Allen, et al., op. cit.

[†] P.S. Carter, Jr., "Mutual Impedance Effects in Large Beam Scanning Arrays," Trans. IRE, PGAP AP-8, 276 (1960).
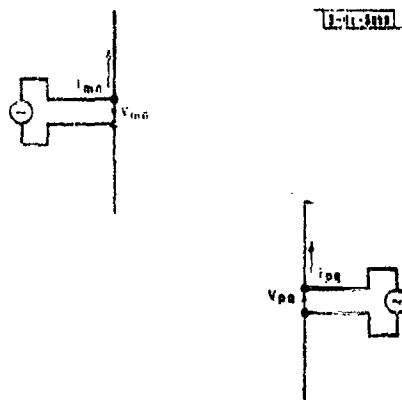
Fig. 3-1. Dipoles and notation.
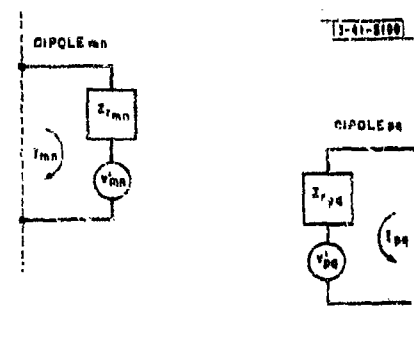
Fig. 3-2. Equivalent circuit of Fig. 3-1 dipoles.
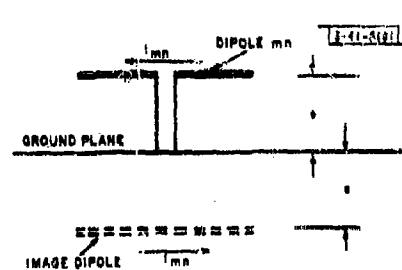
Fig. 3-3. Dipole above ground plane and its image.
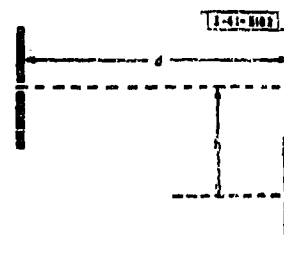
Fig. 3-4. Dipole spacing nomenclature.
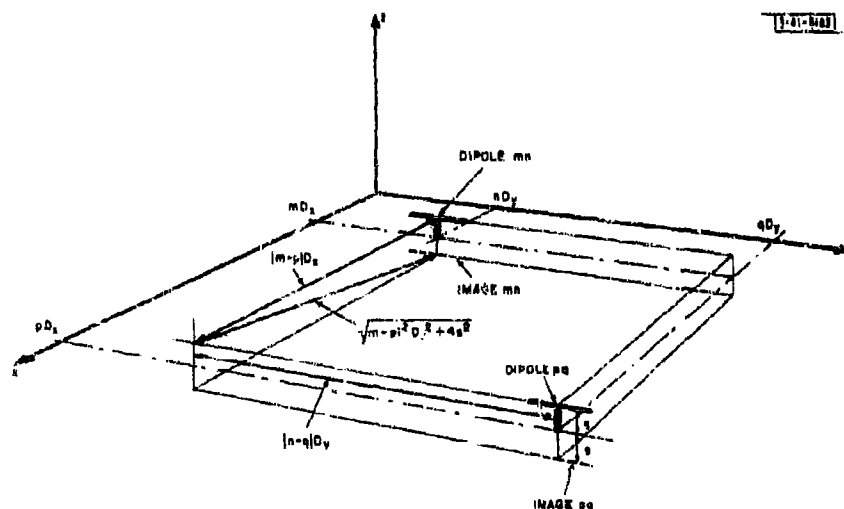
Fig. 3-5. Geometry of dipoles above ground plane (Z = 0 is ground plane).

202

$$Z_{D_{mn}} = \frac{V_{mn}}{I_{mn}} \tag{2}$$

$$= Z_{mn,mn} + Z_{mn,pq} \frac{I_{pq}}{I_{mn}} \tag{3}$$

The basic element of this study will be a dipole above a ground plane, as indicated in Fig. 3-3. However, formulae and tables of mutual impedance are almost exclusively stated in terms of impedance between isolated dipoles. Data for "free-space" dipoles are readily adapted to our "element" by image theory. It can be readily verified[*] that the self-impedance of such an element is

$$Z_{mn,mn} = Z_r - Z_m(2s, 0) \tag{4}$$

where Z_r is the normal dipole radiation impedance, and $Z_m(d, h)$ is the mutual impedance between two dipoles. The dipoles are oriented as indicated in Fig. 3-4, where d is the separation between dipole axes in the plane of the dipoles, and h measures their center displacement perpendicular to d. By writing four equations in a manner similar to Eq. (1) for two dipoles plus two images, the mutual impedance between two such basic elements, $Z_{mn,pq}$, is seen to be the difference of the mutual between the two dipoles of the same orientation in free space and the mutual between one dipole and the image of the other in free space. In the geometry of Fig. 3-5, one can write

$$Z_{mn,pq} = Z(|m - p|D_x, |n - q|D_y) - Z(|m - p|^2 D_x^2 + 4s^2, |n - q|D_y) \tag{5}$$

By the use of Eqs. (4) and (5), then, mesh equations such as (1) can be written directly for an array considering an elemental radiator to be the combination of a dipole and the ground plane.

2. Some Important Assumptions About the Sufficiency of Mutual Impedance as a Description of Coupling

It is apparent that relationships such as Eq. (1) give only terminal information about the antenna currents. In order to apply the results of a study of mutual impedance to array pattern effects, some assumptions must be made regarding the distribution of the current on the antenna. The usual assumption is that the mutually induced currents are distributed in a form identical to that the current would assume on a single driven dipole in free space. It is further assumed that the measurement of the terminal current gives a true indication of the magnitude of the current on the antenna.

For dipoles, there appears to be sufficient justification for the latter assumption if the coupling between feed lines carrying traveling waves, which may give rise to directional coupling, is negligible. The former assumption is generally conceded to be valid for very thin dipoles, and was found (see below) to produce good agreement with experiment even in the case of relatively thick dipoles.

3. Special Assumptions of this Study

An additional requirement for straightforward application of Eq. (1) is that a sufficient description of the networks which drive the dipoles be taken into the equations. It is assumed that

---

[*] J.D. Kraus, Antennas (McGraw-Hill, New York, 1950).
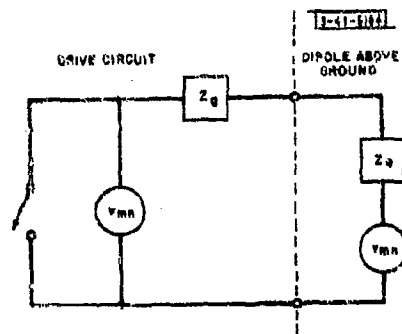
Fig. 3-6. Equivalent circuit of dipole and drive circuit.
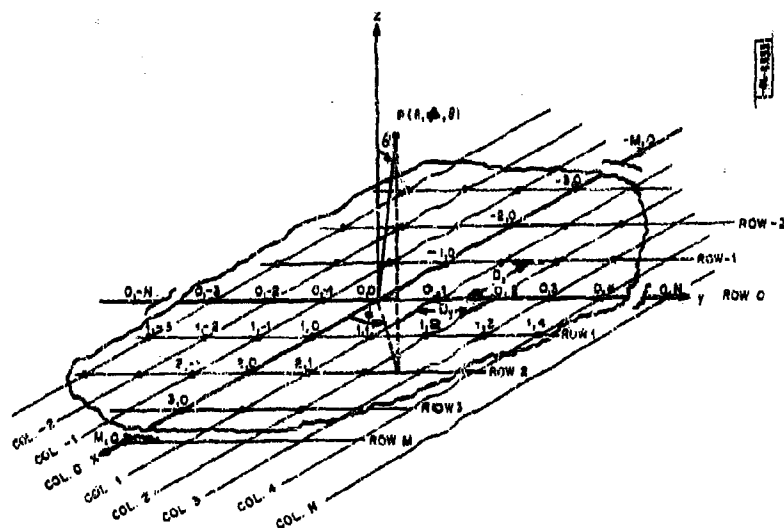
Fig. 3-7. Generalized planar array geometry.

the dipoles are fed by independent constant voltage generators, with the independently adjustable open-circuit voltages. Schematically, the circuit of each dipole is then of the form of Fig. 3-6 (the shorting switch is provided for future use). For simplicity, and since it is the usual case for large arrays, all generator impedances are considered equal and all element self-impedances as given by Eq. (4) are also considered equal ($Z_{mn,mn} = Z_a$, all m and n) implying that the ground plane is enough larger than the array to neglect ground plane edge effects. It is assumed that Z_g includes any matching impedances.

For this type of drive, Eq. (1) can be rewritten in terms of the drive voltages, v_{mn}, as

$$v_{mn} = (Z_g + Z_a) I_{mn} + Z_{mn,pq} I_{pq}$$
$$v_{pq} = Z_{pq,mn} I_{mn} + (Z_g + Z_a) I_{pq} \qquad (6)$$

The assumption of independent drive is valid in arrays using a unilateral amplifier behind each element. It is further well approximated in arrays using passive RF feed networks with directional-coupler junctions. It is, on the other hand, certainly not valid for slotted waveguide arrays and certain other types. While some analyses have been made in general terms of such structures,[*][†] it will not be attempted here.

It is also assumed that no attempt is made in the array driving voltages to compensate for mutual coupling effects. The array elements are taken as equally spaced, as indicated in Fig. 3-7, and the element drives are supposed to be progressively phased and amplitude tapered so that the drive voltages are related to the desired pointing angle by

$$v_{mn}(\tau_o, \mu_o) = a_{mn} e^{-jk[mD_x\tau_o + nD_y\mu_o]} \qquad (7)$$

where the a_{mn} are the real amplitude taper coefficients, and Θ_o, ϕ_o defines the angle at which it is desired to point the beam (in the geometry of Fig. 3-7) through the equivalences

$$\tau_o = \sin\Theta_o \cos\phi_o$$
$$\mu_o = \sin\Theta_o \sin\phi_o \qquad (8)$$

Lastly, it is assumed that reciprocity applies throughout, and the entire analysis is carried out from the viewpoint of a transmitting array.

4. An Exact Formulation of the Element Currents

The relationships of Eq. (6) can be expanded to include any number of elements. For large numbers, it is convenient to use matrix notation

$$v] = [Z] I] \qquad , \qquad (9)$$

where $v]$ and $I]$ are column matrices and $[Z]$ is a square, symmetrical matrix, the elements on the diagonals being $Z_g + Z_a$. A typical equation of the matrix is

[*] J. Blass and S. J. Rabinowitz, "Mutual Coupling in Two-Dimensional Arrays," 1957 IRE WESCON Convention Record, Part 1, pp. 134-139.

[†] I. P. Kaminow and R. J. Stegen, "Waveguide Slot Array Design," Technical Memorandum No. 348, Hughes Aircraft Company, Culver City, California (1 July 1954).

$$v_{mn} = \sum_p \sum_q Z_{mn,pq} I_{pq} \quad . \tag{10}$$

where $Z_{mn,mn} = Z_g + Z_a$.

To exactly (within the previously stated assumptions) formulate the currents in terms of the drive voltages, we formulate an admittance matrix $[Y]$ such that $[Y] = [Z]^{-1}$, and then we have typically

$$I_{mn}(\tau_o, \mu_o) = \sum_p \sum_q Y_{mn,pq} v_{pq}(\tau_o, \mu_o) \quad ,$$

or using (7) for v_{pq}:

$$I_{mn}(\tau_o, \mu_o) = \sum_p \sum_q a_{pq} Y_{mn,pq} \exp\{-jk(pD_x\tau_o + qD_x\mu_o)\} \quad . \tag{11}$$

Equation (11), while it lends little physical insight into mutual effects, will be useful later.

5. The "Element Gain Function" Concept

If one utilizes the shorting switches indicated in the equivalent circuits of Fig. 3-6, any element of the array can be separately energized, while all others are terminated in their normal generator impedance. If the radiation pattern of each element is ascertained under these conditions, the total array field will be the sum of each pattern with the proper phase delay as a function of position:

$$F(\tau,\mu) = \sum_m \sum_n f_{mn}(\tau,\mu) i_{mn} \exp\{jk(mD_x\tau + nD_y\mu)\} \quad . \tag{12}$$

where

$f_{mn}(\tau,\mu)$ is the pattern of the mn^{th} element when all others are properly passively terminated, per ampere of current into the terminals under this condition.

i_{mn} is the current into the terminals of the mn^{th} element with all others properly terminated (it is only part of the I_{mn}'s previously used; hence, we can refer to i_{mn} as a "partial current").

This method of array representation has the virtue that the partial currents are independent of each other and assigns the mutual coupling effects almost entirely to the element pattern (the qualification "almost" is required since even with all other elements passively terminated, the antenna driving impedance is not exactly Z_a).

Defining the gain of the array as the ratio of the main beam power density to the total power available to the array from its generators (thus properly including mismatch effects in the gain), we can write the gain as a function of pointing angle as

$$G(\tau_o, \mu_o) = \frac{4\pi |F(\tau_o, \mu_o)|^2}{\sum_m \sum_n \dfrac{a_{mn}^2}{4R_g}} \quad , \tag{13}$$

where R_g is the real part of the generator impedance, and therefore

$$\sum_m \sum_n \frac{a_{mn}^2}{4R_g}$$

is the power available to the array.

The partial current i_{mn} is given by the value of I_{mn} when all $a_{pq} = 0$ except a_{mn} and is therefore, by (11)

$$i_{mn} = a_{mn} Y_{mn,mn} e^{-jk[mD_x \tau_0 + nD_y \mu_0]}$$

$$= v_{mn} Y_{mn,mn}$$

Thus, (13) becomes

$$F(\tau, \mu) = \sum_m \sum_n f_{mn}(\tau, \mu) a_{mn} Y_{mn,mn} \exp\{jk[mD_x(\tau - \tau_0) + nD_y(\mu - \mu_0)]\} \quad . \tag{14}$$

Both f_{mn} and $Y_{mn,mn}$ depend upon the other (non-driven) dipoles in the array only to the extent that the parasitic currents induced in the other elements couple back into the mn^{th}. It can be established[*] that the mutual coupling between dipoles located a distance s above an infinite ground plane decays asymptotically with separation R as

$$\frac{I_{induced}}{I_{exciting}} \rightarrow K_p s^2 \frac{e^{-jkR}}{R^2} \tag{15a}$$

for parallel dipoles, and

$$\frac{I_{induced}}{I_{exciting}} \rightarrow K_c s^2 \frac{e^{-jkR}}{R^3}. \tag{15b}$$

for collinear dipoles, where K_p and K_c are constants, with these variations becoming quite accurate for spacings as small as a wavelength for s of the order $\lambda/4$. Thus, the parasitic current varies as $1/R^2$ to $1/R^3$ compared to the driven current. Consequently, the effect of the parasitic current on the driven element varies as $1/R^4$ to $1/R^6$.

Thus, both f_{mn} and $Y_{mn,mn}$ should be relatively insensitive to edge effects; for even a moderate sized array, we should be able, with little error, to approximate f_{mn} and $Y_{mn,mn}$ in (14) by f_{00} and $Y_{00,00}$ and write

$$F(\tau, \mu) \approx f_{00}(\tau, \mu) Y_{00,00} \sum_m \sum_n a_{mn} \exp\{jk[mD_x(\tau - \tau_0) + nD_y(\mu - \mu_0)]\} \quad .$$

From (13), we have then that the gain of an array which is large enough to justify these assumptions will be

$$G(\tau_0, \mu_0) = \frac{4\pi |f_{00}(\tau_0, \mu_0)|^2 |Y_{00,00}|^2}{\frac{1}{4R_g}} \frac{[\sum \sum a_{mn}]^2}{\sum \sum a_{mn}^2} \quad . \tag{16}$$

---

[*] J. L. Allen, et al., op. cit., pp. 187-193.

The ratio of the summations is just the product of the efficiency of the amplitude taper η times the total number of array elements N_T. Further, the gain of a single driven element in its array environment, with all other elements terminated in Z_g, is, by the definition of $i_{mn}(\tau, \mu)$, given by

$$g_{mn}(\tau_0, \mu_0) = \frac{4\pi |f_{mn}(\tau_0, \mu_0)|^2 |v_{mn} Y_{mn,mn}|^2}{\dfrac{|v_{mn}|^2}{4R_g}} \quad . \tag{17}$$

Comparison with (16) gives the simple result:

$$G(\tau_0, \mu_0) = g_{00}(\tau_0, \mu_0) \, \eta N_T \quad , \tag{18}$$

indicating that for a fixed number of elements and a fixed amplitude taper, the array gain is completely specified by the element gain function, $g_{00}(\tau_0, \mu_0)$, of a typical element if the array is large enough so that almost all elements have essentially identical gain functions. Note that the element gain function angular variation is determined solely by the pattern of a single typical element in the passively terminated array, $|f_{00}(\tau, \mu)|^2$, as is apparent from (17).

The gain function concept has considerable practical utility and was used extensively in this study. The prime reason for its utility lies in the fact that while (18) is only accurate for arrays in which essentially all gain functions are identical, the gain function can be determined (experimentally or analytically) from an array which is only large enough so that the gain function of the center element is essentially unaffected by enlarging the array. As justified below, for example, a 5 × 5 dipole array is often sufficient.

For computational purposes, it is useful to have an exact analytic expression for the gain function of a center element. From (17), it is seen that all that is required is a formula for $f_{00}(\tau, \mu)$. By the definition of f_{00} and Eq. (11), it is seen that the parasitic current in the mn^{th} element with only v_{00} non-zero is such that the element pattern of the center element can be written as

$$i_{00} f_{00}(\tau, \mu) = f_i(\tau, \mu) \sum_m \sum_n a_{00} Y_{mn,00} \exp[jk(mD_x \tau + nD_y \mu)] \quad ,$$

where $f_i(\tau, \mu)$ is the pattern of an isolated element (above a ground plane). We have that

$$i_{00} = a_{00} Y_{00,00} \quad ,$$

and therefore,

$$f_{00}(\tau, \mu) = \frac{f_i(\tau, \mu)}{Y_{00,00}} \sum_m \sum_n Y_{mn,00} \exp[jk(mD_x \tau + nD_y \mu)] \quad .$$

Further, we note that the maximum gain obtainable from an isolated element is

$$g_{i_{max}}(\tau_0, \mu_0) = \frac{4\pi |f_i(\tau_0, \mu_0)|^2}{\dfrac{|v|^2}{4R_a}} \left| \frac{v}{2R_a} \right|^2 \quad ,$$

where R_a is the real part of the isolated element's self-impedance. Thus, we can write the ratio of the element gain function to the maximum gain obtainable from a free-space element as

$$\frac{g_{oo}(\tau_o, \mu_o)}{g_{i_{max}}(0,0)} = 4R_g R_a \left| \sum_m \sum_n Y_{mn,oo} \exp\left[jk(mD_x\tau_o + nD_y\mu_o)\right] \right|^2 . \qquad (19)$$

For dipoles mounted a distance s above the ground plane, the value of $g_{i_{max}}(0,0)$ can be shown to be[*]

$$g_{i_{max}}(0,0) = 4g_d(0,0) \frac{R_r}{R_a} \sin^2 ks \quad , \qquad (20)$$

where $g_d(0,0)$ is the broadside gain of a single dipole in free space, and R_r is its radiation resistance [for thin, half-wave dipoles,[†] $g_d(0,0) \approx 1.64$ and $R_r \approx 73.2$ ohms]. Thus, the broadside gain-function value is

$$16g_d(0,0) R_g R_r \left| \sum_m \sum_n Y_{mn,oo} \right|^2 \sin^2 ks \quad . \qquad (21)$$

As the array becomes infinite, we shall demonstrate [see Eq. (29)] that

$$g_{oo}(0,0) \rightarrow 4\pi \frac{D_x D_y}{\lambda^2}$$

if the elements are matched when phased such that the beam points at broadside.

In passing, it should also be noted that the derivation of Eq. (18) need not explicitly involve any mutual impedance concepts. The quantity $Y_{mn,mn}$ appearing in the derivation cancels out in the final result, and since its reciprocal is the circuit impedance of the mn^{th} element with all others terminated it is certainly non-zero. Thus, Eq. (18) is valid without some of the restrictive assumptions about the sufficiency of mutual impedance as a coupling description mentioned in Sec. B-3 and should be a valid description of gain for any large array of nominally identical equally spaced elements. The specific form of the gain function given by Eq. (19) is, of course, dependent upon the sufficiency assumption.

6. Some Large Array Approximations

As pointed out in the previous section, the effects of mutual coupling fall off rapidly enough with element separation so that one can, in principle, build an array large enough for any prescribed fraction of the total number of elements to see an environment which is arbitrarily close to the environment that an element would see in an infinite array. Put another way, the array can be made so large that a negligibly small number of elements suffer from "edge effects." For almost all the elements of such an array, one can greatly simplify the expressions for element current, element driving impedance and gain function. How large an array is required to justify these assumptions is a question that we will attempt to answer below.

If the array is essentially infinite, all elements will have identical driving impedances and gain functions, and we can confine our attention for convenience to the center element. We further assume that an infinite array has no measurable amplitude taper over any finite portion and, consequently, we can ignore the amplitude taper and write all drive voltages in the form

$$v_{mn} = v_{oo} \exp\left[-jk(mD_x\tau_o + nD_y\mu_o)\right]$$

---

[*] J. D. Kraus, Antennas (McGraw-Hill, New York, 1950).
[†] Ibid.

for pointing the beam at τ_0, μ_0. Further, all currents will now have the same relation to their drive voltages, and we can approximate

$$I_{mn} = I_{00} \exp[-jk(mD_x\tau_0 + nD_y\mu_0)] \quad .$$

In this case, Eq. (10) becomes

$$V_{00} = I_{00} \sum_m \sum_n Z_{00,mn} \exp[-jk(mD_x\tau_0 + nD_y\mu_0)] \quad .$$

Since $Z_{00,00} = Z_g + Z_a$, the driving impedance for the large array case is simply

$$Z_D(\tau_0, \mu_0) = \frac{V_{00}}{I_{00}} - Z_g$$

$$= Z_a + \sum_{\substack{m \ n \\ m,n \neq 0,0}} Z_{00,mn} \exp[-jk(mD_x\tau_0 + nD_y\mu_0)] \quad , \tag{23}$$

where $m,n \neq 0,0$ implies the summation excludes $Z_{00,00}$.

For deriving an expression for the gain function for a large array, we note that as an alternative to Eq. (12) as a representation of the array far-field, we could formulate an expression using the I_{mn}'s and the pattern of an isolated element, $f_i(\tau, \mu)$:

$$F(\tau, \mu) = f_i(\tau, \mu) \sum_m \sum_n I_{mn} \exp[jk(mD_x\tau + nD_y\mu)] \quad . \tag{24}$$

Since, for almost all elements, the I_{mn}'s are related to the V_{mn}'s by the same driving impedance,

$$I_{mn} = \frac{V_{mn}}{Z_g + Z_D} = \frac{a_{mn}}{Z_g + Z_D} \exp[-jk(mD_x\tau_0 + nD_y\mu_0)] \quad .$$

We can rewrite the array gain expression of (13) in the form:

$$G(\tau_0, \mu_0) = \frac{4\pi |f_i(\tau_0, \mu_0)|^2}{\dfrac{\sum \sum a_{mn}^2}{4R_g}} \frac{\left(\sum_m \sum_n a_{mn}\right)^2}{|Z_g + Z_D|^2} \quad .$$

The maximum (matched) gain obtainable from an isolated element with driving impedance Z_a is

$$g_i(\tau_0, \mu_0) = \frac{4\pi |f_i(\tau_0, \mu_0)|^2}{\dfrac{|V|^2}{4R_a}} \left|\frac{V}{2R_a}\right|^2 = \frac{4\pi |f_i(\tau_0, \mu_0)|^2}{R_a} \quad ,$$

from which we can write the large array gain as

$$G(\tau_0, \mu_0) = \frac{4R_a R_g}{|Z_g + Z_D|^2} g_{i_{max}}(\tau_0, \mu_0) \eta N_T \quad .$$

Comparison of this result with Eq. (18) for the array gain gives a version of Eq. (19) appropriate for large arrays:

$$\frac{g_{oo}(\tau_o, \mu_o)}{g_{i_{max}}(\tau_c, \mu_o)} = \frac{4 R_g R_a}{|Z_g + Z_D(\tau_o, \mu_o)|^2} \quad . \tag{25}$$

Since this form of the gain function expression neatly ties the array gain and element driving impedance together, it has a number of practical uses. First, it is easily established that to maximize the ratio of the array gain at a particular angle[†] to the gain of the isolated element, one should choose

$$Z_g = Z_D^{*}(\tau_1, \mu_1) \quad , \tag{26}$$

where τ_1, μ_1 represents the angle at which it is desired to maximize the ratio. If Z_g is so chosen, the ratio reduces at the angle in question to

$$\frac{g_{oo}(\tau_1, \mu_1)}{g_{i_{max}}(\tau_1, \mu_1)} = \frac{R_a}{R_D(\tau_1, \mu_1)} \quad . \tag{27}$$

If we choose to maximize Eq. (27) at broadside, from Eq. (20), we can write

$$g_{oo}(0, 0) = 4 g_d(0, 0) \frac{R_r}{R_D(0, 0)} \sin^2 ks \quad , \tag{28}$$

where $g_d(0, 0)$ and R_r are the broadside gain and radiation resistance of a single (no ground plane) isolated dipole, respectively. Numerically, for thin, half-wave dipoles as previously stated,

$$R_r g_d(0, 0) = (73.2) (1.64) = 120 \quad .$$

Stark[‡] shows that for an infinite array of thin dipoles at length L,

$$R_D(0, 0) = \frac{460}{\pi} \frac{L^2}{D_x D_y} \sin^2 s \quad .$$

Thus, for $L = 1/2$, for the array matched at broadside,

$$g_{oo}(0, 0) = 4\pi \frac{D_x D_y}{\lambda^2} \quad . \tag{29}$$

Thus, by (18) one has the familiar expression for the gain of a large array matched for the beam pointing at broadside:

$$G(0, 0) = 4\pi \frac{A}{\lambda^2} \eta \quad ,$$

since $N_T D_x D_y = A$, the total array area.

As a further ramification of the dependence of the gain function on the driving impedance, consider a typical matching circuit for a dipole in the array, which matches a real generator

---

[†] An alternate criterion one might investigate is the question of maximizing the average gain over a wide scanning angle. Due to the periodic nature of $Z_D(\tau_o, \mu_o)$, it would appear that $Z_g = Z_o^{*}$ should be a close approximation to the proper impedance. This criterion was not pursued in detail, however.

[‡] L. Stark, "Radiation Impedance of a Dipole in an Infinite Array," Formal Technical Document FL60-230, Hughes Aircraft Company, Fullerton, California (1 May 1960).
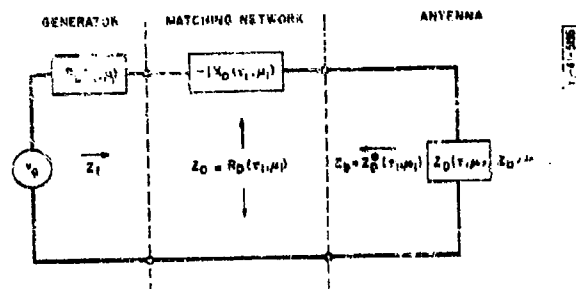
Fig. 3-8. Circuit for matching R_g to $Z_D(\tau_1, \mu_1)$.
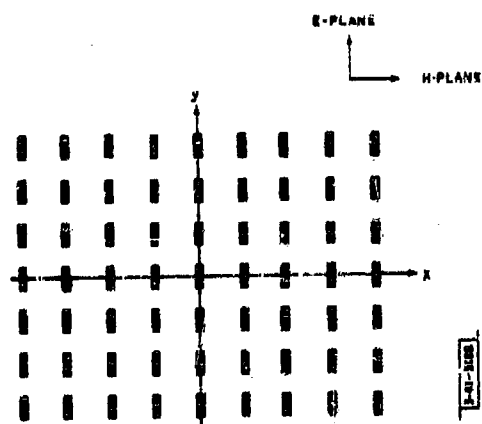
Fig. 3-9. 7×9 element array configuration.

impedance $R_D(\tau_1,\mu_1)$ to the antenna when the array is phased to look at the angle τ, μ is shown in Fig. 3-8. The voltage reflection coefficient looking into the matching network is defined by

$$\Gamma = \frac{Z_f - Z_o}{Z_f + Z_o} \quad ,$$

where Z_f is the impedance seen looking forward into the matching network toward the antenna. It is easily verified that Γ is (zero line length assumed)

$$\Gamma(\tau,\mu) = \frac{Z_D(\tau,\mu) - Z_D(\tau_1,\mu_1)}{Z_D(\tau,\mu) + Z_D^*(\tau,\mu)} \quad .$$

The antenna sees the generator impedance (Z_g of Fig. 3-8) as $Z_D^*(\tau_1,\mu_1)$, and thus, we can write (25) in the form

$$\frac{g_{a}(\tau_o,\mu_o)}{g_{i_{max}}(\tau_o,\mu_o)} = \frac{R_a}{R_D(\tau_1,\mu_1)} \left| 1 - \Gamma(\tau,\mu) \right|^2 \quad , \tag{3 }$$

thus clearly pointing out that the element mismatch depends upon the difference between the ele-ment pattern in the array and the element pattern in free space.

By the use of the relationships developed above, it is possible to compute gain functions and driving point impedances, given expressions for the self- and mutual impedances between dipoles in free space. Even for a relatively small planar array, the calculations rapidly become over-whelming if attempted by hand. For a large array, the calculations even require special tech-niques in programming for a large digital computer. Fortunately, the gain function con-fers the possibility of obtaining meaningful results for large arrays on a modest sized array; consequently, such computations can be managed in a straightforward manner with a computer.

C. THE COMPUTATIONAL PROGRAM

A program was written for the IBM 7090 to compute gain functions and driving impedances of the center element of planar arrays up to 63 elements (limited by storage). Carter's[†] equa-tions for the self- and mutual impedances of infinitely thin, half-wavelength dipoles were used in the program. The ground plane was accounted for by use of Eqs. (4) and (5). The parameters of the program were:

(1) The number of elements in the array (M and N of Fig. 3-7), subject to columns, the restriction that there always be an odd number of rows and

(2) The element-to-element spacings D_x and D_y, subject to the restriction that the element grid be rectangular, as in Fig. 3-7,

(3) The height s of the dipoles above the ground plane,

(4) The value of the generator circuit impedance of the equivalent circuit of Fig. 3-6.

Single-dipole patterns and self-impedances were first computed for ground plane heights $s/\lambda = 0.125, 0.187, 0.250$ and 0.312 ($\frac{1}{8}$ to $\frac{5}{16}$ in steps of $\frac{1}{16}$). Patterns were computed for E-plane, H-plane and diagonal (45°) cuts.

Two different sized arrays were investigated for estimating the effect of array size: a 7-element (collinear direction) by 9-element (parallel) array, as indicated in Fig. 3-9, and a 5 × 5 array.

---

† As given in J.D. Kraus, op.cit.
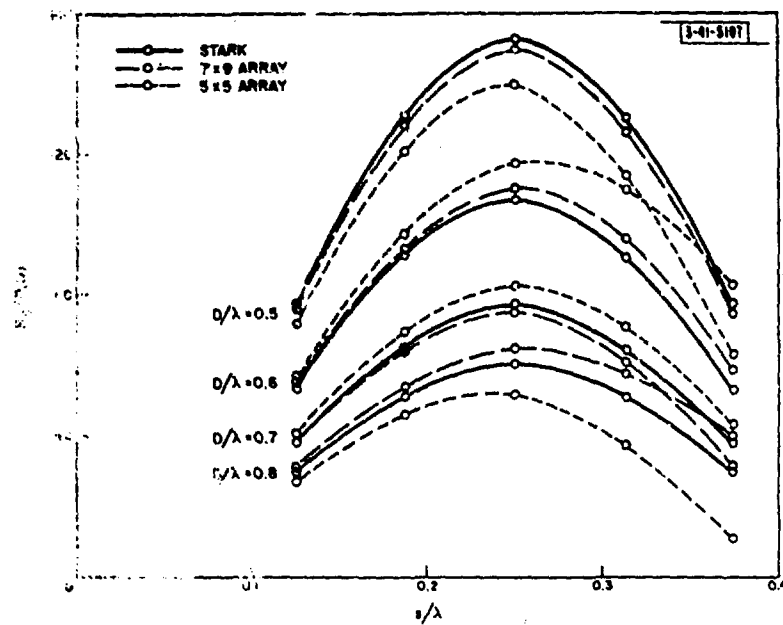
Fig. 1-10. Comparison of broadside driving resistance calculations.

214

Values of the large array driving-point impedance were computed using the large array approximations [Eq. (2.))] for E-plane, H-plane and diagonal scans. Smith Chart plots were made of this impedance normalized by (see Fig. 3-8)

$$Z(\phi_o, \Theta_o) = \frac{Z_D(\phi_o, \Theta_o) - jX_D(0, 0)}{R_D(0, 0)} ,$$

and values of VSWR vs scan angle determined. Impedance data were determined for $s/\lambda = 0.125$, 0.18 0.250, 0.312 and 0. 75 and for square spacings ($D_x = D_y$) of 0.5, 0.6, 0.7 and 0.8 wavelength. computed from Eq. (19) and normalized by dividing by $4\pi(D_xD_y/\lambda^2)$ Gain functions were the alized gain function at $\Theta = \phi = 0$ represents an estimate of the suffi- so that the value of the norm king projections to large arrays. The value should be unity [see ciency of the array size for m elected for the impedance matrix was Eq. (29) since the value of Z_g s

$$Z_g = Z_D^*(0, 0)$$

(computed as described above) in order to maximize the large-array gain at broadside. Also to check some experimental results, gain fu nctions were computed for the 5 × 5 array for another value of Z_g as described in Sec. F. Value s were computed for the values of s and D given above.

D. COMPARISON OF COMPUTED RESULTS WITH KNOWN RESULTS FOR INFINITE ARRAYS

In order to estimate the confidence with whic one may extrapolate the results for the two small array to larger arrays, two theoretical che ks are available. First, as pointed out above, the normalized broadside gain function should approa ch a value of unity for an infinite array when the generator circuit is matched to the broadside drivi ng impedance of the elements. Secondly, by virtue of Stark's[†] results, we have a useful theoretic al prediction of the value of $\bar{R}_D(-,-)$. Since the calculated values of driving impedance were u ed to select the generator circuit im- pedance in the matrix calculations for the element gain fu ction, we will examine the accuracy of the impedance calculations first.

1. Accuracy of Small Array Estimation of Driving Impedance of a Large Array

Since the element driving-point impedance was calculate from a formula which is strictly valid only for infinite arrays, the comparison of the computed values of Z_D with known expres- sions for infinite arrays appears to represent a meaningful tes of the effect of array size on computations of driving impedance. While Stark has given an tic expressions for the complete driving impedance, the resulting representation for the reac part is an infinite series; hence, of little help. His expression for the resistive part of the dr ing impedance, however, consis of only as many terms as there are visible grating lobes for he particular spacing and scan angle.

Utilizing his expression, the curves of Fig. 3-10 were c nstructed, giving the driving resi ance with the array phased to point the beam at broadside. It is seen that the error between our computed results and the results for a truly infinite array inc reases with s. For values of s les than a quarter-wavelength, the 7 × 9 array prediction is corre t within a few per cent, whereas the error in the 5 × 5 array prediction in most cases reaches a value of 10 to 15 per cent for that spacing. For larger values of s, the 7 × 9 array gives close esults for smaller values of D, but in the case of D = 0. , it gives a value in error by almost 0 per cent.

---

† As given in L. Stark, op.cit.
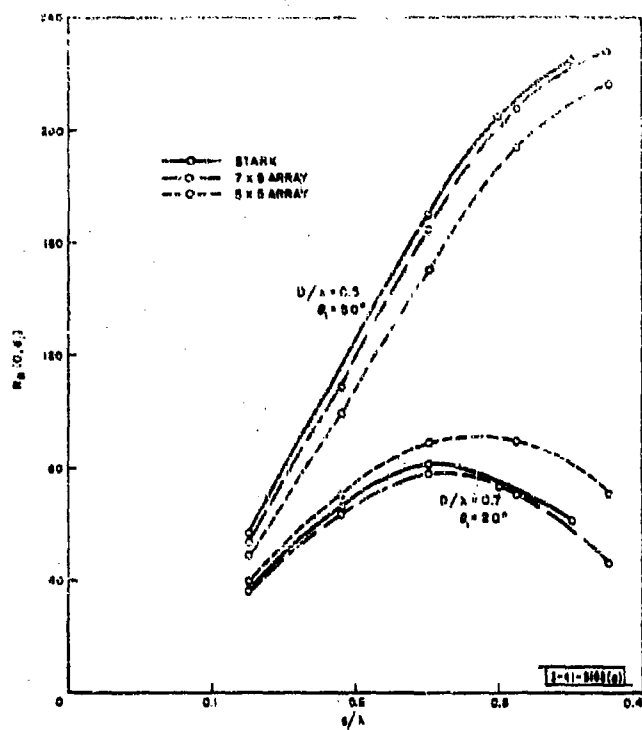
(a) H-plane scan.
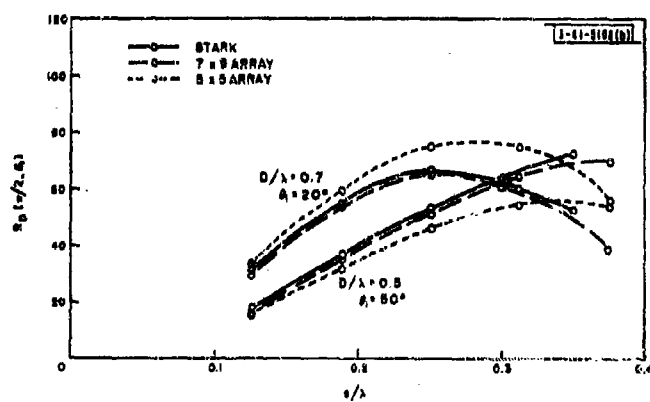
(b) E-plane scan.

Fig. 3-11. Comparison of driving resistance.

The decrease in accuracy with s is due to the increase in mutual coupling that results as the elements are raised off the ground screen, increasing the radiation of the dipoles for angles near 90° from broadside [see Eqs. (15a) and (15b)].

The ability of the small arrays to accurately predict the driving impedance for "wide" angles of scan was also checked. Driving resistances for 50° scans in the E- and H-planes for D = 0.5 were plotted in Figs. 3-11(a) and (b) and are seen to exhibit the same degree of comparison as the data of Fig. 3-10: good agreement for the 7 × 9 array and less agreement for the 5 × 5, particularly for larger values of s. Also computed were E- and H-plane resistances for D = 0.7 for an angle of 20°. The data exhibit the same degree of agreement as previous results.

In order to check the computed values of the dipole reactance as a function of scan angle, the data given by Carter[*] for the driving impedance of the center element of a 64-element (parallel direction) planar array, infinite in extent in the collinear direction, were used. When Carter's data are transformed into the coordinate system used here and plotted against our computed data, the curves of Fig. 3-12 result, for the case of D = 0.5λ, s = 0.2 50λ (the only case for which Carter presents results).

The agreement is generally good. Although for some scan angles the percentage error in $X_D(\phi, \theta)$ is quite large, these errors occur for angles for which the resistive part is large, and the subsequent error in the impedance vector is quite small.

2. Accuracy of Small Array Estimate of Array Broadside Gain

As previously pointed out, the results of Wheeler[†] indicate that the value of the element gain function at broadside, when matched for maximum value at this angle, should be unity. Figures 3-13 and 3-14 compare the computed values of g_{oc} (0, 0) for the 7 × 9 array and the 5 × 5 array, respectively. The 7 × 9 array is seen to produce a value of the normalized gain function that is within 5 per cent of unity for s less than a quarter-wavelength, while the accuracy of the 5 × 5 prediction is about 10 per cent. It should be recalled that the value of the generator impedance chosen for the computation of the gain function was that predicted by the mutual impedance calculation using the large array formula [Eq. (13)]. Consequently, the value of the gain function is subject to the previously described differences between the actual infinite array driving impedance at broadside and that calculated by (13) for the array size in question.

Thus, the gain functions given are those obtainable with whatever built-in mismatch resulted. The fact that some mismatch was present appears to be borne out by the fact that for those cases for which the computed value is considerably less than unity, the gain function computed was actually greater at some small angle from broadside than it was at broadside by a few per cent. For example, Fig. 3-15 shows the computed diagonal-plane gain function for D = 0.5, s = 0.375 for the larger array in which this effect is apparent.

3. Conclusions

Based on the above comparisons, it seems reasonable to conclude that the 7 × 9 array yields quite accurate "large array" data for s up to a quarter-wavelength and reasonably accurate data for greater s. While the information that a 5 × 5 array yields is probably within the bounds of

* P.S. Carter, Jr., "Mutual Impedance Effects in Large Beam Scanning Arrays," Trans. IRE, PGAP AP-8, 276 (1960).
† H.A. Wheeler, "The Radiation Resistance of an Antenna in an Infinite Array or Waveguide," Proc. IRE 36, 478 (1948).

Best Available Copy
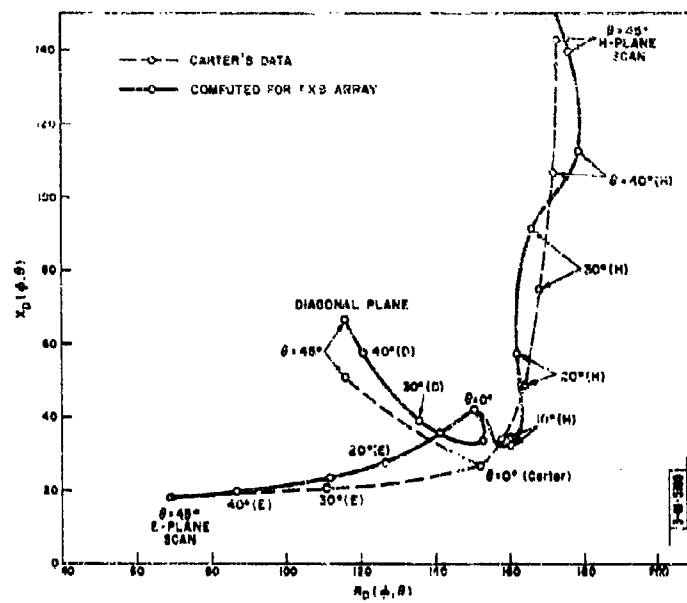
Fig. 3-12. Comparison of $Z_D(\phi, \theta)$ for $D = 0.5\lambda$, $s = 0.2\lambda$, with results of Carter.
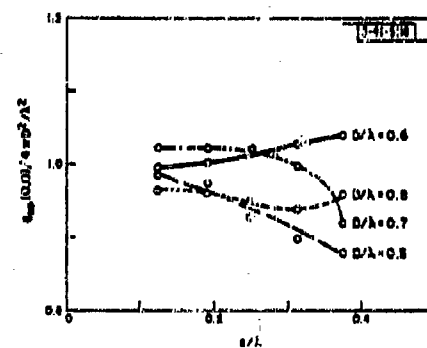
Fig. 3-13. Computed values of normalized broadside element gain function for 7×9 array.
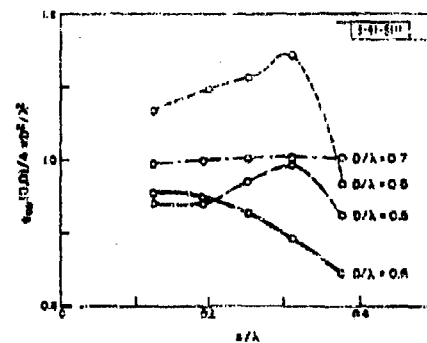
Fig. 3-14. Computed values of normalized broadside element gain function for 5 × 5 array.
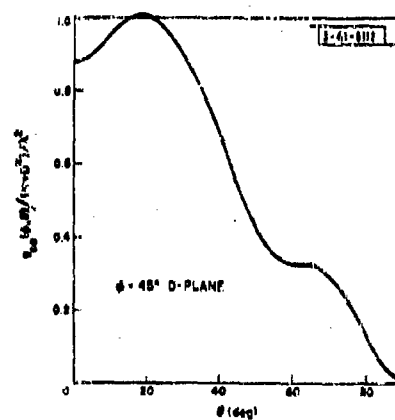
Fig. 3-15. Normalized gain function of thin, half-wave dipoles mounted 3/8λ above ground (φ = 0 is H-plane); D = 0.5λ.
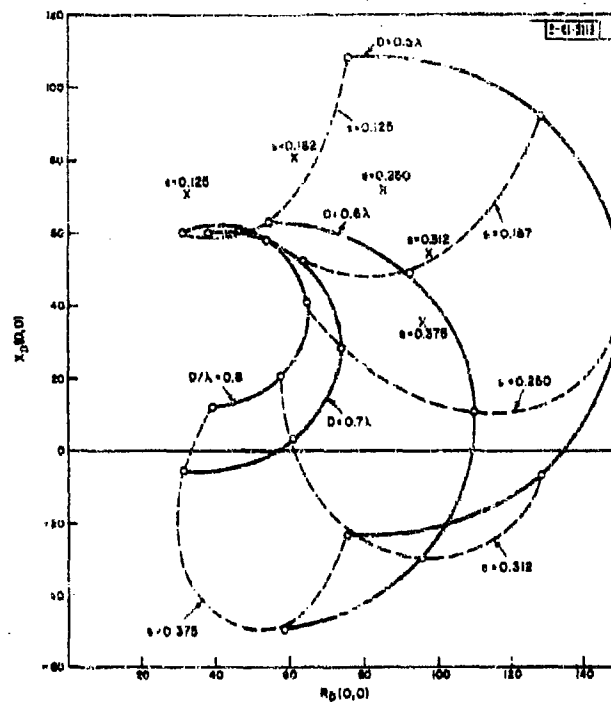
Fig. 3-16. $Z_D(0,0)$ for 7×9 array. (x is impedance of isolated element.)
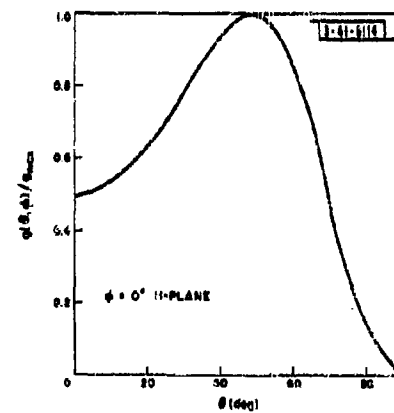
Fig. 3-17. Normalized H-plane pattern of an isolated dipole $3/8\lambda$ above ground.

the usual experimental errors in small e, it is somewhat suspect if the dipoles are mounted more than a quarter-wavelength above ground. It also is seen that the use of the driving impedance of Eq. (23) in the calculation of the element gain function should be avoided if accurate gain function maximization is desired. The alternative is to program the computer to choose Z_g to directly maximize (19) at the desired angle.

E. SUMMARY AND DISCUSSION OF COMPUTED RESULTS*

In this section, the digested facts gleaned from the computations will be described. The broadside driving-point impedance will be plotted and compared with the impedance that a single dipole above ground would have in free space. The angles over which the array beam can be scanned with less than a 3-db loss in gain from the broadside value (assuming the elements matched at broadside) will be given for the principal planes. Finally, the maximum VSWR obtained in scanning to the grating lobe formation angles will be presented (for D = 0.5, the data will be presented for an arbitrary angle of 50°), and it will be shown that an optimum value of d_3 exists for minimum VSWR for a given D and given maximum scan angles.

1. Variation of Broadside Driving Impedance with D and s

Figure 3-16 shows the computed driving impedance of the dipoles in the array when it is phased to radiate in the broadside direction. Also shown is the value of the radiation impedance of an isolated dipole above an infinite ground plane. It is apparent that the array environment completely dominates the element, and the impedance of the dipole in the array varies widely from its free-space value.

The resistive component is seen to decrease monotonically (for the spacings investigated) with D for a fixed s, as is necessary to cause the broadside element gain function to increase in direct proportion to the area allotted to the element.

2. Effects of Coupling on Scan Angle Corresponding to 3-db Decrease in Gain

The gain function 3-db points describe the solid angle over which the beam of a large array can be scanned with less than 3-db decrease in array gain.

The 3-db beamwidth of an isolated dipole depends on how one defines beamwidth, particularly for large s, as can be seen from Fig. 3-17, which illustrates the H-plane pattern of a dipole 3/8λ above ground. The curves of 3-db isolated-element beamwidth vs s of Fig. 3-18 can be generated, depending upon whether the beamwidth is taken 3 db down from the broadside gain, or from the angle of maximum gain. In any event, the beamwidth is quite sensitive to s.

When the dipole is placed in the array, however, the environment takes over almost completely, as indicated in Figs. 3-19 and 3-20, for the gain function 3-db H- and E-plane beamwidths, respectively. The gain function beamwidths are relatively insensitive to s and correspond roughly to the included angle, $2\Theta_{max}$, over which the array can be scanned without grating lobe formation for D > 0.5λ, given by

$$\frac{D}{\lambda} = \frac{1}{1 + \sin|\Theta_{max}|} \quad .$$

---

* Some of the computed gain functions and impedance plots from which these data were extracted are presented in Appendix A.
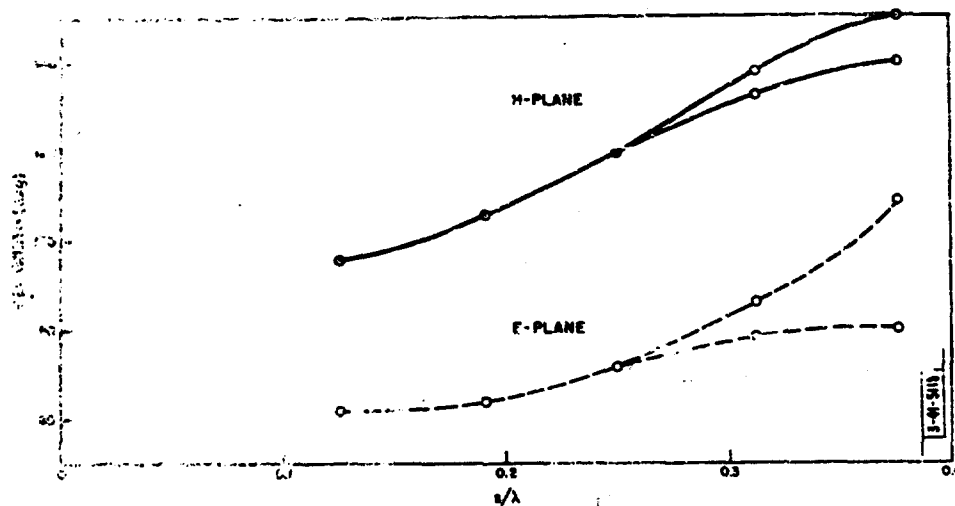
Fig. 3-18. Half-power beamwidth of single dipole vs height s above ground. (Upper curve of each pair is half-power relative to broadside; lower curve is relative to angle of maximum gain.)
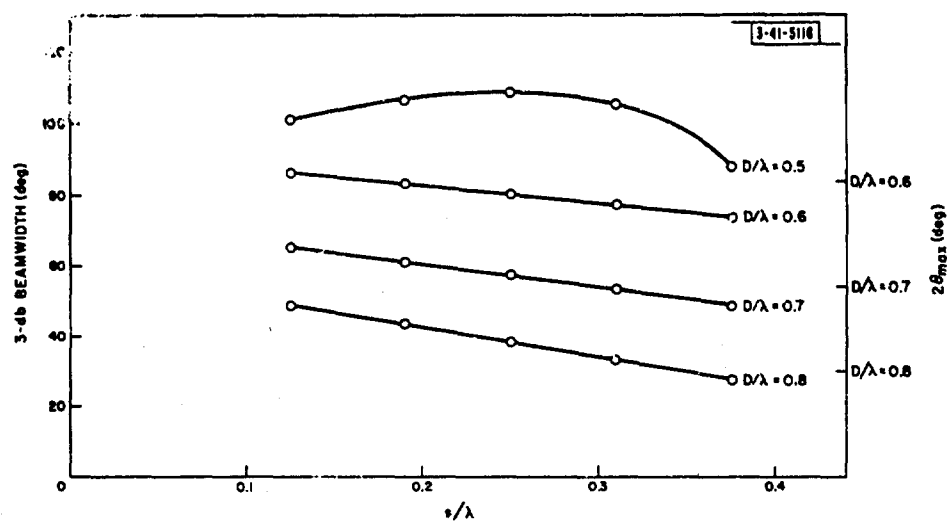
Fig. 3-19. Half-power H-plane beamwidth of gain function for broadside match vs D/λ and s/λ.
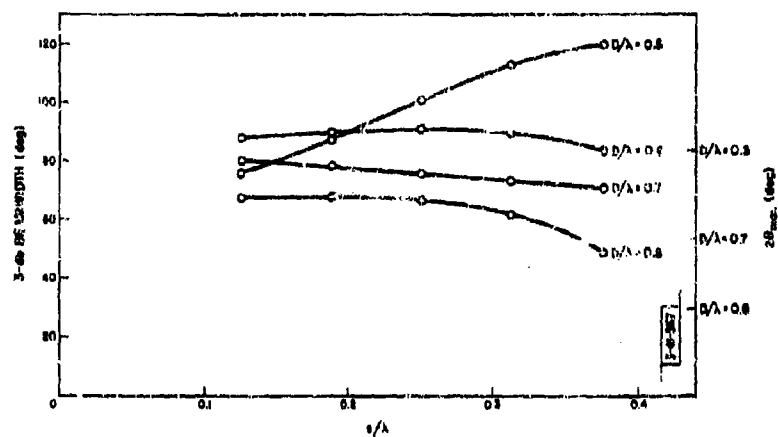
Fig. 3-20. Half-power E-plane beamwidth of gain function for broadside match vs D/λ and s/λ.
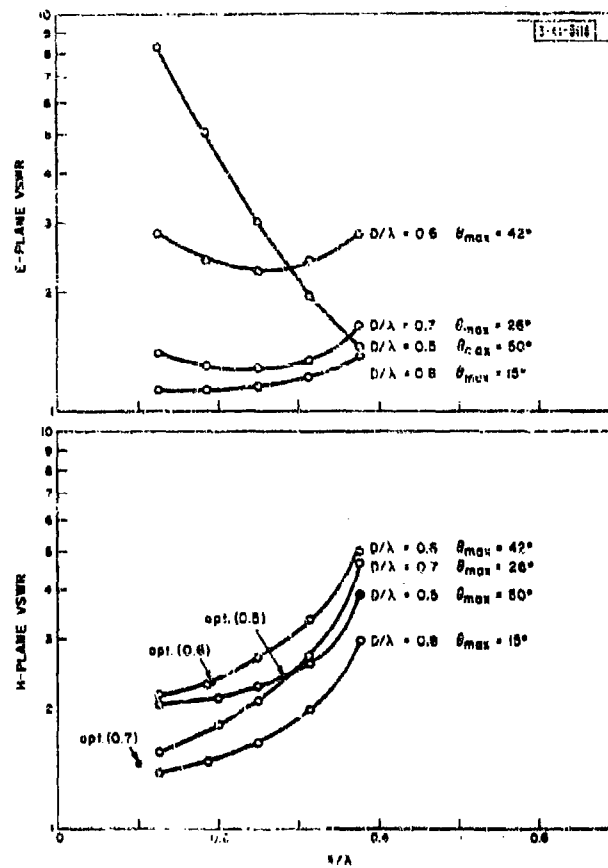
Fig. 3-21. Maximum VSWR to scan to θ_{max} (match at $\theta = 0$).

The angle of 3-db gain decrease and the angle of grating lobe formation occur almost simultaneously for most cases in the H-plane. In the E-plane, if good array pattern control is necessary, the grating lobe formation angle will dictate the maximum usable scan angles.

The gain functions from which these data were plotted were computed under the assumption that the element drives were matched to the element driving impedance with the array phased for broadside radiation, thus maximizing the broadside gain of the array. It is apparent from Eq. (30) that the shape of the gain functions will be altered at the expense of broadside gain if some other value of generator circuit impedance is chosen. Although a detailed study of this effect was not conducted, patterns were computed for the 5×5 array for a generator impedance matched to the impedance of a single isolated element (see Sec. F). It was generally noted that, in addition to the expected broadside gain decrease, this mismatch caused an increase in gain for certain other angles (corresponding to angles for which the element drive impedance was approximately equal to the impedance of an isolated element) and a consequent broadening of the gain function beamwidth. These results indicated that the element generator impedance may offer an interesting tool for accomplishing a certain amount of "tailoring" of the array gain vs angle of scan characteristics and is perhaps worthy of further investigation.

3. Maximum VSWR Incurred During Scan

From the computed data for the 7×9 array, the maximum VSWR that would be incurred in scanning to the grating lobe formation angle Θ_{max}, defined above, was computed, assuming the dipoles were matched when the array was phased for broadside as, for example, by the circuit of Fig. 3-8. For $D = 0.5$, since no grating lobes occur for any scan angles, a value of Θ_{max} of 30° was arbitrarily chosen.

The resulting VSWR plots for scan in the two principal planes are shown in Fig. 3-21. Except for $D = 0.5$, the maximum VSWR is relatively insensitive to s for scan in the E-plane, but increases for s for scan in the H-plane.[*] Consequently, there are values of s which are optimum in the sense of minimum VSWR for a given spacing for specified scan limits in the two principal planes. The values are indicated in the figure for equal scans in the two principal planes, and it is seen that the wider the dipole-to-dipole spacing, the closer the dipoles should be spaced to the ground plane. It is also apparent that, for all cases, one can choose s such that the VSWR does not exceed a value of 3:1 and, for many cases, it can be held to about 2:1.

It should be borne in mind that these VSWR values assume that the dipoles were matched for maximum array gain at broadside. It seems likely that the maximum VSWR could be still further reduced by a choice of generator impedance other than that assumed, at the cost of a small decrease in array gain. While this possibility was not formally investigated, several trial cases were examined by a "cut and try" process, using the computed impedance data (see Appendix A), without marked improvement. However, this was by no means formal inquiry into the possibilities of such a technique.

F. SOME EXPERIMENTAL RESULTS

In order to verify the validity of the foregoing calculated results, and also to test the sensitivity of the effects of mutual coupling on the exact characteristics of the dipoles, some experimental element gain functions were measured.

---

[*] The difference in the r   e of the E-plane curves for $D/\lambda = 0.5$ and those for other spacings is presumably due to the fact that the dipole ends are infinitely close (touching, that is) for half-wavelength spacing.
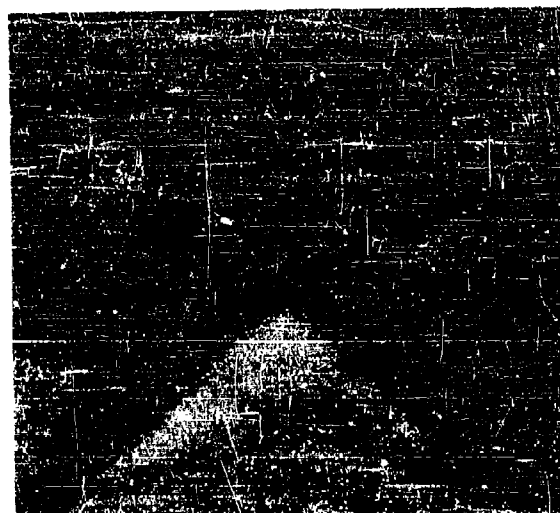
Fig. 3-22. Crossed dipole.
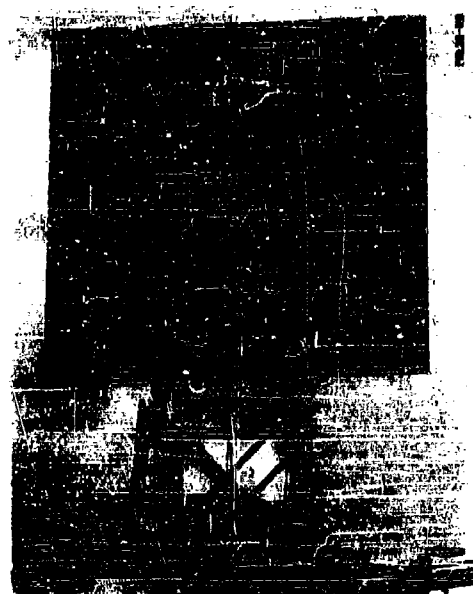
Fig. 3-23. Front view of planar test array.

Fig. 3-24. Rear view of planar test array showing single dipole used as gain standard.

Crossed dipoles were used to facilitate measurement of E- and H-plane patterns, since only a single-axis mount was available. A typical dipole is shown in Fig. 3-22. It is seen to be a poor approximation to the mathematical models assumed in the computations; namely, a thin, half-wavelength dipole with negligible feed structure. The dipole length is 6 inches, or at the operating of 900 Mcps, 0.46λ. The dipole arms are of ¼-inch stock for a ratio of length to thickness of 24. The feed structure is a conventional λ/4 balun, resulting in an appreciable feed structure. The base plates are constructed so that they will fit through square holes in the ground plane, facilitating variation of the height of the element above a ground plane.

The dipole feeds were designed to provide a nominal match at s = λ/4. Measured VSWR's ranged up to 1.4 for this value of s for all such dipoles, with 1.2 being a typical number. Cross-coupling between orthogonal dipoles was typically −30 db.

The dipoles were arrayed on a large (16 × 16-foot) ground plane with interchangeable 6 × 6-foot center sections, as shown in Fig. 3-23. The center dipole was selected to be one with a small VSWR when isolated at s = λ/4. A dipole with good match was mounted a quarter-wave above another large ground plane and used as a reference, as shown in Fig. 3-24. All measurements were made on the 600 foot range of the Lincoln Laboratory Ground Reflection Antenna Range.[*]

Rather than attempt to match all dipoles for each D and s, it was decided to leave the dipoles unmatched. It was assumed that the dipole feed systems matched a 50-ohm generator to the self-impedance of a thin, half-wave dipole at s = λ/4; namely, 85.6 + j72.4 ohms. Put another way, it was assumed that the generator impedance was 85.6 − j72.4 ohms. The computations were then re-run for this value of Z_g for a 5 × 5 array.

Experimental element gain functions were measured for s/λ = 0.125, 0.250 and 0.375 for D/λ = 0.6 and 0.8. The pertinent comparisons between the calculated and measured gain functions are indicated in Table 3-I. Except for s = 0.375, the agreement is seen to be very good with regard to gain, and all beamwidths check closely.

TABLE 3-I

COMPARISON OF MEASURED AND CALCULATED GAIN FUNCTIONS FOR 5 × 5 ARRAY

D/λ	s/λ	Broadside Gain (calculated) (db)	Broadside Gain (measured) (db)	Beamwidth (calculated) H	Beamwidth (calculated) E	Beamwidth (measured) H	Beamwidth (measured) E
0.6	0.125	6.11	6.0	90	83	88	84
	0.250	5.8	5.5	93	103	96	104
	0.375	3.58	4.5	128	119	100	120
0.8	0.125	8.0	8.0	69	64	72	64
	0.250	9.12	9.0	44	63	44	68
	0.375	7.8	8.25	34	66	30	68

If the broadside gain values are adjusted for the assumed mismatch, values within 10 per cent of $4\pi D^2/\lambda^2$ result except for the case D/λ = 0.6, s/λ = 0.375, for which the result is in error by 15 per cent (on the low side).

---

[*] A. Cohen and A. W. Maltese, "The Lincoln Laboratory Antenna Test Range," Microwave J. 4, 57 (April 1961).
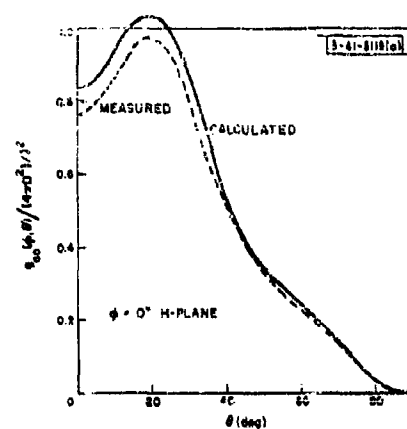
(a) H-plane pattern.
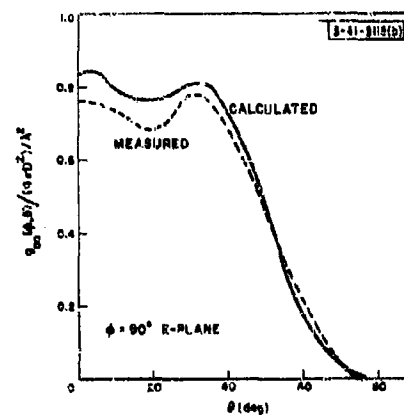
(b) E-plane pattern.

Fig. 3-25. Calculated and measured gain functions for center element of 5×5 array for $D/\lambda = 0.6$, $s/\lambda = 0.250$ and $Z_g = 85.7 - j72.3$ ohms.
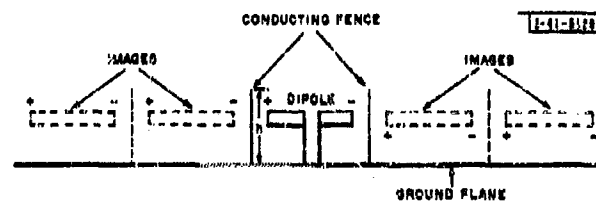
Fig. 3-26. Partial imaging by use of fences.

It was also observed that the effect of the mismatch, while lowering the broadside gain, increased the gain at some other angle, and the gain functions tended to "peak up" at some angles other than broadside, since a matched condition is approached for this angle. Figures 3-25(a) and (b) illustrate such a case.

G. CONCLUSIONS AND OBSERVATIONS

It is apparent from the foregoing results that the array environment, through mutual coupling, dominates the individual element in fixing the array behavior; that is, the properties (gain, beamwidth, impedance) of the individual dipoles are drastically altered when the elements are placed in the array. Roughly speaking, the effects of the coupling on array gain are to:

(1) Render the broadside element gain function equal to $4\pi D^2/\lambda^2$, essentially regardless of the gain of the element when isolated (assuming the elements matched at broadside).

(2) Force the beamwidth of the gain function to conform to the grating lobe formation angles of the array.

These modifications are accomplished through the mechanism of an element driving impedance which varies with array pointing angle to modify the isolated dipole pattern to conform with the above.

Thus, one might make the observation that mutual coupling, rather than being a curse, is at least a partial blessing in the sense that it makes an array behave according to logic (more appropriately, perhaps, according to directivity considerations).

Finally, it is seen that there are still degrees of freedom available to aid in reducing the most troublesome aspect of mutual impedance, at least to the transmitter engineer: the VSWR in the feed line. By virtue of Eq. (30), it is apparent that to minimize the VSWR, one should attempt to choose a radiating "element" having a gain pattern, when isolated, that closely approximates the element gain function that directivity considerations indicate will prevail in the array. Such a choice can consist of either selecting an appropriate value of s, as explored above, or more esoteric schemes, such as placing "fences" between the ends of the dipoles,[*] as indicated in Fig. 3-26.

If the fences' height, h, extended to infinity, the dipole would be imaged as indicated, and is partially imaged for $h \gtrsim s$. Thus, a single "element" (dipole, ground screen and fences) looks like an array in the E-plane direction, phased for broadside, and the isolated element pattern should very closely approximate the gain function. Such fences in the H-plane do not perform a similar function, since the images alternate in sign.

---

[*] As proposed by S. Edelberg and A.A. Oliner, "Mutual Coupling in Large Antenna Arrays II: Compensation Effects," Trans. IRE, PGAP AP-8, 360 (1960).

APPENDIX A

Figures 3-27 through 3-50 present many of the computed gain functions and Smith Chart plots of the normalized impedance looking into a feed circuit, as shown in Fig. 3-8, for the 7 × 9 array. Since several disadvantages of using dipole heights much greater than $s = \lambda/4$ have been pointed out, corresponding plots are omitted.

The gain functions and Smith Charts are presented for E-, H- and diagonal-plane scans, with the numerical values representing the angle θ measured from broadside (Fig. 1-7). The Smith Charts also indicate the impedance of a single dipole above ground, normalized, and the gain function plots indicate the angle over which the beam of the array can be scanned with less than 3-db loss in one-way gain.

$$Z_D(\theta) = R_D(\theta) + iX_D(\theta)$$

$$Z_D(0,0) = 75.4 + i106.8$$

$$Z_a = 32.3 + i70.9$$

Fig. 3-27. Variation in normalized driving impedance, $Z_D(\phi, \theta)/R_D(0,0)$, with scan angle for center element of 9 X 7 array for element spacing $D = 0.5\lambda$ and element height above ground plane $s = 0.125\lambda$. Also given are the impedance of an isolated element, Z_a, and the value of $Z_D(0,0)$. The normalized value of Z_a is indicated on the chart.

Fig. 3-28. Normalized gain function, $g_{oc}(\phi, \theta)/(4\pi D^2/\lambda^2)$, for center element of 9 X 7 array for element spacing $D = 0.5\lambda$ and element height above ground plane $s = 0.125\lambda$. Also indicated is the included angle over which the array may be scanned in each plane with less than 3-db loss in gain.

231

$$Z_D(0,0) = 128.2 + j92.0$$

$$Z_a = 61.1 + j90.3$$

Fig. 3-29. Variation in normalized driving impedance, $Z_D(\phi, \theta)/R_D(0,0)$, with scan angle for center element of 9 X 7 array for element spacing $D = 0.5\lambda$ and element height above ground plane $s = 0.187\lambda$. Also given are the impedance of an isolated element, Z_a, and the value of $Z_D(0,0)$. The normalized value of Z_a is indicated on the chart.

Fig. 3-30. Normalized gain function, $g_{00}(\phi, \theta)/(4\pi D^2/\lambda^2)$, for center element of 9 X 7 array for element spacing $D = 0.5\lambda$ and element height above ground plane $s = 0.187\lambda$. Also indicated is the included angle over which the array may be scanned in each plane with less than the 3-db drop in gain.

$$Z_D(0,0) = 150.3 + j42.3$$

$$Z_a = 85.7 + j72.5$$

Fig. 3-31. Variation in normalized driving impedance, $Z_D(\varphi, \theta)/R_D(0,0)$, with scan angle for center element of 9 X 7 array for element spacing $D = 0.5\lambda$ and element height above ground plane $s = 0.250\lambda$. Also given are the impedance of an isolated element, Z_a, and the value of $Z_D(0,0)$. The normalized value of Z_a is indicated on the chart.

Fig. 3-32. Normalized gain function, $g_{oo}(\varphi, \theta)/(4\pi D^2/\lambda^2)$, for center element of 9 X 7 array for element spacing $D=0.5\lambda$ and element height above ground plane $s = 0.250\lambda$. Also indicated is the included angle over which the array may be scanned in each plane with less than 3-db loss in gain.

$Z_D(0,0) = 54.1 + j 63.5$

$Z_a = 32.3 + j 70.9$
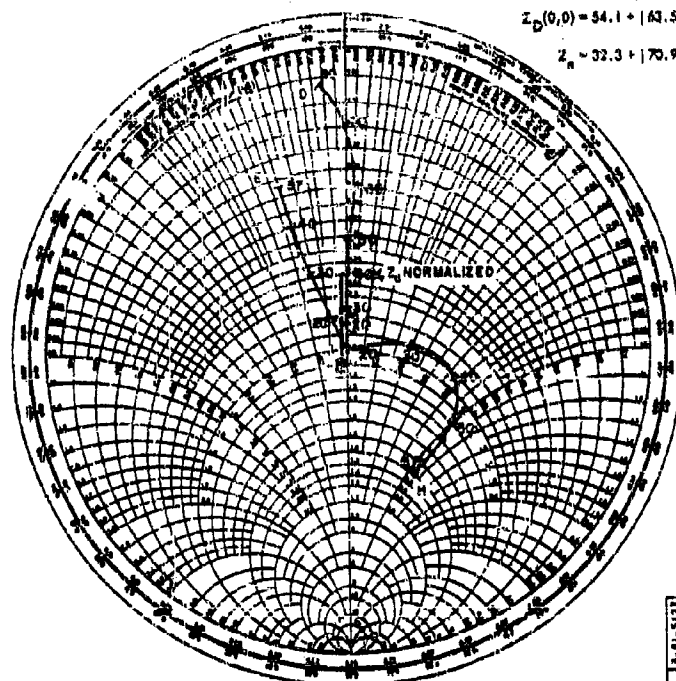
Fig. 3-33. Variation in normalized driving impedance, $Z_D(\phi, \theta)/R_D(0,0)$, with scan angle for center element of 9 X 7 array for element spacing $D = 0.6\lambda$ and element height above ground plane $s = 0.125\lambda$. Also given are the impedance of an isolated element, Z_a, and the value of $Z_D(0,0)$. The normalized value of Z_a is indicated on the chart.

Fig. 3-34. Normalized gain function, $g_{oo}(\phi, \theta)/(4\pi D^2/\lambda^2)$, for center element of 9 X 7 array for element spacing $D = 0.6\lambda$ and element height above ground plane $s = 0.125\lambda$. Also indicated is the included angle over which the array may be scanned in each plane with less than 3-db loss in gain.

$Z_D(0,0) = 92.6 + j42.2$

$Z_a = 61.3 + j60.3$
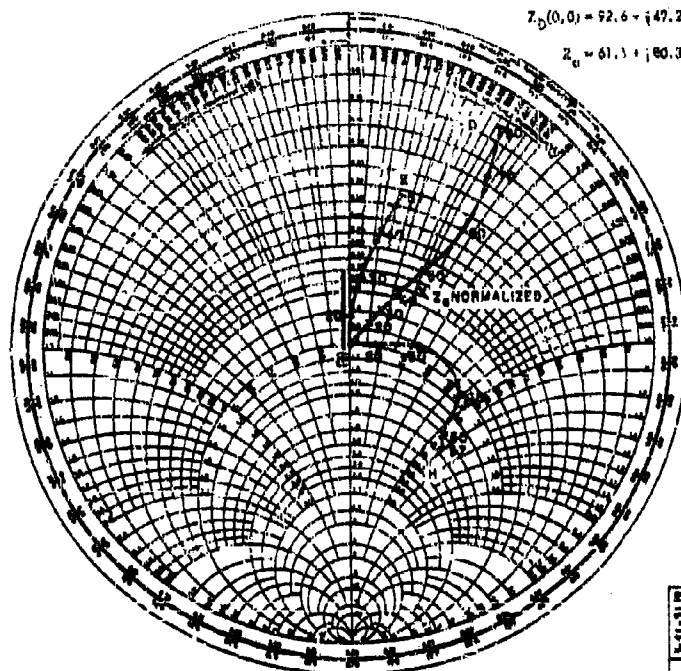
Fig. 3-35. Variation in normalized driving impedance, $Z_D(\phi, \theta)/R_D(0,0)$, with scan angle for center element of 9 X 7 array for element spacing $D = 0.6\lambda$ and element height above ground plane $s = 0.187\lambda$. Also given are the impedance of an isolated element, Z_a, and the value of $Z_D(0,0)$. The normalized value of Z_a is indicated on the chart.

Fig. 3-36. Normalized gain function, $g_{oo}(\phi, \theta)/(4\pi D^2/\lambda^2)$, for center element of 9 X 7 array for element spacing $D = 0.6\lambda$ and element height above ground plane $s = 0.187\lambda$. Also indicated is the included angle over which the array may be scanned in each plane with less than 3-db loss in gain.

235

$Z_D(0,0) = 109.7 + j10.7$

$Z_c = 85.7 + j72.5$
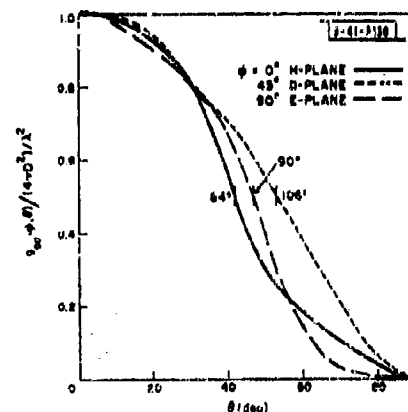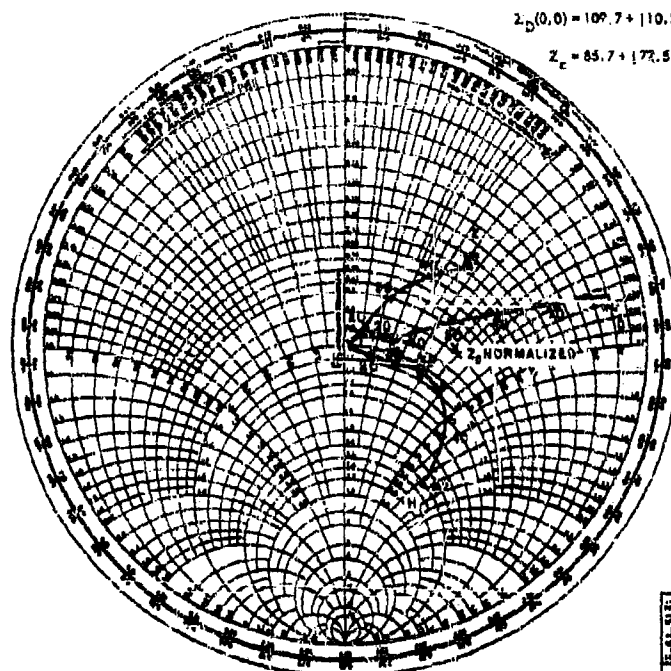
Fig. 3-37. Variation in normalized driving impedance, $Z_D(\phi, \theta)/R_D(0,0)$, with scan angle for center element of 9 X 7 array for element spacing $D = 0.6\lambda$ and element height above ground plane $s = 0.250\lambda$. Also given are the impedance of an isolated element, Z_a, and the value of $Z_D(0,0)$. The normalized value of Z_a is indicated on the chart.

Fig. 3-38. Normalized gain function, $g_{oc}(\phi, \theta)/(4\pi D^2/\lambda^2)$, for center element of 9 X 7 array for element spacing $D = 0.6\lambda$ and element height above ground plane $s = 0.250\lambda$. Also indicated is the included angle over which the array may be scanned in each plane with less than 3-db loss in gain.

236

$Z_D(0,0) = 37.9 + j59.2$

$Z_q = 30.3 + j70.9$
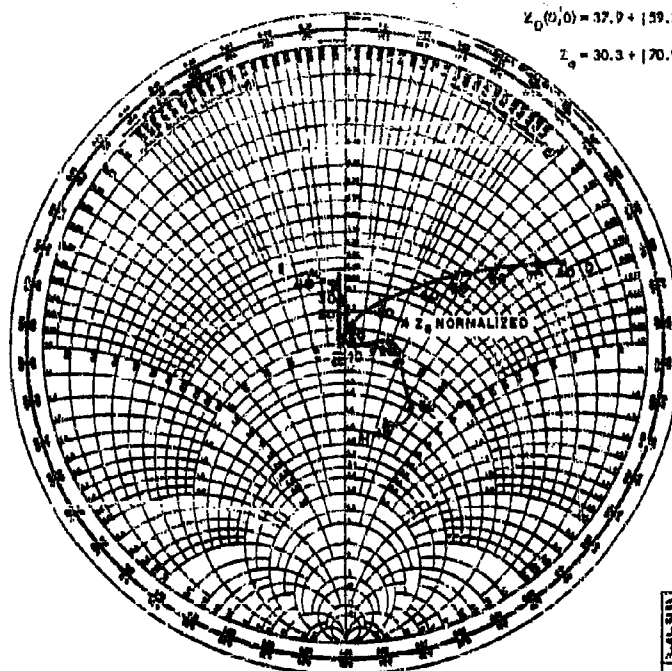
Fig. 3-39. Variation in normalized driving impedance, $Z_D(\phi, \theta)/R_D(0,0)$, with scan angle for center element of 9 X 7 array for element spacing $D = 0.7\lambda$ and element height above ground plane $s = 0.125\lambda$. Also given are the impedance of an isolated element, Z_a, and the value of $Z_D(0,0)$. The normalized value of Z_a is indicated on the chart.

Fig. 3-40. Normalized gain function, $g_{00}(\phi, \theta)/(4\pi D^2/\lambda^2)$, for center element of 9 X 7 array for element spacing $D = 0.7\lambda$ and element height above ground plane $s = 0.125\lambda$. Also indicated is the included angle over which the array may be scanned in each plane with less than 3-db loss in gain.
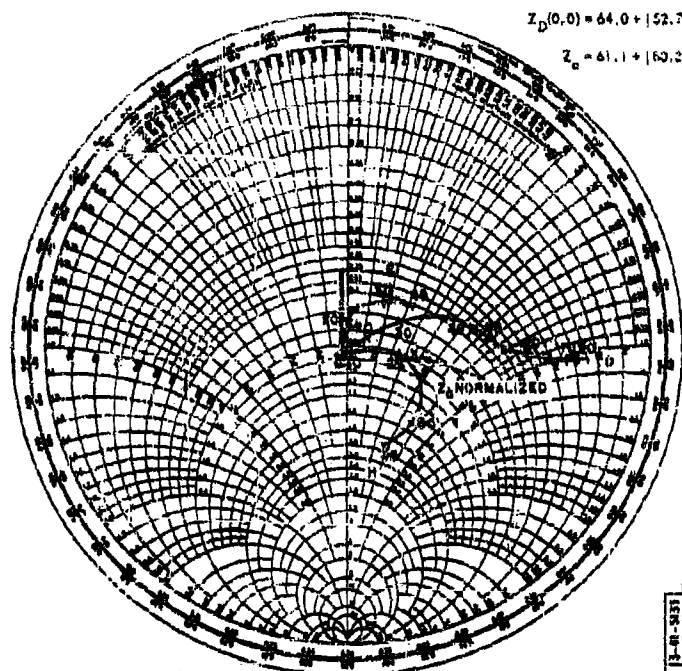
Fig. 3-41. Variation in normalized driving impedance, $Z_D(\varphi, \theta)/R_D(0,0)$, with scan angle for center element of 9×7 array for element spacing $D = 0.7\lambda$ and element height above ground plane $s = 0.187\lambda$. Also given are the impedance of an isolated element, Z_o, and the value of $Z_D(0,0)$. The normalized value of Z_o is indicated on the chart.

Fig. 3-42. Normalized gain function, $g_{oo}(\varphi, \theta)/(4\pi D^2/\lambda^2)$, for center element of 9×7 array for element spacing $D = 0.7\lambda$ and element height above ground plane $s = 0.187\lambda$. Also indicated is the included angle over which the array may be scanned in each plane with less than 3-db loss in gain.

238

$$Z_D(0,0) = 73.9 + j28.2$$

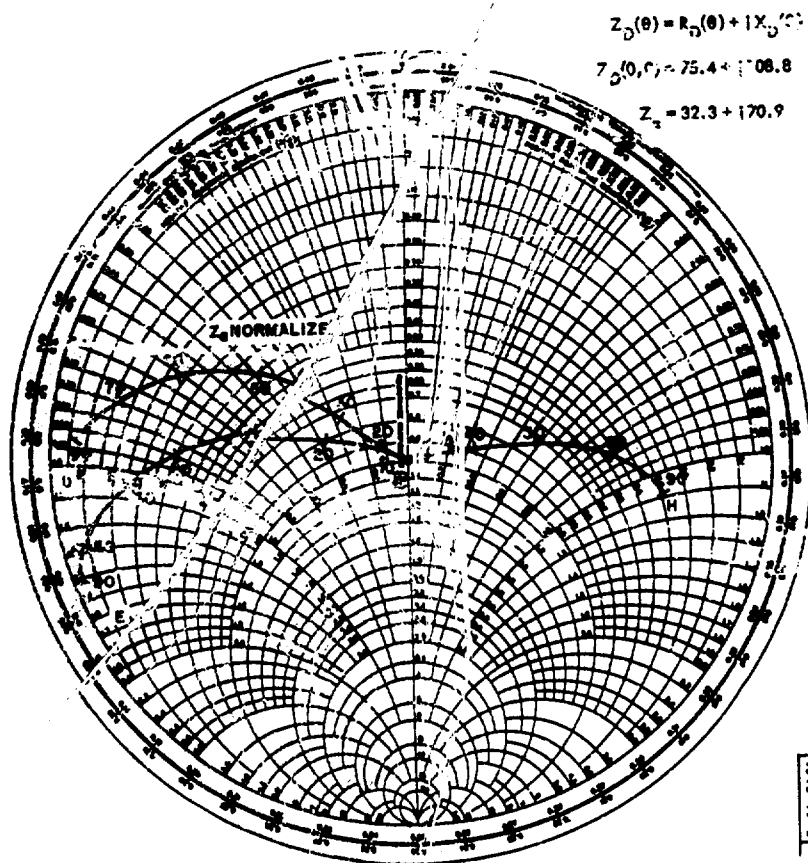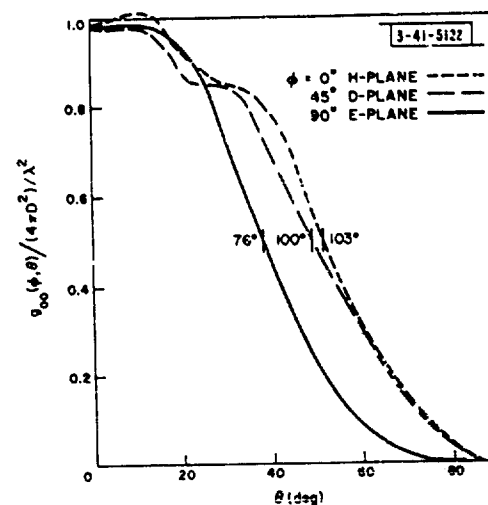$$Z_a = 83.7 + j22.5$$
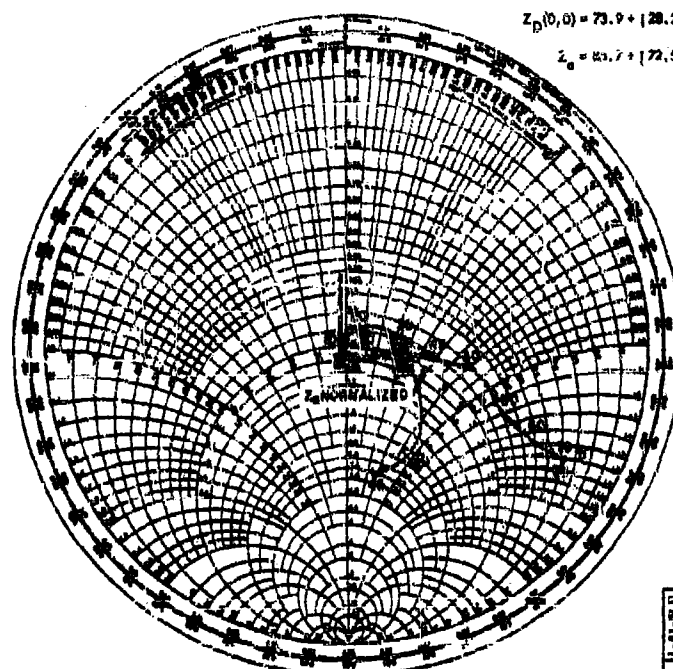
Z. NORMALIZED

Fig. 3-43. Variation in normalized driving impedance, $Z_D(\phi, \theta)/R_D(0,0)$, with scan angle for center element of 9 X 7 array for element spacing $D = 0.7\lambda$ and element height above ground plane $s = 0.250\lambda$. Also given are the impedance of an isolated element, Z_a, and the value of $Z_D(0,0)$. The normalized value of Z_a is indicated on the chart.

Fig. 3-44. Normalized gain function, $g_{\theta\theta}(\phi, \theta)/(4\pi D^2/\lambda^2)$, for center element of 9 X 7 array for element spacing $D = 0.7\lambda$ and element height above ground plane $s = 0.250\lambda$. Also indicated is the included angle over which the array may be scanned in each plane with less than 3-db loss in gain.

239

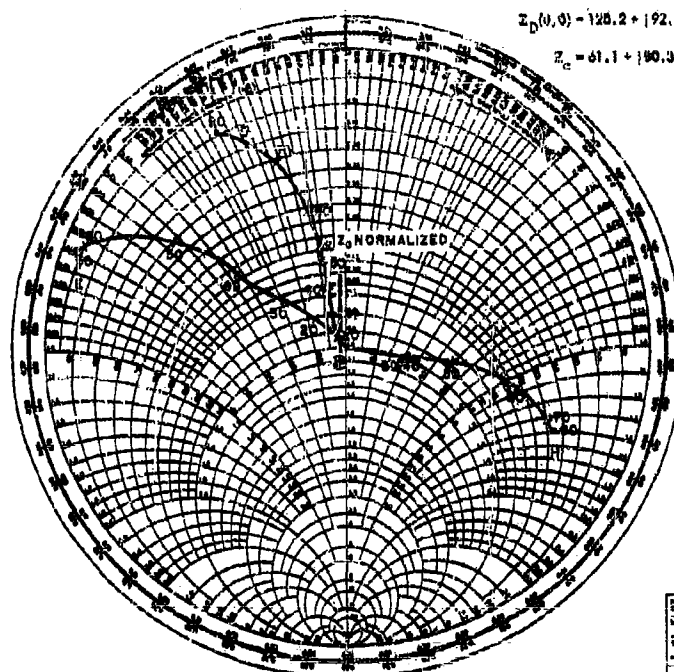$Z_D(0,0) = 31.0 + i69.0$

$Z_a = 33.0 + i70.9$

Fig. 3-45. Variation in normalized driving impedance, $Z_D(\phi,\theta)/R_D(0,0)$, with scan angle for center element of 9 X 7 array for element spacing $D = 0.8\lambda$ and element height above ground plane $s = 0.125\lambda$. Also given are the impedance of an isolated element, Z_a, and the value of $Z_D(0,0)$. The normalized value of Z_c is indicated on the chart.
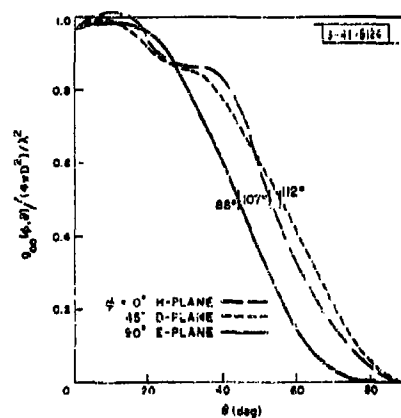

Fig. 3-46. Normalized gain function, $g_{00}(\phi,\theta)/(4\pi D^2/\lambda^2)$, for center element of 9 X 7 array for element spacing $D = 0.8\lambda$ and element height above ground plane $s = 0.125\lambda$. Also indicated is the included angle over which the array may be scanned in each plane with less than 3-db loss in gain.

240

$Z_D(0,0) = 53.3 + j38.1$
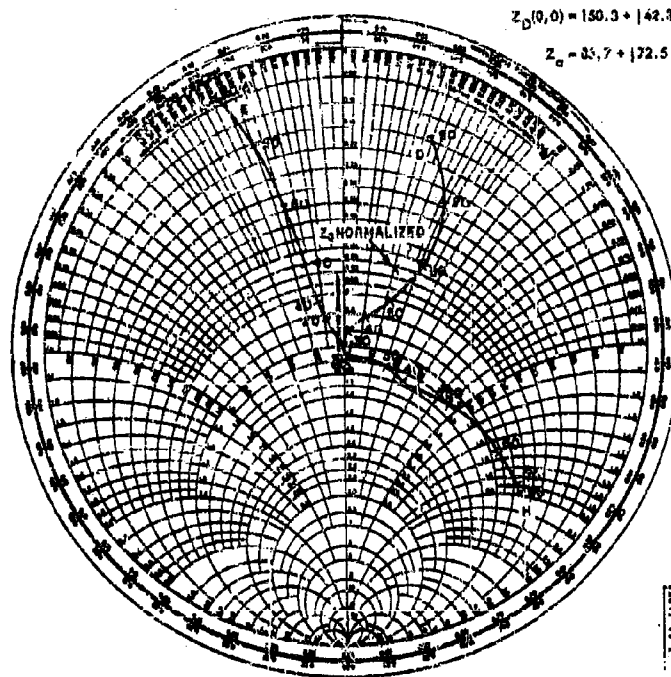
$Z_a = 61.1 + j85.3$

Z_a NORMALIZED

Fig. 3-47. Variation in normalized driving impedance, $Z_D(\phi, \theta)/R_D(0,0)$, with scan angle for center element of 9 X 7 array for element spacing $D = 0.8\lambda$ and element height above ground plane $s = 0.187\lambda$. Also given are the impedance of an isolated element, Z_a, and the value of $Z_D(0,0)$. The normalized value of Z_a is indicated on the chart.

Fig. 3-48. Normalized gain function, $g_{\theta\theta}(\phi, \theta)/(4\pi D^2/\lambda^2)$, for center element of 9 X 7 array for element spacing $D = 0.8\lambda$ and element height above ground plane $s = 0.187\lambda$. Also indicated is the included angle over which the array may be scanned in each plane with less than 3-db loss in gain.
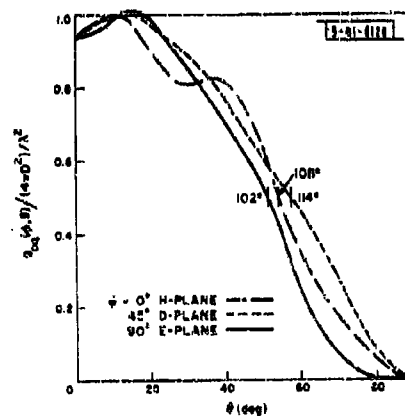

241

$Z_D(0,0) = 64.1 + j40.6$

$Z_a = 85.7 + j72.5$

Z_a NORMALIZED

Fig. 3-49. Variation in normalized driving impedance, $Z_D(\phi, \theta)/R_D(0,0)$, with scan angle for center element of 9 X 7 array for element spacing $D = 0.8\lambda$ and element height above ground plane $s = 0.250\lambda$. Also given are the impedance of an isolated element, Z_a, and the value of $Z_D(0,0)$. The normalized value of Z_a is indicated on the chart.

$\phi = 0°$ H-PLANE ——————
45° D-PLANE — — — —
90° E-PLANE — · — · —

Fig. 3-50. Normalized gain function, $g_{00}(\phi, \theta)/(4\pi D^2/\lambda^2)$, for center element of 9 X 7 array for element spacing $D = 0.8$, and element height above ground plane $s = 0.250\lambda$. Also indicated is the included angle over which the array may be scanned in each plane with less than 3-db loss in gain.
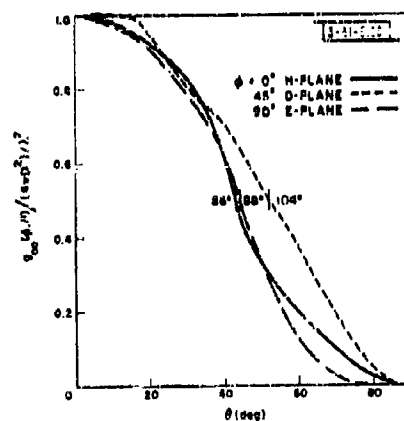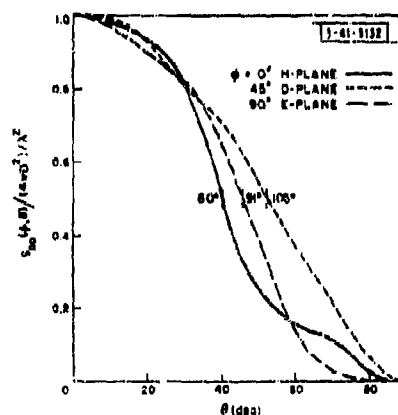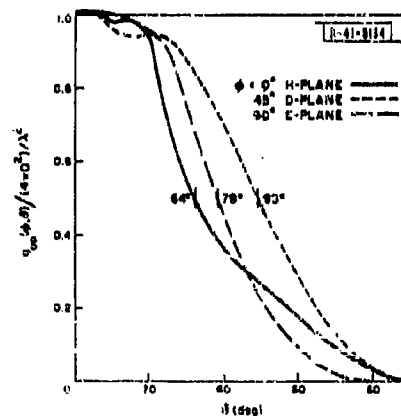
242

CHAPTER II
SHORT-PULSE LIMITATION OF PHASED ARRAYS

SUMMARY   J. R. Sklar

The performance of a large phased (as contrasted to delayed) array radar is known to depreciate as a result of the propagation time across the array if short pulses are transmitted. In this chapter, these effects are analyzed, and quantitative estimates of their magnitudes are determined for arrays using frequency-insensitive phase shifters. The studies will be made for a linear array; similar effects manifest themselves in planar arrays.

Under the assumption that the array uses constant phase shifters for beam positioning and infinitesimal dipoles for radiating, the impulse response of the radar system is derived. The operation of the array radar with uniform amplitude taper and rectangular pulses is then studied in detail. An energy loss which increases as the beam is pointed farther off-broadside is shown to exist, and curves are plotted for the signal-to-noise ratio at the receiver output as a function of the pulse length for two types of matched filters. One is matched to the rectangular pulse; the other is matched to the distorted return.

Radar resolution capability is also studied. Waveforms of the receiver outputs are calculated and compared with the outputs in the undistorted case. For very short pulses, resolution is radically depreciated.

Finally, accuracy limitations are considered. A curve indicating the variance of range estimates is plotted as a function of pulse length.

A. INTRODUCTION

Electronically scanned arrays can be classified according to the technique used for combining the signals from the separate antenna elements into a single coherent array output. If delay lines are used, a delayed array results. If phase shifters are employed, the system is called a phased array. The principal difference between these methods is the variation of carrier phase shift with frequency. A delayed array operates using phase shift that is linear with frequency; a phased array uses phase shift that is insensitive to frequency changes. Although the first system is more desirable for wideband signals, it is difficult to instrument when rapid scanning is desired, and phased arrays are often selected instead. In this report, the operations of a phased array and a delayed array are compared for the wideband signal case.

Polk[*] has analyzed the behavior of large-aperture antennas and has given expressions for the antenna pattern as a function of time for stepped sinusoidal excitation. His analysis reveals an initial transient for the pattern to be established. B. R. Mayo, et al.,[†] have more recently determined the impulse response of a continuous aperture and have applied their results to obtain a generalized ambiguity function. By using similar methods, the impulse response of a discrete linear array using phase shifters insensitive to frequency will be obtained here.

B. ASSUMPTIONS

These assumptions apply in the following analysis:

---

[*]C. Polk, "Transient Behavior of Aperture Antennas," Proc. IRE **48**, 1281 (1960).

[†]B.R. Mayo, P.W. Howells and W.B. Adams, "Generalized Linear Radar Analysis," Microwave J. **4**, 8 (August 1961).
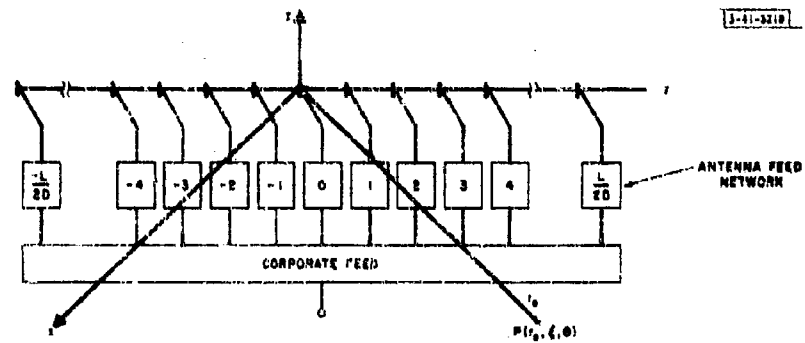
Fig. 3-51. Array orientation and geometry.
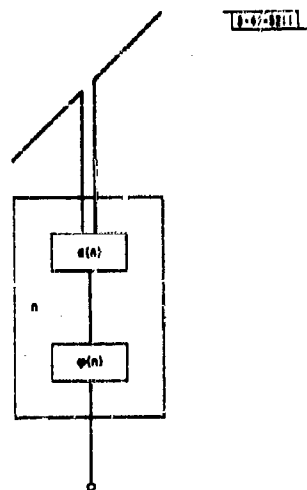
Fig. 3-52. Feed network for n^{th} antenna element.

(1) The linear array is oriented along the y-axis of a rectangular coordinate system (Fig. 3-51).

(2) The effects of interest are due to phenomena in the x-y plane.

(3) The coordinate system of interest is the circular cylindrical system with O measured from the x-axis of the rectangular system.

(4) The radiating elements are infinitesimal dipoles polarized in the z-direction.

(5) The phase shifters operate independently of frequency.

(6) The exponential representation of signals is used throughout; taking the real part is assumed.

(7) The letter K, subscripted by an index, is used as a constant and is different for each index.

C. SIGNAL RESPONSE OF PHASED ARRAY ANTENNAS

1. Impulse Response of Antenna System

We will consider a linear array of length L, with element spacing D, of N infinitesimal dipoles polarized in the z-direction (Fig. 3-51). The nth dipole is fed by a network which amplifies the signal by a gain a(n) and phase shifts the carrier by an angle $\phi(n)$ as in Fig. 3-52.

To determine the impulse response, assume that an impulse is fed into the array feed network. All antenna elements are simultaneously excited by impulses. Now consider the signal received at a point P, which is located in the x-y plane and has the cylindrical coordinates (r_0, ξ, Θ). Each separately excited dipole will act as an independent signal source (ignoring mutual coupling effects) and therefore an impulse will arrive at P from each of the antennas.[*] However, the N impulses will not arrive simultaneously but will be separated in time by

$$t_d = \frac{D}{c} \sin \xi$$

This time delay is due to the differential distance between array elements. The impulse from the nth element will have a magnitude a(n) and, as a result, the impulse train received at P will have an envelope proportional to the array amplitude distribution.

If there is a target located at P, each impulse will be reflected back to the antenna system where it is received by the N dipoles. A particular impulse will be received by successive antennas with a time separation t_d. The signal at each element will be weighted and phase-shifted again before summation in the array feed system. Therefore, if a single impulse is transmitted, the output of the array feed system is a series of 2N impulses with envelope equal to the convolution of the array amplitude distribution with itself. Mathematically, this may be represented by

$$h(t) = \frac{K_6}{2\pi} \sum_{m=-L/D}^{+L/D} \exp\left[j \frac{\omega_0 mD}{c} \sin \xi\right] u_0\left(t - \frac{2r_0}{c} + \frac{mD}{c} \sin \xi\right) \cdot \sum_{n=-L/2D}^{+L/2D} a(n) a(m-n)$$

This expression is readily interpreted as a series of 2N impulses spaced $D/c \sin \xi$ apart. Each is weighted by a factor E(m), and the entire group is delayed by $2r_0/c$, the two-way travel time. A carrier phase shift term is included which is necessary to determine the response to modulated carrier signals.

---

[*] The results of this intuitive argument are verified by a more rigorous analysis in Appendix A, using antenna and signal theory.

The impulse envelope $E(m)$ is defined by

$$E(m) = \sum_{n=-L/2D}^{+L/2D} a(n)\, a(m-n) \quad .$$

This is seen to be the convolution of the array amplitude taper with itself. For a uniform taper, therefore, $E(\ell)$ is triangular. Other amplitude tapers result in other impulse envelopes which can be computed from the above definitions.

2. Response to Signals

Using the impulse response determined in the previous section, it is possible to calculate the response, $O(t)$, to a radar signal, $s(t)$, by convolution:

$$O(t) = \int_{-\infty}^{+\infty} h(\tau)\, s(t-\tau)\, d\tau \quad .$$

However, $h(t)$ consists of a train of impulses with an envelope proportional to the convolution of the array amplitude taper with itself. Exact computation of $O(t)$ involves convolving $s(t)$ with each impulse, weighting the result, and then summing over all impulses. This leads to

$$O(t) = \sum_{\ell=-L/D}^{+L/D} s\left(t - \frac{2r_0}{c} + \frac{D\ell}{c} \sin \xi\right) E(\ell) \quad .$$

Sums of this type are tedious to compute. Therefore, in the remainder of this report, $h(t)$ will be approximated by the continuous envelope. This approximation is equivalent to assuming that $O(t)$ is low-pass-filtered after reception and is reasonable if the signal can be considered well-sampled by samples spaced $D/c \sin \xi$ apart.

It has been demonstrated that $h(t)$ is a series of impulses spaced $D/c \sin \xi$ apart in time and that the nth impulse has weight $E(m)$. When assuming a continuous $h(t)$, it is readily apparent that the value of $h(t)$ at time $t = [(2r_0/c) - mD/c \sin \xi]$ is $E(m)$. That is:

$$h\left(\frac{2r_0}{c} - \frac{mD}{c} \sin \xi\right) = E(m) \quad ,$$

or

$$h(t) = E\left(\frac{2r_0 - tc}{D \sin \xi}\right) \quad .$$

The values of $E(x)$ for non-integral argument are obtained by convolution of the envelope of the array illumination in the same way as the values for integral argument are obtained by convolution of the actual impulses. Consequently,

$$O(t) = \int_{-\infty}^{\infty} h(\tau)\, s(t-\tau)\, d\tau = \int_{-\infty}^{\infty} E\left(\frac{2r_0 - \tau c}{D \sin \xi}\right) s(t-\tau)\, d\tau \quad .$$

The normalization,

$$\int_{-L/2}^{+L/2} a(x)^2\, dx = 1 \quad ,$$

implies that $E(0) = 1$, thereby guaranteeing a return equal to the transmitted signal delayed by

$2r_0/c$, the radar ranging time. For $\xi \neq 0$, the return is no longer a reproduction of the transmission, but has a transient which increases with ξ. The effect of the transient will be examined in greater detail.

3. Response to Square Pulse

Throughout the remainder of this chapter, discussion will be limited to the phenomena resulting when a square pulse is transmitted, and received with a uniformly illuminated array. This will serve to illustrate the more general results obtained in the previous sections and to indicate the extent of the adverse effects brought on by the transient. Other cases could be calculated by the same techniques; however, this particular one is frequently encountered in practice, and the computations can readily be carried out. For this case, $E(m)$, the convolution of the uniform illumination $a(n)$ with itself, is triangular. Assuming unit power to be distributed across the array, $a(n) = 1/\sqrt{L}$, where L is the array length. Consequently, the triangular $E(\ell)$ has base $2L$ and height 1. To obtain the return signal, we convolve the square pulse with $E(\ell)$. Since the convolution of a step and a ramp is a parabolic section, it is clear that the return is composed of parabolic arcs. However, all pulse lengths do not yield the same output; as the pulse length varies in comparison to the traverse time, different returns are obtained. These are given in Appendix B and are illustrated in Fig. 3-53. T is the pulse length and δ is the traverse time $L/c \sin \xi$.

Fig. 3-53. Distorted radar returns. (T = pulse length, δ = traverse time across array.)
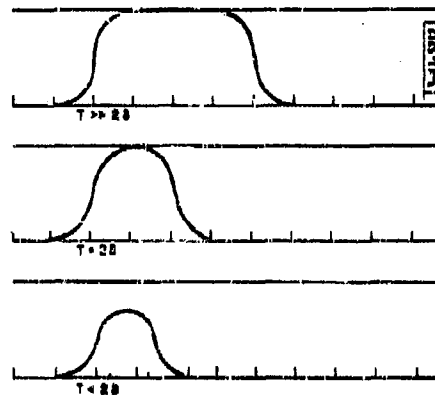
D. SYSTEM PERFORMANCE DEGRADATION FOR SHORT PULSES

1. Energy Loss

It has been shown that the transients due to build-up phenomena lead to parabolic signal envelopes instead of rectangular pulses. The extent of the transient is a sinusoidal function of angle off-broadside. In determining the energy available to the receiver, the signal envelope must be squared and integrated. It is clear that the parabolic signal envelope contains less energy than its rectangular counterpart. As a result, less energy is available to the receiver for detection.

The extent of this energy loss will now be investigated. In radar systems, the ratio of signal-to-noise energy is the key criterion for measurement of energy loss.[*] Therefore, the signal-to-noise ratio (S/N) will be computed and compared with undistorted behavior for two distinct cases:

(a) Receiver is matched to the distorted waveform. In this case, the matched filter would be changed for each beam-pointing angle of interest.

(b) Receiver is matched to a square pulse. Here the S/N obtained is not so great as in the first case. However, the implementation would be less complex, since the same receiver could be used for all beam-pointing angles.

Receiver Matched to Distorted Waveform:-- Define:

$v(t)$ = undistorted signal (square pulse),

$w(t)$ = distorted signal,

$$\eta = \frac{\text{S/N of distorted signal with receiver matched to distortion}}{\text{S/N of undistorted signal with receiver matched to square pulse}} \ .$$

Matched filters are designed to maximize the S/N at their output where the noise is assumed to have white Gaussian statistics.[*] It is well known that the optimum filter subject to this criterion has an impulse response that is proportional to the expected signal but runs backward in time. Therefore, if there is no distortion, the output of the matched filter in the presence of noise is

$$x(t) = C \int v(-\tau) \, v(t-\tau) \, d\tau + C \int v(-\tau) \, n(t-\tau) \, d\tau \quad ,$$

where $n(t)$ is the noise waveform and C is a constant. The maximum ratio of signal-to-noise power in the output with the receiver matched to the square pulse and no distortion $(S/N)_{oo}$, is

$$(S/N)_{oo} = \frac{C^2 [\int v^2(t) \, dt]^2}{C^2 N_o \int v^2(t) \, dt} = \frac{1}{N_o} \int v^2(t) \, dt \quad ,$$

where N_o is the noise spectral density. However, if distortion occurs which can be predicted, a filter can be used that is matched to this distorted signal. Then the output of the matched filter is

$$x'(t) = C \int w(-\tau) \, w(t-\tau) \, d\tau + C \int w(-\tau) \, n(t-\tau) \, d\tau \quad .$$

In this output, the ratio of signal-to-noise power, $(S/N)_{DD}$, is

$$(S/N)_{DD} = \frac{C^2 [\int w^2(t) \, dt]^2}{C^2 N_o \int w^2(t) \, dt} = \frac{1}{N_o} \int w^2(t) \, dt \quad .$$

Consequently,

$$\eta = \frac{\int w^2(t) \, dt}{\int v^2(t) \, dt}$$

---

[*] W. B. Davenport, Jr. and W. L. Root, An Introduction to the Theory of Random Signals and Noise (McGraw-Hill, New York, 1959).

248

Receiver Matched to Square Pulse:– Define v(t) and w(t) as above and

$$\eta' = \frac{\text{S/N of distorted signal with receiver matched to square pulse}}{\text{S/N of undistorted signal with receiver matched to square pulse}} = \frac{(S/N)_{Do}}{(S/N)_{oo}} \quad .$$

If there is no distortion, the output of the matched filter is still x(t). However, when distortion occurs, the output becomes

$$x''(t) = C \int v(-\tau) \, w(t-\tau) \, d\tau + C \int v(-\tau) \, n(t-\tau) \, d\tau \quad .$$

In this output, the maximum ratio of signal-to-noise energy is

$$(S/N)_{Do} = \frac{C^2 [\int v(t) \, w(t) \, dt]^2}{C^2 N_o [v^2(t) \, dt]} \quad .$$

Therefore,

$$\eta' = \frac{[\int v(t) \, w(t) \, dt]^2}{[\int v^2(t) \, dt]^2} \quad .$$

It was indicated earlier that the distorted waveform w(t) varies as a function of the pre-distortion pulse length T and the angle off-broadside ξ. If we define δ as the traverse time, $L/c \sin \xi$. It becomes convenient to measure distortion by the parameter T/δ, the pulse length in multiples of traverse time. Using this notation, the integrals above were calculated as functions of T/δ, and η and η' were plotted against T/δ in Fig. 3-54. The curves drop sharply toward zero for $T/\delta < 2$, and there is about 1 db difference between η and η' in this critical region. At $T/\delta = 1$, the distortion causes about 3 db drop in S/N using a receiver matched to the distorted waveform and another 1 db if no match is attempted. For large T/δ, there is still a noticeable loss.

2. Loss in Resolution

Radar resolution, the ability to distinguish between the returns from two individual targets, depends on the shape of the matched filter output. If rectangular pulses are transmitted, received, and matched-filtered, the result is a triangle with height proportional to the signal energy. Since the base of the triangle equals twice the pulse length, it is clear that short pulses and high power improve resolution capability.

However, the loss and transient phenomena discussed in the previous section tend to limit performance. To indicate the extent of these limitations, matched filter output waveforms are sketched in Figs. 3-55 and 3-56. In Fig. 3-55, the outputs of filters matched to the distorted waveform and to the transmitted rectangular pulse are compared. Due to bandwidth considerations, the rectangular filter gives a slightly better waveform for resolution purposes, even though the S/N is not so good.

In Fig. 3-56, the outputs of matched filters matched to rectangular pulses are sketched for different transmitted pulse lengths. It is clear that the resolution drops off rapidly as pulse length becomes very short
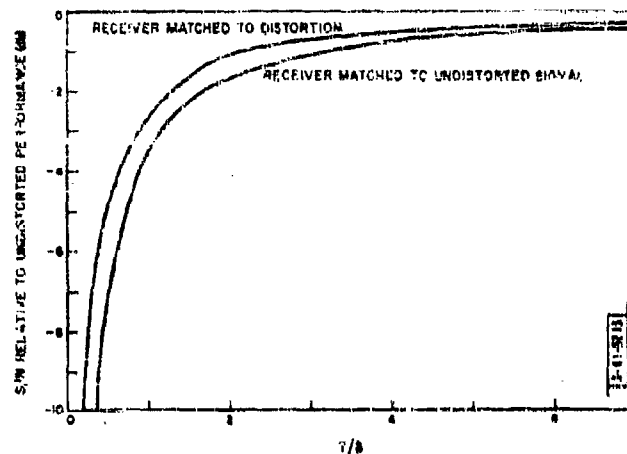
Fig. 3-54. Short pulse array performance.

(a) Filter matched to distorted pulse.

(b) Filter matched to square pulse.
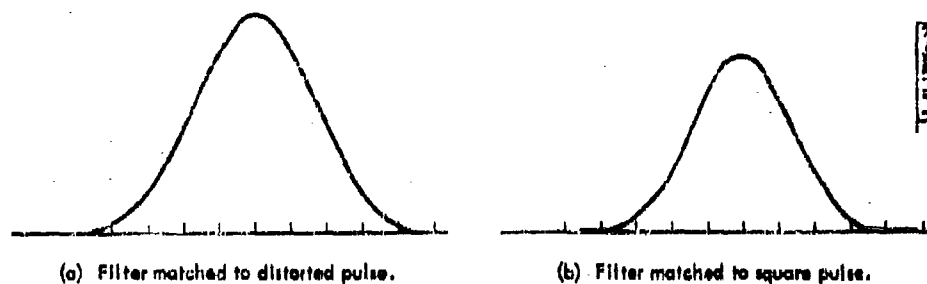
Fig. 3-55. Comparison of outputs of two types of matched filters for pulse length T = 8.
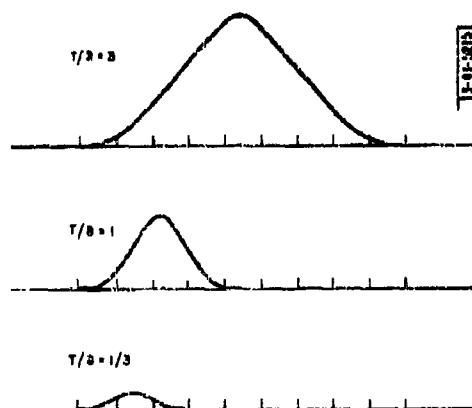
Fig. 3-56. Outputs of filters matched to square pulse with distorted input for various transmitted pulse lengths. Scales adjusted for same noise level in all three cases.

3. Loss in Accuracy

Range accuracy is the third aspect of the radar performance which is depreciated by the distortion considered in this report. Reed, Kelly and Root[*][†] discuss the measurement of range and take as an accuracy criterion the variance of the range estimate around the true value. The principal result is that this variance is inversely proportional to the product of S/N and the square of the effective bandwidth B_0. Here E_0 of a signal with spectrum $g(f)$ is defined by

$$B_0^2 = \int f^2 |g(f)|^2 \, df - \left(\int_{-\infty}^{\infty} f |g(f)|^2 \, df \right)^2 \quad .$$

Thus, B_0 is readily calculated by using the properties of Fourier transforms.

We have seen that a system's response to a pulsed signal is found by convolving the array amplitude taper with itself, and then convolving this result with the pulse. In the case of a uniform illumination and a square pulse, this is the convolution of three rectangular pulses. Since convolution corresponds to multiplication in the frequency domain, the array output spectrum is the product of the three individual spectra. Each rectangular pulse has a $\sin x / x$ frequency response; therefore, the output frequency spectrum is the product of three such functions. Our final concern is the width of this spectrum; consequently, the locations of the pulses do not affect the results, and for simplicity it will be assumed they are centered about the origin. The spectrum of the illumination is given by

$$\frac{L' \sin \frac{\omega L'}{2}}{\frac{\omega L'}{2}} \quad ,$$

where $L' = L/c \sin \xi$, and the spectrum of the transmitted pulse is

$$\frac{T \sin \frac{\omega T}{2}}{\frac{\omega T}{2}} \quad ,$$

where T is the pulse width. The above argument leads to the output spectrum:

$$|H(j\omega)| = \frac{8 \sin^2 \frac{\omega L'}{2} \sin \frac{\omega T}{2}}{\omega^3} \quad .$$

This is centered about $\omega = 0$, making the second integral in the expression for B_0^2 equal to zero. The first can be integrated by parts to yield the bandwidth. In Fig. 3-57, the reduction in B_0^2 is plotted as a function of T/δ. A rapid drop in bandwidth is seen for $T/\delta < 2$. For $T/\delta > 2$, there is virtually no reduction.

Finally, in Fig. 3-58, the increase in measurement variance is plotted as a function of T/δ, taking into account both the reduction in S/N and in bandwidth. Again, a rapid drop is seen for $T/\delta < 2$.

---

*I.S. Reed, E.J. Kelly and W.L. Root, "The Detection of Radar Echoes in Noise. Part I: Statistical Preliminaries and Detector Design," Technical Report No. 158 [U], Lincoln Laboratory, M.I.T. (20 June 1957), ASTIA 150865, H-238.

†I.S. Reed, E.J. Kelly and W.L. Root, "The Detection of Radar Echoes in Noise. Part II: The Accuracy of Radar Measurements," Technical Report No. 159 [U], Lincoln Laboratory, M.I.T. (19 July 1957), ASTIA 150866, H-215.

Best Available Copy
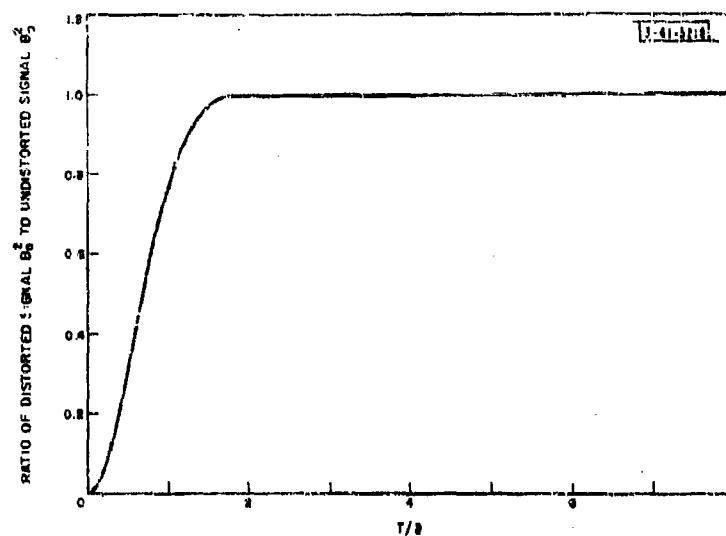
Fig. 3-57. Distorted signal β_0^2 vs pulse length.
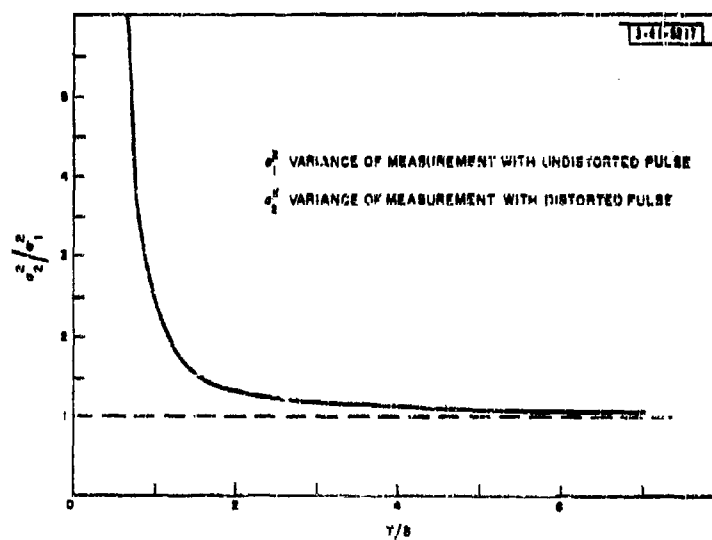
Fig. 3-58. Variance in range measurements vs pulse length.

E. CONCLUDING REMARKS

Effects which depreciate the performance of a large array radar have been shown to exist. These effects become significant in the range $T/\delta < 2$.

The importance of these phenomena is illustrated by a simple example. For a radar operating at L-band, having a 100λ aperture, and pointing at $45°$ off-broadside, δ equals about 70 nanoseconds. Hence, the phenomena discussed here became a consideration for pulse lengths less than 140 nanoseconds.

In summary, it can be said that there is a very rapid depreciation in performance for short pulses below a certain critical length. Above this threshold, the effects are essentially negligible.

APPENDIX A
ANTENNA SYSTEM IMPULSE RESPONSE

To determine the impulse response of the antenna system, assume an arbitrary sinusoidal signal current $s(t) = e^{j\omega t}$ to be transmitted. The signal is routed to each of the N antenna feed systems (Fig. 3-52), where it is first phase-shifted by $\phi(n)$, then weighted by $a(n)$, and finally sent to the antenna element where radiation takes place. $\phi(n)$ and $a(n)$ are functions of n, an index on the antenna elements. Assume that the N antenna elements are infinitesimal dipoles, linearly polarized in the z-direction. Consequently, the current distribution across the array is proportional to

$$\vec{J} = K \left[\sum_{n=-L/2D}^{+L/2D} e^{j\omega t} a(n) e^{j\phi(n)} u_0(x - nD) \right] \vec{a}_z \quad ,$$

where K is an all-purpose constant to absorb all factors of proportionality, and D is the inter-element spacing. Once this distribution is known, the field strength in the far-field can be determined by integration, using the well-known vector potential relationship[*]

$$\vec{A} = \frac{\mu_0}{4\pi} \int_V \frac{\vec{J} e^{-jkr}}{r} \, dv \quad .$$

For far-field calculations, where r is very large compared to array size, r can be taken outside the integral. Then the vector potential becomes proportional to

$$\vec{A} = K_4 \left[\sum_{n=-L/2D}^{+L/2D} \int_{-L/2}^{+L/2} e^{j\omega t} a(n) e^{j\phi(n)} e^{-j(\omega/c)r} u_0(x - nD) \, dx \right] \vec{a}_z \quad .$$

In the far-field, at a point P, r can be approximated by $r_0 - x \sin \xi$, where r_0 is the distance from the center of the array to P, and ξ is the angle between the normal to the array and a line to P from the array center as in Fig. 3-51. Making this substitution,

$$\vec{A} = K e^{j\omega t} \left[e^{-j(\omega r_0/c)} \sum_{n=-L/2D}^{+L/2D} \int_{-L/2}^{+L/2} a(n) e^{j\phi(n)} e^{j(\omega x/c)\sin \xi} u_0(x - nD) \, dx \right] \vec{a}_z \quad .$$

Denote the bracketed part of this expression by A. It is apparent that from this expression for vector potential, the electric and magnetic fields in the far-fields can be calculated[†] according to

$$\vec{E} = E_z \vec{a}_z = -j\omega \vec{A} \quad ,$$

$$\vec{H} = H_\phi \vec{a}_\phi = \sqrt{\frac{\epsilon_0}{\mu_0}} E_z \vec{a}_\phi \quad .$$

This last expression results from the approximate plane-wave characteristic of the wave in the far-field. Poynting's vector is therefore

---

[*]R.B. Adler, L.J. Chu and R.M. Fano, *Electromagnetic Energy Transmission and Radiation* (Wiley, New York, 1960).

[†]R.M. Fano, L.J. Chu and R.B. Adler, *Electromagnetic Fields, Energy and Forces* (Wiley, New York, 1960).

$$\vec{S} = S\vec{a}_r = \vec{E} \times \vec{H} = \sqrt{\frac{\epsilon_0}{\mu_0}}\, E_z^2\, \vec{a}_r = \sqrt{\frac{\epsilon_0}{\mu_0}}\, \omega^2 A^2\, \vec{a}_r \quad .$$

The magnitude of $\vec{S}$ represents the power density in the far-field propagating in the direction of $\vec{S}$. Introducing σ, the target cross section, we can determine the power intercepted by the target:

$$P = \sigma S \quad .$$

When this power is radiated isotropically, some of it returns to the antenna system which is now being operated in the receiving mode. Currents are induced on the dipole elements. These currents are weighted, phase-shifted, and summed in the feed system in identically the same way as when the antenna was operated in the transmitting mode. Let $\vec{S}_1$ be Poynting's vector for the scattered field. Then its magnitude, S_1, is given by

$$S_1 = |\vec{S}_1| = \frac{P}{4\pi R^2} \quad ,$$

where R is the distance from the target to the observation point. If $\vec{E}_1$ is the scattered electric field,

$$E_1 = K_2 \sqrt{S_1} = K_3 \omega A \quad .$$

Calculation of the dipole currents is readily accomplished by utilizing the applicable equivalent circuit for a receiving dipole (see Fig. 3-59).[†] When matched, the load impedance equals the complex conjugate of the dipole input impedance Z_{in}, and the load power is

$$P_L = \frac{(\vec{E}_1 \cdot \vec{d})^2}{2(Z_{in} + Z_{in}^*)} = \frac{(\vec{E}_1 \cdot \vec{d})^2}{4R_{in}} \quad ,$$

where $\vec{E}_1$ is the electric field incident on the dipole and $\vec{d}$ is the equivalent length vector of the dipole.

Fig. 3-59. Equivalent circuit for receiving dipole.
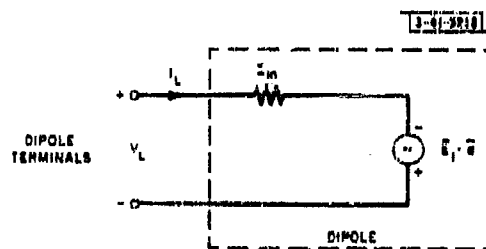
This power is available at each dipole of the array for combination into a single coherent beam in the corporate feed structure. Consideration of power rather than current is necessary, since transformers can always be used to change impedance levels. It is assumed that all such transformers used in the antenna system operate independently of frequency over the bandwidth of interest. This permits us to assume that the currents on the dipole are proportional to $\sqrt{P_L}$

† R.B. Adler, L.J. Chu and R.M. Fano, op. cit.

and that no new frequency terms enter the analysis. We now calculate the currents on the dipoles. Since for a short dipole R_{in} is proportional to ω^2,[*]

$$P_L = \frac{K_3^2 \omega^2 A^2 d^2 \cos^2 \alpha}{4R_{in}} = K_4^2 A^2 \quad ,$$

where α is the angle between $\overline{E}_i$ and $\overline{d}$. Hence, the dipole current is

$$I_d = K_5 A \quad .$$

The constant K_5 accounts for impedance transformations and constants independent of frequency.

It is clear that the electric field at every dipole is not the same. Although the amplitudes are very close to identical, there is a phase difference of $(\omega/c) D \sin \xi$ (or a delay of $D/c \sin \xi$) between successive elements which must be considered in summing the outputs of the N receiving dipoles. This phase term does not affect the power relationships determined above. Consequently, the current at the ℓth dipole is

$$I_{d(\ell)} = K_5 A \exp\left[j\omega\left(t - \frac{r_o}{c} + \frac{\ell D}{c} \sin \xi\right)\right] \quad .$$

The output of the antenna system becomes

$$I = \sum_{\ell=-L/2D}^{+L/2D} a(\ell)\, e^{j\phi(\ell)}\, K_5 A \exp\left[j\omega\left(t - \frac{r_o}{c} + \frac{\ell D}{c} \sin \xi\right)\right]$$

$$= K_6\left[\sum_{\ell=-L/2D}^{+L/2D} a(\ell)\, e^{j\phi(\ell)}\, e^{j\omega \ell D/c\, \sin \xi} \sum_{n=-L/2D}^{+L/2D} a(n)\, e^{j\phi(n)} \right.$$

$$\left. \int_{-L/2}^{+L/2} e^{j\omega x/c\, \sin \xi}\, \mu_o(x - nD)\, dx \right]\, e^{j\omega\left(t - \frac{2r_o}{c}\right)}$$

$$= K_6 \sum_{\ell=-L/2D}^{+L/2D} \sum_{n=-L/2D}^{+L/2D} a(\ell)\, a(n)\, \exp\{j[\phi(\ell) + \phi(n)]\}$$

$$\times \exp\{j \frac{\omega}{c} (\ell + n) D \sin \xi\} \cdot \exp\left[j\omega\left(t - \frac{2r_o}{c}\right)\right] \quad .$$

This expression represents the output of the antenna system in response to an input sinusoid of frequency ω_o. To obtain the impulse response, the following theorem from Fourier theory can be utilized.

If a system has the response $H(j\omega)$ to an input $e^{j\omega t}$, then the response of the system to an impulse is the Fourier transform of $H(j\omega)$ given by

$$h(t) = \frac{1}{2\pi} \int_{-\infty}^{\infty} H(j\omega)\, e^{j\omega t}\, d\omega \quad .$$

*R.B. Adler, L.J. Chu and R.M. Fano, op. cit.

It is also desirable at this point to make the usual assumption of linear phase taper for $\phi(n)$. We assume that the phase shifters are independent of frequency and consequently operate in a band around some carrier frequency ω_o. Pointing the beam at an angle ξ_o requires, then, that

$$\phi(n) = -j \frac{\omega_o nD}{c} \sin \xi_o \quad .$$

Finally, $h(t)$ can be determined:

$$h(t) = \frac{K_0}{2\pi} \sum_{\ell=-L/2D}^{+L/2D} \sum_{n=-L/2D}^{+L/2D} a(\ell)\, a(n)\, \exp\left[j\, \frac{\omega_o}{c} (\ell + n)\, D\, \sin \xi_o\right]$$

$$\times \int_{-\infty}^{\infty} \exp\left\{j\omega\left[t - \frac{2r_o}{c} + (\ell + n)\, \frac{D \sin \xi}{c}\right]\right\}\, d\omega$$

$$= \frac{K_0}{2\pi} \sum_{m=-L/D}^{+L/D} \exp\left[j\, \frac{\omega_o nD}{c} \sin \xi_o\right] u_o\left(t - \frac{2r_o}{c} + \frac{mD}{c} \sin \xi\right)$$

$$\cdot \left(\sum_{n=-L/2D}^{+L/2D} a(n)\, a(m - n) \right) \quad .$$

APPENDIX B
DISTORTED WAVEFORM FORMULAS

I. $T < \delta$

$$w(t) = \frac{(t + \delta)^2}{2} \qquad\qquad -\delta \leqslant t' < -\delta + T$$

$$= \frac{(t + \delta)^2}{2} - \frac{(t + \delta - T)^2}{2} \qquad\qquad -\delta + T \leqslant t' < 0$$

$$= \frac{(t + \delta)^2}{2} - \frac{(t + \delta - T)^2}{2} - t^2 \qquad\qquad 0 \leqslant t' < T$$

$$= \frac{(t + \delta)^2}{2} - \frac{(t + \delta - T)^2}{2} - t^2 + (t - T)^2 \qquad\qquad T \leqslant t' < \delta$$

$$= \frac{(t + \delta)^2}{2} - \frac{(t + \delta - T)^2}{2} - t^2 + (t - T)^2 + \frac{(t + \delta)^2}{2} \qquad \delta \leqslant t' < \delta + T$$

$$= 0 \text{ elsewhere}$$

II. $\delta < T < 2\delta$

$$w(t) = \frac{(t + \delta)^2}{2} \qquad\qquad \delta \leqslant t' < 0$$

$$= \frac{(t + \delta)^2}{2} - t^2 \qquad\qquad 0 \leqslant t' < -\delta + T$$

$$= \frac{(t + \delta)^2}{2} - t^2 - \frac{(t + \delta - T)^2}{2} \qquad\qquad -\delta + T \leqslant t' < \delta$$

$$= \frac{(t + \delta)^2}{2} - t^2 - \frac{(t + \delta - T)^2}{2} + \frac{(t - \delta)^2}{2} \qquad\qquad \delta \leqslant t' \leqslant T$$

$$= \frac{(t + \delta)^2}{2} - t^2 - \frac{(t + \delta - T)^2}{2} + \frac{(t - \delta)^2}{2} + (t - T)^2 \qquad T \leqslant t' < \delta + T$$

$$= 0 \text{ elsewhere}$$

III. $2\delta < T$

$$w(t) = \frac{(t + \delta)^2}{2} \qquad\qquad -\delta \leqslant t' < 0$$

$$= \frac{(t + \delta)^2}{2} - t^2 \qquad\qquad 0 \leqslant t' < \delta$$

$$= \frac{(t + \delta)^2}{2} - t^2 + \frac{(t - \delta)^2}{2} \qquad\qquad \delta \leqslant t' < -\delta + T$$

$$= \frac{(t + \delta)^2}{2} - t^2 + \frac{(t - \delta)^2}{2} - \frac{(t + \delta - T)^2}{2} \qquad\qquad -\delta + T \leqslant t' < T$$

$$= \frac{(t + \delta)^2}{2} - t^2 + \frac{(t - \delta)^2}{2} - \frac{(t + \delta - T)^2}{2} + (t - T)^2 \qquad T \leqslant t' < \delta + T$$

$$= 0 \text{ elsewhere}$$

CHAPTER III
SOME EXTENSIONS OF THE THEORY OF RANDOM ERROR EFFECTS
ON ARRAY PATTERNS

SUMMARY   J. L. Allen

This chapter deals with several extensions of the theory of random errors in arrays:

(1) A rigorous derivation of the far-field probability density function,
without the usual restriction of small and/or Gaussian phase errors,
including element pattern irregularity effects and random element
failure;

(2) A brief review of the effects of such errors on sidelobe levels, both
individually and collectively, including a new, simple result for
directivity degradation;

(3) An investigation of the potentiality of using random element spacing
for grating-lobe suppression;

(4) The limitations of "density" tapering of arrays;

(5) The effects of random errors on the pointing accuracy of both "sum"
and "difference" beams of monopulse arrays.

Detailed summaries appear at the beginning of each section, with the exception of Secs. A
and B.

A. INTRODUCTION

1. Survey of Previous Investigations

Many papers have been published on the effects of random errors on the performance of ar-
ray antennas. Ruze[*] published the first comprehensive work on the subject and pursued the ef-
fect of small phase and amplitude errors on array sidelobe levels and directivity, subject to the
assumption of small Gaussian phase errors. More recently, Elliott[†] has given an analysis of
error effects including error in the mechanical orientation of the radiators, subject to the re-
striction that all errors are small and from a Gaussian distribution.

In their discussion of error effects on sidelobe levels, both Ruze and Elliott confine the bulk
of their attention to the statistics of any one particular point in the sidelobe region and investi-
gate the question of what fraction of a large number of arrays with the given error statistics
would produce a level greater than some preselected value at this predetermined point. The
array designer is usually more concerned with the question of what percentage of sidelobes of a
particular array one should expect to find above a certain level. Elliott briefly indicates an ap-
proximate answer to the problem. Rondinelli[‡] pursues this question in detail, under the as-
sumption that the individual sidelobe levels are independent random variables.

The pointing accuracy of arrays in the presence of random errors has been a subject of
papers by Rondinelli and Leichter.[§] All these investigations have concerned themselves with
beams having a maximum in the desired direction (the "sum" beam, in systems using monopulse).

---

[*] J. Ruze, "Physical Limitations on Antennas," Technical Report No. 248 [U], Research Laboratory of Electronics,
M.I.T. (30 October 1952).

[†] R.S. Elliott, "Mechanical and Electrical Tolerances for Two-Dimensional Scanning Antenna Arrays," Trans. IRE,
PGAP AP-6, 114 (1958).

[‡] L.A. Rondinelli, "Effects of Random Errors on the Performance of Antenna Arrays of Many Elements," 1959 IRE
National Convention Record, Part I, pp. 174-189.

[§] M. Leichter, "Beam Pointing Errors of Long Line Sources," Trans. IRE, PGAP AP-8, 268 (1960).

2. Scope of This Investigation

This report is concerned with several extensions of the theory of random error effects and a critical "second look" at some of the earlier results.

First, the potential sources of error are examined, including the previously neglected effects of non-identical element factors (for example, see Fig. 3-61) and the possibility of catastrophic failures. It is shown that all error effects can be characterized by three parameters:

    (a) The expected fraction of operating elements,

    (b) The total amplitude variance,

    (c) The characteristic function of the element phase errors.

Simple relationships are pointed out between the last two parameters and the corresponding statistics of the various errors possible in each element, under the assumption of independence of the various contributing sources.

A critical derivation of the probability density function of the far-field follows, in which some of the restrictive assumptions of previous derivations are omitted. The derivation given herein is valid for any assumed distributions of the various error sources, with only the restrictions that the errors are essentially independent from element to element, and that corresponding errors in different elements are samples of the same random variable (the error statistics are identical for all elements). It is shown that the pattern statistics may be markedly different in the principal lobe regions and in the sidelobe regions and that two distinct probability density functions are generally necessary for satisfactorily describing the field everywhere.

A brief review of the effects of random errors on sidelobe levels follows, with emphasis on the error effects in regions where errors predominate the design pattern, and a useful "rule of thumb" for allowable errors is presented. The allowable errors for maintaining all sidelobes in this region below a preset threshold with a desired probability are examined (or alternatively, the allowable errors in terms of the percentage of sidelobes one would expect to find below the threshold, from a large number of similar arrays). The assumption of the independence of error effects from sidelobe to sidelobe is critically examined and shown to be only an approximation which tends to yield pessimistic results.

The expected reduction in array directivity due to small errors is derived, and it is shown that a simpler result than that of Ruze[*] can be obtained.

The question of grating-lobe suppression by randomized element placement is then investigated, using the previously derived probability density functions in the form appropriate for large phase errors, and curves are presented giving the probable grating-lobe reduction as a function of the degree of randomization for one particular randomization scheme.

The shaping of array patterns by altering the density, rather than the amplitude, of the elements in an array is analyzed from a probabilistic standpoint, and qualitative comparisons are drawn between "density tapered" and amplitude tapered arrays. Although the idea of density tapering is not new, no general qualitative results have been previously published, to the best of this writer's knowledge.

---

[*] J. Ruze, op.cit.

Lastly, the effects of random errors on the pointing accuracy of arrays are examined. Simple, general expressions in terms of no-error illumination functions are derived for the errors in

    (a) The location of the maximum of a monopulse "sum" pattern (applicable, of course, to the beams obtained from systems not using monopulse),

    (b) The location of the zero of the usual estimating function for monopulse angular interpolation using the ratio of the sum and difference beam outputs.

The resulting formulas are simple, but applicable to any amplitude taper (in contrast to Rondinelli and Leichter, although Leichter's result is actually expressible in the same form). It is shown that Leichter's result for the sum beam error (derived for a line source) is pessimistic for arrays by a factor of $1/\sqrt{2}$. The relations for the difference beam error are believed to be new.

3. Section Organization

This section will begin with an outline of some of the mathematical relationships that will be used frequently in the derivations to follow. The remainder of the section follows essentially the order given above.

For the casual reader, a summary of the important results and underlying assumptions of each investigation will be given at the beginning of each major division of the discussion (those rating upper case titles).

B. MATHEMATICAL PRELIMINARIES

In this section are set forth some mathematical relationships and definitions that will be used frequently in the following derivations. Where the proof is not evident, it is available in standard texts on the appropriate subject.

1. Statistical Averages

If x_n is a sample of a random variable x, having a probability density function (hereafter referred to as pdf), $p(x)$, the expected value of some function of the samples of x, say $f(x_n)$ is given by

$$f(\overline{x_n}) = \int_{-\infty}^{\infty} f(x)\, p(x)\, dx \quad . \tag{1}$$

As special cases, the mean value of x_n is

$$\overline{x_n} = \int_{-\infty}^{\infty} x p(x)\, dx = \overline{x} \quad , \tag{2}$$

and the variance σ_x^2 is

$$\sigma_x^2 = \overline{(x_n - \overline{x_n})^2}$$

$$= \overline{x_n^2} - \overline{x_n}^2 \quad , \tag{3}$$

where

$$\overline{x_n^2} = \int_{-\infty}^{\infty} x^2 p(x) \, dx \quad .$$

Obviously, if $\overline{x_n} = 0$, $\sigma_x^2 = \overline{x_n^2}$.

2. Characteristic Functions

An average playing an important part in the following derivations is of the form

$$\overline{e^{j\alpha\tau}} = \int_{-\infty}^{\infty} p(\tau) \, e^{j\alpha\tau} \, d\tau \quad . \tag{4}$$

This quantity, recognizable as the Fourier Transform of $p(\tau)$ into α-space, is called the characteristic function for the random variable τ,

$$\overline{e^{j\alpha\tau}} = C_\tau(\alpha) \quad . \tag{5}$$

but is a function of α only.

Several properties of $C_\tau(\alpha)$ are useful. First, since the absolute magnitude of an integral is always equal to, or less than, the integral of the magnitude of the integrand,

$$|C_\tau(\alpha)| \leq \int_{-\infty}^{\infty} p(\tau) \, d\tau = C_\tau(0) = 1 \quad . \tag{6}$$

If $p(\tau)$ is an even function of τ, $C_\tau(\alpha)$ is real, and

$$C_\tau(-\alpha) = C_\tau(\alpha) \quad . \tag{7}$$

Note that this implies that $\overline{\tau} = 0$; however, if $p(\tau)$ is even about some non-zero τ_0, a simple change of variable can be affected to utilize (7).

Finally, by expanding $e^{j\alpha\tau}$ under the integral sign in (4), integrating term by term and using (1),

$$C_\tau(\alpha) = \sum_{m=0}^{\infty} (j\alpha)^m \frac{\overline{\tau^m}}{m!} \quad . \tag{8}$$

We will be concerned with either confined pdf's [$p(\tau) = 0$ for τ outside some finite interval] or pdf's "concentrated" in a confined region (e.g., Gaussian distributions) so that, in the case of $\overline{\tau} = 0$, the series is rapidly convergent for $\overline{\tau^2} = \sigma_\tau^2 \ll 1$, and we can approximate

$$C_\tau(\alpha) \approx 1 - \frac{\alpha^2 \sigma_\tau^2}{2} \quad ; \quad \sigma_\tau^2 \ll 1 \quad , \quad \overline{\tau} = 0 \quad . \tag{9}$$

3. Averages of Multiple Summations of Independent Samples

We will frequently be concerned with averages of the form

$$F = \overline{\sum_m \sum_n x_m a_m x_n a_n} \quad ,$$

where a_m and a_n are non-statistical quantities. Obviously, for $m = n$, we have

$$\sum_m \sum_n \overline{\overline{x_m a_m x_n a_n}} = \sum_m \overline{x_m^2 a_m^2} = \overline{x^2} \sum_m a_m^2$$
$$m = n$$

for x_n samples of the random variable x.

For $m \neq n$, assuming x_m and x_n independent,

$$\sum_m \sum_n \overline{\overline{x_m a_m x_n a_n}} = \sum_m \overline{x_m} a_m \sum_n \overline{x_n} a_n = \overline{x}^2 \sum_m \sum_n a_m a_n$$
$$m \neq n \qquad\qquad m \neq n \qquad\qquad m \neq n$$

Thus,

$$\sum_m \sum_n \overline{\overline{x_m a_m x_n a_n}} = \overline{x}^2 \sum_m \sum_n a_m a_n + \overline{x^2} \sum_m a_m^2$$
$$m \neq n$$

This process can be formally handled by writing

$$\sum_m \sum_n \overline{x_m} \overline{x_n} = \overline{x}^2 \left[\sum_m \sum_n a_m a_n - \sum_m a_m^2 \right] + \overline{x^2} \sum_m a_m^2 \tag{10}$$

where the extra term in the brackets excludes the $m = n$ term from the summation multiplied by $\overline{x}^2$ so that it is not counted twice.

C. ERRORS AND THEIR STATISTICAL DESCRIPTION

Summary

It is shown that the analysis of error effects can be carried out in terms of

(1) An "apparent" element amplitude, b_n, given by

$$b_n(\phi, \theta) = \frac{f_n(\phi, \theta)}{\bar{f}(\phi, \theta)} a_n \quad ,$$

where $f_n(\phi, \theta)$ is the element factor, $\bar{f}(\phi, \theta)$ is the average element factor, and a_n is the no-error drive amplitude,

(2) An apparent element phase error,

$$\psi_n(\phi, \theta) = \delta_n + k[x_n \sin \theta \cos \phi + y_n \sin \theta \sin \phi$$

$$+ (z - nD) \cos \theta] \quad ,$$

where δ_n is the element drive phase error, x_n, y_n and z_n are the errors in element radiation center placement, and k is the wave number, $k = 2\pi/\lambda$.

The resulting apparent error statistics are related to the statistics of the individual error sources by

$$\overline{b_n(\phi, \theta)} = P a_n \quad ,$$

$$\overline{b_n^2(\phi, \theta)} = P[1 + \sigma_A^2(\phi, \theta)] a_n^2 \quad ,$$

where, for small amplitude error,

$$\sigma_A^2 \approx \sigma_\mu^2(\phi, \theta) + \sigma_\Delta^2 \quad ,$$

the sum of the variances in element drive amplitude error, σ_Δ^2, and element factor amplitude $\sigma_\mu^2(\phi, \theta)$. P is the fraction of elements actually operating. Finally, the phase statistic of importance is

$$C_{\psi(\phi, \theta)}(\alpha) = C_\delta(\alpha) \ C_x(\alpha k \sin \theta \cos \phi)$$

$$\times C_y(\alpha k \sin \theta \sin \phi) \ C_{(z - nD)}(\alpha k \cos \theta) \quad ,$$

where $C_\delta(\alpha)$ is the characteristic function for the random variable δ, and similarly for the other random variables.

1. Sources of Errors Affecting Array Performance

The possible relevant sources of errors in arrays can be readily recognized once a decision is reached about just what situation constitutes "no error." For the purposes of this report, it will be assumed that the "no-error" far-field,* F_o, of a linear array in the geometry of Fig. 3-60 is that given by the expression

---

*Either the E- or H-field, the vector nature of which will be ignored.

$$F_n(\phi, \nu) = f(\phi, \nu) \sum_{n=o}^{N-1} a_n e^{jn(\nu-\nu_o)} \quad , \qquad \begin{cases} \nu = 2\pi \dfrac{D}{\lambda} \cos\Theta \quad , \\[2mm] \nu_o = 2\pi \dfrac{D}{\lambda} \cos\Theta_o \quad , \end{cases} \tag{11}$$

assuming the array to be linearly phased to point the main beam in the direction Θ_o. The quantity $f(\phi, \nu)$ represents the "element factor"; i.e., the average pattern of the array elements in the array environment (specifically, the average of the patterns obtained by driving one element at a time with all others terminated in their normal driving impedance). The quantity $a_n e^{-jn\nu_o}$, with both a_n and ν_o real, describes the amplitude and phase of the current that would be flowing in the nth element with all others terminated in their normal driving impedance. The nth element is supposed to be located at $x = 0$, $y = 0$, $z = nD$.[*]

Instead of exactly realizing this far-field, one would in practice obtain a field

$$F(\phi, \Theta) = \sum_{n=o}^{N-1} f_n(\phi, \Theta) a_n' e^{-jn\nu_o} e^{j\delta_n} e^{jk\bar{\rho}_n \cdot \hat{R}} \tag{12}$$

where $f_n(\phi, \Theta)$ is the actual pattern of the nth element in its array environment, with respect to a coordinate system centered on the nth element, which may differ considerably from the average element factor as shown in Fig. 3-64 for a particularly extreme case. The quantity a_n' represents the value of a_n with error and δ_n is the phase error of the nth element drive. Finally, the exponential expressing the phase delay of the elements at the far-field point has been generalized to allow for mechanical error in antenna placement. The vector "dot" product is related to the usual spherical coordinates by

$$\bar{\rho}_n \cdot \hat{R} = x_n \sin\Theta \cos\phi + y_n \sin\Theta \sin\phi + z_n \cos\Theta \quad , \tag{13}$$

where the "center of radiation"[†] of the nth element is at x_n, y_n, z_n.

2. Reduction of Various Errors to Pure Phase and Amplitude Errors

It is intuitively apparent from Eq. (12) that the many sources of possible error ultimately manifest themselves as phase and/or amplitude error in the illumination of the particular element in question. This can be seen by rewriting Eq. (12) in the form

$$F(\phi, \Theta) = f(\phi, \Theta) \sum_n b_n(\phi, \Theta) e^{j\psi_n(\phi, \Theta)} e^{jn(\nu-\nu_o)} \quad . \tag{14}$$

where, for particular angles ϕ, Θ, the apparent amplitude of the nth element is given by

$$b_n(\phi, \Theta) = \frac{f_n(\phi, \Theta)}{f(\phi, \Theta)} a_n' \quad , \tag{15}$$

---

[*] Although linear array notation will be used throughout this discussion, the results are directly applicable to planar arrays without modification in most cases, and can be used in many other cases with minor modification.

[†] In the context of this report, the "center of radiation" will be taken as a mechanical reference point; e.g., the "center of gravity" of an element and its image (a ground plane is assumed). Strictly speaking, then, $f_n(\phi, \Theta)$ should be taken as (1) complex, since the element factor may be irregular in both amplitude and phase with respect to this mechanical reference point, and (2) as a vector quantity to account for element rotation. However, we will take $f_n(\phi, \Theta)$ to be a magnitude only, with any variation in phase lumped in with the phase term, δ_n. Not only does this approach simplify the analysis, but also the usual physical case in that only the magnitude of the element factors is known from pattern measurements. Rotational errors have been shown by Elliott (op.cit.) to produce less pattern distortion than translational positioning errors and will not be explicitly considered here.

265
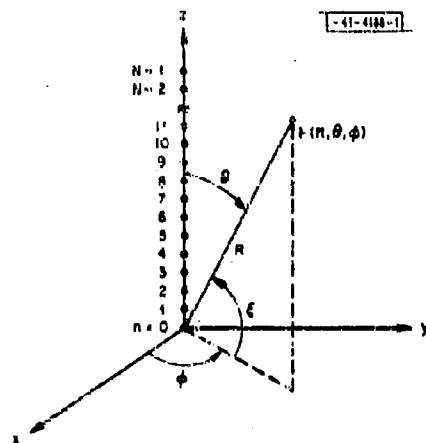
Fig. 3-60. N-element linear array geometry.
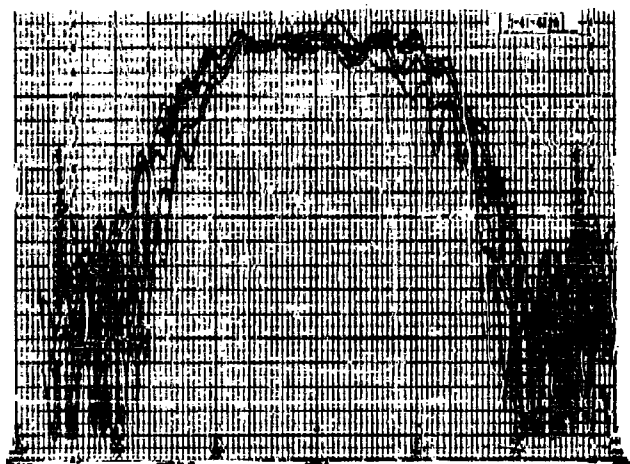
Fig. 3-61. Superimposed element factors of elements of a linear array of log-periodic elements.

and the apparent phase error term, $\psi_n(\phi, \Theta)$, by

$$\psi_n(\phi, \Theta) = \delta_n + k(x_n \sin\Theta \cos\phi + y_n \sin\Theta \sin\phi) + k(z_n - nD)\cos\Theta \quad , \qquad (16)$$

where $k = 2\pi/\lambda$.

In the analysis of the effects of errors on arrays, it will be seen presently that the quantities of significance are the <u>statistics</u> of the apparent phase and amplitude of the elements. Under fairly realistic assumptions, the statistics of the apparent amplitude error and the apparent phase error associated with each element can be quite simply related to the statistics of the individual errors.

First, the statistics of b_n will be derived. The element factor of the nth element for particular angles ϕ, Θ can be written as

$$f_n(\phi, \Theta) = f(\phi, \Theta)\,[1 + \mu_n(\phi, \Theta)] \quad ,$$

where the $\mu_n(\phi, \Theta)$ are samples of a random variable with mean zero and variance σ_μ^2, which can be estimated by taking sample element factors as indicated in Fig. 3-64.

The amplitude error of the drive to the nth element can be handled in a similar manner by assigning a random component, Δ_n, to the drive amplitude. Since it seems physically likely that the amplitude error will be proportional to the no-error drive amplitude,* this random component is usually assigned in a multiplicative manner:

$$a_n' = (1 + \Delta_n)\,a_n \quad ,$$

where the Δ_n are assumed to have a zero mean and variance σ_Δ^2.

This form of a_n' is not readily adaptable to the analysis of complete element failure (or deletion), however. To handle this case, it will be assumed that the a_n's are modified by a reliability factor, r_n, such that

$$a_n' = r_n(1 + \Delta_n)\,a_n \quad . \qquad (17)$$

where $r_n = 1$ with probability P, and zero with probability $1 - P$. For investigations of deliberate element omission, we will later make P a function of position (see Sec. Q), but for analysis of random failures, it seems reasonable to make the probability of a failure independent of position.

Thus, we have

$$b_n = [1 + \mu_n(\phi, \Theta)]\,[1 + \Delta_n]\,r_n a_n \quad . \qquad (18)$$

With these assumptions, the mean and mean-square of the nth element apparent amplitude can be readily calculated as

$$\overline{b_n}(\phi, \Theta) = a_n P \quad , \qquad (19)$$

$$\overline{b_n^2} = P^2\,a_n[1 + \sigma_\mu^2 + \sigma_\Delta^2 + \sigma_\Delta^2 \sigma_\mu^2] \quad . \qquad (20)$$

By separating the catastrophic failure case from the Δ_n factor, the variances in μ and Δ will be much less than unity in practice. Hence, the cross-product term can be dropped with little loss of accuracy. The mean-square value of the apparent amplitude is then seen to be approximately the sum of the variances caused by element pattern irregularity and error in drive amplitude.

---

*For example, a somewhat "smoothed" model of the alignment errors one would expect if the amplitudes are adjusted using a multi-range test meter.

Denoting the sum of the individual variances by σ_A^2, which will henceforth be called the amplitude variance, we can write

$$b_n^2 = F[1 + \sigma_A^2(\phi, \Theta)] a_n^2 \quad ,$$

$$\sigma_A^2 = \sigma_\mu^2(\phi, \Theta) + \sigma_\Delta^2 \quad . \tag{21}$$

For the apparent phase term, $\psi_n(\phi, \Theta)$ given by Eq. (16), we will generally be interested in averages of the form $\overline{e^{j\alpha\psi_n}}$, rather than statistics of ψ_n itself. By Eq. (5) defining the characteristic function of a random variable, it is seen that

$$\overline{e^{j\alpha\psi_n(\phi, \Theta)}} = C_{\psi(\phi, \Theta)}(\alpha) \quad .$$

For $\psi_n(\phi, \Theta)$ as given by (16), if all the random variables are independent,

$$p(\psi_n) = p(\delta_n)\, p(x_n)\, p(y_n)\, p(z_n - nD) \quad ,$$

and

$$\overline{e^{j\alpha\psi_n(\phi, \Theta)}} = \int_{-\infty}^{\infty} p(\delta_n)\, e^{j\alpha\delta_n}\, d\delta_n \int_{-\infty}^{\infty} p(x_n) \exp[j\alpha k\, x_n \sin\Theta \cos\phi]\, dx_n$$

$$\times \int_{-\infty}^{\infty} p(y_n) \exp[j\alpha k\, y_n \sin\Theta \sin\phi]\, dy_n$$

$$\times \int_{-\infty}^{\infty} p(z_n - nD) \exp[j\alpha k(z_n - nD) \cos\Theta]\, dz_n \quad , \tag{22}$$

from which it follows that

$$C_{\psi(\phi, \Theta)}(\alpha) = C_\delta(\alpha)\, C_x(\alpha k \sin\Theta \cos\phi)\, C_y(\alpha k \sin\Theta \sin\phi)$$

$$\times C_{(z-nD)}(\alpha k \cos\Theta) \quad . \tag{23}$$

Thus, it is seen by (21) and (23) that the analysis of error effects can be carried out with complete generality in terms of an apparent amplitude b_n and an apparent element phase ψ_n, both of which involve errors which in general are functions of angle. The results of a statistical analysis based on b_n and ψ_n will then involve the statistical quantities P, σ_A^2 and $C_\psi(\alpha)$. The first, P, is the probable fraction of operating elements. The last two are related to statistics of the individual error sources by Eqs. (21) and (23), and are, in general, also angle dependent.

The remainder of the analysis will then be carried out in terms of the statistics of the amplitude and phase error without explicit reference to the individual components which make up these errors. Needless to say, however, the array designer should carefully bear in mind the many possible sources which can contribute to each error.

Before leaving this topic, one point should be emphasized. As mentioned above, if the elements are mounted above a ground plane, the factor z_n of Eq. (16) must relate to the position of the center of radiation of the element which is on the ground plane. Therefore, while displacement of the antennas parallel to the ground plane contributes phase error, errors in height of the element above a ground plane directly contribute only amplitude error to the quantity $f_n(\phi, \Theta)$ (although the accompanying variation in antenna impedance may cause further effects).

D. THE PROBABILITY DENSITY FUNCTION (pdf) OF THE FAR-FIELD

Summary

It is shown that a pdf for the far-field amplitude, $\rho(\nu) = |F(\nu)|$, can be closely approximated by the use of two distinct pdf's valid in different regions of the far-field, having different variances. The far-field pdf's are shown to be valid without restriction on the error pdf's, so long as the array is sufficiently large to justify the use of the Central Limit Theorem.

In the region near the peak of the main beam (and also any grating lobes), the field is approximately Gaussian:

$$p(\rho) \approx \frac{1}{\sigma_x \sqrt{2\pi}} \exp\left[-\frac{(\rho - \bar{x})^2}{2\sigma_x^2}\right] \quad , \quad \nu - \nu_o \approx 12\pi$$
$$\text{(principal lobe region)} \quad ,$$

where, ignoring the ϕ dependence of the element factor, which we can then write as $f(\nu)$,

$$\bar{x} = f(\nu)\, PC_{\psi(\nu)}(1) \sum_n a_{n}$$

$$= PC_{\psi(\nu)}(1)\, F_o(\nu_o) \quad .$$

$F_o(\nu)$ is the no-error far-field pattern, and

$$\sigma_x^2 \approx \frac{1}{2} f^2(\nu)\, P[A(\nu) + B(\nu)] \sum_n a_{n}^2 \quad .$$

$A(\nu)$ and $B(\nu)$ are related to the error statistics by

$$A(\nu) = 1 + \sigma_A^2(\nu) - P[C_{\psi(\nu)}(1)]^2 \quad ,$$

$$B(\nu) = [1 + \sigma_A^2(\nu)]\, C_{\psi(\nu)}(2) - P[C_{\psi(\nu)}(1)]^2 \quad .$$

In the sidelobe region, the amplitude is distributed in a modified Rayleigh distribution:

$$p(\rho) = \frac{\rho}{\sigma^2} I_o\left(\frac{\rho|\bar{F}|}{\sigma^2}\right) \exp\left[-\frac{(\rho^2 + |\bar{F}|^2)}{2\sigma^2}\right] \quad , \quad \nu - \nu_o \neq 12\pi$$
$$\text{(sidelobe region)} \quad ,$$

where

$$\bar{F} = f(\nu)\, PC_{\psi(\nu)}(1) \sum_n a_n e^{jn(\nu - \nu_o)}$$

$$= PC_{\psi(\nu)}(1) \overline{F_o(\nu)} \quad ,$$

$$\sigma^2 \approx \frac{1}{2} f^2(\nu)\, PA(\nu) \sum_n a_n^2 \quad .$$

These results are shown to be satisfactory approximations as long as

the error statistics and number of elements, N, satisfy

$$\frac{2P[C_{\psi(\nu)}(1)]^2}{1 + \sigma_A^2(\nu)} \, \eta N \gg 1 \quad ,$$

where η is the no-error taper efficiency of the array.

1. The Central Limit Theorem Approach

It would be an extremely difficult, if not impossible, task to directly derive the probability density function of $F(\phi, \Theta)$, given the density function of the various errors. Fortunately, as pointed out by Ruze,[*] the approximate form of the pdf can be inferred under conditions usually met in practice.

It was seen in the previous section that many sources can contribute to the total error in a particular element's contribution to the array far field. If one delves into detailed aspects of the causes of individual errors (e.g., the possible components contributing to an error in element drive amplitude), the sources of error become even more numerous. Thus, it is not unreasonable to assume that the errors in one element will be only loosely correlated with errors in other elements. If we go one step farther and assume the errors in any one element are independent of the errors in all other elements, we can make an appeal to the Central Limit Theorem[†] for the distribution of the far-field. This theorem states that under fairly general conditions, a real variable composed of the sum of N independent, real random variables such as

$$x = \sum_{n=0}^{N} x_n$$

tends to a Gaussian (normal) probability density function.

$$p(x) = \frac{1}{\sigma_x \sqrt{2\pi}} \, \exp\left[-\frac{(x - \bar{x})^2}{2\sigma_x^2}\right]$$

as N becomes large. The mean value of $\bar{x}$ will be given by the sum of the individual means:

$$\bar{x} = \sum_n \bar{x}_n \quad , \tag{24}$$

and the variance of x, σ_A^2, will be given by the sum of the variances of the individual components:

$$\sigma_x^2 = \sum_n \sigma_{x_n}^2 = \sum_n (\overline{x_n^2} - \bar{x}_n^2) \quad . \tag{25}$$

2. Statistics of the Far-Field

To apply the Central Limit Theorem to Eq. (14), note that $F(\phi, \Theta)$ can be considered to be the sum of N complex vectors or phasors, each of which is of the form[‡]

---

[*] J. Ruze, op.cit.

[†] H. Cramér, _Mathematical Methods of Statistics_ (Princeton University Press, 1946), Sec. 17.4.

[‡] We will henceforth suppress the ϕ dependence of the variables under the assumption that all measurements are made in the principal ϕ-plane of the element pattern, and express all Θ dependence in terms of $\nu = 2\pi D/\lambda \cos\Theta$.

$$F_n(\nu) = f(\nu)\, b_n(\nu)\, e^{j\psi_n(\nu)}\, e^{jn(\nu-\nu_o)} \qquad . \tag{26}$$

as illustrated in Fig. 3-62. The x and y components of this vector are then real random variables given by

$$x_n = \mathrm{Re}[F_n(\nu)] \qquad ,$$

$$y_n = \mathrm{Im}[F_n(\nu)] \qquad . \tag{27}$$
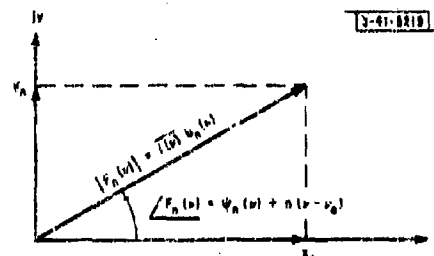
Fig. 3-62. Resolution of far-field into in-phase and quadrature components.

In order to compute the mean and variance of these quantities, it is useful to assume that the error in phase and error in amplitude are independent of each other. Where each element contains many possibilities for both phase and amplitude error, this assumption is probably not grossly inaccurate and will be made throughout the remainder of this report. Thus, the mean of x_n is by definition

$$\overline{x_n} = f(\nu)\, \overline{b_n(\nu)}\, \mathrm{Re}\!\left[e^{j\psi_n(\nu)}\, e^{jn(\nu-\nu_o)}\right] \qquad . \tag{28}$$

The result, from Eqs. (5) and (19), is

$$\overline{x_n} = PC_{\psi(\nu)}(1)\, f(\nu)\, a_n \cos n(\nu - \nu_o) \qquad . \tag{29}$$

In a similar manner, the average value of y_n is easily shown to be

$$\overline{y_n} = PC_{\psi(\nu)}(1)\, f(\nu)\, a_n \sin n(\nu - \nu_o) \qquad . \tag{30}$$

Thus, the means of x and y are, by Eq. (24),

$$\overline{x} = PC_{\psi(\nu)}(1)\, f(\nu) \sum a_n \cos n(\nu - \nu_o) \qquad , \tag{31}$$

$$\overline{y} = PC_{\psi(\nu)}(1)\, f(\nu) \sum a_n \sin n(\nu - \nu_o) \qquad . \tag{32}$$

or, in terms of the no-error far-field, $F(\nu)$,

$$\overline{F(\nu)} = PC_{\psi(\nu)}(1)\, F_o(\nu) \qquad . \tag{33}$$

To compute the variance of x_n and y_n, we note that

$$\overline{x_n^2} = f^2(\nu)\, \overline{b_n^2(\nu)}\, \overline{\cos^2\{\psi_n(\nu) + n(\nu - \nu_o)\}} \qquad .$$

Expanding the cosine term to

271

$$\overline{\cos^2[\psi_n(\nu) + n(\nu - \nu_0)]} = \frac{1}{2} + \frac{1}{2}\ \overline{\cos 2[\psi_n(\nu) + n(\nu - \nu_0)]} \quad ,$$

and noting that the average of the real part of a complex quantity is the real part of the average,

$$\overline{\cos 2[\psi_n(\nu) + n(\nu - \nu_0)]} = \text{Re}\ \overline{\exp\{j2[\psi_n(\nu) + n(\nu - \nu_0)]\}} = C_{\psi(\nu)}\ (2) \cos 2n(\nu - \nu_0) \quad ,$$

we have, by the above and Eq. (21),

$$\overline{x_n^2} = \frac{1}{2}\ P[1 + \sigma_A^2(\nu)]\ f^2(\nu)\ a_n^2[1 + C_{\psi(\nu)}\ (2)\cos 2n(\nu - \nu_0)] \quad .$$

Similarly, for y_n

$$\overline{y_n^2} = \frac{1}{2}\ P[1 + \sigma_A^2(\nu)]\ f^2(\nu)\ a_n^2[1 - C_{\psi(\nu)}\ (2)\cos 2n(\nu - \nu_0)] \quad .$$

Thus, since $\sigma_{x_n}^2 = \overline{x_n^2} - \overline{x}_n^2$,

$$\sigma_{x_n}^2 = \frac{1}{2}\ f^2(\nu)\ \{P[1 + \sigma_A^2(\nu)]\ a_n^2[1 + C_{\psi(\nu)}\ (2)\cos 2n(\nu - \nu_0)]$$

$$- P^2 C_{\psi(\nu)}\ (1)\ a_n^2[1 + \cos 2n(\nu - \nu_0)]\} \quad .$$

Rearranging gives

$$\sigma_{x_n}^2 = \frac{1}{2}\ f^2(\nu)\ a_n^2\ P\{[1 + \sigma_A^2(\nu) - P(C_{\psi(\nu)}\ (1))^2] + [(1 + \sigma_A^2(\nu))\ C_{\psi(\nu)}\ (2)$$

$$- P(C_{\psi(\nu)}\ (1))^2]\cos 2n(\nu - \nu_0)\} \quad . \tag{34}$$

For simplicity, (34) can be written

$$\sigma_{x_n}^2 = \frac{1}{2}\ f^2(\nu)\ P a_n^2\{A(\nu) + B(\nu)\cos 2n(\nu - \nu_0)\} \quad , \tag{35}$$

where

$$A(\nu) = 1 + \sigma_A^2(\nu) - P[C_{\psi(\nu)}\ (1)]^2 \tag{36}$$

$$B(\nu) = [1 + \sigma_A^2(\nu)]\ C_{\psi(\nu)}\ (2) - P[C_{\psi(\nu)}\ (1)]^2 \quad . \tag{37}$$

Using the same procedure, we can show that

$$\sigma_{y_n}^2 = \frac{1}{2}\ f^2(\nu)\ P a_n^2\{A(\nu) - B(\nu)\cos 2n(\nu - \nu_0)\} \quad .$$

Thus, the pattern variances are

$$\sigma_x^2 = \frac{1}{2}\ f^2(\nu)\ P\left[A(\nu)\ \sum a_n^2 + B(\nu)\ \sum a_n^2\cos 2n(\nu - \nu_0)\right] \tag{38}$$

$$\sigma_y^2 = \frac{1}{2}\ f^2(\nu)\ P\left[A(\nu)\ \sum a_n^2 - B(\nu)\ \sum a_n^2\cos 2n(\nu - \nu_0)\right] \quad . \tag{39}$$

The quantity of interest to the array designer is the amplitude of the far-field, which we will denote ρ, given by

$$\rho^2 = x^2 + y^2 \quad . \tag{40}$$

Since ρ is a function of both x and y, it will be necessary to formulate a "joint" distribution of the variables. It is therefore necessary to know the correlation of x and y, σ_{xy}. By definition,

$$\sigma_{xy} = \overline{(x - \bar{x})(y - \bar{y})} = \overline{xy} - \bar{x}\,\bar{y} \quad ,$$

$$\overline{xy} = \sum_{n}\sum_{m} \overline{x_n y_m} \quad . \tag{41}$$

For terms for which $m \neq n$, we can use the fact that x_n and y_m are the real and imaginary parts of independent vectors to arrive at

$$\overline{x_n y_m}\Big|_{n \neq m} = \overline{x_n}\,\overline{y_m} = P^2 [C_{\psi(\nu)}(1)]^2 \, f^2(\nu) \, a_n a_m \, \cos n(\nu - \nu_0) \sin m(\nu - \nu_0) \tag{42}$$

directly from (29) and (30). When $n = m$, from the definitions of x_n and y_n, and the identity $\sin\Theta\cos\Theta = \frac{1}{2}\sin 2\Theta$,

$$\overline{x_n y_n} = \frac{1}{2}\, f^2(\nu)\, \overline{b_n^2(\nu)}\, \overline{\sin 2[\psi_n(\nu) + n(\nu - \nu_0)]} \quad . \tag{43}$$

Since

$$\overline{\sin 2[\psi_n(\nu) + n(\nu - \nu_0)]} = \mathrm{Im}\left[\overline{e^{j2\psi_n(\nu)}}\, e^{j2n(\nu - \nu_0)}\right] = C_{\psi(\nu)}(2)\sin 2n(\nu - \nu_0) \quad ,$$

where Im denotes the imaginary part, we have, using Eq. (24),

$$\overline{x_n y_m} = \frac{1}{2}\, P[1 + \sigma_A^2(\nu)]\, C_{\psi(\nu)}(2)\, f^2(\nu)\, a_n^2 \sin 2n(\nu - \nu_0) \quad . \tag{44}$$

Thus, by the technique of Eq. (10), it follows that

$$\overline{xy} = f^2(\nu)\, P\left\{ P[C_{\psi(\nu)}(1)]^2 \sum_n a_n \cos n(\nu - \nu_0) \sum_m a_m \sin m(\nu - \nu_0) \right.$$

$$- P[C_{\psi(\nu)}(1)]^2 \sum_n a_n^2 \cos n(\nu - \nu_0)\sin n(\nu - \nu_0)$$

$$\left. + \frac{[1 + \sigma_A^2(\nu)]\, C_{\psi(\nu)}(2)}{2} \sum_n a_n^2 \sin 2n(\nu - \nu_0) \right\} \quad . \tag{45}$$

Changing the order of terms, using the double angle identity and Eqs. (31) and (32) for $\bar{x}$ and $\bar{y}$, we have

$$\sigma_{xy}^2 = \frac{1}{2}\, f^2(\nu)\, PB(\nu) \sum_n a_n^2 \sin 2n(\nu - \nu_0) \quad , \tag{46}$$

where B is defined in Eq. (37).

Thus, we have a complete set of statistics for the real and imaginary components of the far-field in Eqs. (31), (32), (38), (39) and (46). These statistics and the Central Limit Theorem allow the expression of the far-field of a large array in the form of a joint Gaussian distribution of x and y.

However, what is really desired is a distribution of ρ. Approximate distributions can be obtained fairly easily by examining the statistics more closely in various regions of the far-field.

3. The Far-Field pdf in the Region of the Principal Lobes

In the region near the peak of the main beam or the peak of any grating lobes of the no-error field, $\nu - \nu_0 \approx i2\pi$, where i is an integer. Thus, the arguments of the trigonometric terms of

the equations of the far-field statistics are approximately multiples of 2π. Thus, in these regions, we can write the approximate relations

$$\bar{x} \approx PC_{\psi(\nu)}(1)\ f(\nu)\ \sum_n a_n \quad , \tag{47a}$$

$$\bar{y} \approx 0 \quad , \tag{47b}$$

$$\sigma_x^2 \approx \frac{1}{2}\ f^2(\nu)\ P[A(\nu) + B(\nu)]\ \sum a_n^2 \quad , \tag{47c}$$

$$\sigma_y^2 \approx \frac{1}{2}\ f^2(\nu)\ P[A(\nu) - B(\nu)]\ \sum a_n^2 \quad , \tag{47d}$$

$$\sigma_{xy} \approx 0 \quad , \tag{47e}$$

when $\nu - \nu_0 = i2\pi$; $i = 0, \pm 1, \pm 2$, etc. (principal lobe regions).

It is observed that the correlation, σ_{xy}, is essentially zero in this region. Hence, we can write the approximate joint density function of x and y in the main-lobe or grating-lobe regions as

$$p(x,y) \approx p(x)\ p(y) = \frac{1}{2\pi\sigma_x\sigma_y}\ \exp\left\{-\left[\frac{(x-\bar{x})^2}{2\sigma_x^2} + \frac{y^2}{2\sigma_y^2}\right]\right\} \quad . \tag{48}$$

The argument of the exponential is seen to be of the form of an ellipse in the x, y-plane centered at $x = \bar{x}$, $y = 0$ having semi-major axes σ_x and σ_y as shown in Fig. 3-63. It is apparent from the figure that the amplitude of the far-field, ρ, will be affected very little by the error in the y-component, so long as both σ_x and σ_y are quite small compared to $\bar{x}$. From (47a), (47c) and (47d), it is seen that

$$\frac{\bar{x}^2}{\sigma_x^2} = \frac{2P[C_{\psi(\nu)}(1)]^2}{A(\nu) + B(\nu)}\ \eta N \quad , \tag{49a}$$

$$\frac{\bar{x}^2}{\sigma_y^2} = \frac{2P[C_{\psi(\nu)}(1)]^2}{A(\nu) - B(\nu)}\ \eta N \quad , \tag{49b}$$

where N is the total number of elements in the array, and η is the no-error efficiency of the array amplitude taper defined by:
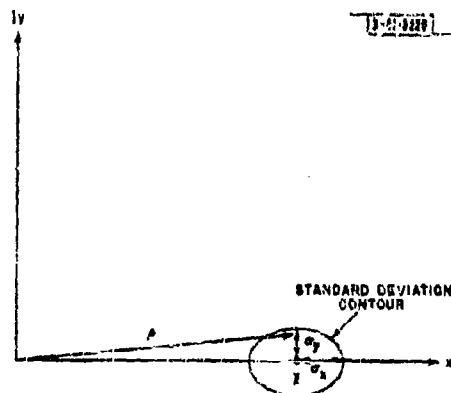
Fig. 3-63. Contour of probability density function of far-field for main-lobe and grating-lobe locations.

$$\eta N = \frac{(\Sigma a_n)^2}{\Sigma a_n^2} \quad . \tag{50}$$

From Eqs. (36) and (37), it is seen that the above relationships are equivalent to

$$\frac{\bar{x}^2}{\sigma_x^2} = \frac{2P[C_{\psi(\nu)}(1)]^2}{[1 + \sigma_A^2(\nu)][1 + C_{\psi(\nu)}(2)] - 2P[C_{\psi(\nu)}(1)]^2} \; \eta N \quad , \tag{51}$$

$$\frac{\bar{x}^2}{\sigma_y^2} = \frac{2P[C_{\psi(\nu)}(1)]^2}{[1 + \sigma_A^2(\nu)][1 - C_{\psi(\nu)}(2)]} \; \eta N \quad . \tag{52}$$

As the errors approach zero variance, $C_{\psi(\nu)}(\alpha) \to 1$, and, as would be expected on physical grounds,

$$\frac{\bar{x}^2}{\sigma_x^2} \to \infty \quad , \quad \frac{\bar{x}^2}{\sigma_y^2} \to \infty \quad .$$

As the errors become large, $C_{\psi(\nu)}(\alpha) \to 0$, and we can write the requirement that if

$$\frac{\bar{x}^2}{\sigma_x^2} \approx \frac{\bar{x}^2}{\sigma_y^2} \approx \frac{2P[C_{\psi(\nu)}(1)]^2}{1 + \sigma_A^2(\nu)} \; \eta N \gg 1 \quad , \tag{53}$$

the effect of y on ρ will be negligible, and the far-field distribution in the main-lobe and grating-lobe regions can be well approximated by

$$p(\rho) \approx \frac{1}{\sigma_x \sqrt{2\pi}} \exp\left[-\frac{(\rho - \bar{x})^2}{2\sigma_x^2}\right] \quad , \quad \nu - \nu_0 \approx 12\pi \quad , \tag{54}$$

where $\bar{x}$ and σ_x are as given in (47) for the appropriate angles. If (53) is not satisfied, it is obvious that x is not normally distributed; and we have, in fact, an array which is too small in terms of the errors for the Central Limit Theorem to be a good approximation.

4. Far-Field pdf in the Sidelobe Region

In the sidelobe regions of the pattern, the terms of Eqs. (38) and (39) involving the cosine factor will be small everywhere[*] compared to the first terms of each equation, except for a region of approximately one beamwidth halfway between principal lobes (since the argument of the trigonometric term is the second harmonic of the original pattern). Ignoring this latter region temporarily, it is seen that in the sidelobe region the variances in x and y will be approximately given by

$$\sigma^2 \approx \frac{1}{2} f^2(\nu) \, PA(\nu) \sum a_n^2 \quad , \tag{55}$$

and the cross-correlation is small by comparison to the variances. Thus, the joint probability density function of x and y in this region can be written as

---

[*]By the sidelobe ratio at the appropriate double angle of an antenna with amplitude taper a_n^2.

$$p(x, y) = \frac{1}{2\pi\sigma^2} \exp\left[-\frac{(x - \bar{x})^2 + (y - \bar{y})^2}{2\sigma^2}\right] \quad .$$ (56)

By the trigonometric substitutions,

$$x = \rho \cos \theta$$

$$y = \rho \sin \theta$$

$$\rho^2 = x^2 + y^2$$

one can derive by well-known means[*] the pdf for ρ in the form

$$p(\rho) = \frac{\rho}{\sigma^2} I_0 \left(\frac{\rho |\bar{F}|}{\sigma^2}\right) \exp\left[-\frac{(\rho^2 + |\bar{F}|^2)}{2\sigma^2}\right] \quad , \quad \nu - \nu_0 \neq 12\pi \quad ,$$ (57)

where $|\bar{F}|$ is the average magnitude of the far-field related to the "no-error" field magnitude, $|F_0|$, by

$$|\overline{F(\nu)}| = PC_{\psi(\nu)} (1) |F_0(\nu)| \quad ,$$ (58)

and $I_0(x)$ is the Bessel Function of the first kind of order zero, of imaginary argument. The form of this distribution is indicated in Fig. 3-64. The distribution is commonly referred to as "modified Rayleigh."
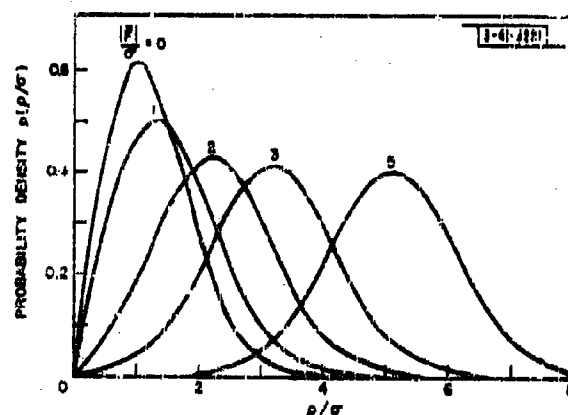
Fig. 3-64. Probability density function of ρ. (From S. O. Rice, "Mathematical Analysis of Random Noise," Noise and Stochastic Processes, N. Wax, Ed. (Dover, New York, 1954).]

For angles corresponding to nulls of the no-error pattern, $|\bar{F}| = 0$, the distribution is the familiar Rayleigh distribution

$$p(\rho) = \frac{\rho}{\sigma^2} e^{-\rho^2/2\sigma^2} \quad , \quad |\bar{F}| = 0 \quad ,$$ (59)

having statistics

$$\left. \begin{array}{l} \bar{\rho} = \sqrt{\frac{\pi}{2}} \, \sigma \\[2mm] \overline{\rho^2} = 2\sigma^2 \end{array} \right\} \quad , \quad \text{when } |\bar{F}| = 0 \quad .$$

---

[*] W. R. Bennett, "Methods of Solving Noise Problems," Proc. IRE **44**, 609 (1956).

In regions where $|\overline{F}|/\sigma$ is large, the asymptotic expansion of $I_0(x)$ can be used to show that the distribution approaches Gaussian (as is apparent from Fig. 3-64)

$$p(\rho) \sim \frac{1}{\sigma\sqrt{2\pi}} \exp\left[-\frac{(\rho-|\overline{F}|)^2}{2\sigma^2}\right] \quad , \quad \frac{|\overline{F}|}{\sigma} \gg 1 \quad . \tag{60}$$

having mean

$$\bar{\rho} = |\overline{F}|$$

and variance σ^2. In the transition region, the statistics are difficult to come by directly, but can be obtained from tabulations (see Sec. E).

For the special region halfway between grating lobes, it is noted that the variances in x and y take on the form appropriate for the principal maximum locations given by (47), while both $\bar{y}$ and σ_{xy} are essentially zero. Thus, in this region, the pdf is the same as that of Eq. (48). However, in this region, $\bar{x}$ will be small (of the order of $1/N$ compared to its value at $\nu = \nu_0$) and negligible compared to σ_x in cases of interest. If $\bar{x}$ is taken as essentially zero, then $\bar{x} = \bar{y} = \sigma_{xy}^2 = 0$, one could make the substitutions made in (57) and arrive at a pdf for ρ for this region. However, since this region is so narrowly confined, special attention will not be further devoted to it, and we will generally proceed with the assumption that the distribution of Eq. (57) is satisfactory throughout the sidelobe region.
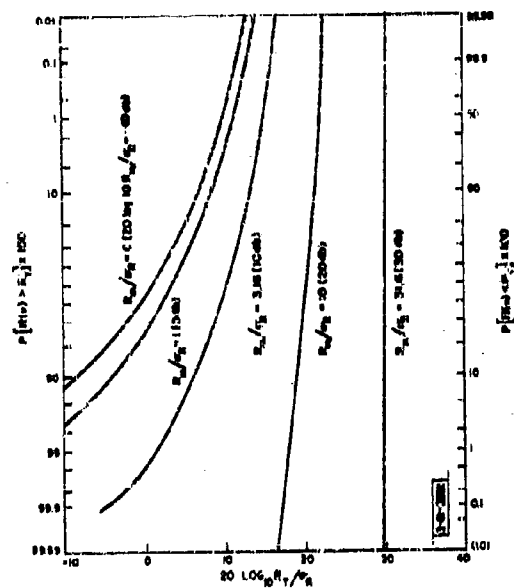
Fig. 3-65. Sidelobe ratio cumulative probabilities.
$R_m(\nu)$ is defined by Eq. (67a) and is ap-
proximately the "no-error" sidelobe ratio.
$\sigma_R(\nu)$ is the rms sidelobe ratio error.

$$\sigma_R^2(\nu) \approx 1/2 \left[\frac{f(\nu)}{f(\nu_o)}\right]^2 \frac{\sigma^2(\nu)}{\eta PN}$$

E. THE EFFECTS OF RANDOM ERRORS ON THE SIDELOBE RATIO OF LARGE ARRAYS

Summary

It is shown that[*] the pdf of the sidelobe ratio of a large array at a specific angle, ν, is of the form of a modified Rayleigh distribution:

$$p[R(\nu)] = \frac{R}{\sigma_R^2} \, I_0 \left(\frac{RR_m}{\sigma_R^2} \right) \exp\left[-\frac{R^2 + R_m^2}{2\sigma_R^2} \right] \quad .$$

where $R_m(\nu)$ is related to the no-error sidelobe level at the angle ν through the characteristic function of the phase errors

$$R_m(\nu) = \frac{C_{\psi(\nu)}(1)}{C_{\psi(\nu_0)}(1)} \frac{F_0(\nu)}{F_0(\nu_0)}$$

(and consequently, is approximately the no-error sidelobe ratio, $F_0(\nu)/F_0(\nu_0)$, if the characteristic functions are only weakly angle dependent). The parameter σ_R^2 is given by

$$\sigma_R^2(\nu) = \frac{1}{2} \left[\frac{f(\nu)}{f(\nu_0)} \right]^2 \frac{A(\nu)}{[C_{\psi(\nu_0)}(1)]^2} \frac{1}{\eta PN} \quad .$$

For the case of small errors in phase, it is shown that σ_R^2 can be written approximately as

$$\sigma_R^2 \approx \frac{1}{2} \left[\frac{f(\nu)}{f(\nu_0)} \right]^2 \frac{\epsilon^2(\nu)}{\eta PN} \quad , \qquad \epsilon^2(\nu) \approx (1-P) + \sigma_A^2(\nu) + P\sigma_\psi^2(\nu) \quad .$$

The probability of the sidelobe ratio at any given angle exceeding or not exceeding some arbitrary threshold value, R_T, is given by the curves of Fig. 3-65. It is shown that for large arrays, in order to maintain the sidelobe level at a particular angle in the regions of the pattern far from the main beam (where errors tend to predominate), the numerical value of $20 \log_{10} \sigma_R$ must be held about 10 db below the desired threshold level. Numerical examples are given of the implication of the curves of Fig. 3-65 on allowable tolerances for 100-element arrays and 10,000-element arrays.

The question of the allowable errors in terms of holding essentially all far-out sidelobes below some threshold value is discussed, and it is shown that a somewhat conservative error requirement can be justified. For an N-element array, one should choose the probability of any single sidelobe in the region exceeding R_T to be $1/N$ of the desired probability that no sidelobes exceed R_T, and determine the allowable errors accordingly. The previous numerical examples of allowable error are reworked to conform to this specification.

---

[*] The results in this section are essentially the same as those obtained by previous authors, except for the result for the directivity degradation.

Finally, the effect of random errors on array directivity is considered, and it is shown that if the parameter $\epsilon(\nu)$ is not strongly angle dependent, the degradation in directivity is given simply by

$$\frac{U(\nu_o)}{U_o(\nu_o)} \approx \frac{1}{1 + \epsilon^2/P}$$

The implication of this result on the loss or deletion of a large fraction of the elements in a random manner is given.

1. Some Remarks on the Extension of the Results of this Section to Planar Arrays

In this section, we will examine the effects of the random errors discussed on the sidelobe level of large arrays.

Although the work will be formulated in linear array notation, the results are directly applicable to planar arrays if the assumptions regarding element-to-element error independence are met. In many planar arrays, however, the physical structure of the array is such that the elements are first combined into subarrays and then the output of the subarrays combined; e.g., combining first by rows and then by columns. In this case, there may be errors in the column combining networks which affect an entire row of the planar array. This situation can be handled as necessary by considering the second combining network to be a linear array, each element of the column linear array being in itself a linear array which has been analyzed by the previous method. Intuitively, it is apparent that the effect of errors in the second level combining equipment would be to raise the sidelobe level primarily in the column principal plane, with little effect in the sidelobes of the row principal planes.

2. The pdf of the Sidelobe Ratio

In this section, we will investigate the effects of errors on the ratio of the power at a particular angle on the sidelobe region to the power density at the peak of the main beam. This ratio, which we will denote R, is given by

$$R(\nu) = \frac{|F(\nu)|}{|F(\nu_o)|} \tag{63}$$

Since the pdf's of quotients are difficult to work with, we first note from Eq. (53) that the ratio of the expected value of the pattern at the peak of the main beam to the variances in x and y is likely to be quite large for reasonable values of error. Thus, the percentage error in the denominator of Eq. (63) will be very small if we replace $|F(\nu_o)|$ by its average value, $\overline{X}$, as given by Eq. (47a). Under this assumption, (63) can be written as

$$R(\nu) = \frac{|F(\nu)|}{C_{\psi(\nu_o)}(1)\,|F(\nu_o)|\,\Sigma\,a_n} \tag{64}$$

where we assume $C_{\psi(\nu_o)}(1) \neq 0$. But $|F(\nu)| = \rho(\nu)$ of the previous section, and thus, of course, R is merely a scale factor of ρ; hence, the same pdf's apply. Therefore,

$$\rho(R) = \frac{R}{\sigma_R^2}\,I_o\left(\frac{RR_m}{\sigma_R^2}\right)\exp\left[-\frac{R^2 + R_m^2}{2\sigma_R^2}\right] \tag{65}$$

280

where, by (64) and analogy to Eq. (57),

$$R_m = \frac{|\overline{F(\nu)}|}{|F(\nu_o)|} \tag{66}$$

$$\sigma_R^2 = \frac{1}{2}\left[\frac{f(\nu)}{f(\nu_o)}\right]^2 \frac{A(\nu)}{C_{\psi(\nu_o)}^2(1)} \frac{1}{\eta PN} \tag{67}$$

from which it is seen that $R_m(\nu)$ is the sidelobe ratio of the no-error pattern if $C_{\psi(\nu_o)}(1)$ is approximately independent of angle, and $f(\nu)$ is flat over the region of interest. More generally,

$$R_m(\nu) = \frac{C_{\psi(\nu)}(1)}{C_{\psi(\nu_o)}(1)} \frac{F_o(\nu)}{F_o(\nu_o)} \tag{67a}$$

Since the antenna engineer is normally interested in obtaining low sidelobes, the variance in R must be kept within small bounds, implying that the error variances must also be small. Under this assumption, the factor involving the errors can be somewhat simplified. By use of Eq. (9) in Sec. B-2, and Eq. (36), we have that for small errors ($\sigma_\psi^2 \ll 1$),

$$\frac{A(\nu)}{C_{\psi(\nu_o)}^2(1)} \approx \frac{[1 + \sigma_A^2(\nu)] - P[1 - \sigma_\psi^2(\nu)]}{1 - \sigma_\psi^2(\nu_o)}$$

where we approximate $[1 - (\sigma_\psi^2/2)]^2 \approx 1 - \sigma_\psi^2$. This result can be further simplified by neglecting $\sigma_\psi^2(\nu_o)$ in the denominator, and rewritten as

$$\frac{A(\nu)}{C_{\psi(\nu_o)}^2(1)} \approx (1 - P) + \sigma_A^2(\nu) + P\sigma_\psi^2(\nu) \tag{68}$$

Thus, we can write σ_R^2 for small phase errors as

$$\sigma_R^2 \approx \frac{1}{2}\left[\frac{f(\nu)}{f(\nu_o)}\right]^2 \frac{\epsilon^2(\nu)}{\eta PN} \tag{69}$$

where, for brevity, we let

$$\epsilon^2(\nu) \approx (1 - P) + \sigma_A^2(\nu) + P\sigma_\psi^2(\nu) \tag{70}$$

Note that if no elements are missing, the relationship for ϵ^2 is that previously given by Ruze.[*]

It is seen that for small phase errors the variance in the sidelobe ratio is directly proportional to the fraction of failed elements, $1 - P$, and the sum of the total amplitude and phase variance for small phase errors. On the other hand, the variance is inversely proportional to the number of operating elements, PN. It is also weighted by the ratio of the element factor at the angle in question to the element factor at the center of the main beam.

---

[*] J. Ruze, op. cit.

3. The Probability of the Sidelobe Ratio Not Exceeding a Value R_T at a Specified Angle

In this section, we will discuss the magnitude of errors allowable in terms of holding the sidelobe ratio below some arbitrary value, R_T, at one particular angle. Specifically, we desire a statement about the outcome of an experiment in which we:

(a) Construct a very large number of arrays, identical in their no-error characteristics, including their no-error pattern, $F_0(\nu)$;

(b) Insert errors in each array, all errors being chosen from the same error distribution, which is characterized by a specific value of ϵ;

(c) Pick a particular angle, ν, and measure the sidelobe ratio of each array at that angle;

(d) Compute the fraction of arrays yielding a sidelobe ratio at this angle less than some desired R_T.

As the number of arrays tested approaches infinity, we designate the fraction having $R(\nu_1) < R_T$ by the cumulative probability $P[R(\nu_1) < R_T]$.

Note that the result of this experiment yields information only about the sidelobe ratio at a single angle, $R(\nu)$. The extension of this experiment to a range of angles will be taken up later.

The above experiment is mathematically performed simply by integrating Eq. (65):

$$P[R(\nu) < R_T] = \int_0^{R_T} \frac{R}{\sigma_R^2} I_0\left(\frac{R R_m}{\sigma_R^2}\right) \exp\left[-\frac{R^2 + R_m^2}{2\sigma^2}\right] dR \quad . \tag{71}$$

The performance of the experiment on paper is not quite so easy as it may appear, since the integration cannot be performed in closed form. However, since the function in question also has been extensively studied in detection theory, it is tabulated.[*]

The result has also been plotted many times by many writers. This writer's contribution appears in Fig. 3.-65 in a form that has been found useful. The probability of $R(\nu)$ exceeding (or not exceeding) R_T is plotted against the ratio of R_T to σ_R in db. The ratio of the no-error sidelobe level, R_m, to σ_R is used as a parameter.

Among other features, this plot makes evident previous statements about small percentage error in pattern regions where $R_m/\sigma_R \gg 1$. It is seen, for example, that in a region where R_m/σ_R is of the order of 30 db, the obtained value of R will almost certainly be within $\pm\frac{1}{2}$ db of R_0. On the other hand, it is apparent that in regions where R_0 is essentially zero, the pattern may actually obtain values of 10 db or more above σ_R.

Thus, the places one would expect to find the most noticeable effects of small errors are in the far-out sidelobe regions of array patterns and in the no-error pattern nulls. In particular, if one considers the no-error far-field of the uniformly illuminated array, the lowest sidelobe ratio will be on the order of $1/N^2$ power, and lower still for low sidelobe amplitude tapers. Thus, it can be seen from Eq. (69) that unless ϵ^2 is of the order of $1/N$ or smaller, the effects of errors will predominate the far-out sidelobe level and, over a large region of the pattern, the average value of the far-field will often be negligible compared to the variance in the sidelobe level.

---

[*] J. I. Marcum, "A Statistical Theory of Target Detection by Pulsed Radar: Mathematical Appendix," Report R-113 [U], RAND Corporation, Santa Monica, California (July 1948).

To be more exact, and to further illustrate the use of Fig. 3-65, if it is desired to hold a 40-db far-out sidelobe power level ($R_m \approx 0$) at a point with a probability of 0.99 and it is assumed that the ratio of element factors is approximately unity at the value of ν of interest, then the figure indicates that

$$20 \log_{10} \frac{R_T}{\sigma_R} \gtrsim 10 \, db \quad ,$$

indicating that

$$20 \log_{10} \sigma_R \leqslant -50 \, db \quad ; \quad \sigma_R \leqslant 3.17 \times 10^{-3} \quad .$$

If we assume a 100-element array with a uniform taper, we have

$$\epsilon \approx 4.5 \times 10^{-2} \quad .$$

To get a feeling for this number, it implies that in the absence of any other errors, we can tolerate from Eq. (70):

    (a)   Essentially no failed elements, or

    (b)   Approximately 0.35-db rms amplitude error, or

    (c)   0.045 radian (2.56°) rms phase error.

Thus is seen the difficulty in maintaining a very low far-out sidelobe level with a small number of elements.

On the other hand, Fig. 3-65 suggests that if we use a large number of elements, the requirement on ϵ can be relaxed. For example, with a 10,000-element array, we could tolerate:

    (a) $P \approx 0.8$, or about 2000 failed elements,

    (b)   2.67-db rms amplitude error, or

    (c)   25.6° rms phase error.

The effect of this error on portions of the pattern where the no-error sidelobe level is large, compared to the standard deviation, is small. On the -13 db first sidelobe of our uniformly illuminated array, the error would be expected to be less than a fraction of a db. However, in regions where $R_0 \approx -30 \, db$, Fig. 3-65 indicates ($R_0/\sigma_R \approx 20$ db) that the 30-db sidelobe will on the average ($P \approx 50$ per cent) be no greater than 30 db, but on about one out of 100 such arrays, it may be only -28 db.

Figure 3-66 compares the predictions of Fig. 3-65 with the actual effects of some phase errors on a 16-element linear array.[*] Indicated on each pattern is $\sigma_R(\nu)$ in db as determined by the inserted phase errors and the average element factor.

4. Allowable Errors for Maintaining the Sidelobe Ratio Over a Range of Angle

Up to this point, we have been concerned only with the probability of the sidelobes exceeding a certain threshold level at one specific point. The question of most direct interest, however, is usually that of the error tolerance required to hold the sidelobes below a certain threshold level over a region which may include all visible space of the antenna. An exact solution to this problem

[*] W. P. Delaney in J. L. Allen, et al., "Phased Array Radar Studies, 1 July 1959 to 1 July 1960," Technical Report No. 228 [U], Lincoln Laboratory, M.I.T. (12 August 1960), ASTIA 249470, H-335.
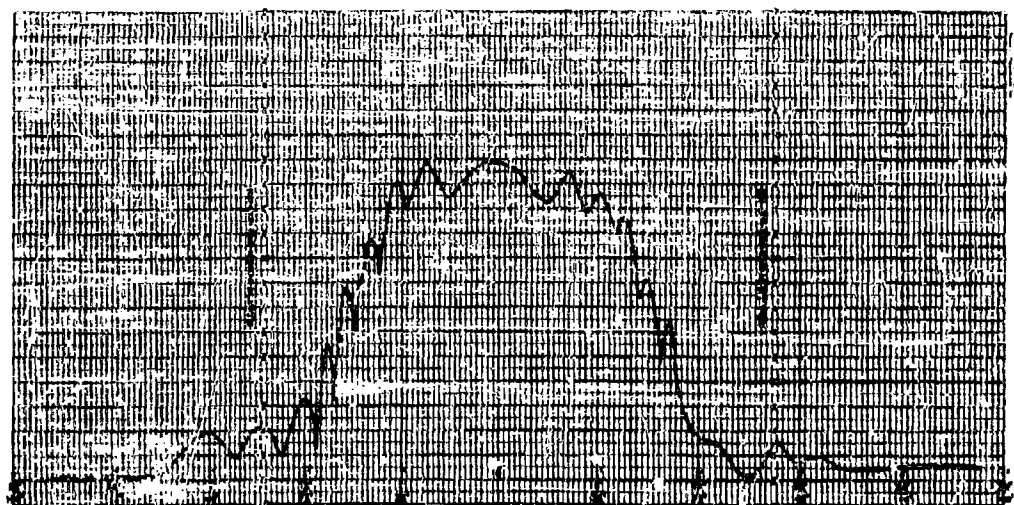
(a) Average element factor.
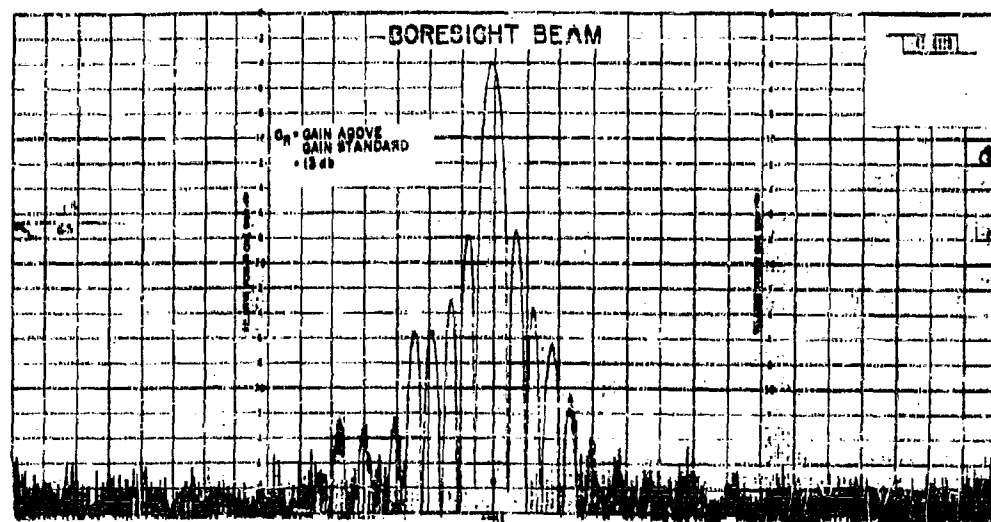
(b) No error.

Fig. 3-66. Phase error patterns.
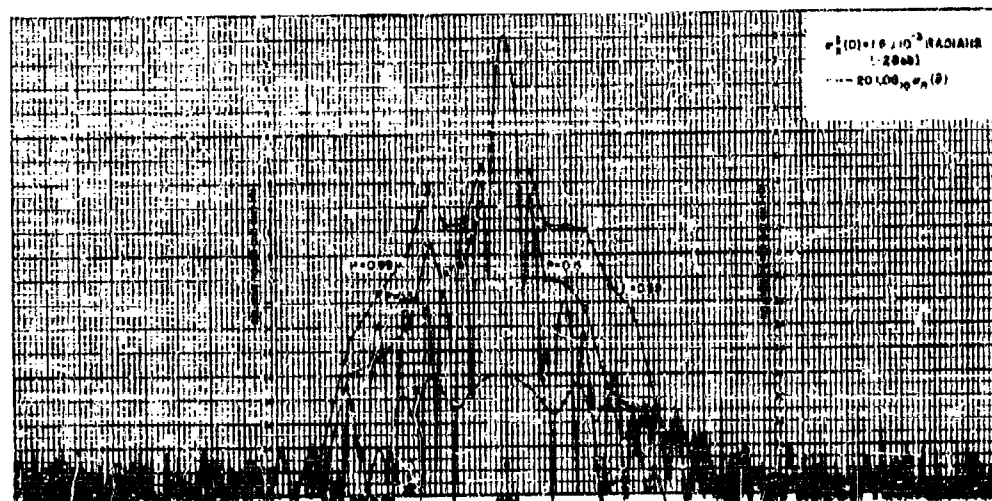
(c) $\sigma_R = 13°$.
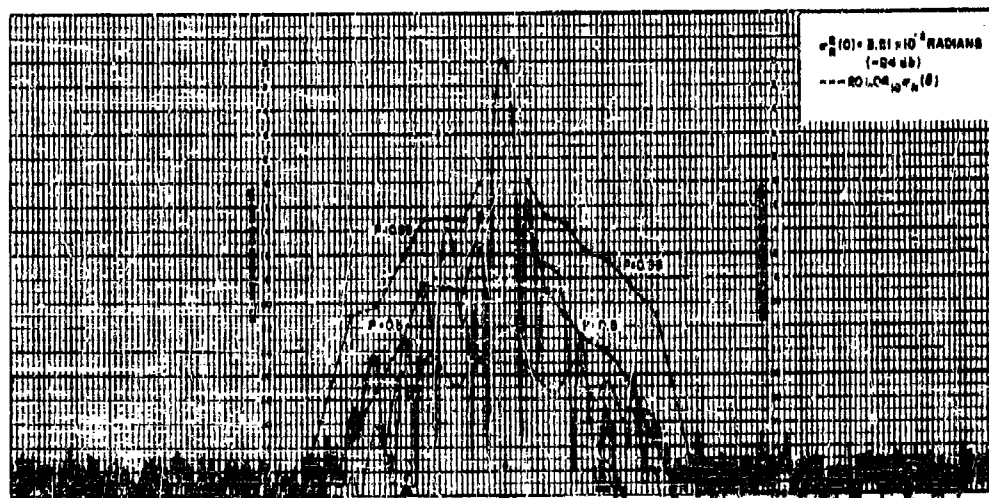
(d) $\sigma_R = 20°$.

has never been obtained, to the best of the writer's knowledge, and it is probably not amenable to exact solution. A simple approximate solution can be obtained rather easily, however, since we have established the probabilities for individual points of the pattern. Let us inquire into the correlation from point to point through the autocorrelation function of the errors of the far-field.

By definition, the autocorrelation function of the far-field error is

$$A.F.(\nu) = \frac{1}{2\pi} \int_{-\pi}^{\pi} [F(\nu_1) - F_o(\nu_1)] [F(\nu + \nu_1) - F_o(\nu + \nu_1)]^* \, d\nu_1 \quad , \tag{72}$$

where the integral is taken over one period of the array factor. Substituting the far-field expression of Eq. (14), neglecting the element factor and possible angular variation of the errors in the interest of getting a usable approximate answer:

$$A.F.(\nu) = \frac{1}{2\pi} \int_{-\pi}^{\pi} \sum_n \sum_m \left(b_n e^{j\psi_n} - a_n\right) e^{jn(\nu_1)} \left(b_m e^{-j\psi_m} - a_m\right) e^{-jm(\nu+\nu_1)} \, d\nu_1 \quad , \tag{73}$$

$$A.F.(\nu) = \sum_n \sum_m \left(b_n e^{j\psi_n} - a_n\right) \left(b_m e^{-j\psi_m} - a_m\right) \exp\left\{-jm\nu \left[\frac{1}{2\pi} \int_{-\pi}^{\pi} e^{j(n-m)\nu_1} \, d\nu_1\right]\right\} \quad . \tag{74}$$

The integral in brackets is seen to be a delta function; thus, one can write that the autocorrelation function of ν is given by

$$A.F.(\nu) = \sum_m |i_m(e) - i_m(o)|^2 e^{-jm\nu} \quad , \tag{75}$$

where $i_m(e)$ is the drive to the mth element in the presence of errors, and $i_m(o)$ is the no-error drive. The quantity $|i_m(e) - i_m(o)|^2$ is certainly positive. Thus $A(\nu)$ is of the form of an average pattern from an array having an amplitude taper $a'_m = |i_m(e) - i_m(o)|^2$, "phased" to point the beam at broadside.

Since the "amplitude taper" of this "beam" is quite rough, the width of the main lobe of the autocorrelation function is likely to be several beamwidths of the "no-error" array pattern. Thus, the correlation between adjacent sidelobes may be appreciable.

The probability of holding the sidelobes over a region all below some threshold level thus lies somewhere between the probability of holding all sidelobes below this level (under the assumption of complete decorrelation) and the probability of holding any one point below this level (which would prevail for the whole region if the correlation were unity throughout). The previous result on the autocorrelation function would tend to indicate that the true probability lies somewhere in between.

If we tentatively proceed under the approximation that the errors are completely decorrelated from sidelobe to sidelobe, we could state that the probability of holding n sidelobes, the ith located at ν_i, below some threshold level, R_T, which we will denote $P[nR_i < R_T]$, is

$$P[nR_i < R_T] = \prod_i P[R(\nu_i) < R_T] \quad . \tag{78}$$

For a large array, most of the sidelobes will lie in the far-out region previously discussed. If almost all these sidelobes lie in the region where errors predominate, we can approximate that the probability of holding the entire far-out region below R_T is given by

$$P\{NR_i < R_T\} \approx \{1 - P(R_f > R_\eta)\}^{N}$$ (79)

where R_f designates the sidelobe ratio at some "typical" point in the far-out region. If a large number of sidelobes are involved, this approximation should be fairly reasonable if the statistics of R assumed represent an average value over the region of interest (these statistics will vary with angle due to the element factor, if for no other reason). Thus, by the following manipulation, assuming that the probability of any individual sidelobe exceeding R_T is very small, we can arrive at the result

$$P\{NR_i < R_T\} \approx 1 - NP\{R_f > R_T\} \quad . $$ (80)

Thus, for example, if it is desired to hold essentially the entire far-out region of a 100-element array below R_T with a probability of 0.99, one must choose the error bounds such that the probability of any individual sidelobe in the hash region being below R_T is 0.9999. With this modification, Fig. 3-65 is applicable to the approximate calculation of the errors allowable for good sidelobe control over all visible space.

Taking the previous example in which a 0.99 probability of one sidelobe being below 40 db was desired and changing the requirement to one of holding all sidelobes below that level with the same probability, it is seen from Fig. 3-65 that we must now hold σ_R to a value about 3 db below that allowable to hold one point below R_T for a 100-element array. The allowable errors in the absence of all others are then:

For the 100-element array,

    (a) No elements missing,

    (b) 0.23-db rms amplitude error,

    (c) 1.95° rms phase error.

For 10,000 elements, calculations indicate about a 4.4-db decrease in σ_R, and approximate allowable errors:

For the 10,000-element array,

    (a) 500 elements missing,

    (b) 1.8-db rms amplitude error,

    (c) 13.1° rms phase error.

Again recalling the previous result about error correlation, these values are probably pessimistic, the truly allowable error lying between these values and those previously given for the single sidelobe case.

5. Effect of Random Errors on Array Directivity

In order to compute the effect of random errors on the directivity of the array, it is useful to formulate the average power pattern of the array normalized to a no-error peak value of unity. By definition, this average power pattern is given by

$$\overline{P(\nu)} = \overline{[F(\nu)\, F^*(\nu)]} = \overline{|F(\nu)|^2} \quad . $$ (84)

Inserting the value of the far-field in terms of the illumination as given by Eq. (14), and performing the indicated averaging, gives the result

$$\overline{|F(\nu)|^2} = P^2 C_{\psi(\nu)}^2 (1) f^2(\nu) \left| \sum_n a_n e^{jn(\nu-\nu_0)} \right|^2 + PA(\nu) 1^2(\nu) \sum_n a_n^2 \quad , \qquad (82)$$

where $A(\nu)$ is given by Eq. (36).

The factor in bars is the no-error power pattern, $|F_0(\nu)|^2$, while the second term is directional only by virtue of the element factor and any angular variation of $A(\nu)$.

Since, for directivity calculation, the absolute value of $|F(\nu)|^2$ is immaterial, let us divide (82) by $P^2 C_{\psi(\nu)}^2 (1)$ and use the form

$$\overline{|F(\nu)|^2} = |F_0(\nu)|^2 + f^2(\nu) \frac{A(\nu)}{PC_{\psi(\nu)}^2 (1)} \sum_n a_n^2 \quad . \qquad (83)$$

For small errors, we have from (68) that

$$\frac{A(\nu)}{C_{\psi(\nu)}^2 (1)} \approx (1 - P) + \sigma_A^2(\nu) + P\sigma_\psi^2(\nu)$$

$$= \epsilon^2(\nu) \quad .$$

Further, by Eq. (50),

$$\sum_n a_n^2 = \frac{|\Sigma a_n|^2}{\eta N} = \frac{|F_0(\nu_0)|^2}{f^2(\nu_0) \eta N} \quad ,$$

so that

$$|F_0(\nu_0)|^2 = |f(\nu_0)|^2 | \sum a_n|^2 \quad .$$

Therefore, we can write (83) as

$$\overline{|F(\nu)|^2} = |F(\nu)|^2 + |F_0(\nu_0)|^2 \left[\frac{f^2(\nu)}{f^2(\nu_0)} \frac{\epsilon^2(\nu)}{\eta NP} \right] \quad . \qquad (84)$$

We have previously seen that the percentage pattern error near the beam maximum is trivial (or else the Central Limit Theorem is not applicable). Further, if the array is large and the correlation interval of the far-field is small, we would expect that the total radiated power would vary only minutely from the average for nearly all such arrays with the random error. Thus, one would expect that a directivity value derived using (84) as the actual power density distribution over all space would be a satisfactory approximation. The main beam directivity is given by

$$U(\nu_0) = \frac{4\pi |F(\nu_0)|^2}{\int\limits_{\substack{all \\ space}} |F(\nu)|^2 \, d\Omega} \quad , \qquad d\Omega = \sin\theta \, d\theta \, d\phi \quad . \qquad (85)$$

Inserting (84), and neglecting the second term of (84) in the numerator, we have

$$U(\nu_0) = \frac{4\pi |F_0(\nu_0)|^2}{\int |F_0(\nu)|^2 \, d\Omega + \frac{|F_0(\nu)|^2}{\eta NP} \int \epsilon^2(\nu) \frac{f^2(\nu)}{f^2(\nu_0)} \, d\Omega} \quad . \qquad (86)$$

Denoting the no-error directivity by $U_0(\nu_0)$, we can divide numerator and denominator of (86) by $4\pi|F_0(\nu_0)|^2$ and write

$$U(\nu_0) = \cfrac{1}{U_0^{-1}(\nu_0) + \cfrac{1}{4\pi\,\eta\,NP}\int \epsilon^2(\nu)\,\cfrac{f^2(\nu)}{f^2(\nu_0)}\,d\Omega} \qquad (87)$$

Let us examine the angle dependence of $\epsilon^2(\nu)$. Recall that σ_A^2 contains two factors [Eq. (21)]:

$$\sigma_A^2(\nu) = \sigma_\mu^2(\nu) + \sigma_\Delta^2 \quad .$$

The factor σ_Δ^2 is invariant with angle. The factor $\sigma_\mu^2(\nu)$, relating to the element factor variance about its average value at ν, may vary with angle and may well become larger as $f(\nu)$ becomes small (the sidelobe region of the element factor) as seen in Fig. 3-61. For small phase errors, by (23) and the small error representation of the characteristic function, (9), we have, to a first order,

$$\sigma_\phi^2(\phi, \Theta) = \sigma_\delta^2 + k^2[\sigma_x^2 \sin^2\Theta \cos^2\phi + \sigma_y^2 \sin^2\Theta \sin^2\phi + \sigma_{(z\text{-nD})}^2 \cos^2\Theta] \quad ,$$

where σ_x^2, σ_y^2 and $\sigma_{(z\text{-nD})}^2$ are the variances in element radiation center location. If all these variances are roughly equal, which seems reasonable, then the angle dependence of σ_ϕ^2 vanishes:

$$\sigma_\phi^2 = \sigma_\delta^2 + k^2 \sigma_x^2 \quad .$$

Finally, the $1 - P$ factor is obviously angle invariant.

Thus, we see that in many cases of practical interest, $\epsilon^2(\nu)$ is only weakly angle dependent. For these cases, noting that

$$\frac{1}{4\pi}\int \frac{f^2(\nu)}{f^2(\nu_0)}\,d\Omega = \frac{1}{4\pi f^2(\nu_0)/\int f^2(\nu)\,d\Omega} = \frac{1}{u(\nu_0)} \qquad (88)$$

where $u(\nu_0)$ is the element directivity in the ν_0 direction, we have

$$U(\nu_0) = \cfrac{1}{U_0^{-1}(\nu) + \cfrac{\epsilon^2}{u(\nu_0)\,\eta\,NP}} \quad .$$

By analogy to the gain formula for a large array [Part 3, Ch. I, Eq. (18)], which states that

$$G(\nu_0) = g(\nu_0)\,\eta\,N \quad ,$$

where $G(\nu_0)$ and $g(\nu_0)$ are the gains of the array and a typical element in its array environment, respectively, we can write the no-error array directivity as

$$U_0(\nu_0) = u(\nu_0)\,\eta\,N \quad .$$

Hence, we have the simple result.*

---

* Ruze gives (in our notation)

$$\frac{U(\nu_0)}{U_0(\nu_0)} \approx \frac{1}{1 + \frac{3}{4}\pi(\frac{D}{\lambda})^2\,\epsilon^2} \quad ,$$

where D/λ is the interelement spacing under the assumption of a specific element factor.

$$\frac{U(\nu_0)}{U_0(\nu_0)} = \frac{1}{1 + (\epsilon^2/P)} \quad . \tag{39}$$

For the values of ϵ^2/P necessary for good sidelobe control, the loss in gain is modest if N is not too large. For example, for the previously discussed 100- and 10,000-element arrays, if ϵ is chosen to hold all far-out sidelobes below 40 db with $P = 0.99$, the gain degradation is about 0.1 per cent and 5 per cent, respectively. However, if the sidelobe requirement for the 10,000-element array were relaxed to -30 db, it is found that an rms phase error (only) of 47.5° is allowable,[*] based solely on sidelobe requirements or an $\epsilon^2 = 0.69$. The gain degradation in this case is non-negligible: about 2 db.

Thus, for very large arrays with relaxed sidelobe requirements, gain degradation may be the limiting factor on errors.

---

[*] The small phase error approximation of Eq. (68) is not usable in this case. The above number was computed assuming Gaussian phase errors for which $C_\varphi(a) = 1 - (a^2\sigma^2/2)$. Consequently, by (68) and (36),

$$\frac{A(\nu)}{C_\varphi^2(1)} = \frac{1 - \sigma_\varphi^2/2}{\sigma_\varphi^2/2} = \epsilon^2 \quad .$$

F. SUPPRESSION OF GRATING LOBES BY RANDOMIZED ELEMENT SPACING

Summary

In this section, the ability to suppress grating lobes by the use of randomized element spacing is examined. It is shown that such randomization is capable of suppressing grating lobes; however, the effectiveness of this technique is seen to be strongly dependent on the number of elements in the array. It is shown that the grating-lobe suppression follows a modified Rayleigh distribution, the variance of which, for a substantial suppression of the grating lobe, becomes only a function of the number of elements in the array and the array taper efficiency. Curves are presented for the probability of suppressing grating lobes on arrays of 16 and 500 elements.

It is shown that the randomization of the grating lobes has little effect on the sidelobe structure of the array close to the main beam (ignoring the possible substantial errors in array illumination due to mutual coupling effects between the nonuniformly spaced elements), but in the region around the grating-lobe location, the sidelobes are likely to be as large as the suppressed grating lobe.

Finally, one particular pdf for the element spacing randomization is examined in detail, and a probabilistic description is given for the grating-lobe suppressing for arrays with $\eta N = 16$, 50 and 500.

The results obtained by the randomized element spacing are compared with the results of an investigation of nonrandom, nonuniform element spacing in arrays and shown to be roughly commensurate.

1. The Normal Constraints on Element Spacing

It is well known that to marginally prevent* the formation of grating lobes in scanning arrays with attendant loss in main beam gain and possible directional ambiguity, the projected element spacing in the plane of interest must satisfy

$$\frac{D}{\lambda} \leq \frac{1}{1 + \sin|\theta_{max}|} \quad , \tag{90}$$

where ξ_{max} is the maximum angle of scan of interest in the plane, measured from broadside, assuming the elements have little directivity in their own right. On the other hand, if the elements are directive, they can be spaced farther apart, with the narrow element beamwidth at least partially suppressing the grating lobes for angles of scan that are small. Even in this case, however, it is evident that one will have lost approximately 3 db in array gain when the angle of scan is such that the main lobe and first grating lobe are symmetrically disposed about broadside, which occurs at a scan angle given by

$$\sin|\xi_{max}| = \frac{1}{2D/\lambda} \quad . \tag{91}$$

---

* The criterion puts a grating lobe at endfire when the beam is scanned to ξ_{max}.

It is therefore apparent that the basic limitation on element spacing is the grating-lobe formation. The question then follows: Can the grating lobes be suppressed? If so, how well and at what price?

2. Nonuniform Element Spacing and Some Limitations and Cautions

The obvious approach to grating-lobe suppression is to remove the periodicity from the array factor, which can be done by use of nonuniform element spacing. Several papers have been published on the use of nonuniform spacing, ranging from presentations of formal synthesis techniques[*†] to presentations of results of enlightened "cut and try" procedures.[‡] As yet, however, little information has been obtained on the ultimate possibilities of such techniques.

A statistical analysis based on randomizing the element positions according to some pdf has the virtue of indicating some of the limitations of nonuniform spacings, at the expense of an explicit description of the resulting field. While this writer would not care to make a flat statement that a description based on randomized spacing is applicable to what one might expect from a carefully chosen systematic nonuniform spacing, the results will be seen to agree reasonably well (in a probabilistic sense) with the results of King, et al., for systematic nonregular spacings.

Before undertaking an analysis of the effect of random spacing, one very important limitation of such a technique should be emphasized. It was seen in Ch. I that in large, uniformly spaced arrays, the effect of the mutual impedance was to make the element gain proportional to the element spacing, for angles near broadside, and (crudely) inversely proportional to spacing for angles for which grating lobes form for the indicated spacing. With a nonuniformly spaced array, if the nonuniformity is great (as we shall presently see it must be for effective grating-lobe suppression), the mutual coupling situation is quite complex. It would certainly seem likely to cause appreciable variation in element patterns from element to element, such variation being roughly proportional to the degree of nonuniformity present.

Since we will not attempt to include the effects of mutual coupling in the following analysis, the reader should beware of taking the results as the last word in accuracy until such mutual effects are evaluated.[§]

3. The Far-Field Description

In this section, we will investigate the use of one particular scheme of randomized spacing, i.e., we will start with a linear array of equally spaced elements, as indicated in Fig. 3-60, and perturb each element from its "no-error" position according to some specified pdf.

In mathematical formulation, the nth element is assumed to be located at $z_n = nD + d_n$, where d_n is a sample of a random variable having a pdf $p(d_n)$ which is independent of n, and will be assumed to have mean zero.

Further, in order to insure that the error effects are essentially zero (excluding the mutual effects) near the main beam, the element phase will be chosen to be correct for the perturbed position:

* H. Unz, "Linear Arrays with Arbitrarily Distributed Elements," Report R-56 [U], Electronics Research Laboratory, University of California, Berkeley (2 November 1956).

† R.F. Harrington, "Sidelobe Reduction by Nonuniform Element Spacing," Trans. IRE, PGAP AP-9, 187 (1961).

‡ D.D. King, R.F. Packard and R.K. Thomas, "Unequally Spaced, Broad-Band Antenna Arrays," Trans. IRE, PGAP AP-5, 380 (1960).

§ A test array for nonuniform spacings is presently under construction by this project but will not be completed in time for this report.

$$\xi_n = a_n \exp[-jk(nD + d_n) \sin \xi_0] \quad ,$$

where we choose to use ξ, the complement of Θ as indicated in Fig. 3 60, as our angular variable. Thus, assuming no other errors, the far field of the array will be given by

$$F(\phi, \xi) = f(\phi, \xi) \sum_n a_n \exp[jk(nD + d_n)(\sin \xi - \sin \xi_0)] \quad . \tag{92}$$

In the main lobe, all errors vanish, and

$$F(\phi, \xi_0) = f(\phi, \xi_0) \sum_n a_n \quad . \tag{93}$$

In the absence of other errors, we have, from averaging (92), that

$$\overline{F(\phi, \xi)} = C_d[k(\sin \xi - \sin \xi_0)] F_0(\phi, \xi) \quad . \tag{94}$$

where $C_d(\alpha)$ is the characteristic function of the random variables d_n. In the grating-lobe regions, $\sin \xi_1 - \sin \xi_0 = l2\pi/D$, where l is an integer. Thus,

$$\overline{F(\phi, \xi_1)} = C_d(l2\pi/D) f(\phi, \xi_1) \sum_n a_n \quad . \tag{95}$$

Further, from (36) and (37), for this case

$$A(\xi) = 1 - C_d^2[k(\sin \xi - \sin \xi_0)] \quad , \tag{96}$$

$$B(\xi) = C_d[2k(\sin \xi - \sin \xi_0)] - C_d^2[k(\sin \xi - \sin \xi_0)] \quad . \tag{97}$$

Combining (95) and (96) with the variance expressions in (47a) and (47b) yields, in the grating-lobe region,

$$\sigma_x^2(\xi_1) = \frac{1}{2} f^2(\phi, \xi_1) [1 + C_d(l4\pi/D) - 2C_d^2(l2\pi/D)] \sum_n a_n^2 \quad , \tag{98}$$

$$\sigma_y^2(\xi_1) = \frac{1}{2} f^2(\phi, \xi_1) [1 - C_d(l4\pi/D)] \sum_n a_n^2 \quad . \tag{99}$$

From (93) and (94), it is seen that the ratio of the expected power density at the grating-lobe peak to the main beam power density, $\overline{R}_{gl}^{-2}$, is given by

$$\overline{R}_{gl}^{-2} = \frac{f^2(\xi_1)}{f^2(\xi_0)} C_d^2(l2\pi/D) \quad . \tag{100}$$

Thus, for significant reduction beyond that obtainable by the element factor alone, it is obvious that $C_d^2(l2\pi/D)$ must be small; e.g., for an expected 10-db reduction, $C_d^2(l2\pi/D) = 0.1$. Thus, $C_d(l4\pi/D)$ will usually be quite small also, and

$$\sigma_x^2(\xi_1) \approx \sigma_y^2(\xi_1) \approx \frac{1}{2} f^2(\xi_1) \sum_n a_n^2 \quad . \tag{101}$$

Thus, from previous analysis, R_{gl} will be distributed in the modified Rayleigh distribution in the form of Eq. (57):

$$p(R_{gl}) = \frac{R_{gl}}{\sigma_{gl}^2(\xi_1)} I_0 \left(\frac{R_{gl} R_A}{\sigma_{gl}^2(\xi_1)} \right) \exp \left[-\frac{R_{gl}^2 + R_A^2}{2\sigma_{gl}^2(\xi_1)} \right] \quad , \tag{102}$$
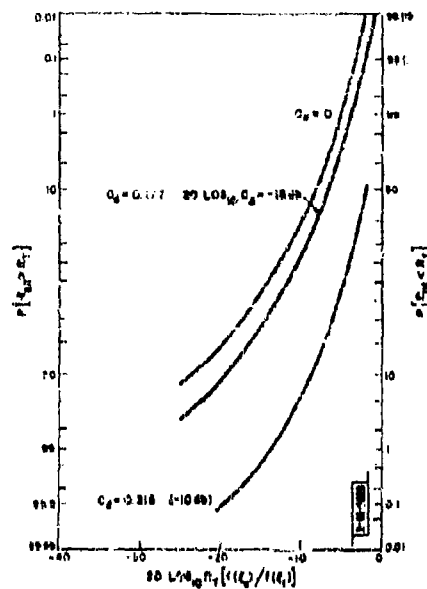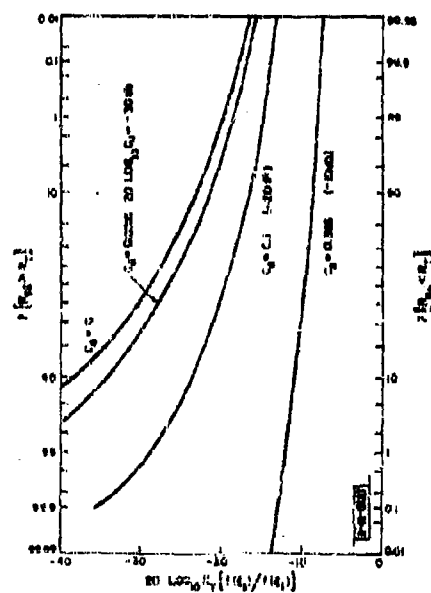
Fig. 3-67. Probability that a grating lobe exceeds R_T vs $C_d(12\pi)$ for array of $2\eta N = 32$.

Fig. 3-68. Probability that a grating lobe exceeds R_T vs $C_d(12\pi)$ for array of $2\eta N = 1000$.

where

$$R_A \cdot \frac{\overline{F(\xi_1)}}{F(\xi_o)} = \frac{f(\xi_1)}{f(\xi_o)} C_d(2\pi/D) \quad . \tag{103}$$

and, by (101) and (50),

$$\sigma_{g\ell}^2 = \frac{\sigma^2(\xi_1)}{F^2(\xi_o)} \approx \frac{1}{2} \frac{f^2(\xi_1)}{f^2(\xi_o)} \frac{1}{\eta N} \quad , \tag{104}$$

Hence,

$$\frac{R_A}{\sigma_{g\ell}} = \sqrt{2\eta N} \, C_d(2\pi/D) \tag{105}$$

The curves of Fig. 3-65 are thus applicable by replacing R_o by R_A and σ_R by $\sigma_{g\ell}$ as long as $C_d(2\pi/D)$ is small enough to justify the approximation of (104).

From Fig. 3-65, it is seen that if it is desired to suppress the grating lobe below some level R_T with probability P, the ability to do so is a strong function of N, the number of elements in the array. Since

$$20 \log_{10} \frac{R_T}{\sigma_{g\ell}} = 20 \log_{10} R_T + 10 \log_{10} 2\eta N - 20 \log_{10} \frac{f(\xi)}{f(\xi_o)} \quad ,$$

we can re-label the abscissa of Fig. 3-65, for a given ηN to create curves for grating-lobe suppression.

The resulting curves for $2\eta N = 32$ and $2\eta N = 1000$ are shown in Figs. 3-67 and 3-68, respectively. One of the most striking features about the curves of Fig. 3-67, for $2\eta N = 32$, is that the variance predominates the distribution to the point that even if $C_d(2\pi/D)$ is made vanishingly small, the grating lobe will be suppressed only about 13 db in half of the cases ($P = 0.5$), and on one pattern out of ten we should expect the grating lobe to be as high as only 5 db down. Thus, it is apparent that for an array of 16 or so elements, one is not likely to accomplish much grating-lobe suppression by most of the sample distributions chosen from $p(d_n)$. From Fig. 3-68, it is apparent that the situation improves as the number of elements increases, but not with great rapidity.

4. The Effects of Randomized Spacing on Sidelobe Level

From Eqs. (67) and (96), we have that in the no-error sidelobe region

$$\sigma_R^2 = \frac{1}{2} \frac{f^2(\xi)}{f^2(\xi_o)} \frac{1 - C_d^2[k(\sin\xi - \sin\xi_o)]}{\eta N} \quad , \tag{106}$$

indicating that σ_R^2 varies from zero (no-error) at ξ_o to the value of $\sigma_{g\ell}^2$ of (104), near the grating lobes.

By (67a), the parameter of R_o of the sidelobe distribution is

$$R_o(\xi) = C_d[k(\sin\xi - \sin\xi_o)] \frac{F_o(\xi)}{F_o(\xi_o)} \quad , \tag{107}$$
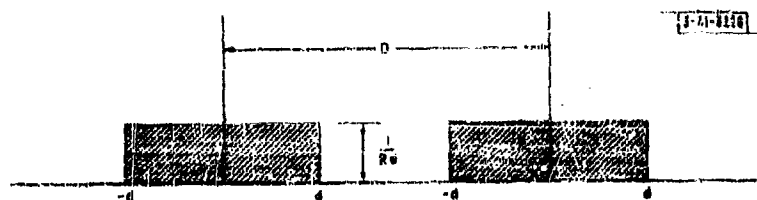
295

Fig. 3-69. Assumed probability density function of d_n.
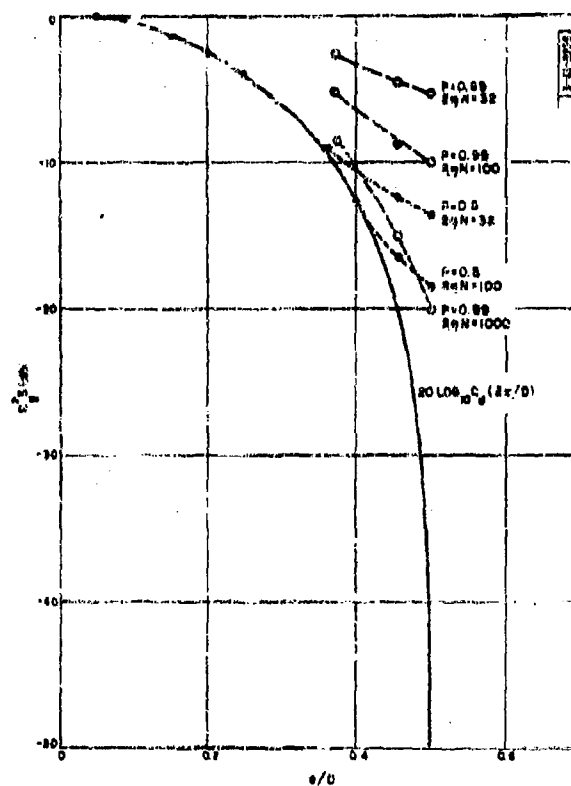

Fig. 3-70. Grating-lobe suppression vs d/D for

$$p(d_n) = \begin{cases} 1/2d, & |d_n| < d \quad , \\ 0, & |d_n| > d \quad . \end{cases}$$

indicating that for this type of angle-dependent error, $R_o(\nu)$ is not the no-error sidelobe ratio. Near the grating-lobe location,

$$R_o(\xi) \approx C_d(i2\pi/D) \frac{F_o(\xi_1)}{F_o(\xi_o)} \quad , \tag{108}$$

indicating that R_o will be suppressed in this region along with the grating lobes. Thus, we should expect errors to p. dominate the sidelobes in this region, and the curves of Figs. 3-67 and 3-68 for $C_d = 0$ should closely predict sidelobe levels.

5. A Numerical Example

To examine the implication of these results, let us consider a specific case:

$$p(d_n) = \begin{cases} \frac{1}{2d} \, , & |d_n| < d \\ 0 \, , & |d_n| > d \end{cases} \quad , \quad d < \frac{D}{2} \quad , \tag{109}$$

as indicated in Fig. 3-69. Then

$$C_d(i2\pi/D) = \int_{-d}^{d} \frac{1}{2d_n} \exp\left[j2\pi i \frac{d_n}{D}\right] d(d_n)$$

$$= \frac{\sin 2\pi i \frac{d}{D}}{2\pi i \frac{d}{D}} \quad . \tag{110}$$

The resultant probability of suppressing one grating lobe, for arrays of various sizes, is given in Fig. 3-70 for the assumed $p(d_n)$.

It is apparent from the figure that large grating-lobe suppressions are obtainable only if nearly all the "no-error" interelement spacing is available for perturbing the element position. Therefore, only elements whose physical size is small compared to D are of potential usefulness with this technique, unless one is willing to attempt design using elements of different sizes, with attendant complexity in providing proper element drives to obtain satisfactory patterns. It is also apparent from the figure that the average grating-lobe suppression is of direct significance only for very large arrays.

The curves of Fig. 3-70 can also be used for sidelobe level information for the region near the grating lobe by locating the proper value of R_o as given by (108) and the no-error sidelobe level in question on the curve for $C_d(2\pi/D)$. The curve for the desired probability and number of elements will yield the range of sidelobe levels to be anticipated in the region near the grating lobe. For example, if the no-error array were uniformly illuminated, the sidelobe immediately adjacent to the normal grating-lobe location would be about 13 db down. The curves indicate that if a grating-lobe suppression of 10 db is desired with a 99 per cent probability on a 500-element array, $d/D \approx 0.4$ would be chosen, yielding $\overline{R_{g\ell}}^2 = -12.5$ db. Thus, $\overline{R_o}^2 = 25.5$ db, and any one adjacent sidelobe would be down at least 17.5 db with a 99 per cent probability.

It should be pointed out that the pdf assumed for d_n for this example is obviously not the best. A distribution more peaked at the edges would yield a characteristic function which would produce nulls for smaller d/D ratios. Theoretically (at least in the sense of the existence of point sources), there is probably little reason to be restricted to less than D/2, and we could randomize

over several lin... ...spacings. However, for small numbers of elements, it is apparent that little would be ... ...the predominance of errors over averages. For large arrays, the limitation ... ...be the physical size of the antenna elements which limits the allowable dispersion.

6. Comparison with Nonrandom Spacings

King, et al.[*] ...puted array factors for five nonuniform spacing schemes applied to arrays of about 20 elements. The ratios of minimum to maximum spacing chosen were of the order of 1.5 to 1 up to ...5 to ... corresponding to values of d/D of 0.1 to 0.28 (the "correspondence" is admittedly rough). All patterns tended to have lobes near the grating-lobe region that were only 5 or 6 db below the main beam, although the pattern with the most "dispersion" had only two lobes out of 25 above about -5 db in the region out to and including the first grating-lobe location. Granting the possibility that the methods chosen for element spacing correspond roughly to a narrower characteristic function, it is nonetheless apparent that the results are being limited basically by the small number of elements used.

[*]D. D. King, et al., "Unequally-Spaced, Broad-Band Antenna Arrays," Trans. IRE, PGAP AP-8, 380 (1960).

L. BEAM SHAPING BY OMISSION OF ELEMENTS ("SPACE TAPERING" OR "DENSITY TAPERING")

Summary

The question of array pattern shaping by varying the density of active elements rather than the amplitude of the element drives is examined in a probabilistic analysis. It is shown that the density taper can be compared to an array with an amplitude taper of the same character, and that the main beam structures of the two arrays are essentially identical. The density tapered array will have less gain than the amplitude tapered array for the same array area, but the difference may be made quite small if the maximum density of active elements is maintained. The decrease in array gain raises the far-out sidelobe level of the density tapered array.

Simple formulas are developed for the expected density tapered directivity and sidelobe ratio in terms of the equivalent amplitude taper, and curves and examples are given for "cosine-squared-on-a-pedestal" tapers for both linear and circular planar arrays.

1. Introduction

It has been known for some time that it is possible to shape the beam of an array by judicious deletion of the drive from elements of a regularly spaced grid, combined with passive termination of the antennas from which the drive has been removed (the latter to regularize the environment the element antennas "see" to avoid pattern deterioration due to mutual effects).

Although the above statement is made in a transmitting array frame of reference, it applies by reciprocity to receiving arrays using a receiver behind each element. It is, however, perhaps most important when viewed from a transmitting context, since there are several methods for synthesizing receiving arrays without the use of individual element receivers. However, for achieving the full promise of arrays for high peak power operation, there appears to be no substitute for a large number of transmitters. Further, to avoid problems of switching high powers at microsecond rates, it appears advisable to put the individual transmitters behind the radiators in many systems.

It is well known that for efficient operation, transmitters should be operated in a saturated mode. Thus, amplitude tapering such a transmitting array for low sidelobes or a shaped beam requires either a considerable sacrifice in efficiency or a fabrication of several different transmitters to operate efficiently at different power levels.

It is known by "cut and try" approaches[*] that if one conceptually constructs an array without amplitude taper and then deletes element drives in such a manner that a plot of the "density" of active elements becomes similar in shape to some desirable amplitude taper, one achieves pattern structure which, at least close to the main lobe, resembles that of the corresponding amplitude taper. In fact, it has been found that such a technique can be used to drastically reduce the number of active elements in an array of a given area while still retaining a beam shape roughly equivalent to a "full" array. However, the gain, and consequently the average sidelobe level, is still dictated by the number of active elements.

---

[*] F.C. Ogg, Jr., "Steerable Array Radars," Trans. IRE, PGMIL MIL-5, 00 (1961).

In this section, we present a probabilistic analysis of this "density tapering" technique which, while not removing the necessity for a good deal of "cut and try" in the design of such tapers, does shed qualitative light on some of the aforementioned observations of the properties of such elements. The analysis was suggested by a similar analysis carried out by Cogdell[a] on the effects of completely random element placement.

The analysis will be carried out for a linear array to simplify notation, but the results are directly applicable to planar arrays and will be so applied in the examples.

2. The Statistics of the Far-Field

We begin by postulating an equally spaced array, with no amplitude taper, in which the probability that the nth element is active is a_n, so that obviously

$$0 \leqslant a_n \leqslant 1 \quad .$$

We will ignore all other errors, which assumes all inactive elements are terminated in a passive impedance equal to the driving impedance of the active elements, so that all element patterns are nominally equal.

Thus, the drive current, i_n, to the nth element can be stated probabilistically as

$$i_n = r_n e^{-jn\nu_0} \quad ,$$

where r_n is unity with probability a_n, and zero otherwise.

Thus, the far-field is

$$F(\nu) = f(\nu) \sum_n r_n e^{jn(\nu - \nu_0)} \quad . \tag{111}$$

The average power density is

$$\overline{P(\nu)} = \overline{|F(\nu)|^2}$$

$$= f^2(\nu) \sum_m \sum_n \overline{r_m r_n} \exp\{j(m - n)(\nu - \nu_0)\} \quad . \tag{112}$$

The distribution of r_n is such that

$$\overline{r_n} = a_n \quad ,$$

$$\overline{r_n^2} = a_n \quad ,$$

and consequently, performing the indicated averaging of (112) gives

$$\overline{F(\nu)} = \left| f(\nu) \sum_n a_n \exp\{jknD(\nu - \nu_0)\} \right|^2 + f(\nu)^2 \sum_n a_n (1 - a_n) \quad . \tag{113}$$

---

[a] J. R. Cogdell, private communication.

Near the peak of the main beam, the first summation is of order N^2, while the second is of order N.

Thus, it is seen that near the peak of the main beam, the first term predominates. This term is seen to be just the power density emitted from an array with amplitude taper, a_n.

To examine the effect of the density taper on the sidelobe region, we note that if (113) is normalized to a peak value of unity, we have

$$\bar{p}(\nu) = p_0(\nu) + \left|\frac{f(\nu)}{f(\nu_0)}\right|^2 \frac{\Sigma\, a_n(1 - a_n)}{(\Sigma\, a_n)^2} \quad , \tag{114}$$

where $p_0(\nu)$ is the no-error pattern normalized so that $p_0(\nu_0) = 1$. We assume the sidelobe ratio to be modified Rayleigh distributed as in Eq. (65) with $R_m(\cdot)$ the no-error sidelobe ratio associated with an amplitude taper a_n. The variance in sidelobe ratio, σ_R^2, is easily obtained by recalling that the mean square value of a Rayleigh distributed ($R_m = 0$) variable is $2\sigma^2$. Thus, from (114),

$$\sigma_R^2 = \frac{1}{2}\left|\frac{f(\nu)}{f(\nu_0)}\right|^2 \frac{\Sigma\, a_n(1 - a_n)}{(\Sigma\, a_n)^2} \quad . \tag{115}$$

We note that the taper efficiency of the equivalent amplitude taper η is given by

$$\eta N_T = \frac{(\Sigma\, a_n)^2}{\Sigma\, a_n^2} \quad . \tag{116}$$

where N_T is the total (active plus inactive) number of elements. By use of (116), we can write (115) in the form

$$\sigma_R^2 = \left|\frac{f(\nu)}{f(\nu_0)}\right|^2 \frac{\left(\dfrac{\Sigma\, a_n}{\Sigma\, a_n^2} - 1\right)}{2\eta N_T} \quad , \tag{117}$$

which, by comparison with Eq. (69), indicates that for a density taper, the sidelobe behavior is that of an N_T element array with equivalent amplitude taper a_n, with an error variance analogous to ϵ^2/P of (69) given by

$$\frac{\epsilon^2}{P} = \frac{\Sigma\, a_n}{\Sigma\, a_n^2} - 1 \quad . \tag{118}$$

Note that, by (117)

$$\frac{\Sigma\, a_n}{\Sigma\, a_n^2} = \frac{\eta N_T}{N_A} \quad , \tag{119}$$

where $N_A = \Sigma\, a_n$ is the expected number of active elements in the array.

To evaluate the effect of space tapering on sidelobe levels and gain, the value of (118) was computed for an array density of the "cosine-squared on a pedestal" class

$$a(x) = \begin{cases} P[h + (1-h)\cos^2 \frac{\pi x}{L}] & , \quad |x| \leqslant L/2 \\ 0 & , \quad |x| > L/2 \end{cases}$$

for a centered array, where $a_n = a(nD)$, and P denotes the maximum density ($P \leqslant 1$) in the center of the array, where the term in brackets is unity. Thus, h represents an "element thinning factor."

By the use of integrals rather than summations, it is found that for a large array

$$\frac{\sum a_n}{\sum a_n^2} \approx \frac{1}{P} \frac{4(1+h)}{3 + 2h + 3h^2}$$

Thus, the solid curves of Fig. 3-71 can be computed for ϵ^2/P for various values of P. The ratio of the number of active elements to the total can be determined from the curves of Fig. 3-71 by (118) and (119) to be

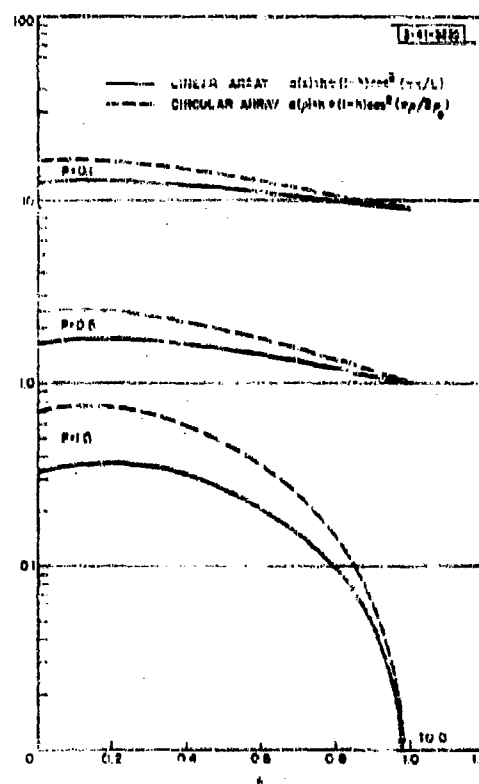$$\frac{N_A}{N_T} = \frac{\eta}{\epsilon^2/P + 1}$$

Fig. 3-71. Curves of ϵ^2/P for density taper for cosine-squared-on-a-pedestal taper.

For comparison, (118) can be simply generalized to a planar array:

$$\frac{\epsilon^2}{P} = \frac{\sum_m \sum_n a_{mn}}{\sum_m \sum_n a_{mn}^2} - 1 \quad . \tag{120}$$

For comparison to the linear array case, if a cosine-squared taper is assumed for a circular array,

$$a(\rho) = \begin{cases} P\left[h + (1 - h) \cos^2 \frac{\pi\rho}{2\rho_o}\right] & , \quad \rho \leqslant \rho_o \quad , \\ 0 & , \quad \rho > \rho_o \quad . \end{cases}$$

It is found that

$$\frac{\sum \sum a_{mn}}{\sum \sum a_{mn}^2} \approx \frac{1}{P} \cdot \frac{\left(\frac{1}{4} - \frac{1}{\pi^2}\right) + h\left(\frac{1}{4} + \frac{1}{\pi^2}\right)}{\left(\frac{3}{16} - \frac{1}{\pi^2}\right) + \frac{h}{8} + h^2\left(\frac{3}{16} + \frac{1}{\pi^2}\right)} \quad ,$$

from which the dashed curves of Fig. 3-71 are computed.

3. The Effect of Density Taper on Array Far-Out Sidelobe Level

In the regions of the pattern where errors predominate ($R_m/\sigma_R \ll 1$), the curves of Fig. 3-65 indicate that the 50 per cent probability sidelobe ratio is about 1.2 σ_R, and the 99 per cent probability ratio is about 12 σ_R^2. If we ignore the element factor in (118), and concentrate attention on $h = 1/3$, which yields a first sidelobe level of about -25 db for both the linear and circular array, it is seen that:

(a) For the linear array, it is easily verified that $\eta = 8/9 \approx 0.89$ and for this value of h, and if the density of elements near the center is maximum ($P = 1$),

$$\sigma_R^2 \approx \frac{0.2}{N} \quad ,$$

indicating the average sidelobe ratio to be about 7 db below 10 $\log_{10} N$, and a 99 per cent sidelobe ratio about 3 db above that value.

If P becomes appreciably less than unity,

$$\frac{\epsilon^2}{P} \approx \frac{1}{P} \quad ,$$

and

$$\sigma_R^2 \approx \frac{1}{2\eta NP} \quad ,$$

or, for $\eta = 0.85$,

$$\sigma_R^2 \approx \frac{0.59}{NP} \quad ,$$

for an average sidelobe ratio about 3 db below 10 log NP, and a 99 per cent ratio about 7 db above.

303

(b) For the circular array, for $h = 1/3$, $\eta \approx 0.85$, and for $P = 1$,

$$\sigma_R^2 \approx \frac{0.4}{N}$$

indicating an average sidelobe ratio about 4 db below $10 \log_{10} N$, etc.
For $P \ll 1$, the value approached is approximately the same as for the linear case.

Thus, it is seen that density tapering tends to render the far-out sidelobe level essentially dependent upon the number of active elements in the array, particularly for $P < 1$ and/or for low sidelobe tapers.

4. The Effect of Density Taper on Directivity and Number of Active Elements

By analogy to Eq. (89), the ratio of the directivity of a density tapered array $U_d(\nu_o)$, compared to an array with the equivalent amplitude taper $U_a(\nu_o)$, is

$$\frac{U_d(\nu_o)}{U_a(\nu_o)} = \frac{1}{1 + \dfrac{\Sigma a_n}{\Sigma a_n^2} - 1} \qquad (121a)$$

or by (119),

$$\frac{U_d(\nu_o)}{U_a(\nu_o)} = \frac{N_A}{\eta N_T} \qquad (121b)$$

From Eq. (121a) and the curves of Fig. 3-74, it is seen that if $P = 1$, the difference in directivity for an amplitude tapered and an equivalent density tapered array is less than 1.5 db for a linear array and about 2.2 db for a planar array. For the value $h = 1/3$ of the previous example, for $P = 1$, it is found that

(a) For a linear array, $N_A/N_T \approx 0.67$.

(b) For a circular array, $N_A/N_T \approx 0.51$.

indicating that one saves about 1/3 or 1/2 of the required number of active elements for this taper. Note that (121b) also implies that for a fixed number of active elements, one may increase the gain of the array for a fixed sidelobe level by "spreading out" the elements in a space taper instead of amplitude tapering.

5. Conclusions

The analysis of this section has verified from a probabilistic standpoint the general properties attributed to density or space tapering, and has placed qualitative estimates on these properties.

It is seen that the density tapering technique does offer a convenient method of shaping the pattern of an array without amplitude tapering. The main beam structure is essentially the same as would be obtained with an amplitude taper having the same shape as the element density over the array. If the active elements are maintained at unity density in the center of the array (all elements near the center active), it has been shown that the difference in directivity (assuming all inactive antenna elements in place and passively terminated) between the amplitude tapered

array and the equivalent density tapered array is small (less than 2.5db for —25 db first sidelobes) and dependent upon the degree of tapering, with the amplitude taper having the greater gain for a fixed array area, while the density taper has greater gain for a fixed number of active elements. If the density in the array center is not maximum, the array directivity is reduced in proportion to the center density. The decrease in gain with the density taper is manifested in higher far-out sidelobes, the height of which are essentially dictated by the number of active elements, as is the directivity.

H. THE EFFECT OF RANDOM ERRORS ON THE POINTING ACCURACY OF ARRAYS

Summary

The following expressions for the rms pointing error of the sum and difference beams of an N-element array, for large N and small errors are proven:

$$\left(\frac{\Delta \nu}{\nu_s}\right)_{sum} = \frac{\sigma_\psi N}{2\pi\sqrt{P}} \frac{\left(\sum\limits_{n=-N_1}^{N_1} n^2 a_n^2\right)^{1/2}}{\sum\limits_{n=-N_1}^{N_1} n^2 a_n}$$

$$\approx \frac{\sigma_\psi L\sqrt{D}}{2\pi\sqrt{P}} \frac{\left(\int_{-L/2}^{L/2} x^2 a^2(x)\, dx\right)^{1/2}}{\int_{-L/2}^{L/2} x^2 a(x)\, dx}$$

where

L = ND is the array length,

P = fraction of operating elements,

σ_ψ = rms phase error (assumed: $\sigma_\psi^2 \ll 1$ radian),

a_n = sum beam amplitude taper, an even function of n for a centered array,

$a(x)$ = continuous function for which $a_n = a(nD)$,

$$N_1 = \begin{cases} \dfrac{N}{2}, & \text{if N is even,} \\[2mm] \dfrac{N-1}{2}, & \text{if N is odd,} \end{cases}$$

$\nu_s = 2\pi/N$, the equivalent of a "standard" beamwidth of $1/(ND/\lambda)$ radians.

For the difference beam under the assumption that the error contributed by each element to the sum and to the difference patterns is identical (unity correlation) the rms error

$$\left(\frac{\Delta \nu}{\nu_s}\right)_{diff} = \frac{\sigma_\psi N}{2\pi\sqrt{P}} \frac{\left(\sum\limits_{n=-N_1}^{N_1} d_n^2\right)^{1/2}}{\sum\limits_{n=-N_1}^{N_1} n d_n}$$

$$\approx \frac{\sigma_\psi L\sqrt{D}}{2\pi\sqrt{P}} \frac{\left(\int_{-L/2}^{L/2} d^2(x)\, dx\right)^{1/2}}{\int_{-L/2}^{L/2} x d(x)\, dx}$$

where d_n is the difference beam amplitude taper, an odd function of n, and $d(x)$ is a continuous function for which $d_n = d(nD)$.

It is seen that both errors are dependent (for small phase errors) only on the phase error variance, and are independent of σ_A^2, the amplitude variance. More exact expressions for large phase errors can be obtained from (122) for the sum beam and from (147) for the difference beam.

For common illumination functions, the ratios of summations of the above equations are of the order $1/N^{3/2}$, indicating that the dependence of $\Delta\nu/\nu_3$ on N is

$$\frac{\Delta\nu}{\nu_3} \propto \frac{1}{\sqrt{N}} \quad .$$

1. Introduction

In this section, we will consider the effect of random errors on the pointing accuracy of arrays. Since the use of monopulse for accurate angular determination has become common, we will investigate the effects of these random errors on both the sum and difference beams associated with a monopulse array. The results for this sum beam are, of course, applicable to the case where monopulse information is not used.

The effects of pointing accuracy of beams corresponding to the sum beams of this discussion have been investigated in published papers by Rondinelli[*] and Leichter.[†]

Rondinelli, whose investigation was limited to a few specific cases of array size, a few specific error variance values and uniform illumination only, nevertheless provided the key for both Leichter's investigation and for that following in pointing out the applicability of the Taylor Series Expansion technique used below.

Leichter approached the problem from the standpoint of line sources and inferred the array performance from this analysis. Although his final results were stated specifically only for uniform and Taylor illuminations, his result can be generalized to give a result of the same form as the result obtained here for the sum beam pointing error, differing by a factor of $\sqrt{2}$, which can be accounted for.

To the best of this author's knowledge, no one has investigated the question of the accuracy of the null position for monopulse difference patterns. Such will be presented herein, in a form applicable to generalized difference illuminations.

2. The Pointing Error of Monopulse Sum Beams

In this section, we will consider the effect of errors on the pointing accuracy of the sum beam of the monopulse pair. We will assume that the sum beam is given by

$$F_s(\phi,\nu) = f(\phi,\nu) \sum_n b_{s_n}(\nu)\, e^{j\phi_n(\nu)}\, e^{ju(\nu-\nu_0)} \quad , \tag{122}$$

where

$$\overline{b_{s_n}(\nu)} = P\, s_n \quad , \tag{123}$$

[*] L.A. Rondinelli, "Effects of Random Errors on the Performance of Antenna Arrays of Many Elements," 1959 IRE National Convention Record, Part I, pp. 174-189.

[†] M. Leichter, "Beam Pointing Errors of Long Line Sources," Trans. IRE, PGAP AP-8, 268 (1960).

where s_n is the no-error amplitude of the nth element illumination for transmitting a sum pattern (the receiving behavior is then inferred by reciprocity).

For convenience, we will assume the array to be centered on the z-axis of the coordinate system and take s_n to be an even function of n for all sum patterns.

The pointing direction of the sum beam will be defined as that angle at which the sum power pattern has zero slope. In order to arrive at any reasonable answer, it is necessary to neglect the effect of the average element pattern, although the variance in the element patterns can be considered. The effect of the element factor may by no means be trivial and, as a general rule, probably outweighs the effect of the random errors unless the array is very large.[*] Knowing the element factor, however, this effect is a systematic one and amenable to systematic calculation.

Thus, neglecting the element factor, the far-field power density as a function of ν can be written as

$$P(\nu) = \sum_m \sum_n b_{s_m}(\nu) \, b_{s_n}(\nu) \, \exp\{j[\psi_m(\nu) - \psi_n(\nu)]\} \, \exp[j(m-n)(\nu - \nu_0)] \quad . \quad (124)$$

In order to find the angle of zero slope, we would like to set the first derivative of the power pattern equal to zero. This derivative, which we will denote S, is given by

$$S(\nu) = j \sum_m \sum_n (m-n) \, b_{s_m}(\nu) \, b_{s_n}(\nu) \, \exp\{j[\psi_m(\nu) - \psi_n(\nu)]\} \, \exp[j(m-n)(\nu - \nu_0)] \quad . \quad (125)$$

To directly solve this equation for a zero in terms of the difference, $\Delta\nu$, between the desired pointing angle and the actual pointing angle seems impossible. However, an approximate solution can be obtained, as Rondinelli pointed out, by resorting to a Taylor Series approximation:

$$S(\nu) \approx S(\nu_0) + \Delta\nu \, S'(\nu_0) \quad , \quad (126)$$

and thus we have, setting $S(\nu)$ equal to zero,

$$\Delta\nu \approx -\frac{S(\nu_0)}{S'(\nu_0)} \quad , \quad (127)$$

The quantities involved are given by

$$S(\nu_0) = j \sum_m \sum_n (m-n) \, b_{s_m} \, b_{s_n} \, e^{j(\psi_m - \psi_n)} \quad , \quad (128)$$

and

$$S'(\nu_0) = - \sum_m \sum_n (m-n)^2 \, b_{s_m} \, b_{s_n} \, e^{j(\psi_m - \psi_n)} \quad , \quad (129)$$

from Eq. (125), where all angle-variable quantities (b_{s_n}, ψ_n) are henceforth understood to be evaluated at ν_0.

In order to infer the pdf for the quantity $\Delta\nu$, we again resort to the Central Limit Theorem, as pointed out by Leichter, since for large arrays the total pointing error is the sum of small errors in the vector direction of the contribution of each element. Under this assumption of a Gaussian pdf, we need only to determine the mean and variance of $\Delta\nu$ to completely describe the pdf of $\Delta\nu$.

_____

[*] For example, see W.P. Delaney in J.L. Allen, et al., op. cit., pp. 33-38.

However, immediate difficulties are incurred due to the factor of $S'(\nu_o)$ in the denominator of Eq. (127), since the average of quotients is not easy to come by. The relative magnitude of S and S', however, can be effectively utilized to circumvent this difficulty for a large array. From Eqs. (128) and (123), it is seen that the no-error value of $S(\nu_o)$ will be zero, since the a_n's are even functions of n. On the other hand, the value of $|S'(\nu_o)|$ in the absence of errors is

$$|S'(\nu_o)|_{no-error} = \sum_m \sum_n (m^2 - 2mn + n^2)\, a_m\, a_n$$

$$= 2 \sum_m m^2\, a_m \sum_n a_n \quad , \tag{130}$$

since sums of the form $\sum_m m\, a_m$ vanish due to the evenness of c_m. The indicated product of sums is of the order of N^4. Further, S' is a second derivative of the power pattern and, since the first derivative is zero in this region, a large variance in S' would imply considerable distortion in the main beam shape of the pattern. But, from the previous analysis of the effect of random errors on the far-field in the region near the main beam, it is apparent that the variance in the main beam region is small. Thus, since the average value of $S'(\nu_o)$ is large and its variance small, replacing S' by its average in the denominator of Eq. (127) will have little effect on the accuracy of the result. Thus, we can write $\Delta\nu$ as

$$\Delta\nu \approx -\frac{S(\nu_o)}{\overline{S'(\nu_o)}} \quad . \tag{131}$$

The value of $\overline{S'(\nu_o)}$ is found from (129) to be (noting from (129) that terms for $m = n$ vanish, as well as the cross product $(m \times n)$ terms):

$$\overline{S'(\nu_o)} = 2P^2 C_\psi^2(1) \sum_m m^2\, a_m \sum_n a_n \quad . \tag{132}$$

The mean value of the pointing angle will then be given by

$$\overline{\Delta\nu} = -\frac{\overline{S(\nu_o)}}{\overline{S'(\nu_o)}} \quad .$$

From Eq. (130), and the fact that $m \neq n$ terms of the summations are zero, and the fact that $\sum_m m\, a_m = 0$ due to the even nature of a_n, we have

$$\overline{\Delta\nu} = 0 \quad .$$

Thus, the average pointing error will be zero as one would physically expect. To compute the variance in $\Delta\nu$, noting that by (131) we first compute the variance in S given by $\overline{\Delta\nu^2} = \overline{S^2(\nu_o)}/(\overline{S'(\nu_o)})^2$.

$$\overline{S^2(\nu_o)} = -\sum_m \sum_n \sum_p \sum_q (m-n)(p-q)\, \overline{b_{a_m} b_{a_n} b_{a_p} b_{a_q}}\, \exp[j(\psi_m - \psi_n + \psi_p - \psi_q)] \quad . \tag{133}$$

The actual summation as indicated represents a formidable and tedious task, since the averages depend upon the equalities and inequalities among the indices. However, a good deal of the work can be avoided by noting certain characteristics of the sum dependent upon these equalities and inequalities among the various indices.

First, the sum is obviously zero for $m = n$ or $p = q$ or all four indices equal. Also, if the sum can be separated into two separable double summations involving the quantities $(m - n)$ and $(p - q)$ separately, the result will be zero due to the even character of the no-error amplitude illumination. Thus, one is left with only six distinct possible combinations of indices which will result in non-zero sums. These six can be enumerated as below with the understanding that no equalities other than those specifically mentioned for each case are permitted:

$$m \neq p \qquad n \neq p \qquad m \neq p; \; n \neq q$$
$$m \neq q \qquad n \neq q \qquad n \neq q; \; n \neq p$$

If one further investigates several trial sums of the above character, it soon becomes apparent that the sums will be of the order N^{ℓ}, where ℓ is proportional to the number of non-equal indices. Thus, for large arrays, significant contribution will only be obtained from the first four cases cited above. Thus, we can approximate the mean squared value of S for large arrays as (where a.i.d. signifies all indices distinct)

$$\overline{S^2(\nu_o)} = -P^4 C_\psi^4(1) \sum_m \sum_n \sum_p \sum_q (m - n)(p - q)\, a_m a_n a_p a_q$$
$$\text{(a.i.d.)}$$

$$-P^3(1 + \sigma_A^2)\, C_\psi^2(1)\, C_\psi(2) \left[\sum_m \sum_n \sum_q (m - n)(m - q)\, a_m^2 a_n a_q \right.$$
$$\text{(a.i.d.)}$$

$$+ \left. \sum_m \sum_n \sum_p (m - n)(p - n)\, a_m a_n^2 a_p \right]$$
$$\text{(a.i.d.)}$$

$$-P^3(1 + \sigma_A^2)\, C_\psi^2(1) \left[\sum_m \sum_n \sum_q (m - n)(n - q)\, a_m a_n^2 a_q \right.$$
$$\text{(a.i.d.)}$$

$$+ \left. \sum_m \sum_n \sum_p (m - n)(p - n)\, a_m^2 a_n a_p \right] \quad,$$
$$\text{(a.i.d.)}$$

where we must include the case of all indices distinct, although the fourfold sum is zero, due to terms of like indices which must be subtracted off in the manner of Eq. (iv) of Sec. B. Since we are free to interchange indices as desired, it is apparent that there are only two distinct sums represented in the last four terms of the above relationship, and the result can be further reduced to

$$\overline{S^2(\nu_o)} = -P^4 C_\psi^4(1) \sum_m \sum_n \sum_p \sum_q (m - n)(p - q)\, a_m a_n a_p a_q$$
$$\text{(a.i.d.)}$$

$$-2P^3(1 + \sigma_A^2)\, C_\psi^2(1)\, C_\psi(2) \sum_m \sum_n \sum_q (m - n)(m - q)\, a_m^2 a_n a_q$$
$$\text{(a.i.d.)}$$

$$-2P^3(1 + \sigma_A^2)\, C_\psi^2(1) \sum_m \sum_n \sum_q (m - n)(n - q)\, a_m a_n^2 a_q \quad.$$
$$\text{(a.i.d.)}$$

If one performs the indicated summations and subtracts out the forbidden combinations from the sums, it is found that the forbidden combinations are all also of order of N^2 or less, except for the first term where the exclusions of interest are the combination of indices that appear in the last two terms. Thus, one can neglect the other exclusions and work out the result (the exclusions of the first term of order N^3 cancel exactly) which is:

$$S^2(\nu_0) = 2P^3 [1 + \sigma_A^2] C_\psi^2(1) [1 - C_\psi(2)] \sum_m m^2 s_m^4 \left(\sum_n s_n \right)^2 .$$

(134)

Then, using (132), the variance in $\Delta\nu$ becomes

$$\overline{(\Delta\nu)^2} = \frac{[1 + \sigma_A^2] [1 - C_\psi(2)] \sum n^2 s_n^4}{2P C_\psi^2(1) (\sum n^2 s_n)^2} .$$

(135)

For small phase errors, using the approximation

$$C_\psi(\alpha) = 1 - \frac{\alpha^2 \sigma_\psi^2}{2} ,$$

(136)

we can make the approximation that

$$\frac{[1 + \sigma_A^2] [1 - C_\psi(2)]}{C_\psi^2(1)} = \frac{2\sigma_\psi^2 [1 + \sigma_A^2]}{1 - \sigma_\psi^2} \approx 2\sigma_\psi^2 ,$$

(137)

indicating that the result, as pointed out by Leichter, is independent of amplitude errors to a first order.

It is of interest to express the fractional pointing error in some sort of a meaningful standard. The beamwidth of most high-gain antennas in terms of radians is approximately

$$\theta_s = \frac{1}{ND/\lambda} ,$$

(138)

which in terms of ν yields the standard beamwidth

$$\nu_s = \frac{2\pi}{N} .$$

(139)

Thus, normalizing the variance in $\Delta\nu$ by this quantity, we have the result that the rms error in standard beamwidths is

$$\left(\frac{\Delta\nu}{\nu_s} \right)_{rms} = \frac{\sigma_\psi N}{2\pi\sqrt{P}} \frac{\left(\sum_{n=-N_1}^{N_1} n^2 s_n^2 \right)^{1/2}}{\sum_{n=-N_1}^{N_1} n^2 s_n} ,$$

(140)

where the sums extend over a range of n symmetrical about zero, so that $N_1 = N/2$ for even N and $(N - 1)/2$ for odd N.

It appears from (140) that the rms pointing error increases with increasing N. However, this is not the case as can be seen by inserting some values for the illumination function. For example, for the case of uniform illumination, $s_n = 1$ for all n, the ratio involving the s_n's approaches, for large even N,

$$\frac{\left(\sum\limits_{n=-N/2}^{N/2} n^2 s_n^2\right)^{1/2}}{\sum\limits_{n=-N/2}^{N/2} n^2 s_n} = \frac{\left(\sum\limits_{n=-N/2}^{N/2} n^2\right)^{1/2}}{\sum\limits_{r=-N/2}^{N/2} n^2} \underset{N \to \infty}{\approx} \frac{\frac{N^3}{12}}{\frac{N^3}{12}} = \frac{2\sqrt{3}}{N^{3/2}} \quad . \tag{141}$$

so that (140) becomes

$$\left(\frac{\Delta \nu}{\nu}\right)_{rms} \approx \frac{N}{\pi} \frac{\sigma_x}{\sqrt{NP}} \quad ,$$

indicating that the rms beam pointing error actually decreases with the square root of the number of elements, or equivalently, the variance in beam pointing is inversely proportional to the number of elements as has been seen to be the case where other variances related to the effect of random errors on arrays.

For the case of large arrays with illumination functions chosen as samples of some continuous function, $s(x)$,

$$s_n = s(nD) \quad ,$$

it is more useful to have the result expressed in integral notation. In making the change from summation to integral, it should be noted that an extra factor of D is required to give the summation the dimensions of area equivalent to the integral:

$$D \sum_{n=-N_1}^{N_1} s_n \exp[jknD \sin \xi] \approx \int_{-L/2}^{L/2} s(x) \exp[jkx \sin \xi] \, dx \quad , \tag{142}$$

and by successive differentiation with respect to $\sin \xi$,

$$D^{m+1} \sum_{n=-N_1}^{N_1} n^m s_n \approx \int_{-L/2}^{L/2} x^m s(x) \, dx \quad . \tag{143}$$

The result can then be expressed in either of the two equivalent forms

$$\left(\frac{\Delta \nu}{\nu_s}\right)_{rms} = \frac{\sigma_\phi N}{2\pi\sqrt{P}} \frac{\left(\sum\limits_{n=-N_1}^{N_1} n^2 s_n^2\right)^{1/2}}{\sum\limits_{n=-N_1}^{N_1} n^2 s_n} \tag{144a}$$

$$\approx \frac{\sigma_\phi L \sqrt{D}}{2\pi\sqrt{P}} \frac{\left(\int_{-L/2}^{L/2} x^2 s^2(x) \, dx\right)^{1/2}}{\int_{-L/2}^{L/2} x^2 s(x) \, dx} \tag{144b}$$

for large N.

Leichter's results can be shown to be expressible in this form, except that his results predict an rms error larger by $\sqrt{2}$ for the same σ_ϕ, N_1 and P. A close examination of Leichter's derivation (which was actually carried out for line sources, as indicated by the title) shows that

no assumed an error correlation function of the form $e^{-x/\Delta}$ for the line source errors. In his application of the results to arrays, Δ was set equal to the element spacing. However, when the array errors are assumed independent from element to element, the correlation function is zero outside an interval of one spacing. If one replaced Leichter's assumption of $\Delta = L/\lambda$ with the closer fitting assumption $\Delta = dD/\lambda$, equivalent results are obtained.

3. The Effect of Random Errors on the Pointing Accuracy of Monopulse Pattern Nulls

In this section, we will examine the effect of random errors on the null position of a monopulse difference pattern given by (neglecting the element factor)

$$F_d(\nu) = \sum_{n=-N_1}^{N_1} b_{d_n} e^{j\Psi_n} e^{jn(\nu-\nu_0)} \qquad (145)$$

where

$$\overline{b_{d_n}} = P d_n \qquad (146)$$

where d_n is the no-error illumination of the nth element when transmitting a difference pattern, the receiving case being identical by reciprocity. In order to place a null in the desired direction, the d_n's will be odd functions of n when the array is centered on a coordinate system ($d_{-n} = -d_n$).

The common methods of obtaining the so-called "sum" and "difference" patterns for monopulse angular determination are:

    (a) Adding and subtracting the outputs of two halves of an array as indicated in Fig. 9-72,

    (b) Adding and subtracting two adjacent beams from an array capable of forming simultaneous beams.

In either case, it seems likely that the error in the illumination associated with the sum beam and the illumination associated with the difference beam in any one element is likely to be highly correlated. The assumption will be made throughout this section that the errors are identical.

If the analysis of the error in the difference pattern pointing accuracy is pursued in the same manner as that for the sum beam (on the basis of determining the characteristics of the power pattern), the result will run into difficulty due to the fact that in the presence of errors, the power pattern "null" will not be zero. Furthermore, the power pattern does not contain "sense information" in that it cannot give information about the direction of the target from the beam center. Thus, instead of pursuing this analysis in the manner of the previous one, we will analyze the statistics of the function usually used† to determine monopulse accuracy, which we will designate the "angle estimator," $E(\Delta\nu)$. This function is obtained mathematically by taking the ratio of the difference pattern to the complex conjugate of the sum pattern:

$$E(\Delta\nu) = \text{Re}\left[j \frac{F_d(\nu)}{F_s^*(\nu)}\right] \qquad (147)$$

In the absence of errors, the term in brackets is a real function, since $F_d(\nu)$ is pure imaginary and $F_s(\nu)$ is pure real, and is almost a linear function of target displacement from the null (at

---

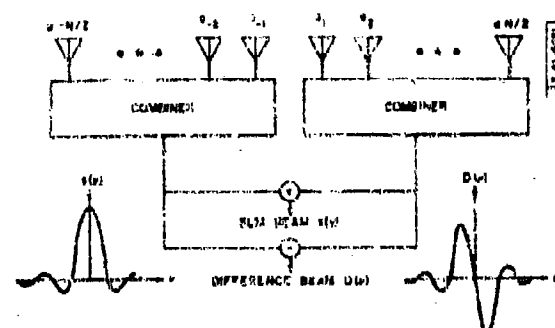† See Fig. 3-71 for an idealized circuit for forming $E(\Delta\nu)$.

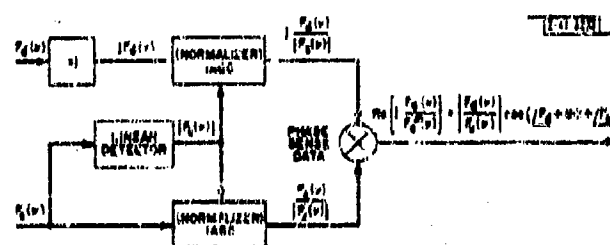Fig. 3-72. A method of realizing a set of monopulse beams.

Fig. 3-73. Circuit for monopulse angle estimator.

least for angles near the null. An idealized circuit for determining E is shown in Fig. 3-73, where the mathematical function of each "box" is indicated.

As was done for the sum beam, we will attempt to find the value of $\Delta\nu$ which reduces the estimator $E(\Delta\nu)$ to zero by the use of Taylor expansion. Performing this expansion gives

$$E(\Delta\nu) = E(\nu_0) + (\Delta\nu) \, E'(\nu_0) \quad . \tag{148}$$

Hence,

$$(\Delta\nu) \approx -\frac{E(\nu_0)}{E'(\nu_0)} \quad . \tag{149}$$

In evaluating $E'(\nu_0)$, to avoid difficulties due to the "real part" restriction, we note that $F_d(\nu)$ is a rapidly changing function of ν near ν_0, while $F_s(\nu)$ varies comparatively slowly; hence,

$$E'(\Delta\nu) \approx \mathrm{Re}\left[\frac{jF'_d(\nu_0)}{F_s^*(\nu_0)}\right] \quad .$$

Equivalently,

$$E'(\Delta\nu) = \frac{\mathrm{Re}[jF'_d(\nu_0) \, F_s(\nu_0)]}{|F_s(\nu_0)|^2} \quad .$$

Writing (147) similarly, we have

$$E(\Delta\nu) = \frac{\mathrm{Re}[jF_d(\nu_0) \, F_s(\nu_0)]}{|F_s(\nu_0)|^2} \quad .$$

By these results and the fact that $\mathrm{Re}(jz) = -\mathrm{Im}(z)$, we can write (149) in the form

$$\Delta\nu \approx -\frac{\mathrm{Im}[F_d(\nu_0) \, F_s(\nu_0)]}{\mathrm{Im}[F'_d(\nu_0) \, F_s(\nu_0)]} \quad . \tag{150}$$

Let us examine the denominator of the above equation in the hope that we can, with little error, replace the denominator by its average as was done in the examination of the sum beam case, thus circumventing formidable difficulties in computation. From Eq. (145) for the difference far-field, and Eq. (122) from the previous section for the sum far-field, the denominator of the expression can be written as

$$D = \left[\sum_m \sum_n m \, b_{d_m} \, b_{s_n} \, e^{j(\psi_{in} + \psi_n')}\right] \quad . \tag{151}$$

Hence, the average value of the denominator can be written as

$$\bar{D} = \left[\sum_m \sum_n m \, \overline{b_{d_m} \, b_{s_n}} \, e^{\overline{j(\psi_{in} + \psi_n')}}\right] \quad . \tag{152}$$

Averaging gives

$$\bar{D} = F\left\{ PC_\psi^2 \, (1) \left[\sum_m \sum_n m \, d_m \, s_n - \sum_m m \, d_m \, s_m\right] \right.$$
$$\left. + [(1 + \sigma_A^2) \, C_\psi \, (2)] \sum_m m \, d_m \, s_m \right\} \quad . \tag{153}$$

The second summation is zero due to the even and odd characteristics of the sum and difference illumination, respectively. Consequently, we can write the average value of the denominator as

$$\overline{D} = P\left\{PC_\psi^2(1) \sum_m m\, d_m \sum_n s_n + [(1 + \sigma_A^2)C_\psi(2) - PC_\psi^2(1)] \sum_m m\, d_m\, s_m\right\} \quad . \quad (154)$$

To develop a feeling for the order of this expression, let us assume a monopulse system of the first type cited earlier in this section where the sum illumination is uniform and phase errors are small. In this case, the average value of the denominator is simply (for large N)

$$\overline{D} \approx P\left\{(1 - \sigma_\psi^2)\frac{N^3}{6} + [(1 - F) + \sigma_A^2 - \sigma_\psi^2]\frac{N^2}{4}\right\} \quad .$$

Thus, the average value of the denominator is of the order of N^3 and will be quite large for large N (and it is also apparent that the second term can be neglected for $C_\psi^2(1)\, N \gg 1$).

Thus, the first requirement for replacing the denominator of Eq. (150) by its average value is fulfilled.

With regard to the variance of D, it is seen from Eq. (151) that D is the sum of N^2 terms, each of which is assumed to have small variance in phase and amplitude. Thus, by the Central Limit Theorem, the variance in D should be the sum of N^2 variances much less than unity. Since we have demonstrated that the average value of D is of order N^3, it is apparent that the variance will be small compared to the square of the average value. We are indeed justified in replacing the denominator of Eq. (150) by its average value for large arrays and write

$$\Delta\nu \approx \frac{Im[F_d(\nu_o)\, F_s(\nu_o)]}{P^2 C_\psi^2(1) \sum\limits_{m=-N_1}^{N_1} m\, d_m \sum\limits_{n=-N_1}^{N_1} s_n} \quad . \quad (155)$$

With this question resolved, it can then be stated that the numerator, $\Delta\nu$, is the sum of many independent contributions from the components of $F_d(\nu_o)$ and $F_s^*(\nu_o)$, and therefore by the Central Limit Theorem, will approach a Gaussian distribution. Thus, as with the sum beam error, we need only determine the mean and variance of $\Delta\nu$.

The average value of the numerator of Eq. (145) is given by

$$\overline{F_d(\nu_o)\, F_s(\nu_o)} = \sum_m \sum_n \overline{b_{d_m}\, b_{s_n}}\, \overline{e^{j(\psi_m + \psi_n)}}$$

$$= P^2 C_\psi^2(1)\left[\sum_m \sum_n d_m\, s_n - \sum_m d_m\, s_m\right]$$

$$+ P[1 + \sigma_A^2]\, C_\psi(2) \sum_m d_m\, s_m \quad . \quad (156)$$

By virtue of the even and odd character of the sum and difference illumination, it is seen that all sums vanish and, as one would physically expect, the average value of $\Delta\nu$ is zero.

The variance in $\Delta\nu$ is therefore given by

$$\overline{(\Delta\nu)^2} = \frac{\overline{\{Im[F_d(\nu_o)\, F_s(\nu_o)]\}^2}}{P^4 C_\psi^4(1)\left(\sum\limits_m m\, d_m\right)^2 (\Sigma\, s_n)^2} \quad . \quad (157)$$

The variance of the numerator, L, of this equation in terms of the illumination of the sum and difference pattern is given by the quadruple sum

$$L = \sum_m \sum_n \sum_p \sum_q \overline{b_{d_m} b_{s_n} b_{d_p} b_{d_q}} \; \overline{\sin(\psi_m + \psi_n) \sin(\psi_p + \psi_q)} \tag{158}$$

which can be written, by use of trigonometric identities,

$$L = \frac{1}{2} \sum_m \sum_n \sum_p \sum_q \overline{b_{d_m} b_{s_n} b_{d_p} b_{d_q}} \; \overline{[\cos(\psi_m + \psi_n - \psi_p - \psi_q)}$$

$$\overline{- \cos(\psi_m + \psi_n + \psi_p + \psi_q)]} \tag{159}$$

As was the case with the sum beam error, the complete summation as indicated would be extremely difficult, since the statistics vary with the degree of distinctness between the different indices. However, as with the sum beam error, we can greatly short circuit this process for large arrays.

First, it is apparent, due to the odd nature of the difference illumination, that only terms for which m and p are equal (those containing d_n^2) will yield non-zero sums. Furthermore, the absolute magnitude of each of the component sums arising from different combinations of indices will be of order N^ℓ, where ℓ is the number of distinct summations as indicated in the previous section. Thus, we are basically interested only in terms which yield at least three distinct sums. There are exactly two conditions which yield sums of this type. One such term can arise in the computation in the case where all indices are distinct from the subtraction process of Eq. (10) of Sec. B. This term is zero by virtue of the cosine term averages being equal.

The other highest-order sum arises directly from the case for the m and p indices equal and all others distinct, in which case we have

$$L = \frac{1}{2} \sum_m \sum_n \sum_q \overline{b_{d_m}^2 b_{s_m} b_{s_q}} \; \overline{[\cos(\psi_n - \psi_q)} - \overline{\cos(2\psi_m + \psi_p + \psi_q)]}$$
(a.i.d.)

where, as before, (a.i.d.) indicates all indices distinct. Since the like index terms which must be excluded are all of order less than the threefold summation,

$$L \approx \frac{1}{2} P^3 [1 + \sigma_A^2] C_\psi^2(1) [1 - C_\psi(2)] \sum_m d_m^2 \left(\sum_n s_n \right)^2$$

Hence, to a first order, we have a variance of $\Delta\nu$ given by

$$\overline{(\Delta\nu)^2} = \frac{[1 + \sigma_A^2][1 - C_\psi(2)]}{2PC_\psi^2(1)} \; \frac{\displaystyle\sum_{n=-N_1}^{N_1} d_n^2}{\left(\displaystyle\sum_{n=-N_1}^{N_1} n\, d_n \right)^2} \; . \tag{160}$$

The terms multiplying the summations are identical to those of (13); hence, for small errors we can write the rms fractional error for the difference beam estimate as

317

$$\left(\frac{\Delta \nu}{\nu_s}\right) = \frac{\sigma_\psi N}{2\pi\sqrt{P}} \frac{\left(\sum\limits_{n=-N_1}^{N_1} d_n^2\right)^{1/2}}{\sum\limits_{n=-N_1}^{N_1} n\, d_n} \quad . \tag{161}$$

As was the case for the sum beam error, it appears from the above equation that the rms pointing error increases with the number of elements. However, the ratio of the summation alters this variation. For example, if the d_n's are derived from uniform illumination, $d_n = 1$, $n > 0$ and $d_n = -1$, $n < 0$.

$$\frac{(\sum d_n^2)^{1/2}}{\sum n\, d_n} = \frac{(\sum 1)^{1/2}}{\sum\limits_n n} \underset{N \to \infty}{\approx} \frac{4}{N^{3/2}} \tag{162}$$

for large arrays, indicating that the variance actually is inversely proportional to the number of operating elements, PN.

Using the relationship between summations and integrals given in the previous discussions on the sum beam error, Eq.(161) can be expressed in integral notation [see Eq. (164) below].

4. A Summary of Results and Some Conclusions

We have the following expressions for the rms pointing error of the sum and difference beams of an N-element array for large N and small errors.

$$\left(\frac{\Delta \nu}{\nu_s}\right)_{sum} = \frac{\sigma_\psi N}{2\pi\sqrt{P}} \frac{\left(\sum\limits_{n=-N_1}^{N_1} n^2 s_n^2\right)^{1/2}}{\sum\limits_{n=-N_1}^{N_1} n^2 s_n}$$

$$\approx \frac{\sigma_\psi L\sqrt{D}}{2\pi\sqrt{P}} \frac{\left(\int_{-L/2}^{L/2} x^2 s^2(x)\, dx\right)^{1/2}}{\int_{-L/2}^{L/2} x^2 s(x)\, dx} \tag{163}$$

where

$L = ND$ is the array length,

P = fraction of operating elements,

σ_ψ = rms phase error (assumed: $\sigma_\psi^2 \ll 1$ radian),

s_n = sum beam amplitude taper, an even function of n for a centered array,

$s(x)$ = continuous function for which $s_n = s(nD)$,

$$N_1 = \begin{cases} \dfrac{N}{2}, & \text{if N is even,} \\[2mm] \dfrac{N-1}{2}, & \text{if N is odd.} \end{cases}$$

$\nu_s = 2\pi/N$, the equivalent of a "standard" beamwidth of $1/(ND/\lambda)$ radians.

Best Available Copy

For the difference beam, the rms error is

$$\left(\frac{\Delta\nu}{\nu_s}\right)_{\text{diff}} = \frac{\sigma_\psi}{2\pi\sqrt{P}} \left\{ \frac{\left(\sum\limits_{n=-N_1}^{N_1} d_n^2\right)^{1/2}}{\sum\limits_{n=-N_1}^{N_1} n\, d_n} \right\}$$

$$\approx \frac{\sigma_\psi \sqrt{P}}{2\pi\sqrt{P}} \left\{ \frac{\left(\int_{-L/2}^{L/2} d^2(x)\, dx\right)^{1/2}}{\int_{-L/2}^{L/2} x\, d(x)\, dx} \right\} \qquad (16)$$

where d_n is the difference beam amplitude taper, an odd function of n, and $d(x)$ is a continuous function for which $d_n = d(nl)$.

It is seen that both errors are dependent (for small phase errors) only on the phase error variance, and are independent of σ_A^2, the amplitude variance. More exact expressions for large phase errors are given by (135) for the sum beam and by (160) for the difference (the referenced equations give $\Delta\nu^2$, rather than $\Delta\nu/\nu_s$).

For common illumination functions, the ratios of summations of (135) and (160) are of the order $1/N^{3/2}$, indicating the true dependence of $\Delta\nu$ on N is

$$\Delta\nu \sim \frac{1}{\sqrt{N}} \quad .$$

For specific illuminations, the results can be simply expressed. For example, we have the following results for some simple cases:

Monopulse Type	Rms Sum Beam Error	Rms Difference Beam Error
Sum and difference of two halves of array (uniform sum taper, step difference taper)	$0.55 \dfrac{\sigma_\psi}{\sqrt{NP}}$	$0.64 \dfrac{\sigma_\psi}{\sqrt{NP}}$
Sum and difference of two adjacent beams (cosine sum taper, sine difference taper)	$0.67 \dfrac{\sigma_\psi}{\sqrt{NP}}$	$0.56 \dfrac{\sigma_\psi}{\sqrt{NP}}$

It will be recalled from our previous examples of the phase error allowable for good sidelobe control that in the case of phase errors only, the sidelobe ratio variance, given by (neglecting element factors)

$$\sigma_R^2 \approx \frac{\sigma_\psi^2}{\eta N} \quad ,$$

was required to be about 10 db below the desired far-out sidelobe level, say −30 to −40 db, indicating corresponding pointing errors of 3 per cent down to about 0.7 per cent. Thus, it is quite likely that if good sidelobe control is maintained, the beam pointing error due to random error effects will be small; and one should carefully examine other sources of beam pointing error (e.g., the element factor).